

	Document Nr. <b>AE-RP-DLR-L1B-001</b>	Issue: <b>4.4</b>	Date: <b>20.04.2018</b>	Page: <b>1/117</b>	
	Doc. Title: <b>ADM-Aeolus ATBD Level1B Products</b>				

<u>Doc.-Nr.:</u>	<b>AE-RP-DLR-L1B-001</b>
<u>Doc.-Title:</u>	<b>ADM-Aeolus</b> <b>Algorithm Theoretical Basis Document</b> <b>ATBD</b> <b>Level1B Products</b>
<u>Number of pages:</u>	117 pages
<u>Prepared by:</u>	Oliver Reitebuch (DLR, Oberpfaffenhofen, Germany, responsible) Dorit Huber (DoRIT, Munich, Germany) Ines Nikolaus (Physics Solution, Munich, Germany)

	Document Nr. <b>AE-RP-DLR-L1B-001</b>	Issue: <b>4.4</b>	Date: <b>20.04.2018</b>	Page: <b>2/117</b>	
	Doc. Title: <b>ADM-Aeolus ATBD Level1B Products</b>				

## Document Change Log

Issue	Date	New pages	Modified pages	Observations	Name
Draft	23.02.2005	--	--	Draft	Reitebuch
1.0	18.03.2005			Version 1.0	Reitebuch, Huber, Nikolaus
1.1	31.05.2005	27	9,11, 19, 26, 28, 43, 46, References in text, TOC, chapter 4.2.3 and 4.2.4 swapped	Version 1.1. with e-mail comments from H. Nett from 06.04.2005 included	Reitebuch, Huber
2.0	10.05.2006			inclusion of ESA comments from 14.06.2005, content for chapter 2, 3 included, update of chapter 1, 4, 5, 9, 10, 11 no update of chapter 6,7,8 except inclusion of ESA comments	Reitebuch, Huber, Nikolaus, Paffrath
3.0	30.11.2006			inclusion of ESA comments from 31.05.06; changes are marked in blue except for minor, editorial changes	Reitebuch, Huber
4.0	02.02.2012	52-66	ch. 2 and ch. 4	chapter 8.3 (Rayleigh wind processing) included; chapter 11 (references) extended; chapter 2 and 4 revised for instrument updates to continuous mode	Reitebuch
4.1	18.07.2014	69-76, 86,- 87	Ch. 1-11	Inclusion of ESA comments from 02.02.2012, Revision of Chapter 1-10, order of ch. 8.2 and 8.3 reversed and extended, changes highlighted in blue	Reitebuch, Huber
4.2	10.07.2017	28, 43, 46, 50	Ch. 1-11	revision of all chapters; inclusion of ESA comments from Sep 2014 and AE- IPF-160 comment 152	Reitebuch, Huber
4.3	24.11.2017	83-99	Ch. 1-13	new ALADIN instrument parameters and L1B processing parameters, new ch. 9 about IRC included	Reitebuch
4.4	20.04.2018		all chapters	revision after review by Th. Kanitz (ESA)	Reitebuch
4.5	end 2018		Ch. 10	inclusion of Ch. 10 planned for end 2018	Reitebuch
5.0	end 2019			update of ATBD with experience of first in-orbit	

	Document Nr. <b>AE-RP-DLR-L1B-001</b>	Issue: <b>4.4</b>	Date: <b>20.04.2018</b>	Page: <b>3/117</b>	
	Doc. Title: <b>ADM-Aeolus ATBD Level1B Products</b>				

## Table of Contents

Document Change Log .....	2
Table of Contents .....	3
1 Introduction and Purpose of Document .....	5
2 ADM-Aeolus Mission Overview and Requirements .....	6
3 Lidar Principle and Atmospheric Processes .....	8
3.1 Lidar Principle .....	8
3.2 Beam Propagation and Range Equation .....	9
3.3 Aerosol and Molecular Scattering .....	9
3.4 Doppler-Shift and Spectral Lineshape of Aerosol and Molecular Return .....	13
3.5 Earth Background Radiation .....	15
4 ALADIN Instrument .....	16
4.1 Overview .....	16
4.2 Laser Transmitter .....	19
4.3 Telescope and Front Optics .....	19
4.4 Mie Spectrometer MSP .....	20
4.5 Rayleigh Spectrometer RSP .....	21
4.6 Detection Front End Units DFU and ACCD .....	22
4.7 Instrument Operation .....	24
4.7.1 Timing Sequence within one Observation .....	24
4.7.2 Timing Sequence within one Laser Pulse Acquisition .....	24
4.7.3 Instrument Modes .....	24
5 Data Product Content .....	29
5.1 Raw Telemetry Data .....	29
5.2 General Data Product Structure .....	30
5.3 Level 0 .....	31
5.4 Level 1A .....	32
5.5 Level 1B .....	33
5.6 Auxiliary Calibration Products .....	35
6 Geolocation, Coordinate Systems, and AOCS Processing .....	37
6.1 Coordinate Systems .....	38
6.1.1 J2000 Reference Frame .....	38
6.1.2 LVLH Frame .....	38
6.1.3 Pitch, Roll and Yaw .....	39
6.1.4 ECEF Frame .....	39
6.1.5 Geodetic Coordinates .....	40
6.2 Orbit .....	40
6.3 Surface Reference Systems .....	40

	Document Nr. <b>AE-RP-DLR-L1B-001</b>	Issue: <b>4.4</b>	Date: <b>20.04.2018</b>	Page: <b>4/117</b>	
	Doc. Title: <b>ADM-Aeolus ATBD Level1B Products</b>				

6.3.1	WGS84 reference ellipsoid .....	41
6.3.2	Geoid Correction.....	41
6.3.3	Digital Elevation Model .....	41
6.4	Geometrical Processing .....	42
6.4.1	Attitude and Orbit Control System Data .....	42
6.4.2	Satellite Attitude .....	42
6.4.3	Earth Locations of Observations.....	42
6.5	Time .....	43
7	Algorithm Theoretical Baseline L0 and L1A Products.....	44
7.1	Processing from raw data to L0 .....	44
7.1.1	Pseudo-Algorithm for Extracting and Sorting .....	44
7.1.2	Pseudo-Algorithm for Validation .....	45
7.2	Processing from L0 to L1A.....	45
7.2.1	Housekeeping Processing .....	45
7.2.2	Reference Pulse Processing .....	45
7.2.3	MSP and RSP Data Processing .....	46
7.2.4	Data Quality Processing .....	46
8	Algorithm Theoretical Baseline L1B Products.....	47
8.1	Wind Velocity Determination.....	48
8.1.1	Quality Control and Averaging of Measurements to Observations .....	49
8.1.2	Correction of Detection Chain Offset.....	50
8.1.3	Determination of Mean Frequency of Atmospheric signal and Internal Reference .....	50
8.1.4	Determination of the Frequency Shift from the Atmospheric Wind Velocity.....	52
8.1.5	Determination of LOS and HLOS Velocity.....	53
8.2	Wind Measurement Processing Rayleigh.....	55
8.2.1	General description of double-edge wind retrieval method .....	55
8.2.2	Specific implementation for ALADIN Rayleigh wind retrieval .....	61
8.3	Wind Measurement Processing Mie .....	71
9	Instrument Response Calibration.....	84
9.1	Mie response calibration .....	86
9.2	Rayleigh Response Calibration.....	93
10	Additional algorithms .....	101
10.1	Ground Return Detection and Harmonic Bias Estimator .....	101
10.2	Signal Amplitude, SNR and Scattering Ratio for Mie .....	101
10.3	Signal Amplitude and SNR for Rayleigh .....	101
10.4	Quality Control and Quality Flags, Corrupted Data, Error Quantifiers .....	101
11	Abbreviations .....	102
12	Symbols and Constants.....	106
	References .....	110

	Document Nr. <b>AE-RP-DLR-L1B-001</b>	Issue: <b>4.4</b>	Date: <b>20.04.2018</b>	Page: <b>5/117</b>	
	Doc. Title: <b>ADM-Aeolus ATBD Level1B Products</b>				

## 1 Introduction and Purpose of Document

The Algorithm Theoretical Basis Document ATBD defines the theoretical basis for the ADM-Aeolus ground processing algorithms up to Level 1B (geolocated horizontal line-of-sight wind observations). It covers Task 1.5 of the SoW AE-SW-ESA-GS-011, Issue 01a (ESA 2004a), DLR Technical proposal Work-Package WP15000 (DLR 2004a) and WP 1200 from DLR (2014).

This ATBD will be updated regularly. A first issue of the ATBD (1.0 from 31.05.2005) was prepared by Oliver Reitebuch (DLR, responsible), Dorit Huber (DLR), and Ines Nikolaus (PSoL). Ulrike Paffrath (DLR) contributed to the second issue from 10.05.2006. This third issue was updated after the final delivery of the TN for the L1B sensitivity analysis (DLR 2006, AE-TN-DLR-L1B-002). The 4<sup>th</sup> and 4.1<sup>th</sup> issue was updated by Reitebuch and Huber after the delivery of Issue 6 and 7 of the “Level 1B Master Algorithm Document” by EADS-Astrium (2013a) and the Version 6.03 from the operational L1B processor and Version 3.04 from the End-to-End Simulator. The 4.2<sup>th</sup> issue was updated by Reitebuch and Huber with a revision of all chapters including the latest mission and instrument status including the Issue 9 of the “Level 1B Master Algorithm Document” by ADS (2017) and the Version 7.01 from the operational L1B processor and Version 4.01 from the End-to-End Simulator (DoRIT and MDA 2017 a,b,c). Version 4.3 includes now a description of the instrument response calibration algorithms in chapter 9. Version 4.4 was prepared after review by Th. Kanitz (ESA).

Chapter 2 describes the ADM-Aeolus mission and observational requirements, and chapter 3 gives a short introduction to atmospheric processes relevant to the lidar instrument for ADM-Aeolus. Chapter 4 describes the ADM-Aeolus instrument with emphasis on those functionalities and units with relevance to the algorithm development. Chapter 5 introduces the ADM-Aeolus data products up to Level 1B and chapter 6 gives an outline of geolocation processing. Chapter 7 describes the Level 0 to Level 1A processing and chapter 8 gives the theoretical basis for the processing steps from Level 1A to Level 1B for the wind mode data. Chapter 9 describes the instrument response calibration and chapter 10 contains any other algorithms with relevance to the L1B wind product.

	Document Nr. <b>AE-RP-DLR-L1B-001</b>	Issue: <b>4.4</b>	Date: <b>20.04.2018</b>	Page: <b>6/117</b>	
	Doc. Title: <b>ADM-Aeolus ATBD Level1B Products</b>				

## 2 ADM-Aeolus Mission Overview and Requirements

The Atmospheric Dynamics Mission ADM-Aeolus will provide global wind profile observations with the aim to demonstrate improvement in atmospheric wind analyses for the benefit of numerical weather prediction and climate studies. ADM-Aeolus is the first satellite wind lidar mission worldwide and the first lidar mission of the European Space Agency (ESA, lidar: light detection and ranging).

The concept of the mission is shown in Fig. 2-1. A Doppler wind lidar (DWL) called ALADIN (Atmospheric LAsEr Doppler INstrument) is accommodated on a satellite flying in a polar, sun-synchronous orbit at an altitude of about 320 km (N. B. the orbit altitude was lowered from 408 km to 320 km in 2016, due to the gain in lidar signal with a lower orbit, which was feasible due to a lower solar activity). The DWL will measure profiles of the projection of the wind vector on the line-of-sight (LOS) under a slant angle of  $35^\circ$  versus nadir perpendicular to the flight track. Thus the satellite ground track and the measurement ground track are separated by 230 km. The incidence angle between the LOS and the local normal direction at the measurement ground point is not  $35^\circ$  but about  $37.6^\circ$  due to the earth curvature (see also Fig. 6-1).

Profiles of the projection of the measured LOS wind speed on the horizontal plane HLOS (horizontal LOS) are obtained every 90 km, which corresponds to a travel time of the satellite of 12 s. The HLOS wind profile observations with an along-track horizontal integration length of 90 km are obtained from individual measurements with a horizontal sub-sample length of minimal 3 km. The 90 km wind observation consists of the return of 600 individual laser pulses during a period of 12 s. The wind profile is determined from the backscattered signals from aerosols and molecules separately and is thus contained in separate vertical layers spanning from below ground to up to 30 km altitude. The distance of the vertical layers is depending on the altitude referenced to the WGS84 (World Geodetic System of 1984) ellipsoid. The vertical resolution can be commanded separately for the aerosol and molecular layers with multiples of 250 m, such that the boundaries of the aerosol vertical layers will coincide with the boundaries of the molecular layers. The actual commanded vertical resolution will be typically in the range of 250 m to 2 km, with lower values chosen such as to enhance the sampling of large vertical gradients in the atmospheric and ground return signal.

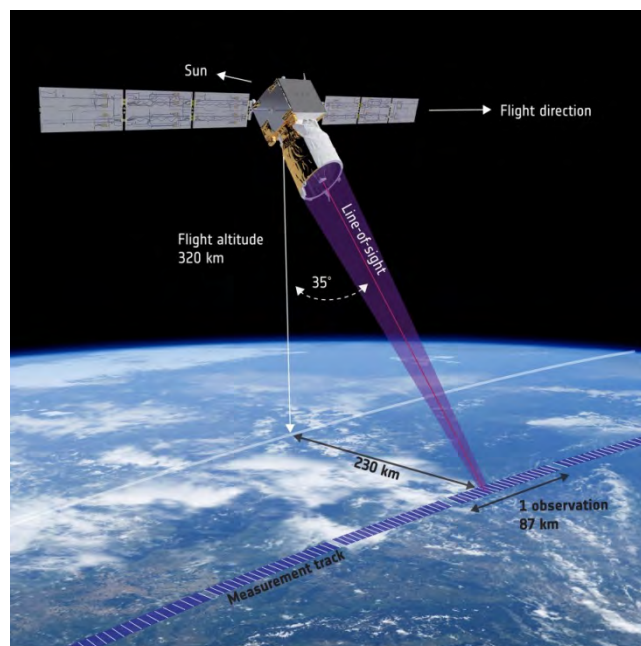


**Figure 2-1:** Schematic view of Aeolus measurement geometry with a polar-orbiting satellite at 320 km altitude and a telescope pointing direction of  $35^\circ$  off-nadir and perpendicular to the satellite flight direction, which separates satellite (white) and measurement track (purple stripes indicating raw measurement data resolution) by 230 km; line-of-sight wind profiles are obtained from the measurement data every  $\approx 3.5$  km and after on-ground averaging over 87-90 km to one observation depending on satellite ground speed (Fig. ESA/ATG-Medialab); subsequently 90 km is used in the text as observation length scale.

	Document Nr. <b>AE-RP-DLR-L1B-001</b>	Issue: <b>4.4</b>	Date: <b>20.04.2018</b>	Page: <b>7/117</b>	
	Doc. Title: <b>ADM-Aeolus ATBD Level1B Products</b>				

The observational requirements for the ADM-Aeolus mission have been carefully chosen to be able to demonstrate the beneficial impact of DWL winds (ESA 1999, 2008, 2016, Stoffelen et al. 2005) and are listed in Tab. 2-1 for the continuous mode operation baseline (ESA 2010, 2016, LeRille et al. 2012, Reitebuch 2012b). The vertical domain of the observations spans from the Planetary Boundary Layer (PBL) to the lower stratosphere with an altitude dependent vertical resolution from 0.5 km to 2 km of the observations (N. B. the instrument can be commanded with a minimum vertical resolution of 0.25 km, but the requirement for the PBL refers to 0.5 km). The requirement on the precision (random error given as root-mean-square rms value) of the HLOS component is related to the corresponding vertical resolutions in that altitude range and a horizontal integration length of 100 km below 14 km and 140 km above 14 km. It is worth to note, that the precision requirement on the measured LOS component is even more stringent by a factor of 0.61 for an incidence angle of 37.6°. The unknown bias should not exceed 0.7 ms<sup>-1</sup> for the HLOS-component and should be considered as root-mean-square (rms) values. In the System Requirement Document SRD (ESA 2010) the unknown bias is further split into a wind speed dependent part of 0.7 % (wind speed slope error) and a constant part of 0.5 ms<sup>-1</sup> (zero-wind bias). The ADM-Aeolus L1B data products must be available latest 3 hours after the actual observation to the primary users as meteorological services, e.g. the European Centre for Medium-Range Weather Forecasts ECMWF.

Parameter	Mission Requirements		
	PBL	Troposphere	Stratosphere
vertical domain	0-2 km	2-16 km	16-20 (30) km
vertical resolution	0.5 km	1 km	2 km
horizontal domain	global		
Minimum horizontal track data availability (before QC)	95%		
horizontal integration length per observation	90/100/140 km*		
horizontal subsample length per measurement	3 km		
precision HLOS component	1 ms <sup>-1</sup>	2.5 ms <sup>-1</sup>	3 (3-5) ms <sup>-1</sup>
unknown bias (HLOS)	0.7 ms <sup>-1</sup>		
probability of gross errors	5 %		
data availability, timeliness	3 hour		
length of observational data set	3 years		

**Table 2-1:** Observational requirements for ADM-Aeolus (ESA 2016); \*90 km horizontal length is used as observation length for L1B product; 100 km integration is applied for wind accuracy requirement below 14 km, while 140 km is applicable for altitudes above 14 km; a top altitude of 30 km with a precision of 3-5 ms<sup>-1</sup> is desirable.

ADM-Aeolus satellite is operating in a polar, sun-synchronous orbit at an inclination of 97° and a mean altitude of 320 km with a variation between 314 km and 341 km (see chapter 6.2). The orbit period is 90.8 minutes with an orbital velocity of about 7700 ms<sup>-1</sup> and a ground track velocity of about 7200 ms<sup>-1</sup>. Although the observation is performed perpendicular to the satellite velocity, which should result in a zero LOS component from the satellite, a residual velocity component from the Earth rotation is obtained. This is compensated by yaw steering of the satellite.

### 3 Lidar Principle and Atmospheric Processes

#### 3.1 Lidar Principle

A lidar consists of three main subsystems: the laser transmitter, the receiver, and the detection system (Fig. 3-1). The laser transmitter is the source which generates laser pulses and directs them into the atmosphere. The optical receiver unit of a lidar collects the backscattered signal via a telescope and analyses the spectral content of the signal via filters and a detection unit. For the case of a Doppler wind lidar the backscatter signal is analysed to obtain the LOS wind speed by the properties of the wavelength of the backscatter light.

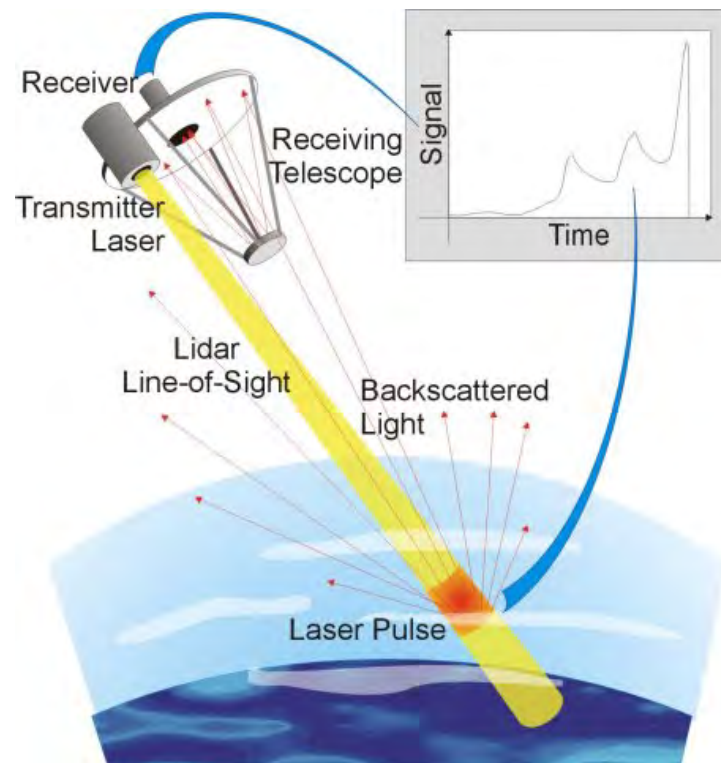


**Figure 3-1:** Sketch of the principle of a lidar, where a transmitter laser sends out laser pulses, which are backscattered in the atmosphere by particles and molecules, collected by a receiving telescope, and analysed by an optical and electronic receiver unit; note that the actual implementation of the ALADIN instrument is not a bistatic configuration of transmitter and receiving telescope, as shown on this figure, but a transceiver configuration as shown in Figure 4-1.

The lidar equation is used to determine the energy of the backscatter signal and takes into account both the instrumental parameters and the atmospheric variables. The backscatter laser energy at a distance  $r$  from the lidar is given by:

$$E(\lambda, r) = E_L \cdot \frac{\Delta R}{r^2} \cdot A_0 \cdot C(\lambda) \cdot \beta(\lambda, r) \cdot T^2(\lambda, r) \quad (3.1)$$

where  $E_L$  is the energy and  $\lambda$  the wavelength of the transmitted laser pulse.  $A_0/r^2$  is the acceptance solid angle of the receiving optics with  $A_0$  the collecting area of the telescope (optical aperture). An atmospheric volume with a length of  $\Delta R$  (range resolution) is sampled by the lidar. The instrumental constant  $C(\lambda)$  takes into account the response of the receiver, such as the spectral transmission factors and the overlap function of the telescope. The transmission coefficient  $T^2(\lambda, r)$  describes the range-dependent transmission factor of the atmosphere due to extinction. The atmospheric backscatter coefficient  $\beta(\lambda, r)$  characterizes the illuminated atmospheric volume backscatter from aerosol, cloud particles and molecules. In case of a return from the earth surface the product of  $\beta(\lambda, r) \Delta R$  is replaced by the albedo value  $a$ , which is the ratio of the radiation reflected by a surface to the incident energy. Mean albedo values  $a$  are 0.03 of soil, 0.5 of ice, 0.8 of dry

	Document Nr. <b>AE-RP-DLR-L1B-001</b>	Issue: <b>4.4</b>	Date: <b>20.04.2018</b>	Page: <b>9/117</b>	
	Doc. Title: <b>ADM-Aeolus ATBD Level1B Products</b>				

snow, and 0.14 of water for a 355 nm source (Vaughan et al. 1998). For the case of inclined incidence of light at an angle  $\varphi$ , the albedo of a Lambertian reflector is calculated by  $a(\varphi) = a / \pi \cos(\pi - \varphi)$ . In case of water surfaces the reflectance is strongly depending on incidence angle and is composed of several contributors, which are discussed in Li et al. (2010) for UV wavelengths. Airborne observations of surface reflectances in the UV spectral range from the ALADIN airborne demonstrator are discussed in Manninen (2012). Monthly climatological reflectance values from 300 nm to 4000 nm with high spatial resolution (10 km) based on different satellite observations are available through ESA's ADAM project (Noveltis (2013)). Monthly mean UV reflectance values at 355 nm are available for nadir and off-nadir pointing geometries from the ADAM database for end-to-end simulations.

Doppler wind lidar systems determine the LOS wind speed as a function of range using the change in wavelength or frequency of the emitted laser pulse. The atmospheric particles that are moving with the wind velocity cause a frequency shift of the backscatter signal due to the Doppler effect. The frequency shift is related directly to the wind velocity along the laser beam (see Chap. 3.4). A detailed and current introduction to lidar fundamentals is contained in Measures (1992), Weitkamp (2005), Paffrath (2006) and Reitebuch (2012a) focussing on wind lidars.

### 3.2 Beam Propagation and Range Equation

The lidar instrument uses a slant angle  $35^\circ$  off nadir from a 320 km orbit, which was chosen to optimise the accuracy of the instrument. The direction of the emitted laser signal is chosen perpendicular to the flight direction, to compensate for the Doppler shift due to spacecraft motion and the earth rotation.

The laser pulse duration  $t_L$  limits the minimal vertical atmospheric resolution  $\Delta R_{min} = t_L c/2$ , where  $c$  is the speed of light. For the pulse duration of the ALADIN laser transmitter  $t_L = 30$  ns, the minimal resolution is 4.5 m. The feasible vertical resolution depends on the integration time of detector and the slant angle. A minimum vertical resolution of 250 m is achieved for ALADIN due to the slant angle of  $35^\circ$  (mean incidence angle of  $37.6^\circ$ ) and a minimum integration time of the electronic detection unit of 2.1  $\mu$ s, which results in a range resolution  $\Delta R$  of 315 m along the LOS. The overall vertical measurement range is limited by the detectors capability to store data for 25 range bins (see chapter 4.2.5).

### 3.3 Aerosol and Molecular Scattering

When light from a laser propagates through the atmosphere, it is scattered and absorbed by the atmospheric constituents, resulting in a change in intensity and spectral characteristics of the scattered light. Backscattered light from molecules, whose diameter is much smaller than the wavelength, results from a Rayleigh scattering process. Mie scattering occurs for aerosol and clouds particles, whose size is comparable or larger than the wavelength.

The intensity of the return signal from Mie scattering depends on the number density of aerosols, which varies largely over different geographical locations and altitude and increases strongly for clouds, fog, or haze. A convenient approach to estimate the Mie backscatter coefficient is the usage of climatological databases derived from measurements and applying scaling laws for the wavelength dependency. The ESA Reference Model Atmosphere (RMA) was obtained from airborne measurements over Atlantic regions during the period 1988-1990 (Vaughan et al. 1995 and 1998). The RMA comprises data of different aerosol backscatter (Fig. 3-2), cloud backscatter, extinction, background radiance, and ground albedo.

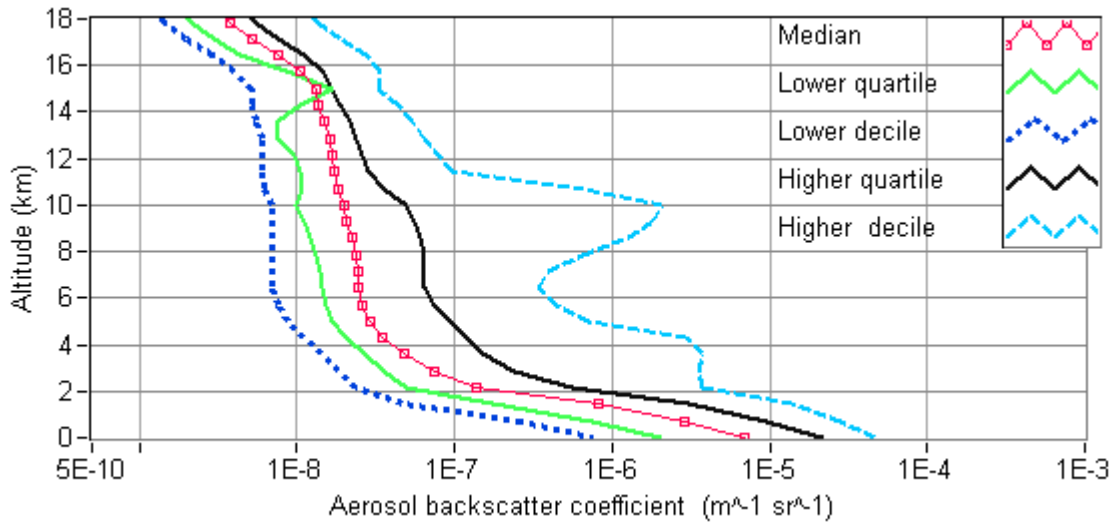


**Figure 3-2:** Aerosol backscatter coefficients of different aerosol models versus altitude for a wavelength of 355 nm used for ALADIN (adapted from Vaughan et al. 1998). The percentiles are those values of backscatter at which a given percentage of the data is greater or less than this value. Thus the upper/lower quartiles have 25% of data greater/less than, whilst the upper lower deciles have 10% of data greater/less than. The enhanced backscatter due to clouds is seen in the higher decile profile (light blue).

The cloud backscatter and extinction coefficients from the RMA model for different type of clouds and their typical altitude range are listed in Table 3-1.

Types of cloud	Backscatter coefficient $\beta_{cloud} [m^{-1} sr^{-1}]$	Extinction coefficient $\alpha_{cloud} [m^{-1}]$	Altitude [m]
Stratus	$5 \times 10^{-3}$	$9 \times 10^{-2}$	200 - 700
Cumulus	$6 \times 10^{-4}$	$1.2 \times 10^{-2}$	750 - 1000
Cumulonimbus	$1 \times 10^{-2}$	$1.8 \times 10^{-1}$	2000 - 4000
Altostratus	$1 \times 10^{-3}$	$1.8 \times 10^{-2}$	4000 - 4500
Cirrus	$1.4 \times 10^{-5}$	$2 \times 10^{-4}$	8500 - 9500
Polar Stratospheric Cloud	$3.0 \times 10^{-7}$	$6 \times 10^{-6}$	16000 - 17000

**Table 3-1:** Backscatter and extinction coefficients for different type of clouds and their typical altitude range for a wavelength of 355 nm from the RMA model.

Rayleigh scattering from air molecules occurs in the case of a clear atmosphere. The intensity of the return signal depends on the number of molecules per  $m^3$  (Eq. (3.3)) and the backscatter cross section per molecule (Eq. (3.2)), which indicates the theoretical effective area, where light is scattered back in a solid angle of  $2\pi$  sr. The Rayleigh backscatter cross section ( $m^2 sr^{-1}$ ) for a mixture of atmospheric gases of altitudes up to 100 km is calculated from (Measures 1992, p. 42):

$$\sigma_{Mol} = \left[ \frac{0.55 \times 10^{-6} m}{\lambda} \right]^4 \cdot 5.45 \times 10^{-32} m^2 sr^{-1} \quad (3.2)$$

and the number of molecules  $N_{Mol}$  per  $m^3$  depending on altitude  $z$  is given by (Measures 1992 p. 42):

$$N_{Mol}(z) = \left[ \frac{273.15K}{T(z)} \right] \cdot \left[ \frac{p(z)}{1.01325 \times 10^5 Pa} \right] \cdot N_L \quad (3.3)$$

with temperature  $T$ , pressure  $p$  and the Loschmidt's number  $N_L = 2.68 \times 10^{25} m^{-3}$  for a temperature of 273.15 K and a pressure of  $1.01325 \times 10^5 Pa$ . Hence, the backscatter coefficient per volume  $\beta_{Mol} (m^{-1} sr^{-1})$  is found from:

$$\beta_{Mol}(z) = N_{Mol}(z) \cdot \sigma_{Mol} \quad (3.4)$$

Since the amount of molecular backscatter energy is proportional to  $\lambda^{-4}$  (Eq. (3.2)), shorter wavelengths are scattered far more than longer wavelengths, illustrated in Fig. 3-3. Assuming a temperature and pressure profile from a reference atmosphere (U.S. standard atmosphere, Champion 1985) the resulting molecular backscatter coefficients are shown in Fig. 3-3 at 10  $\mu m$ , 2  $\mu m$ , and 0.355  $\mu m$  wavelengths, which increase by three orders of magnitude with each transition to a shorter wavelength

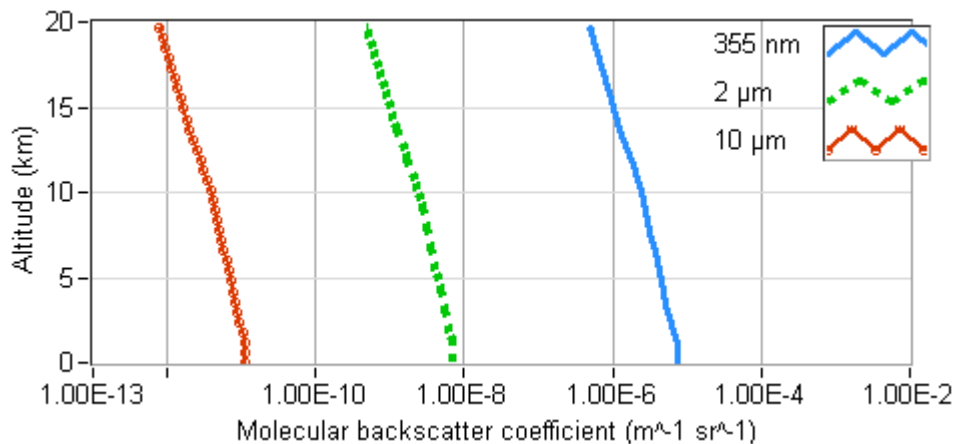


**Figure 3-3:** The molecular backscatter coefficients for the U.S. standard atmosphere temperature and pressure profiles at different wavelengths (355 nm, 2  $\mu m$ , and 10  $\mu m$ ) versus altitude.

The 355 nm wavelength was selected for ALADIN to obtain high molecular backscatter even in regions of the atmosphere with low aerosol loading in the upper troposphere and lower stratosphere. Shorter wavelengths than 355 nm, e.g. the fourth-harmonic of a Nd:YAG laser transmitter at 255 nm was abandoned, because of absorption from ozone in the stratospheric ozone layer.

### Scattering ratio

The scattering ratio  $B$  (also called backscatter ratio) describes the ratio of the total backscatter from aerosols (including clouds)  $\beta_A$  and molecules  $\beta_{Mol}$  to the backscatter from molecules  $\beta_{Mol}$ .

$$B = \frac{\beta_A + \beta_{Mol}}{\beta_{Mol}} \quad (3.5)$$

In case of pure backscatter from molecules the scattering ratio is 1, whereas it is higher than 1 in case of aerosol and molecular backscatter. For the wavelength of 355 nm and the aerosol backscatter coefficients from the RMA model (Fig. 3-2), the scattering ratio can reach values up to 2 for the median aerosol model and up to 5 for the higher decile model in the boundary layer below 2 km. In case of clouds the scattering ratio can exceed a value of 10 and reach values up to several hundred.

	Document Nr. <b>AE-RP-DLR-L1B-001</b>	Issue: <b>4.4</b>	Date: <b>20.04.2018</b>	Page: <b>12/117</b>	
	Doc. Title: <b>ADM-Aeolus ATBD Level1B Products</b>				

### Extinction and lidar ratio

The atmospheric two-way transmission  $T^2(\lambda, r)$  depends on the aerosol, cloud, and molecular extinction coefficient  $\alpha_A$  resp.  $\alpha_{Mol}$  by the Lambert-Beer law:

$$T(\lambda, r) = e^{-\int_0^r \alpha(\lambda, z) dz} \quad (3.6)$$

The extinction coefficients can be derived from the backscatter coefficients by use of the lidar ratio  $L$ . The lidar ratio for aerosols  $L_a$  has been discussed by many authors (Doherty et al. 1999, Liu et al. 2002, Evans 1988, Spinhire et al. 1997). It was shown that a linear relationship applies for monodispersed spherical particles:

$$L_a = \frac{\alpha_A}{\beta_A} \quad (3.7)$$

Values of  $L_a$  depend on the wavelength  $\lambda$  and vary over a large range depending on the type of the aerosol (size, shape, composition) (Ansmann and Müller 2006).

The extinction coefficient for molecules  $\alpha_{Mol}$  is derived from the molecular backscatter  $\beta_{mol}$  coefficient by using the constant molecular lidar ratio  $L_m$  (Measures 1992):

$$L_m \frac{\alpha_{Mol}}{\beta_{Mol}} = \frac{8\pi}{3} \text{sr} \quad (3.8)$$

### Depolarisation

The ALADIN instrument transmits circular-polarized light in order to allow separation of transmit and receive path by polarization optics. Only the co-polar (parallel) component  $P_{\parallel}$  of the backscattered light is detected by ALADIN. This will cause a systematic underestimation of the backscatter coefficient for depolarizing targets, i.e. ice clouds and non-spherical aerosol particles. From scattering theory, a relationship between linear  $\delta_{lin}$  and circular depolarization  $\delta_{circ}$  follows (Gimmetstad 2008, Ansmann and Wandinger 2013):

$$\delta_{circ} = \frac{2 \cdot \delta_{lin}}{1 - \delta_{lin}} \quad (3.9)$$

For typical linear depolarization ratios  $\delta_{lin}$  of 0.4 – 0.6 for cirrus clouds and 0.35 for large dust and ash particles, circular depolarization ratios of 1.3 – 3 for ice clouds and 0 – 1 for aerosols are obtained, i.e. the cross-polar component can be up to three times higher than the co-polar component in ice clouds. The ratio of the co-polar component  $P_{\parallel}$  from the total backscatter  $P_{\parallel} + P_{\perp}$  as measured by ALADIN is obtained from

$$\frac{P_{\parallel}}{P_{\parallel} + P_{\perp}} = \frac{1}{1 + \delta_{circ}} = \frac{1 - \delta_{lin}}{1 + \delta_{lin}} \quad (3.10)$$

Therefore, ALADIN will underestimate the backscatter coefficient by 55% to 75% in ice clouds and by up to 50% in dust and ash containing aerosols. Extinction measurements are not influenced by depolarization effects. Thus the particle lidar ratio  $L_m$  will be overestimated by the same factor by which the backscatter coefficient is underestimated. Aerosol typing and discrimination between ice and water clouds will be only possible with supplementary information (Wandinger et al. 2011).

### 3.4 Doppler-Shift and Spectral Lineshape of Aerosol and Molecular Return

The Doppler effect was first described by the Austrian physicist Christian Johann Doppler in 1842 (Doppler 1842). The Doppler effect is the change of a wave's frequency or wavelength caused whenever there is a relative motion between a source of waves and the observer of the wave. The optical frequency of light is shifted by a factor of  $v/c$ , where  $v$  is the speed at which the observer is approaching or receding from the source, and  $c$  is the speed of light. Actually only the component of the wind along the line between the source and the observer is resulting in a Doppler effect. This wind component is obtained by projection of the three-dimensional wind vector onto this line, and is subsequently called line-of-sight LOS wind  $v_{LOS}$ .

The first shift in frequency occurs with the scattering air particles, which constitute a moving observer. The second shift arises because the particles in the air then act as moving sources. Since  $v \ll c$ , the Doppler frequency shift  $\Delta f_D$  detected at the lidar is given by (Werner 2005, Reitebuch 2012a):

$$\Delta f_D = f_a - f_0 = 2f_0 \frac{v_{LOS}}{c} \quad (3.11)$$

with  $f_0$  the frequency of the transmitted laser pulse and  $f_a$  the frequency of the backscattered light from the atmosphere. The sign convention for the Doppler shift frequency  $\Delta f_D$  is such, that a positive sign ( $\Delta f_D > 0$ ,  $f_a > f_0$ ) is related to a LOS wind speed in the direction towards the instrument ("blue wavelength shift"), while a negative sign ( $\Delta f_D < 0$ ,  $f_a < f_0$ ) indicates a LOS movement away from the instrument ("red wavelength shift"). Thus  $v_{LOS}$  is positive for movements towards the lidar, while  $v_{LOS}$  is negative for movements away from the lidar in this context. Using the same sign convention for the Doppler wavelength shift  $\Delta \lambda_D$  and  $v_{LOS}$  the equation contains a different sign:

$$\Delta \lambda_D = \lambda_a - \lambda_0 = -2\lambda_0 \frac{v_{LOS}}{c} \quad (3.12)$$

with the wavelength of the laser  $\lambda_0$  and the backscattered atmospheric signal  $\lambda_a$ .

For the laser transmitter wavelength of 355 nm of ALADIN, which corresponds to a frequency of 845 THZ, the Doppler shift in frequency and wavelength is given in Table 3-2 for  $1 \text{ ms}^{-1}$  LOS and  $1 \text{ ms}^{-1}$  HLOS for an incidence angle of  $37.6^\circ$ .

	<b>1 ms<sup>-1</sup> LOS</b>	<b>1 ms<sup>-1</sup> HLOS</b>	<b>1 fm</b>	<b>1 MHz</b>
<b>1 ms<sup>-1</sup> LOS</b>	1	1.638	2.37	5.639
<b>1 ms<sup>-1</sup> HLOS</b>	0.610	1	1.446	3.441
<b>1 fm</b>	0.423	1.446	1	2.380
<b>1 MHz</b>	0.1775	0.291	0.425	1

**Table 3-2:** Conversion table for a wavelength of 355 nm using EQ 3.9 and an incidence angle of  $37.6^\circ$  to convert from LOS to HLOS; e.g. a  $1 \text{ ms}^{-1}$  LOS corresponds to  $1.638 \text{ ms}^{-1}$  HLOS and a Doppler shift of 2.37 fm or 5.639 MHz (first line); these conversion values will change slightly for the actual laser wavelength (354.8 nm from the satellite characterisation test)

But not only the mean movement of the molecules and the aerosol particles by the atmospheric wind are affected by a Doppler shift. Also the individual thermal movement of the molecules (Brownian motion) results in a Doppler shift and thus leads to a spectral broadening of the Rayleigh line. The most significant factor for the Rayleigh line shape is the Doppler broadening, which may be described by a Gaussian line profile function (Measures 1992 p. 99):

$$W(\lambda) = \frac{1}{\sqrt{2\pi\sigma^2}} e^{-\frac{\lambda^2}{2\sigma^2}} \quad (3.13)$$

where  $\sigma$  is the standard deviation of the Rayleigh spectrum which is given by:

$$\sigma = \frac{2\lambda}{c} \sqrt{\frac{kTN_A}{m_{air}}} \quad (3.14)$$

where  $m_{air}$  is the mean molecular air mass ( $2.885 \times 10^{-2} \text{ kg mol}^{-1}$ ),  $\lambda$  the wavelength of the laser,  $k$  the Boltzmann constant ( $1.38 \times 10^{-23} \text{ J K}^{-1}$ ),  $c$  the speed of light,  $T$  the atmospheric temperature and  $N_A$  the Avogadro constant ( $6.022 \times 10^{23} \text{ mol}^{-1}$ ). Thus, the broadening of the Rayleigh backscatter spectrum depends on atmospheric temperature  $T$  (Eq. (3.13)). The wavelength spectra for backscatter from Mie and Rayleigh is shown in Fig. 3-4. Due to the much higher mass of aerosols no spectral broadening occurs due to the motion of the aerosols. Thus the spectral width of the Mie signal is the same as for the transmitted laser pulse.

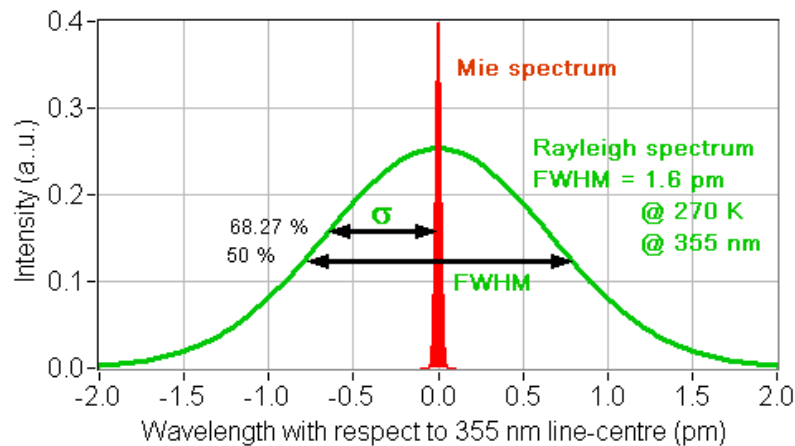


**Figure 3-4:** Wavelength spectra for the backscatter signals from aerosols (Mie spectrum, red) and from molecules (Rayleigh spectrum, green) illustrating the different spectral widths ( $\sigma$ , Full Width Half Maximum  $FWHM=2\sqrt{2\ln 2}\sigma$ ) at a laser wavelength of 355 nm for  $0 \text{ ms}^{-1}$  wind speed.

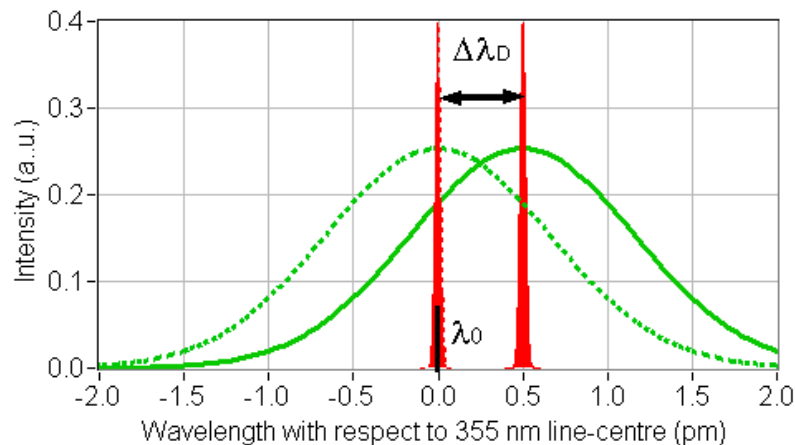


**Figure 3-5:** Wavelength spectra for the backscattered Mie (red) and Rayleigh (green) signal for a 355 nm source at  $\lambda_0$  (dotted lines) and a Doppler shift  $\Delta\lambda_D$  (bold lines); the indicated Doppler shift of 0.5 pm corresponds to a LOS wind speed of  $\sim 200 \text{ ms}^{-1}$ .

	Document Nr. <b>AE-RP-DLR-L1B-001</b>	Issue: <b>4.4</b>	Date: <b>20.04.2018</b>	Page: <b>15/117</b>	
	Doc. Title: <b>ADM-Aeolus ATBD Level1B Products</b>				

It should be noted, that the vertical sampling grid for the Mie and the Rayleigh spectrometer can be different, which results in different vertical atmospheric volumes for each receiver. This may produce a different Doppler shift on the Mie and Rayleigh signal for the case the HLOS wind speed differs within each of the atmospheric volumes. It is assumed in Fig. 3-5, that the same volume is sensed for the Mie and the Rayleigh signal.

Even in the case of sampling the same atmospheric volume for the Mie and Rayleigh spectrometer, different HLOS wind speed could be obtained in the presence of a vertical gradient in the backscatter coefficients combined with a vertical gradient in wind speed (Sun et al. 2014). This is caused by the vertical weighting of the atmospheric signal with the backscatter profile. Only in case of assuming a constant backscatter profile or a constant wind speed within one vertical range bin, the mean wind speed of this range bin is sensed. In case of strong vertical gradients, e.g. in the presence of a cloud within the range bin, the wind speed from the Mie and Rayleigh spectrometer could differ significantly.

The actual lineshape from molecular backscatter differs from a pure Gaussian lineshape due to Rayleigh-Brillouin scattering in the atmosphere (Witschas et al. 2010, Witschas 2011a, Witschas 2012, Witschas et al. 2012), which can be described by a model of Tenti et al. (1974). A parameterized version applicable for UV wavelengths and air was developed by Witschas (2011b). The Rayleigh-Brillouin lineshape model needs to be included for the wind retrieval from molecular backscatter (Dabas et al. 2008).

### 3.5 Earth Background Radiation

In addition to the backscatter from molecules and particles also the earth background radiation contributes to the signal received at the lidar telescope. The earth background radiant energy  $E_{bck}$  at the satellite is due to the solar spectral radiance  $L_\lambda$  [ $\text{Wm}^{-2}\mu\text{m}^{-1}\text{sr}^{-1}$ ], which is the solar power [Watt] per unit wavelength interval [ $\mu\text{m}$ ], per area  $\text{m}^2$ , and per solid angle [steradian sr]. The spectral radiance is depending on the wavelength  $\lambda$  and the viewing geometry wrt. the sun with solar zenith  $\Theta$  and azimuth  $\varphi$  angle. Due to the sufficiently narrow spectral width of the receiver ( $\Delta\lambda = 1 \text{ nm}$ , see Tab. 4-1) the energy may be assumed to be constant and the solar radiant energy  $E_{bck}$  [J] can be written as (Measures 1997 p. 225):

$$E_{bck} = C(\lambda) \cdot L_\lambda(\Theta, \varphi, \lambda) \cdot \Omega_0 \cdot A_0 \cdot t_D \cdot \Delta\lambda \quad (3.15)$$

where  $\Omega_0$  is the acceptance solid angle (derived from FOV  $\theta=18.1 \mu\text{rad}$  with  $\Omega_0 = \pi \cdot \theta^2/4$ ),  $A_0$  the area of the telescope ( $A_0 = \pi \cdot D^2/4$  with  $D=1.5 \text{ m}$ ),  $t_D$  the detection time for the lidar and solar background range gates, and  $C(\lambda)$  the optical transmission of the ALADIN instrument for the Mie and the Rayleigh channel. The solar spectral radiance  $L_\lambda$  can be derived from the solar spectral irradiance  $M_\lambda$  with the solar zenith angle  $\Theta$ , an effective albedo of the atmosphere  $\rho_{\text{eff}}$  and the 2-way transmission  $T^2$ :

$$L_\lambda = M_\lambda \cdot \cos(\Theta) \cdot \frac{\rho_{\text{eff}}}{\pi} \cdot T^2 \quad (3.16)$$

A value of  $1100 \text{ Wm}^{-2}\mu\text{m}^{-1}\text{sr}^{-1}$  is typical for the solar spectral irradiance  $M_\lambda$  at the UV wavelength of  $354.8 \text{ nm}$  (Vaughan et al. 1998). The solar background is mainly resulting from diffusively scattered solar radiation in the atmosphere (molecules, particles, clouds) and from the ground. Thus, the effective albedo  $\rho_{\text{eff}}$  and two-way transmission  $T^2$  is depending strongly on the atmospheric scene and the occurrence of clouds of visibility and albedo of the ground. Effective albedo values of 0.23 (clear-sky) and 0.65 (cloudy-sky) are reported by McGill et al. (1999) for the UV. A value of  $\rho_{\text{eff}}=0.8$ ,  $T^2=1$  and varying solar zenith angles are used for Aeolus end-to-end simulations to assess the maximum influence on the random error performance. The solar zenith angle  $\Theta$  is depending on the orbital position of the satellite wrt. the sun. Due to the dawn-dusk orbit of Aeolus this value can vary along the orbit between  $0^\circ$  and  $90^\circ$ . Thus the solar radiance  $L_\lambda$  at the satellite can vary along the orbit between 0 to  $280 \text{ Wm}^{-2}\mu\text{m}^{-1}\text{sr}^{-1}$  using the above values and assumptions; a mean value of  $72 \text{ Wm}^{-2}\mu\text{m}^{-1}\text{sr}^{-1}$  would result from a solar zenith angle of  $75^\circ$ , which is within the range of  $57 \text{ Wm}^{-2}\mu\text{m}^{-1}\text{sr}^{-1}$  to  $161 \text{ Wm}^{-2}\mu\text{m}^{-1}\text{sr}^{-1}$  reported by McGill et al. (1999).

	Document Nr. <b>AE-RP-DLR-L1B-001</b>	Issue: <b>4.4</b>	Date: <b>20.04.2018</b>	Page: <b>16/117</b>	
	Doc. Title: <b>ADM-Aeolus ATBD Level1B Products</b>				

## 4 ALADIN Instrument

### 4.1 Overview

The ADM-Aeolus lidar instrument ALADIN is based on a direct-detection Doppler lidar operating in the ultraviolet (UV) spectral region at 355 nm. The receiver consists of two interferometers (also called spectrometers), which sense the Doppler shift from particles (aerosol, cloud particles) as well as from molecules, yielding profiles of the LOS wind speed throughout the whole troposphere and part of the stratosphere with high vertical resolution (250-2000 m). The spectrometer, which is mainly sensitive to molecular backscatter, uses the double-edge technique using two Fabry-Perot interferometers (Chanin et al. 1989, Flesia et al. 2000, Gentry et al. 2000). The spectrometer, which is sensitive to aerosol and cloud returns, is based on a Fizeau interferometer (EADS-Astrium 2004b, Schillinger et al. 2003, Morancais et al. 2004). The instrument concept of ALADIN combines new techniques, like a novel combination of the molecular and aerosol receiver, and the use of an Accumulation Charge Coupled Device (ACCD) to improve detection sensitivity. Also the use of a sequential implementation of the two Fabry-Perot interferometers with different maximum transmissions and spectral widths for the two channels of the Fabry-Perot interferometer was never applied before. The use of novel technologies within this instrument in addition with the first deployment of a Doppler lidar on a satellite raises several topics for the ground processing algorithm theoretical basis.

An overview of the optical architecture is given in Fig. 4-1 and main instrument parameters are summarized in Tab. 4-1. The ADM-Aeolus satellite will be placed in a polar, sun-synchronous orbit at a mean altitude of 320 km, resulting in a mean orbital speed of about  $7.7 \text{ km s}^{-1}$ . The ALADIN instrument points perpendicular to the satellite ground speed vector with a slant angle  $35^\circ$  off nadir (Fig. 2-1). The satellite is steered in yaw angle to compensate for earth rotation and to compensate for systematic orbit height variations. Measurements are performed with an adjustable, in-flight commandable vertical resolution between 250 m and 2 km from ground up to 30 km. The maximum number of vertical range gates is 25, where 24 range gates are used for atmospheric return measurements and one range gate is used to characterize the background light contribution due to earth or cloud albedo. Atmospheric returns for each vertical range gate of subsequent measurements are horizontally integrated over 90 km to obtain one observation. The observations are obtained continuously without significant gaps (ESA 2010, LeRille et al. 2012, Reitebuch 2012b), in contrast to the earlier mission concept of burst-mode operation of the laser (ESA 2008).

The ALADIN instrument is equipped with two fully redundant Power Laser Heads (PLH nominal n and redundant r), where one PLH acts as a spare and a Flip-Flop Mechanism (FFM) switches between both PLH's. The two PLH's are coupled via an optical fibre to a Reference Laser Head (RLH n, RLH r) each, which provides the narrowband, continuous wave (cw) laser light as reference. The laser pulses are sent out via a half-wave plate (HWP), polarising beam splitter (Pol), quarter-wave plate (QWP), beam expander and the telescope to the atmosphere with circular polarisation. Small amounts of the outgoing laser pulse are reflected and directly transmitted via mirrors to the spectrometers to obtain a reference measurement. As the same telescope is used for transmitting the laser pulse and receiving the atmospheric backscatter signal it is used in a transceiver configuration. This allows to limit the Field-Of-View (FOV) for background light to very small values ( $18.1 \mu\text{rad}$  full angle) and no active co-alignment between transmit and receive optic is necessary. The backscattered light is received by the telescope, and directed through the beam expander. The circular polarized backscattered light changes its polarization to linear after the quarter-wave plate (QWP) and is therefore transmitted through the polarizer (Pol) towards the interference filter (IFF) and laser chopper mechanism (LCM). The depolarized component of the backscattered light is reflected at the polarizer (Pol) towards the laser and is considered as a signal loss for the ALADIN instrument. The LCM blocks stray light at the receiver input, while the laser pulse is sent out. An interference filter (IFF) is used to filter out background light with an equivalent bandwidth of 1 nm centred at 355 nm. The field stop limits the receiver FOV of the telescope to only  $18.1 \mu\text{rad}$  and the aperture stop limits the beam diameter at the input of the spectrometers to 20 mm. A half-wave plate (HWP) at the output of the transmit/receive optics is used to obtain linearly polarized light of defined direction at the input of the spectrometers.

At the input of the Rayleigh spectrometer (RSP) the beam is reflected at a polarising beam splitter (Pol) towards the Mie spectrometer (MSP) and increased in diameter by a beam expander to 36 mm to reduce the divergence on the MSP. The MSP is composed of a Fizeau interferometers producing linear fringes at the output, which are imaged to an ACCD within the Detection Front-End Unit Mie (DFU-M). As the Fizeau interferometer transmits only a small spectral band around the laser wavelength, it acts mainly as a sensor for the Mie signal (chapter 4.2.3 and Fig. 4-3). The reflected part of the signal spectrum from the MSP is

directed towards the RSP on the same beam path and linearly polarised in such direction, that the beam is now transmitted through the polarising beam splitter within the RSP.

The RSP is composed of two Fabry-Perot interferometers, which act as a spectral filter for the backscattered signal from molecules. The beam is at first directed to one Fabry-Perot interferometer, which is called subsequently filter A. The transmitted signal of the filter A and B is of circular spatial shape (spot) and is directed towards the imaging zone of an ACCD within the DFU-R (DFU-Rayleigh). The reflected part of the signal of the filter A is rotated in polarisation in such a way that it is directed towards the other Fabry-Perot interferometer of the RSP, which is called subsequently filter B. It is composed of the same reflecting plates, but with a slightly decreased distance by a deposited step, which results in a small wavelength shift of the transmission maximum of filter A wrt. filter B. The signal of filter B is directed towards the same ACCD within DFU-R, but illuminating another half of the ACCD than filter A (section 4.2.4 and Fig. 4-2). One half of the imaging zone of the ACCD is illuminated by the signal of filter A, while the other half is illuminated in parallel by the signal of filter B. Thus a sequential, double-edge Fabry-Perot interferometer is realised for detecting the molecular return signal with two filters A and B. The Transmit-Receive Optics (TRO), both spectrometers MSP and RSP, and both detection units DFU-M and DFU-R are mounted on a common structure – the Optical Bench Assembly (OBA).

The following sub-chapters describe the units of ALADIN in more detail.

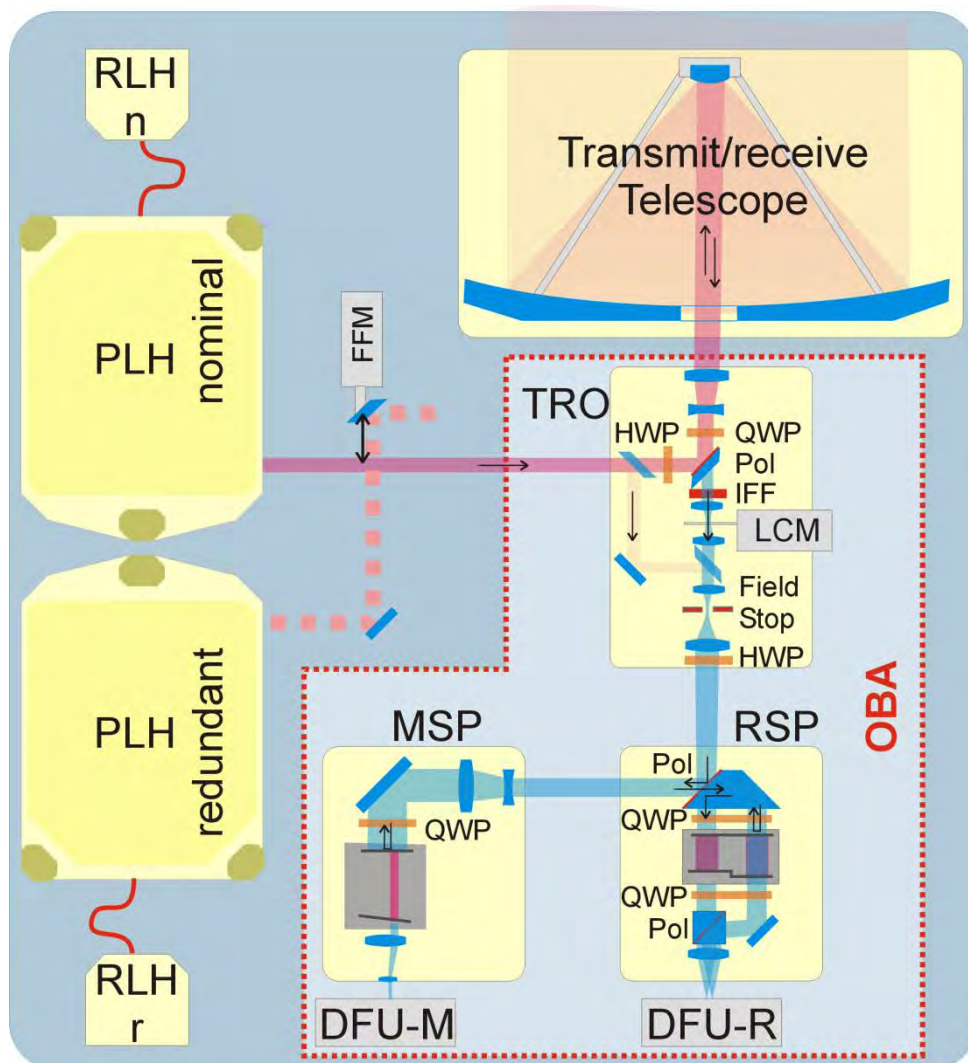


Figure 4-1: Optical architecture of ALADIN (from ESA (2008)).

Unit	Parameter	Value
<b>Satellite</b> polar, sun-synchronous	mean altitude	320 km
	mean orbital velocity	7.7 kms <sup>-1</sup>
<b>ALADIN instrument</b> direct-detection Doppler wind lidar	slant angle at satellite	35 ° off nadir
	incidence angle at ground	37.6 ° wrt local zenith*
	vertical resolution	250 m – 2 km
	number of range gates	24 atmosphere and 1 background light
	range	ground to 30 km
	horizontal averaging length	90 km per observation
<b>Laser Transmitter</b> Nd:YAG, frequency-tripled, diode-pumped	wavelength	354.8 nm
	energy per pulse	80 mJ
	repetition rate	50.5 Hz
	linewidth	50 MHz FWHM
	pulse-to-pulse frequency stability	6-8 MHz rms
<b>Telescope/Front Optics</b> afocal Cassegrain, SiC structure	primary mirror diameter	1.5 m
	background light filter bandwidth	1 nm
	receive FOV	18.1 µrad
	transmit beam divergence	20 µrad (86% EE)**
<b>Mie Spectrometer</b> fringe imaging Fizeau interferometer	Fizeau Free Spectral Range	0.91 pm / 2177 MHz
	Fizeau Useful Spectral Range	0.66 pm / 1582 MHz
	Fizeau FWHM	67 nm / 159 MHz (atm.) 53 nm / 125 MHz (int.)
	total radiometric efficiency	0.71 % (BOL)
<b>Rayleigh Spectrometer</b> double edge Fabry-Perot interferometer, 2 filters, sequential	Fabry-Perot Free Spectral Range	4.56 pm / 10913 MHz
	filter separation	2.33 pm / 5547 MHz
	filter FWHM (direct/reflected)	1551 MHz / 1531 MHz
	total radiometric efficiency	6.4 % (BOL)
<b>Detection Unit</b> Accumulation CCD for Mie and Rayleigh receiver	Quantum efficiency	85 %
	Detection chain noise for each measurement / read-out	3.9 (Mie) – 4.7 (Ray) e <sup>-</sup> / pixel
	Dark current	1.9 e <sup>-</sup> / (pixel · s)
	Number of used pixels	16 lines * 25 rows

**Table 4-1:** Main ALADIN instrument parameter (ESA 2008, ESA 2018a, BOL: begin of life, EE: encircled energy, e<sup>-</sup>: electrons); \* 37.6 needs to be verified for lower orbit, \*\* laser divergence from IFP (Instrument Full Performance) test in 2016.

	Document Nr. <b>AE-RP-DLR-L1B-001</b>	Issue: <b>4.4</b>	Date: <b>20.04.2018</b>	Page: <b>19/117</b>	
	Doc. Title: <b>ADM-Aeolus ATBD Level1B Products</b>				

## 4.2 Laser Transmitter

A diode-pumped Neodymium doped Yttrium-Aluminium-Garnet (Nd:YAG) laser emitting at 1064.4 nm is used to generate the 354.8 nm pulses with a frequency-tripling stage by use of non-linear Lithium-Borate (LBO) crystals. Stringent requirements are set to the laser transmitter in terms of frequency stability of only 6-8 MHz root-mean-square (rms) pulse to pulse variation (Mondin and Bravetti 2014). This corresponds to a stability of  $5 \cdot 10^{-9}$  relative to the laser frequency of 845.3 THz. The laser frequency must be tuneable over a large spectral range of 11 GHz for calibration purpose (see 4.3.3). In order to achieve these stringent requirements a Maser Oscillator Power Amplifier (MOPA) configuration (Cosentino 2004, 2012) was chosen with injection seeding of continuous-wave (cw) laser radiation of very high frequency stability from a tuneable Reference Laser Head (RLH). During calibration the laser has to be tuned over  $\pm 5.5$  GHz in steps of 250 MHz and 25 MHz with an accuracy of 1 MHz rms noise (UV) and a slow drift of below 1.7 MHz (UV) during the calibration time of 30 minutes. After calibration the laser transmitter frequency will be tuned to the centre of the useful spectral range of the MSP. The output beam diameter of the laser transmitter is 6.1 mm. The laser beam is expanded and transmitted via the ALADIN telescope of diameter of 1.5 m with a laser beam diameter of about 0.9 m. An output divergence of 20  $\mu$ rad (full angle, 86% encircled energy EE for IFP (Instrument Full Performance) tests on FM-B in 2016) is obtained in the atmosphere in order to obtain eye-safe operation.

The laser transmitter is used to generate laser pulses at a wavelength of 354.8 nm with a repetition rate of 50.5 Hz and average laser energy per pulse of 80 mJ with a length of 20 ns (FWHM). Because of the electrical power limitations on the satellite it was planned during earlier mission phases to operate the laser not continuously but in a burst mode, where 700 pulses are transmitted during 7 s with a higher pulse repetition frequency of 100 Hz (ESA 2008). After a period of 7 s, the PLH power amplifier's would have been switched-off for a period of 21 s, because of the electrical power limitations. This concept was changed to a continuous mode operation of the laser (ESA 2010, LeRille et al. 2012) in order to achieve higher thermal-mechanical stability of the laser. In order to cope with the power limitations on the satellite the repetition rate had to be decreased from 100 Hz to 50.5 Hz. Thus the averaging length for one observation had to be increased to 90 km to obtain sufficient signal levels from a number 600 pulses (before 700 pulses), which are emitted during a period of 12 s (N.B. The observation period in the L1B product refers to a length of 600 pulses within 90 km, while the requirements for random error refer to a range of 100 km below 14 km and 140 km above 14 km). A similar laser concept with an injection-seeded, frequency-tripled power laser in MOPA configuration, frequency tuning capabilities and laser energies of 60 mJ at 354.9 nm was realized for the ALADIN airborne demonstrator (Schröder et al. 2007, Lemmerz et al. 2017).

## 4.3 Telescope and Front Optics

The laser pulses are directed through a beam splitter, where small amounts of the outgoing laser pulse are directed to the spectrometers for internal laser frequency reference measurements. The linear-polarised beam from the laser transmitter is converted to circular polarised light with a quarter-wave plate and adapted to the telescope optics by a beam expander.

The telescope is a 1.5 m diameter afocal Cassegrain telescope with a focus adjustment by thermal control of the tripod holding the secondary mirror. The divergence of the output laser beam is only 20  $\mu$ rad, as it is expanded to 0.9 m by the telescope. This results in a spot diameter on ground of 6 m in a distance of 404 km (320 km altitude with 37.6° off nadir angle). The backscattered signal from the atmosphere is collected by the primary mirror and send to the transmit/receive optics. The circular polarized light is converted to linear polarisation by a quarter-wave plate. The depolarised part of the backscattered light is not transmitted to the spectrometers, but reflected on the first polarising beam splitter (Pol). Thus this portion is discarded and results in a signal loss, depending on the circular depolarisation ratio. A laser chopper mechanism avoids stray-light entering the spectrometer, while the laser pulse is send out, and a narrow bandwidth filter of 1 nm with a peak transmission of 80 % limits the broadband earth and atmospheric radiometric background from ground or cloud albedo. The receive beam FOV is limited by the field stop to 18.1  $\mu$ rad and the beam diameter is limited to 20 mm by the aperture stop. A half-wave plate rotates the linear polarised light in a direction that the beam is reflected by the polarising beam-splitter at the input of the RSP towards the MSP.

## 4.4 Mie Spectrometer MSP

The reflected beam from the polarising beam splitter of the RSP passes a beam expander, thus reducing the beam divergence and a quarter-wave plate before illuminating the Fizeau interferometer of the MSP. The Fizeau interferometer, which is composed of two reflecting plates with a wedge angle of  $4.77 \mu\text{rad}$ , acts as a narrowband filter with a Full Width Half Maximum (FWHM) of  $0.067 \text{ pm}$  ( $159 \text{ MHz}$ ) for the atmospheric path and  $0.053 \text{ pm}$  ( $125 \text{ MHz}$ ) for the internal reference path. This difference in FWHM is related to a different illumination of the internal and atmospheric path on the MSP. It transmits the central part of the backscattered atmospheric spectrum including the narrow bandwidth aerosol return superimposed on the broadband molecular return, and constant background signal. Due to the wedge angle of the Fizeau interferometer, different wavelengths interfere on different lateral positions of the Fizeau interferometer along the wedge. Thus a wavelength shift results in a shift of the interference pattern (fringe), which is imaged on the ACCD detector within the DFU-M. The Fizeau interferometer is designed to have a Free Spectral Range (FSR) of  $0.91 \text{ pm}$ . Only a portion of  $0.66 \text{ pm}$ , which is called Useful Spectral Range (USR) is imaged onto the ACCD for the atmospheric path. Fig. 4-2 shows the principle of the MSP.

The peak transmission of the Mie spectrometer (MSP) including the Fizeau spectrometer is  $31.5 \%$ , whereas the overall Mie radiometric efficiency is predicted as  $0.71 \%$  (BOL: begin of life), defined by the ratio of photons at the input of the telescope divided by the mean number of photons at the output the MSP multiplied with the transmission of the laser emission path (but excluding the quantum efficiency of the ACCD). This radiometric efficiency results from the transmission of all optics (transmit path  $0.773$ , receive path  $0.34$ , MSP peak transmission  $0.315$ ), the spectral efficiency of the Fizeau interferometer ( $0.135$ ) and the pupil truncation from the circular Fizeau aperture to the square ACCD aperture ( $2/\pi$ ).

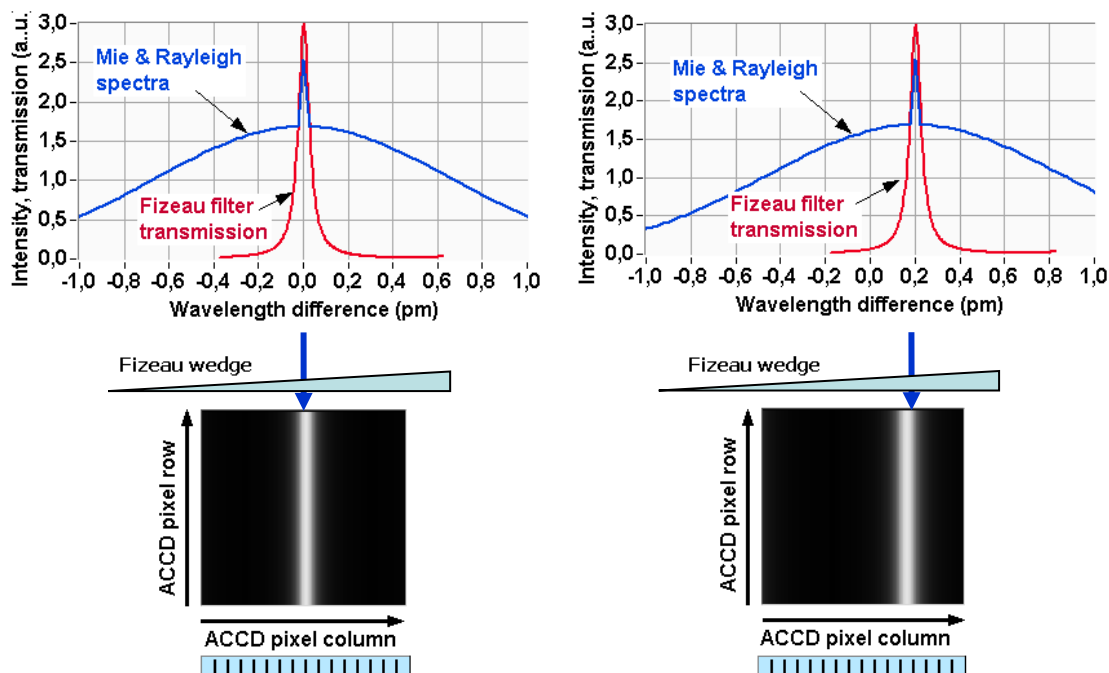


**Figure 4-2:** Principle of the MSP with Fizeau interferometer; the central part of the Rayleigh spectrum und the Mie spectrum (blue) is transmitted through the Fizeau interferometer for zero-Doppler shift (left) and non-zero Doppler shift (right); the Fizeau filter transmission curve (red) has its central transmission on different lateral positions of the Fizeau interferometer wedge, which results in a fringe located at different pixels on the ACCD (bottom); the fringe is laterally imaged onto 16 ACCD pixel columns.

	Document Nr. <b>AE-RP-DLR-L1B-001</b>	Issue: <b>4.4</b>	Date: <b>20.04.2018</b>	Page: <b>21/117</b>	
	Doc. Title: <b>ADM-Aeolus ATBD Level1B Products</b>				

## 4.5 Rayleigh Spectrometer RSP

The beam from the transmit/receive optics is first reflected towards the MSP. The reflected light from the MSP is mainly composed from the broadband molecular return. Most of the broadband Rayleigh signal is reflected at the MSP with a mean reflection of about 0.9, which is shown in Fig. 4-3. The periodic structure is caused by the FSR of 0.92 pm of the MSP.

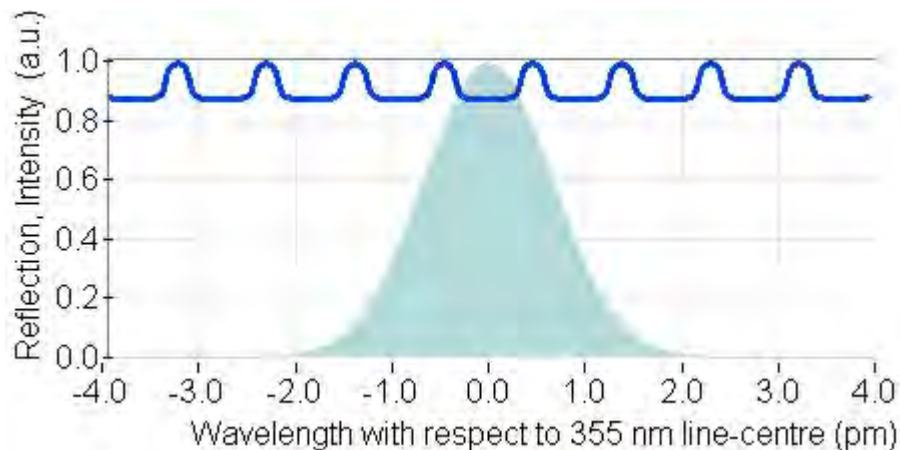


**Figure 4-3:** Broadband reflection coefficient of the MSP (solid line) with a FSR of 0.92 pm and the spectral shape of the Rayleigh signal (shaded area) sketched for the optical path of the atmospheric backscatter signal; the reflection function is slightly different for the internal reference path due to the different illumination of the Fizeau interferometer for the internal and atmospheric path.

Not only the Rayleigh signal is reflected on the MSP, but also portions of the narrowband Mie return, which contaminates the signal within the RSP. This results in a cross-talk effect between MSP and RSP, which yields to an error in the Rayleigh wind speed estimate depending on the scattering ratio. This is caused by different response curves for the Mie and Rayleigh signal, because of a factor of 100 smaller bandwidth of the Mie signal compared to the Rayleigh signal. As the scattering ratio can be estimated from the measurements on the MSP, the cross-talk effect can be corrected (Dabas et al. 2008), which is performed for the L2B but not for the L1B products.

The RSP is based on the double-edge technique, where two spectral filters with a FWHM of 0.65 pm (1551 MHz for direct and 1531 MHz for reflected path; total FWHM including defects) are separated by 2.33 pm centred on the transmitted wavelength. The two spectral filters are realised by two Fabry-Perot interferometers, where the two distinct spacing of the reflecting plates are realised by an additional deposited step for one filter. The two spectral filters are illuminated sequentially by using the reflection from one spectral filter to feed the other. The use of two filters within the RSP leads to a differential measurement of the backscattered signal, thus allowing to determine the frequency shift with the use of a response curve. The basic principle of the RSP is illustrated in Fig. 4-3.

This sequential implementation of the double-edge technique is a novel approach to gain higher radiometric efficiency for the Rayleigh spectrometer, which was not realised in other double-edge systems before. It results in different maximum transmissions for both filters, compared to a parallel implementation of the double-edge technique. The peak transmission of both filters are 81 % and 67 % respectively, whereas the overall Rayleigh radiometric efficiency is 6.4 % (BOL), defined by the ratio of photons at the input of the telescope divided by the number of photons at the output of one Rayleigh filter multiplied with the transmission of the laser emission path (but excluding the quantum efficiency of the ACCD). This radiometric efficiency results from the transmission of the optics (transmit path 0.773, receive path 0.34, RSP peak transmission 0.74 as mean of both filters), and the spectral efficiency of both Fabry-Perot interferometers for a molecular signal (33%).

Thermally tuning of the RSP in the range of  $\pm 1.1$  GHz, which corresponds to one FSR of the MSP, is used to centre the RSP on the centre of useful spectral range of the MSP.

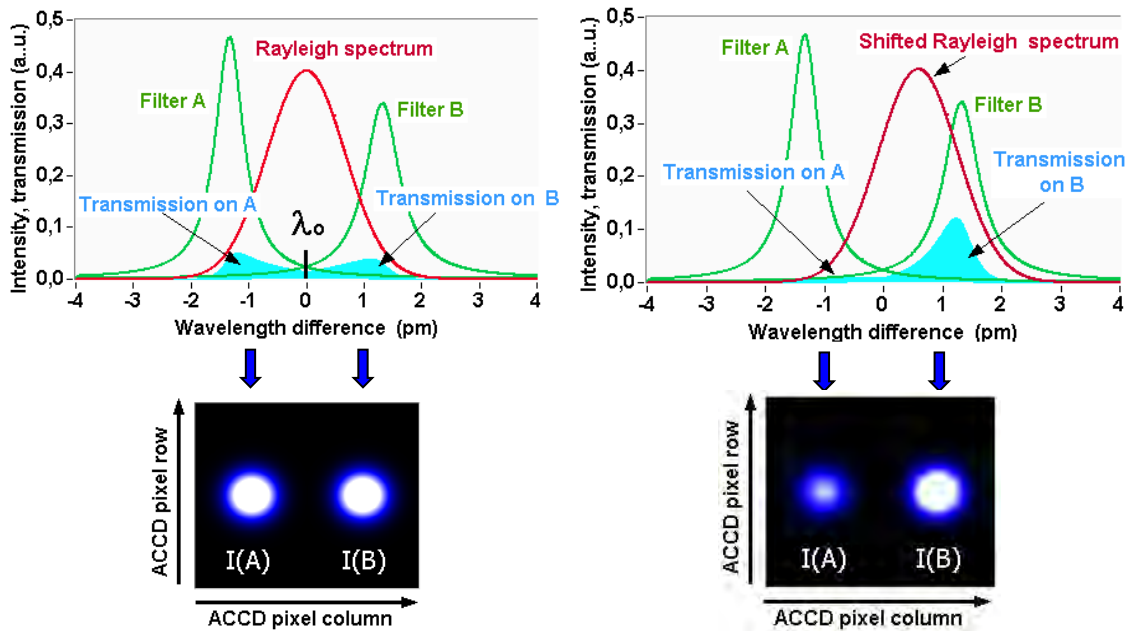


**Figure 4-3:** Principle of the sequential, double edge RSP: Rayleigh spectrum (red) and transmission curves of RSP Filter A and B (green) for zero Doppler shift (left) and a significant Doppler shift (right); the transmitted signal intensity through the filters is shown in light-blue; for a non-zero Doppler shift (right) the transmitted signal on B is higher than on A; the spots on the ACCD image zone are shown in the two figures below.

## 4.6 Detection Front End Units DFU and ACCD

Two DFUs are used for detecting the output of the MSP and the RSP. Elements of the DFU are the ACCD and an electronic pre-amplifier stage. The ACCD is optimised for operation in the UV (thinned and back-side illuminated) to yield high quantum efficiency of 85% and cooled to  $-30\text{ }^{\circ}\text{C}$  for low electronic noise. The beams of the spectrometers are imaged onto  $16 \times 16$  pixels of an ACCD. This results in 16 spectral channels for the MSP. The two spots from the two filters of the RSP are imaged to 8 pixels of the ACCD each. A novelty of the ALADIN detection unit is the usage of an accumulation CCD, where the atmospheric backscattered signals from consecutive laser pulses are accumulated within a memory zone of the ACCD (see Fig. 4-4). The charges of the memory zone are read out with low frequency to minimise read-out noise after accumulation of P-1 laser pulse. The duration of 1 pulse is necessary for read out, thus reducing the number of on-chip accumulated pulses to P-1. As the memory zone contains 25 rows, a maximum number of 25 range gates can be acquired with the ACCD. The duration of the transfer from the image to the ACCD memory of  $1\text{ }\mu\text{s}$  limits the minimum time for one range gate to  $2.1\text{ }\mu\text{s}$ , which corresponds to a vertical resolution of 250 m. The charge transfer leads to a temporal and spatial overlap of consecutive range gates of  $1.1\text{ }\mu\text{s}$ , corresponding to 130 m altitude, which was observed with the ALADIN airborne demonstrator (DLR 2012a, DLR 2012d, Marksteiner 2012). The timing sequence of both ACCD's is programmable, giving flexibility in range gate resolution within one profile for both the Mie and Rayleigh return independently. Also the number of accumulated shots P on the ACCD is programmable as a parameter valid for both the Mie and Rayleigh ACCD.

The photons at the input of the ACCD are converted to electrons with a quantum efficiency of 85%, and a total random noise of 3.9 electrons (Mie) and 4.7 electrons (Rayleigh) per pixel and read-out thus allowing quasi-photon counting. In addition a dark current with a rate of 1.9 electrons per second and pixel is mainly accumulated in the memory zone of the ACCD, which needs to be corrected from the raw signals. After pre-amplification the charges are digitised with 16 bit. The response linearity of the detection chain was characterised on ground for the Rayleigh channel to be better than 0.1% (EADS-Astrium 2012). Due to this high linearity, a correction of the RSP signals is considered negligible.

In addition to the range-gated lidar mode, the ACCD can be used in an imaging mode, where images of  $16 \times 16$  pixels are acquired. The imaging mode is used for verifying the collimation of the optical path during

the Instrument Defocus Characterisation IDC mode, for verifying the laser beam profile in Laser Beam Monitoring LBM mode, and for characterisation of the detector noise of the ACCD in Dark Current Calibration mode (see 4.3.3).

In addition to the 16 illuminated pixels per line (range gate), there are 4 additional read-out sequences per line ("virtual pixels", which are not illuminated (not shown in Fig. 4-4)). These additional read-out sequences are also digitized and stored leading to a total number of 20 pixels per line (range gate). Two of these 4 additional pixels are used for detection chain offset correction.

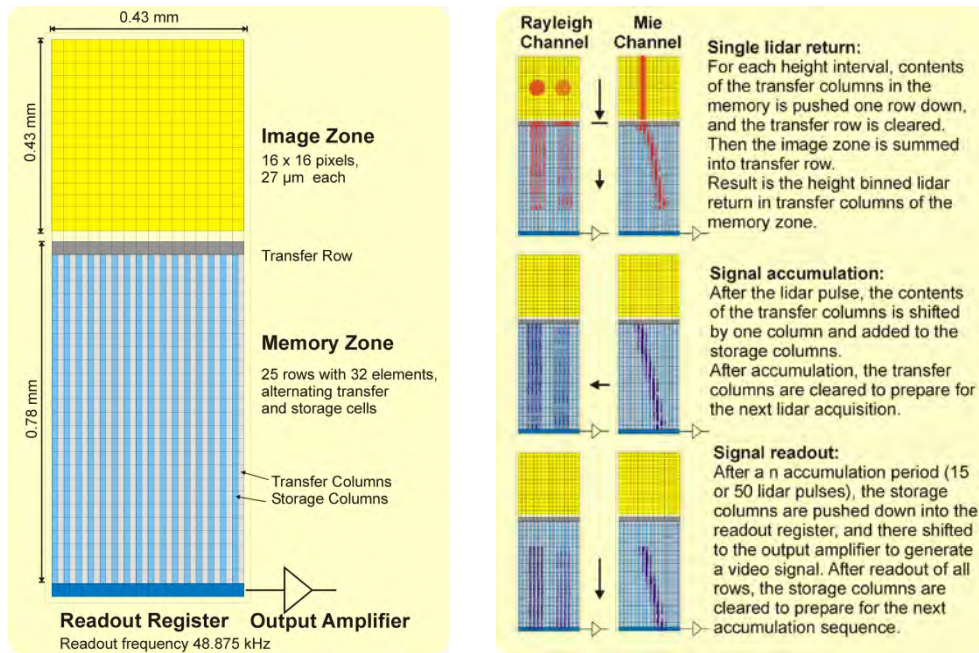


**Figure 4-4:** Illustration of the ACCD (left) illuminated image zone with 16\*16 pixels, and the memory zone of 32\*25 pixels, where the charges are accumulated on-chip and the register for read out of the pixel charges after accumulation; the principle of the signal detection, signal accumulation and signal readout is shown on the right (from ESA 2008).

	Document Nr. <b>AE-RP-DLR-L1B-001</b>	Issue: <b>4.4</b>	Date: <b>20.04.2018</b>	Page: <b>24/117</b>	
	Doc. Title: <b>ADM-Aeolus ATBD Level1B Products</b>				

## 4.7 Instrument Operation

### 4.7.1 Timing Sequence within one Observation

The backscattered signal of a number of P laser pulses is accumulated directly on the ACCD. The value of P is typically between 20 and 50, which results in a time for one measurement between 0.4 s and 1 s and an along-track distance of 3 km to 7 km. These on-board accumulated signals are called one measurement, and every measurement is included in the downlinked data packages. These measurements are processed on-ground to form one observation, which is then a result of N measurements. Each observation consists of a total number of 600 returns from laser pulses, resulting in a duration of 12 s and a horizontal averaging length of about 90 km. Thus the product of N and P equals to 600 and the nominal settings are N=30 and P=20. The actual number of backscattered returns is only  $N*(P-1)$ , because of the loss of 1 pulse per measurement due to read-out duration. The timing sequence for a number of  $N*P$  pulses (nominal 600) is called basic repeat cycle (BRC) and is repeated every 12 s.

### 4.7.2 Timing Sequence within one Laser Pulse Acquisition

The sequence of detecting the signal of one transmitted laser pulse is called acquisition. A small amount of the transmitted laser pulse is directed towards both spectrometers and detected by the ACCD. This detected reference signal is read out from the ACCD for every single laser pulse without accumulation on the ACCD, as there is sufficient time (2.7 ms) between the detection of the laser pulse reference and the first atmospheric range gate.

A programmable time delay between the transmission of the laser pulse and the acquisition of the first atmospheric sample starts the acquisition of atmospheric range gates. This time delay takes into account the change of satellite altitude (314 km – 341 km) during the orbit with respect to the WGS84 ellipsoid. Within one observation a variable time delay for every measurement is adjusted such that all measurements are acquired at a constant altitude above WGS84.

In addition information from a digital elevation model (DEM) is included in the on-board satellite software to provide knowledge about the height of the ground (above the WGS 84 ellipsoid) along the expected track of the satellite within one week (orbit repeat cycle) in form of a Look-Up Table (LUT). This information is used to optimise the number of detectable ground echoes and minimize the number of lost range bins below the ground. Thus an additional time delay for the start of acquisition of the atmospheric bins could be introduced for every observation (and not measurement as for the satellite altitude compensation) depending on the ground altitude (Marksteiner 2009).

The time delay and therefore the start of the highest range gate could be set separately for the Mie and the Rayleigh spectrometer, as well as the resolutions for every single range gate. Thus the vertical sampling grid for the Mie and Rayleigh range gates could be set independently. After the acquisition of 24 atmospheric range gates, the acquisition of the background light is started after an additional time delay, which is sufficiently long after the ground return at zero altitude. All the timing parameters are programmable in-flight and 8 different timing sequences could be programmed for one orbit to allow climate zone dependent sampling.

### 4.7.3 Instrument Modes

The different ALADIN instrument operation modes are summarized in Tab. 4-2 and illustrated in Fig. 4-5. Besides the nominal Wind Velocity Measurement (WVM) mode, nine calibration, characterisation and health-check modes are implemented (EADS-Astrium 2004a, EADS-Astrium 2013a, ADS 2017). Some modes are planned to occur regularly as the Instrument Response Calibration consisting of the Mie Response Calibration (MRC) and Rayleigh Response Calibration (RRC). Also the Instrument Defocus Characterisation (IDC) occurs regularly, whereas others are used on-ground or during commissioning phase, or for health check on specific user request (oR). For Instrument Spectral Registration (ISR) and Instrument Auto Test (IAT) the transmitter frequency is tuned over a spectral range of  $\pm 5500$  MHz resp.  $\pm 5000$  MHz in steps of 25 MHz and 250 MHz, for IRC over  $\pm 500$  MHz in steps of 25 MHz; also during the Laser Beam Monitoring (LBM) mode the laser frequency is varied. During Dark Current Calibration (DCC) and Dark Current in Memory zone (DCMZ), the laser is operated in the so called Laser Burst Warmup (LBWU) Mode, where no laser pulses are emitted. For the Laser Chopper Phase (LCP) adjustment, IDC and the nominal Wind Velocity Measure-

	Document Nr. <b>AE-RP-DLR-L1B-001</b>	Issue: <b>4.4</b>	Date: <b>20.04.2018</b>	Page: <b>25/117</b>	
	Doc. Title: <b>ADM-Aeolus ATBD Level1B Products</b>				

ment (WVM) mode the laser is operated at a fixed frequency. The detector ACCD is operated in imaging mode for LBM, DCC, and IDC, whereas it is operated in lidar mode for all other modes. For ISR, IAT, DCC, and LCP only the internal laser reference signal is processed and those modes are thus independent from atmospheric conditions and surface properties. Also the DCMZ mode is independent from atmospheric conditions although here the atmospheric range gates are processed, because no laser pulses are emitted. The atmospheric range gate with the signal from ground return on the MSP and RSP data is used for processing of data obtained during MRC and RRC, and several atmospheric range gates detected by the RSP are processed for RRC in addition to the internal reference signal. The calibration scheme for RRC using atmospheric signals could cause problems arising from atmospheric inhomogeneities (e.g. clouds) and a quality-control scheme was investigated (DLR 2011). The atmospheric signal and the internal reference signal detected by both spectrometers are used during nominal WVM.

The purpose and realisation of the different modes is as follow:

**Instrument Spectral Registration:** The laser transmitter is tuned in frequency over one FSR of the Fabry-Perot interferometer of the RSP including several FSR of the Fizeau interferometer of the MSP. Purpose is to obtain the spectral transmission of the two filters of the RSP, and the spectral response of the MSP. From that the frequency  $f_1$  will be determined, where the two transmission curves of the RSP filters are crossing and the closest centre frequency  $f_0$  of the MSP. This is used to tune the laser transmitter frequency to  $f_0$  and to shift the crossing frequency  $f_1$  of the RSP to  $f_0$  by thermally tuning the RSP. The ISR mode is also used to characterize the instrument for L2A (aerosol) and L2B (wind) processing (Dabas et al. 2008, Flamant et al. 2013, ECMWF 2014b).

**Instrument Auto Test:** Similar as during ISR the laser transmitter will be tuned in frequency to obtain the spectral transmission of the RSP and the MSP. The transmission curves of the RSP will be used to determine the spectral parameters as FWHM and spectral spacing for both RSP filters. The response curve of the MSP will be derived with the mean slope and the deviation from the best fit as well as the FWHM of the fringe of the MSP for different frequencies. These numbers are used to monitor the stability of the spectrometers and to determine the internal response calibration parameters for MSP and RSP.

**Dark Current Calibration:** The dark current of the detection chain is measured during LBWU mode, where no laser pulses are emitted and using the imaging mode of the ACCD. The laser can be either operated to investigate stray-light or is switched off for pure detector dark current investigation (LBWU mode). Thus the mean dark signals, the dark signal noise, and dark signal non-uniformity can be characterized.

**Instrument Defocus Characterisation:** The ACCD is used in imaging mode to obtain a two-dimensional image of the two spots from the two RSP filters and of the linear fringe of the MSP. The data from the RSP is used to determine the centroid position and the size of the two filter spots. These parameters allow to determine the collimation of the optical path of ALADIN and to thermally adjust the focus of the telescope in order to minimize the spot sizes on the RSP.

**Laser Beam Monitoring:** The near-field pattern of the optical beam profile of the outgoing laser pulse can be monitored with the MSP in imaging mode and the laser frequency varied over the Mie USR. This allows estimating the laser beam profile and correlating it with the laser intensity per area (fluence), which is important for securing no damage on the optics. On the other hand this mode can be used to characterize the illumination of the Mie ACCD by the internal path, which is only partly illuminating the Mie ACCD (in contrast to the atmospheric path, which is fully illuminating the Mie ACCD).

**Laser Chopper Phase:** The laser chopper is blocking the outgoing laser pulse for the optical receiver chain. This mode is used to vary the time delay (phase) of the laser chopper wrt. laser pulse emission and to determine the optimal value for this phase in lidar mode for both Mie and Rayleigh channel. Although both the internal reference path and the atmospheric path signals are analysed from the detector, this mode does not rely on atmospheric backscatter signal. Thus it is considered as an internal reference signal mode only.

	Document Nr. <b>AE-RP-DLR-L1B-001</b>	Issue: <b>4.4</b>	Date: <b>20.04.2018</b>	Page: <b>26/117</b>	
	Doc. Title: <b>ADM-Aeolus ATBD Level1B Products</b>				

Instrument Operation	Acronym	Occurrence	Purpose	Transmitter frequency (range/step)	ACCD mode	processed data
Instrument Spectral Registration	ISR	on-ground and in-orbit	centre laser transmitter frequency and calibration for L2	[-5.5, +5.5 GHz] step 25 MHz	lidar	internal
Instrument Auto Test	IAT	on-ground and/or in-orbit health check (oR)	verify Mie/Rayleigh receiver spectral transfer functions and co-registration of Mie and Rayleigh centers	[-5.0 , -0.75 GHz] and [0.75, 5.0 GHz] with 250 MHz steps [-0.75, +0.75 GHz] with 25 MHz steps	lidar	internal
Dark Current Calibration	DCC	on-ground, in-orbit (oR)	characterise detection chain in darkness	no laser emission (LBWU)	lidar	internal
Dark Current in Memory Zone	DCMZ	on-ground, in-orbit (oR)	characterize dark current in memory zone	no laser emission (LBWU)	image	atmospheric
Instrument Defocus Characterisation	IDC	in-orbit, weekly	characterize defocus of TEL by measuring Rayleigh spot size	fixed	image	atmospheric
Laser Beam Monitoring	LBM	On-ground, in-orbit (oR)	Monitor laser beam profile	varying	image	internal
Laser chopper phase	LCP	on-ground, in-orbit (oR)	optimisation of laser chopper phase	fixed	lidar	internal
Instrument (Mie, Rayleigh) Response Calibration	IRC MRC RRC	weekly	to measure MSP and RSP response with satellite in nadir	[-0.5, +0.5 GHz] step 25 MHz	lidar	internal and ground return on MSP and atmosphere on RSP
Wind Velocity Measurement	WVM	nominal mode	nominal wind measurement mode	fixed	lidar	internal and atmosphere and ground return on MSP and RSP

**Table 4-2:** ALADIN instrument operation modes (oR: on request) according to Airbus (2017).

All the above instrument operation modes are used for characterising, tuning and health-check. Data from these modes will not be used for processing the raw instrument data to the L1B wind product, whereas the L2A (aerosol) and L2B (wind) processing is using the ISR mode data for calibration (Fig. 4-5, Dabas et al. 2008, Flamant et al. 2013, ECMWF 2014b). In contrast the data from Mie and Rayleigh calibration during IRC will be used to obtain calibration data, which is used for L1B wind processing. IRC applies an end-to-end calibration of the instrument including signal from the atmosphere. For this mode the whole satellite is rolled

	Document Nr. <b>AE-RP-DLR-L1B-001</b>	Issue: <b>4.4</b>	Date: <b>20.04.2018</b>	Page: <b>27/117</b>	
	Doc. Title: <b>ADM-Aeolus ATBD Level1B Products</b>				

by 35° so that the ALADIN is pointing near nadir (with an angular offset of a few mrad), in order to obtain a zero frequency shift from the horizontal wind velocity (see Fig. 4-6). A zero vertical wind speed for the horizontal length of the integration (over two observation of 90 km) has to be assumed for processing. During IRC the laser transmitter frequency is tuned over  $\pm 500$  MHz with steps of 25 MHz, corresponding to a range of maximum detectable wind speeds of  $\pm 89$  ms<sup>-1</sup> (LOS) and  $\pm 145$  ms<sup>-1</sup> (HLOS). It is planned to perform this calibration mode about every week. The derived parameters from the calibration mode will be used for the wind velocity determination, and monitoring and maintenance of the co-registration of the center of the Mie USR with the Rayleigh filter crossing point.

**Instrument Response Calibration:** The IRC mode is composed of the following two response calibration modes:

**Mie Response Calibration:** Only the range gate, where a signal from the earth surface – called ground return - is used for further processing. The frequency of the ground return range gate is assumed to be zero, which is a good approximation over land and also over the ocean in nadir-pointing. The response of the MSP for the range of transmitted frequencies is used to derive the linearity parameters (slope and offset) for the MSP as well as its non-linearity from pixel to pixel.

**Rayleigh Response Calibration:** The atmospheric range gates, where negligible cross-talk from the aerosol signal and negligible vertical velocity is expected (e.g. between 6 and 16 km) is used to determine the Rayleigh response for different transmitted frequencies. In addition the ground return range gate is analysed wrt the Rayleigh response, as the spectral response from the ground is different as from the atmosphere for the Rayleigh receiver. The ground return can be considered as a narrowband spectral signal. As for the MRC the linearity parameters (slope and offset) and the non-linearity of the RSP will be characterized for atmospheric and ground return range gates independently. The calibration scheme for RRC using atmospheric signals could cause problems arising from atmospheric inhomogeneities (e.g. clouds) and approaches were studied, including the use of the scattering ratio from the MSP signal for quality-control of the RSP signal (DLR 2011).

**Dark Current in Memory Zone:** The dark currents in the memory zone of the ACCD are accumulating with time and thus depend on the number of accumulated pulses P on the ACCD. These dark currents act as a constant electronic offset and need to be subtracted from the raw signal. The dark current per accumulated laser pulse (dark current rate) is characterized in lidar mode without laser pulse emission for both Mie and Rayleigh channel ACCD.

The nominal mode of the instrument, which is used permanently until a command for mode switch is received is:

**Wind Velocity Measurement:** The instrument is operated with a fixed laser frequency with the satellite pointing to 35° off nadir. The internal reference signal and the atmospheric and ground return signal are sampled with the programmed vertical sampling scheme for Mie and Rayleigh independently and the horizontal sampling scheme determined by the number of accumulated pulses P and the number of measurements per observation N.

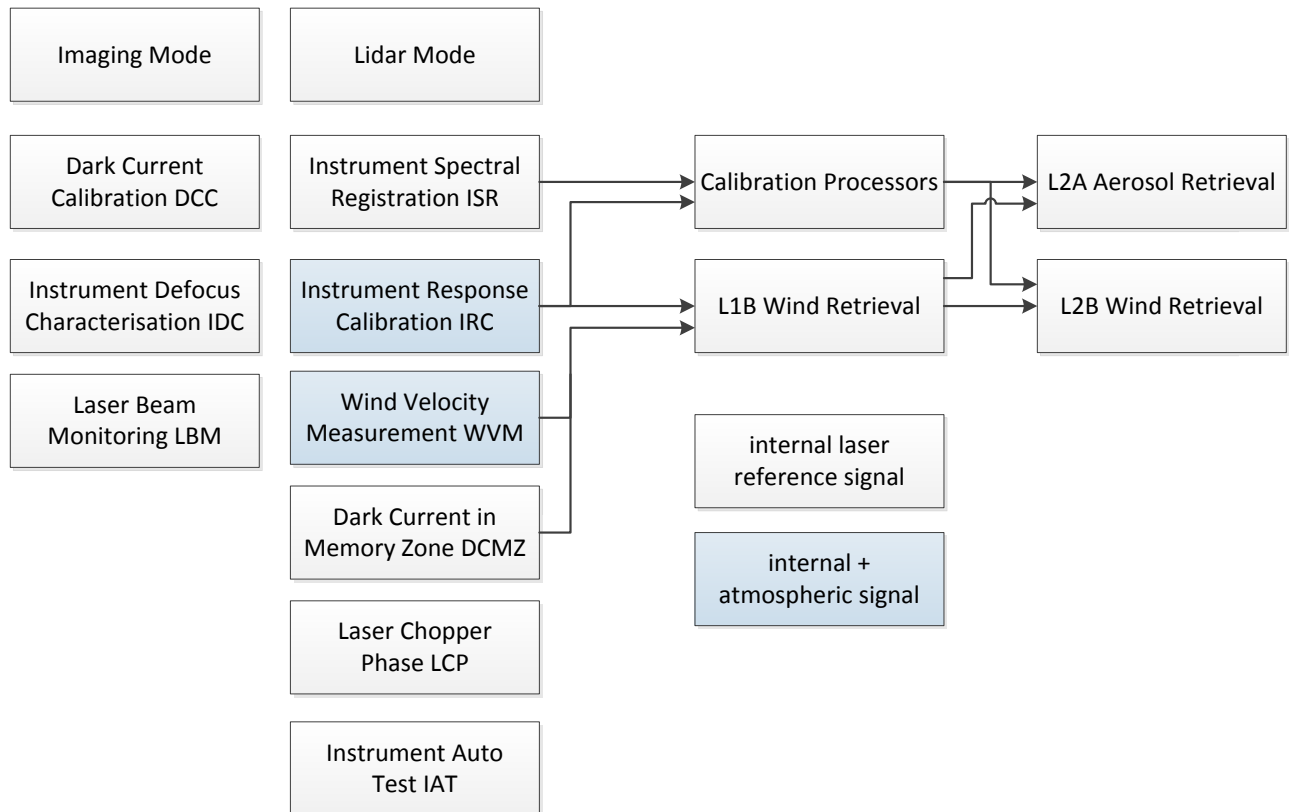


**Figure 4-5:** ALADIN instrument modes with ACCD detector operating in imaging mode (left column) and lidar mode (right column); most modes use only the laser internal reference signal (grey), while response calibration IRC and wind mode WVM (blue) are relying on both the internal and the atmospheric path signal; ISR and IRC mode data are used for calibration processors and subsequent L2A aerosol and L2B wind retrieval, which is indicated by arrows; wind WVM, response IRC and dark current DCMZ mode data are used as input for L1B wind retrieval and subsequently L2A aerosol and L2B wind retrieval; all other modes are for instrument monitoring and data is not directly used for aerosol and wind retrievals.

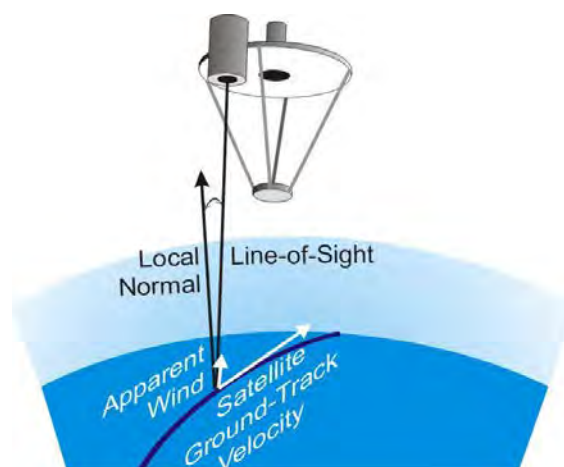


**Figure 4-6:** ADM-Aeolus in nadir pointing mode during instrument response calibration IRC (from ESA 2008).

	Document Nr. <b>AE-RP-DLR-L1B-001</b>	Issue: <b>4.4</b>	Date: <b>20.04.2018</b>	Page: <b>29/117</b>	
	Doc. Title: <b>ADM-Aeolus ATBD Level1B Products</b>				

## 5 Data Product Content

According to the processing level, the ADM-Aeolus data products are grouped into Level 0, Level 1 and Level 2 data products (Tab. 5-1). Starting point for the processing are the raw telemetry data, as transferred from the ground station to the Payload Data Segment (PDS).

Data Product	Content
<b>Level 0</b>	Time-ordered source packet (measurement, housekeeping, platform, and AOCS data) streams.
<b>Level 1A</b>	Housekeeping source packet fully processed, AOCS source packets (geolocation) processed and assigned to measurement data, measurement data unprocessed.
<b>Level 1B</b>	Fully processed, calibrated and georeferenced measurement data including HLOS winds, viewing geometry, ground echo data and product confidence data (PCD)
<b>Level 2A</b>	Additional aerosol/cloud optical properties, as optical depth, extinction coefficient, co-polarized backscatter coefficient, cloud classification and PCD.
<b>Level 2B</b>	L2B products represent “consolidated” HLOS wind data and include corrections using actual pressure and temperature information as obtained from numerical models from a NWP centre. Additional corrections are based on retrieved optical properties. Measurements are grouped after a scene classification.
<b>Level 2C</b>	L2C products contain two-component wind vector profiles on the location of the ADM-Aeolus ground track as obtained after the assimilation process of L2B products at a NWP centre. L2C products mainly contain information from the NWP model.

**Table 5-1:** Content of data products for ADM-Aeolus.

This document describes the algorithms for the Level 0 and Level 1 products. For further information on the Level 2 products refer to ESA (2004b), ECMWF (2016 a,b), and Flamant et al. (2017).

### 5.1 Raw Telemetry Data

Baseline for the processing is the raw telemetry data (AISP: Annotated Instrument Source Packet), which is then processed to L0 product.

Raw telemetry data is either lidar mode data or imaging mode data (see chapter 4.2.5). In both cases, the telemetry data contains 34 data packets, which may be basically divided into five different types:

- Attitude and Orbit Control System (AOCS) data
- Housekeeping data
- Auxiliary data – Mie
- Auxiliary data - Rayleigh
- Measurement data

The *AOCS data* contains information about the satellite orbital position. The time, position, velocity, and attitude information of the satellite is repeated every 125 ms starting at the beginning of an observation.

Data of the on board ALADIN Control and Data Management Unit, as cavity lock status, instrument mode, laser frequency, or UV energy, is stored in the *Housekeeping data* packet. Furthermore this packet contains information about the number of measurements N and number of shots per measurement P.

The internal references of the Mie channel are stored in the *Auxiliary data - Mie* packet, the Rayleigh channel internal references in the *Auxiliary data – Rayleigh* packet. These two packets are only filled with data for the lidar mode.

The AOCS, Housekeeping, and the Auxiliary data packets Mie & Rayleigh are mandatory for processing (see chap. 7.1).

The *Measurement data* packet is repeated 30 times for the lidar and the imaging mode. These packets contain the ACCD readouts.

## 5.2 General Data Product Structure

ESA has developed a general Ground Segment File Format Standard (ESA 2003), which applies to all data files exchanged between ground segment systems within the Earth Explorer Missions.

This standard introduces the following logical file structure: A logical file is split into two main blocks, a header section followed by a data section. The header section comprises the fixed header (FH) and the variable header (VH), which in turn is split into two parts, the main product header (MPH) and the specific product header (SPH). For every file the FH contains information about the file itself (name, type, and version), validity time, and source information (tool, version, date). The MPH contains information that applies to every file of a certain type, and a SPH contains information which is only valid for a specific file of a certain type. The SPH is completed by the data set descriptors (DSDs), which give information about the data sets following the header. In Figure 5-1 which sketches the product structure, the additional header (red box) shows that Aeolus binary products deviate from this standard (see the description for large data volume below).

There are three different types of data sets, the measurement data sets (MDSs), the annotation data sets (ADSs), and the global annotation data sets (GADS). Whereas the MDSs contain actual measurement data the ADSs will include data required for the full interpretation of the measurement data, as geolocation or product quality information. Calibration data will be contained in GADS.

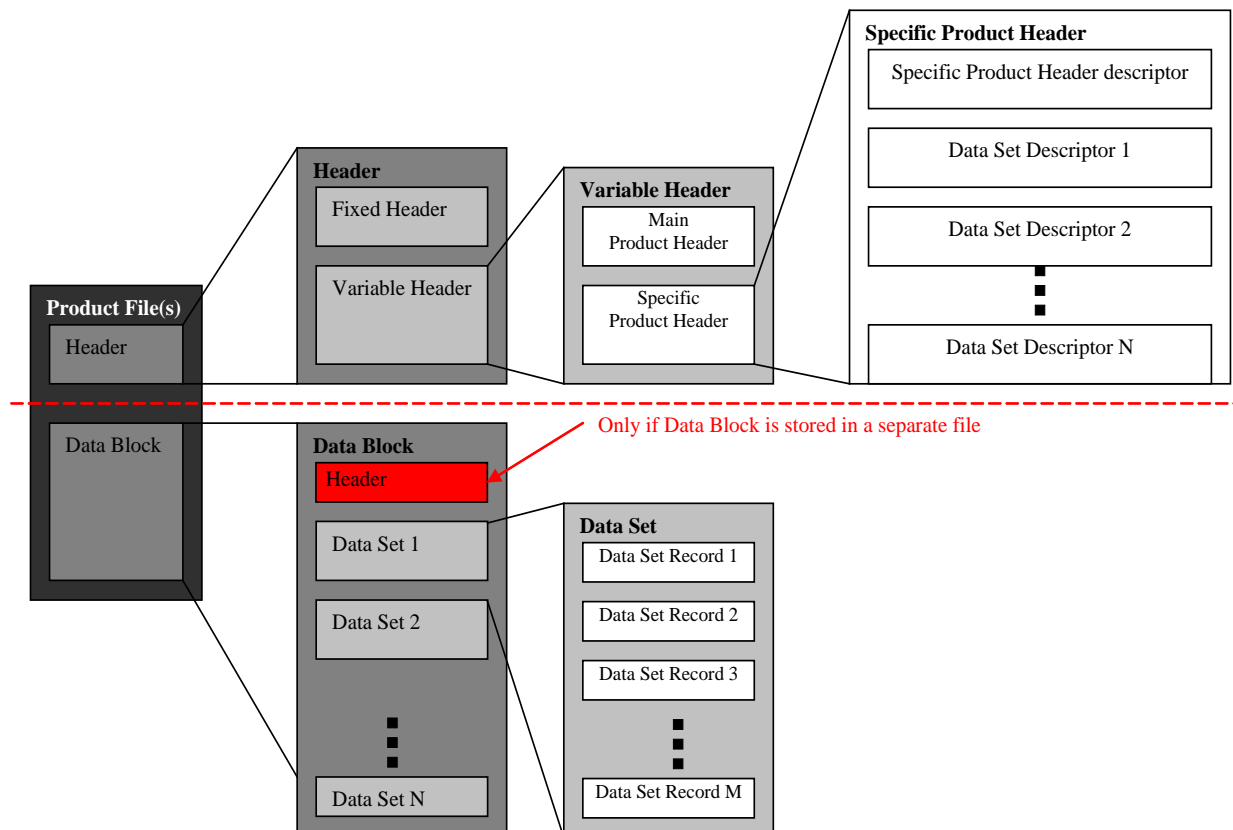


**Figure 5-1:** General product structure for Aeolus file types derived from the Ground Segment File Format Standard with an additional header (red box) for the data block.

**For small data volume**, the header section and the data section are stored in one file written in the Extensible Markup Language (XML) standard.

**For large data volume**, the header section is stored in a file written in the XML standard and the data section is written in a second file as binary data, preceded by a copy of the VH written in the Key Value Terminator (KVT) format (see ESA (2003) for further information).

The following sections briefly introduce the Level 0 and Level 1 products, detailed information may be found in DoRIT and MDA (2017b).

### 5.3 Level 0

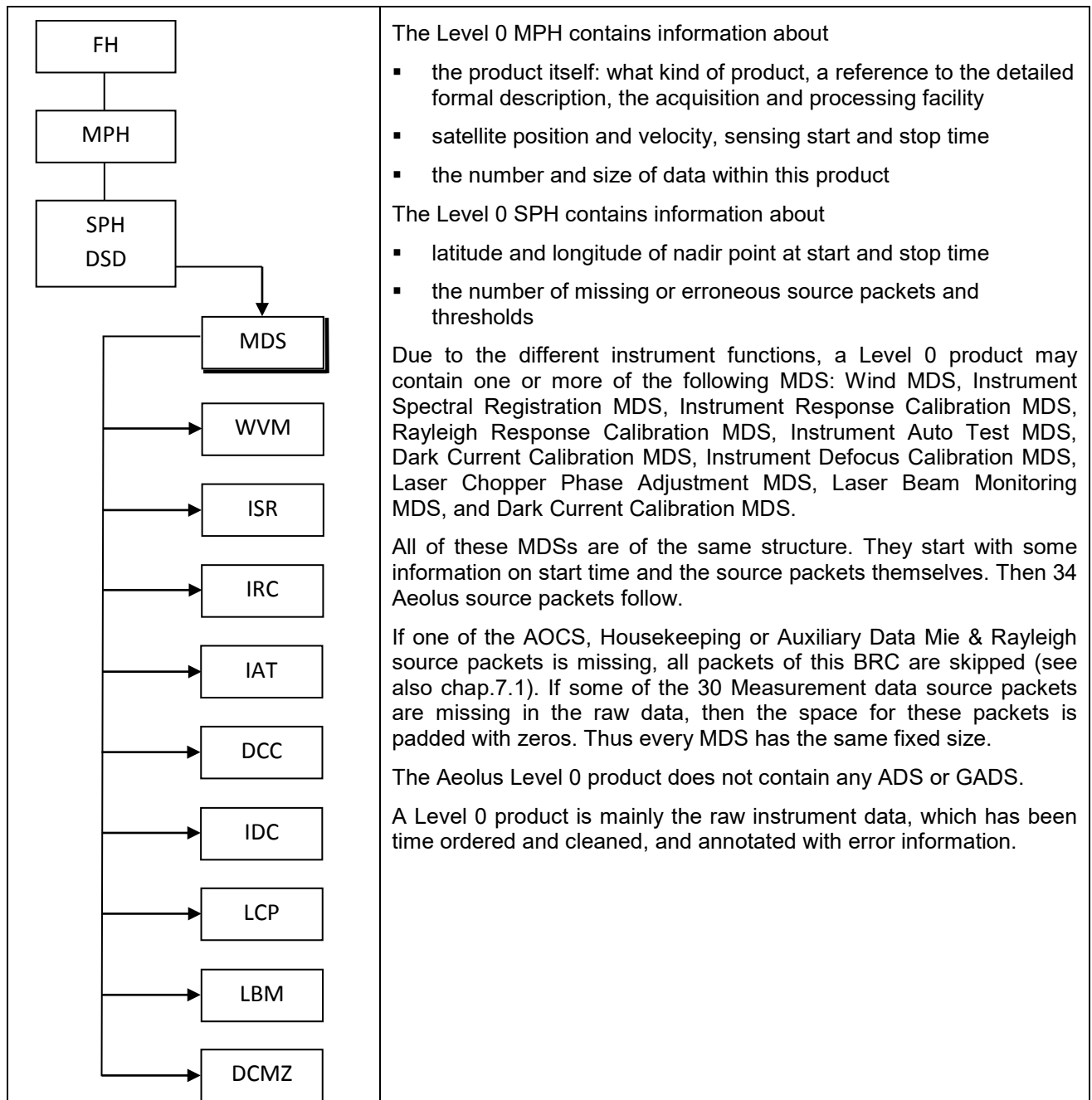
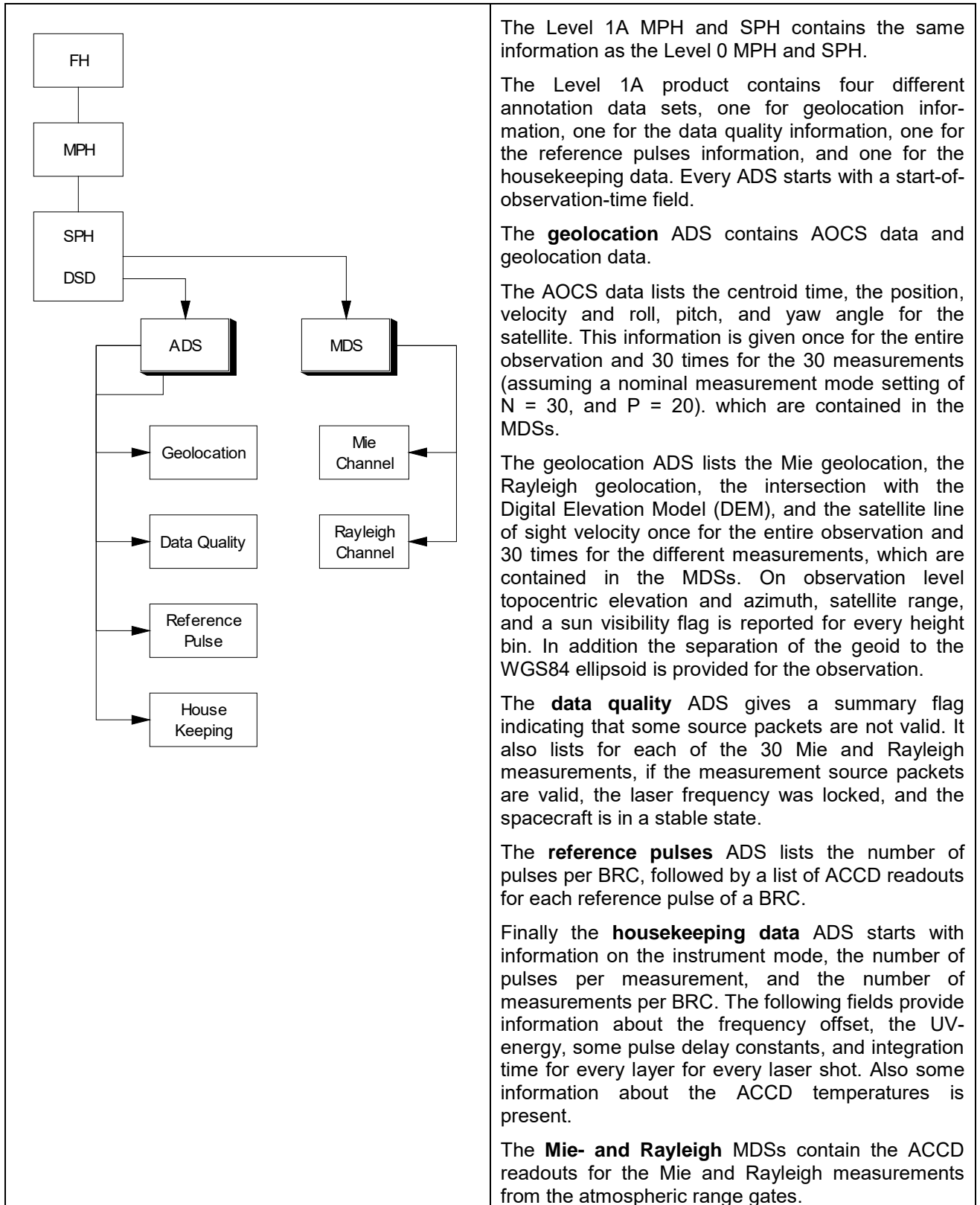


**Table 5-2:** Content of Level 0 data product for ADM-Aeolus.

## 5.4 Level 1A



The Level 1A MPH and SPH contains the same information as the Level 0 MPH and SPH.

The Level 1A product contains four different annotation data sets, one for geolocation information, one for the data quality information, one for the reference pulses information, and one for the housekeeping data. Every ADS starts with a start-of-observation-time field.

The **geolocation** ADS contains AOCS data and geolocation data.

The AOCS data lists the centroid time, the position, velocity and roll, pitch, and yaw angle for the satellite. This information is given once for the entire observation and 30 times for the 30 measurements (assuming a nominal measurement mode setting of  $N = 30$ , and  $P = 20$ ). which are contained in the MDSs.

The geolocation ADS lists the Mie geolocation, the Rayleigh geolocation, the intersection with the Digital Elevation Model (DEM), and the satellite line of sight velocity once for the entire observation and 30 times for the different measurements, which are contained in the MDSs. On observation level topocentric elevation and azimuth, satellite range, and a sun visibility flag is reported for every height bin. In addition the separation of the geoid to the WGS84 ellipsoid is provided for the observation.

The **data quality** ADS gives a summary flag indicating that some source packets are not valid. It also lists for each of the 30 Mie and Rayleigh measurements, if the measurement source packets are valid, the laser frequency was locked, and the spacecraft is in a stable state.

The **reference pulses** ADS lists the number of pulses per BRC, followed by a list of ACCD readouts for each reference pulse of a BRC.

Finally the **housekeeping data** ADS starts with information on the instrument mode, the number of pulses per measurement, and the number of measurements per BRC. The following fields provide information about the frequency offset, the UV-energy, some pulse delay constants, and integration time for every layer for every laser shot. Also some information about the ACCD temperatures is present.

The **Mie- and Rayleigh** MDSs contain the ACCD readouts for the Mie and Rayleigh measurements from the atmospheric range gates.

**Table 5-3:** Content of Level 1A data product for ADM-Aeolus.

The main step from L0 to L1A product is the processing of the housekeeping data and the geolocation of measurements and observations.

## 5.5 Level 1B

The content of the L1B WVM product is shown in Table 5-4:

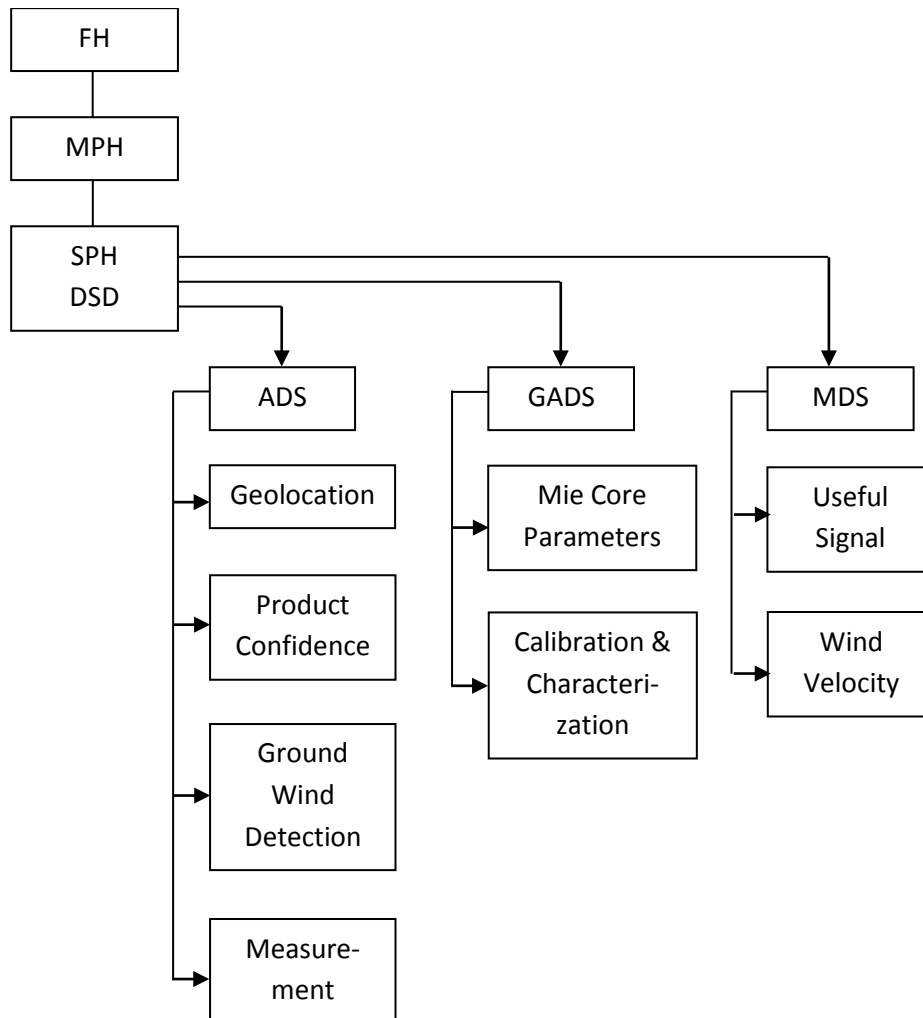


**Table 5-4:** Content of Level 1B data product for ADM-Aeolus.

The Level 1B MPH is the same as Level 1A MPH.

In the first block of the **SPH** latitude and longitude of the satellite nadir point and the LOS intersection with earth ellipsoid at the sensing start and stop time of the MPH are listed. The second block gives information about the number of measurements per BRC, number of pulses per measurement, and the total number of observations, measurements, and reference pulses. The third block states the number of observations and measurements used to estimate wind velocity and the number of Mie/Rayleigh reference pulses used. The fourth block gives information about the number of observations, in which Mie/Rayleigh zero wind was detected and the number of Mie/Rayleigh ground bins detected. The last block reports on the number of measurements and pulses with a laser transmitter unlocked, measurements with satellite not on target and number of corrupted Mie/Rayleigh measurements and reference pulses.

	Document Nr. <b>AE-RP-DLR-L1B-001</b>	Issue: <b>4.4</b>	Date: <b>20.04.2018</b>	Page: <b>34/117</b>	
	Doc. Title: <b>ADM-Aeolus ATBD Level1B Products</b>				

The Level 1B product consists of four different ADS, two GADS, and two MDS. Again, every ADS, GADS and MDS starts with the start-of-observation-time field. The **geolocation** ADS is a copy of the Level 1A geolocation ADS.

The **product confidence data** ADS starts with a block reporting on the number of laser frequencies not locked, satellite not on target for measurements and pulses, the number of corrupted Mie/Rayleigh measurements and pulses, some error quantifiers, information about the laser frequency and energy, Mie/Rayleigh quality information for wind and signal, and the number of invalid measurements and reference pulses for Mie/Rayleigh. The information in this block refers to the entire observation. This block is followed by at most 30 structural identical blocks for the 30 measurements containing the product confidence information for each measurement. The various product confidence information comprises processor settings, statistical parameters on valid and corrupt data, standard deviation of typical laser characterization parameters, and signal quality information like signal to noise ratio, scattering ratio and Mie core fitting results.

The **Mie Core Parameters** GADS contains a copy of the Mie Core parameters as set in the AUX\_PAR\_1B file used for processing this data. These parameters are picked up by the L2B processor who runs an identical Mie Core algorithm.

The **calibration & characterization** GADS reports a copy of selected data of the processing input L1bP auxiliary files 'Satellite Characterisation', 'Mie Response Calibration', and 'Rayleigh Response Calibration'. It contains satellite error quantifiers for the Mie/Rayleigh channels, tripod obscuration correction data, and Mie/Rayleigh frequency step data statistics.

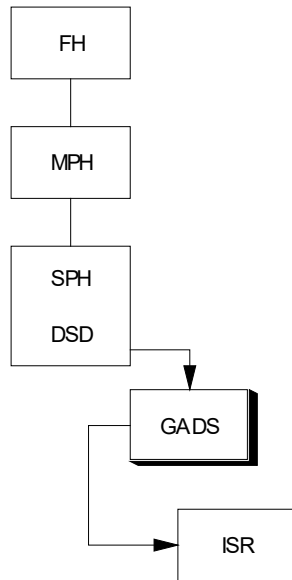
The **ground wind detection** ADS reports the ground correction weighting factors, the average ground bin altitudes and thicknesses above DEM for Mie/Rayleigh, the number of Mie/Rayleigh ground bins detected and for every measurement the detected ground bin number and bin thickness above DEM for Mie/Rayleigh.

The **measurement** ADS copies and pre-processes data from the L1A input product to the L1B product. It contains copies and pre-processed Mie/Rayleigh reference pulse data, Mie measurement data, Mie/Rayleigh time delay information, and validity indicators for the Mie measurement data.

The processed scientific measurement data is stored in two different MDS, the useful signal MDS and the wind velocity MDS.

The **useful signal** MDS reports on the useful signal strength for observations and each measurement for all 25 height bins in the Mie channel and Rayleigh channels A and B, whereas the **wind velocity** MDS reports the derived wind velocity for observations and each measurement for all the height bins in the Mie and Rayleigh channels. In both MDSs the values reported are annotated with quality bit flags.

## 5.6 Auxiliary Calibration Products



### General Auxiliary Calibration Products Structure

The auxiliary calibration products are an output of the Level 1A to Level 1B processing. From the nine MDS on Level 0, see Table 5-1, ten different calibration products are derived on Level 1b: ZWC (retrieved from WVM data), ISR, MRC & RRC (retrieved from IRC), IAT, DCC, IDC, LCP, LBM, and DCMZ. Except for the specific data sets, they share a common structure.

Their MPH is a copy of the Level 1B MPH. Their SPH is a subset of the Level 1B SPH reporting the second, third, and last block of the Level 1B SPH.

Every data set starts with the start of observation times for the first and last BRC of the measurement data used to generate the calibration output.

Every auxiliary calibration then contains exactly one global annotation data set. As an example the figure to the left represents the Instrument Spectral Registration Calibration product.

**Table 5-6:** Content of Auxiliary Calibration Products for ADM-Aeolus for the ISR.

The auxiliary calibration products are written as XML-structure files in a single physical file. The list of auxiliary output products matches the list of instrument modes (Tab. 4-2), except for the wind measurement mode and an additional GADS for the Zero-Wind Calibration ZWC.

The **ISR** GADS contains for each frequency step the ISR results, the laser frequency offset, the Mie/Rayleigh spectral response and some additional statistics data, as the number of used Mie/Rayleigh pulses, and number of corrupted pulses. Furthermore, it contains an overall result of the frequency offset of the Rayleigh filter centre and the frequency offset of the Mie Channel USR closest to the Rayleigh filter centre and the temperatures from the RSP and MSP.

The **IAT** GADS reports for each frequency step the Mie FWHM and Mie response, as well as the Rayleigh transmission of both filters A and B, and the Rayleigh spectral response. As a main result it reports the mean slope of the Mie and Rayleigh channel response and the Rayleigh filter FWHM and filter spectral spacing. In addition, it contains statistics information and RSP and MSP temperatures.

The **DCC** GADS contains all the measurement and reference pulses dark signals and noise, their average values and standard deviations (dark signal non uniformity) over measurements and observations. Additionally, it contains the ACCD temperatures during the data acquisition.

The **IDC** GADS gives a map of mean image pixel intensity values and information about the energetic centroid of channel 1 and 2, as row and column value closest to the energetic centroid, row and column values of image pixel intensities along the centroid, and the size (standard deviation) of the spots. Additionally, the temperatures of the telescope (struts, mirrors) are provided.

The **LBM** GADS characterizes the beam shape. It provides the minimum mean intensity, maps of mean image pixel intensities above minimum, barycentre's for the Rayleigh spots, and a list of derivatives for the beam spot on the Mie ACCD to define the edge of the spot and fitting ellipse parameters.

The **DCMZ** GADS contains only two parameters, the dark current rate of the Mie and Rayleigh ACCD.

The **LCP** GADS contains the laser chopper phase (time delay) and the respective Mie and Rayleigh intensities (mean, maximum, minimum) from the laser internal reference and atmospheric path signal.

The **MRC** GADS first gives an overall flag, indicating the Mie response calibration validity, based on acceptable ranges of calibration results for measurement (ground-return) and reference pulse and the number of valid frequencies. Then it gives detailed information about the measurement and reference pulse

	Document Nr.	Issue:	Date:	Page:	
	<b>AE-RP-DLR-L1B-001</b>	<b>4.4</b>	<b>20.04.2018</b>	<b>36/117</b>	
Doc. Title: <b>ADM-Aeolus ATBD Level1B Products</b>					

calibration validity, the channel response, its mean sensitivity, zero frequency, and response non-linearity. In addition it contains statistics information.

The **RRC** GADS has the same structure as the MRC GADS and contains the equivalent Rayleigh values for the reference pulse, the atmospheric range gates and the ground returns.

Finally, the **ZWC** GADS contains in the first block geolocation and instrument angle information for the centre of the observation. The second block may contain Mie zero wind and/or Rayleigh zero wind results depending on the Mie/Rayleigh ground correction factor. The zero wind results comprise information about the ground echo bin detection and the Mie and Rayleigh channel and the raw LOS wind velocity estimate for the ground bins.

## 6 Geolocation, Coordinate Systems, and AOCs Processing

Complex geometrical problems have to be solved for geolocation of satellite observations (see Kidder and von der Haar (1995) for an introduction). It is necessary to know the Earth coordinates (latitude and longitude) of the particular scene the instrument is viewing. In the ADM-Aeolus mission the sensed data are wind velocity along the direction of the laser beam line-of-sight (LOS). Therefore, it has to be determined in which direction with respect to an Earth fixed local coordinate system the laser beam was pointing during the observation. In addition to the atmospheric wind vector, the movement of the satellite itself and the Earth rotation contribute to the sensed LOS velocity, which has to be corrected. All these tasks require an accurate knowledge of the position of the satellite in its orbit, the orientation of the satellite (attitude) and the scanning geometry of the instrument.

Not only is the location on the Earth's surface important for analysing the observations but also the local surface altitude. The surface altitude from a Digital Elevation Model (DEM) is used to determine the distance from the satellite to the Earth's surface. This is important to identify the ground return bin of the lidar signal among the data. To solve these geometrical problems different coordinate systems, surface models and appropriate geometrical algorithms are needed.

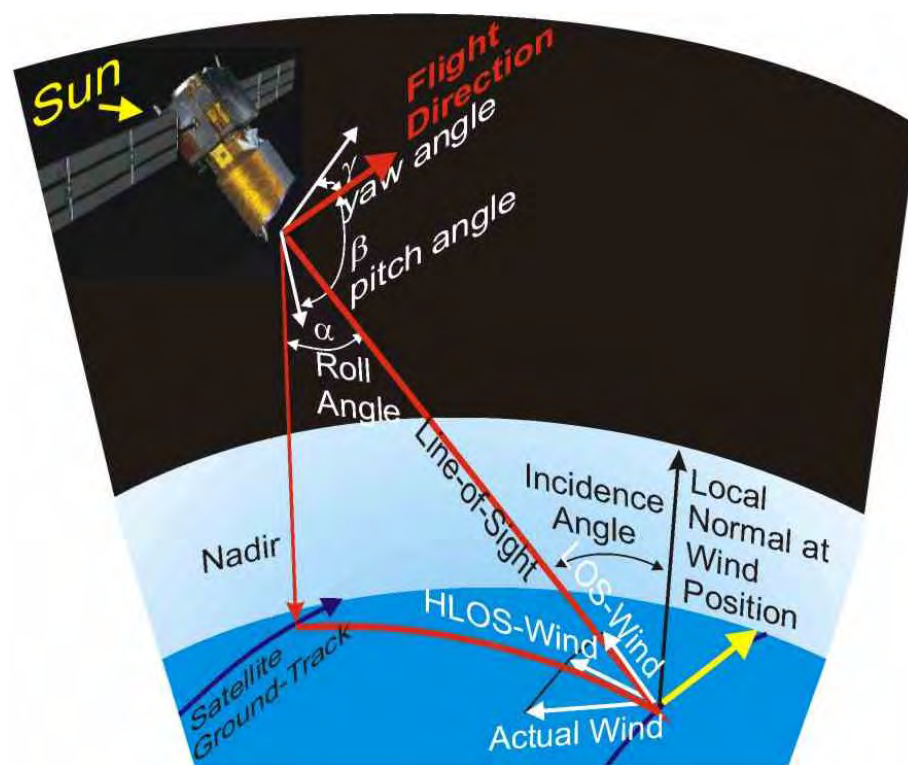


**Figure 6-1:** Pointing geometry of Aeolus, indicating yaw  $\gamma$ , pitch  $\beta$  and roll angle  $\alpha$ . The instrument is pointing towards the line-of-sight; note that the incidence angle between LOS and local normal (at wind position) is different from the roll angle, because of the earth curvature; thus the incidence angle is slightly altitude dependent.

	Document Nr. <b>AE-RP-DLR-L1B-001</b>	Issue: <b>4.4</b>	Date: <b>20.04.2018</b>	Page: <b>38/117</b>	
	Doc. Title: <b>ADM-Aeolus ATBD Level1B Products</b>				

## 6.1 Coordinate Systems

The following coordinate systems are used

- the **J2000** reference frame as an inertial coordinate system for orbit calculations.
- a Local Horizontal/Local Vertical (**LVLH**) reference frame for determination of LOS direction.
- The standard Euler angle sequence of satellite **yaw**, then **pitch**, then **roll** from a (0,0,0)- LVLH coordinate system for overall satellite-ground communications on attitudes.
- an Earth fixed local coordinate system for Earth locations of measurements. The standard Earth fixed local coordinate system is the Earth Centred Earth fixed (**ECEF**) coordinate system.
- The use of a reference ellipsoid allows for the conversion of the ECEF Cartesian coordinates to the more commonly used geodetic coordinates of latitude, longitude, and altitude.

### 6.1.1 J2000 Reference Frame

J2000 is an inertial right-handed Cartesian coordinate system centred in the Earth's core (Fig. 6-2). The x-axis is at the intersection of the mean ecliptic plane with the mean equatorial plane and is directed towards the mean vernal equinox at noon on January 1, 2000. The z-axis points out the North pole along the Earth's rotational axis and is orthogonal to the mean equatorial plane. The y-axis completes the right handed coordinate system.

The satellite on-board processor transforms the GPS position and velocity into the J2000 frame. These are contained in the satellite AOCS data for every 125 ms as a 3d vector for position and velocity (in the J2000 frame) and a 4d quaternion, which represents the transformation from inertial space (J2000) to satellite reference frame.

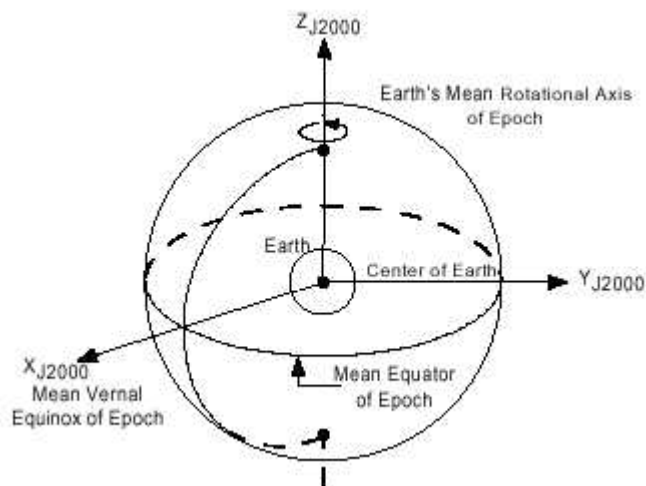
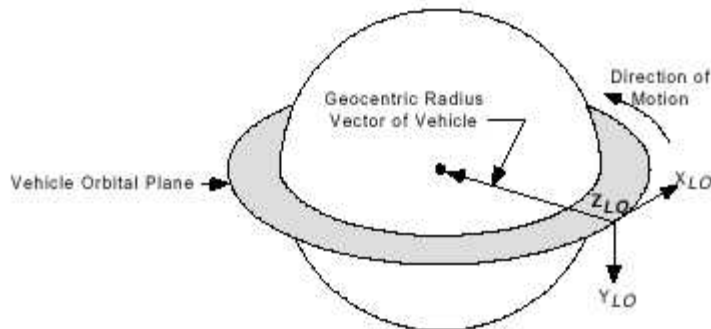


Figure 6-2: J2000 reference frame.

### 6.1.2 LVLH Frame

The origin of the LVLH coordinate system is located at the satellite. In the LVLH reference frame the z-axis is pointing to the centre of the Earth (nadir vector). The y-axis is parallel to the orbit momentum vector and the x-axis completes the right handed coordinate system. The LVLH reference frame is used for the satellite and the instrument.



**Figure 6-3:** LVHV reference frame; the spacecraft is located at the centre of the coordinate system.

### 6.1.3 Pitch, Roll and Yaw

Pitch, roll and yaw are angles of rotation about three axes that are perpendicular to each other. Here pitch, yaw and roll are related to the LVHV coordinate system to define the satellite attitude (Fig. 6-1). Roll is the angle of rotation about the x-axis (flight direction), pitch about the y-axis (perpendicular to the flight direction) and yaw about the z-axis (nadir). Note that the rotations have to be performed in order yaw, pitch and roll. In nominal mode the spacecraft z-axis is rotated by  $-35^\circ$  from nadir about the roll axis (x-axis). Additionally the AOCS system steers the satellite such, that there is no relative velocity along the LOS including the earth rotation. In nominal mode the satellite is steered around the yaw-axis (z-axis) depending on the satellite latitude with a maximum earth rotation of 465 m/s at the equator and 0 m/s at the poles. In nadir-pointing mode the satellite is steered around the pitch-axis.

### 6.1.4 ECEF Frame

The Earth Centred Earth Fixed (ECEF) reference frame is a right-handed Cartesian coordinate system (x, y, z) and is the most recently defined International Terrestrial Reference Frame (ITRF). It's origin is the mass centre of gravity of the Earth (Fig. 6-4). The x-axis is directed towards the intersection of equator ( $0^\circ$  latitude) and Greenwich meridian ( $0^\circ$  longitude). The z-axis points out the North pole along the Earth's mean rotational axis. The y-axis completes the right handed coordinate system and, therefore, intersects the equator at a longitude of  $90^\circ$  East.

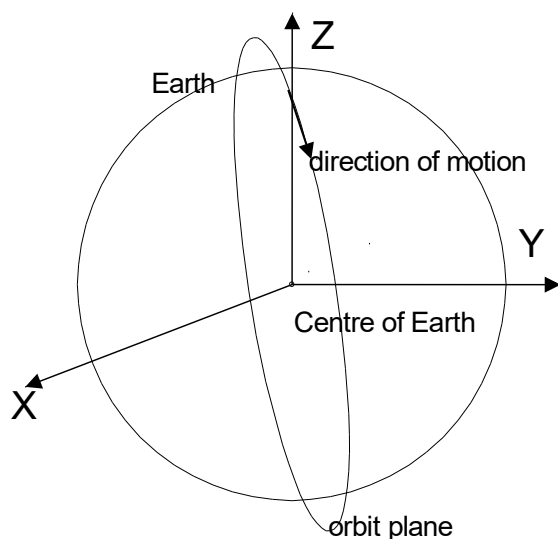


**Figure 6-4:** ECEF System of coordinates with x-axis pointing to equator and  $0^\circ$  meridian, and z-axis towards the North pole along the rotation axis.

	Document Nr. <b>AE-RP-DLR-L1B-001</b>	Issue: <b>4.4</b>	Date: <b>20.04.2018</b>	Page: <b>40/117</b>	
	Doc. Title: <b>ADM-Aeolus ATBD Level1B Products</b>				

### 6.1.5 Geodetic Coordinates

The use of a reference ellipsoid allows for the conversion of the ECEF Cartesian coordinates to the more commonly used geodetic mapping coordinates of latitude, longitude, and altitude. The altitude is defined here as the perpendicular distance above the reference ellipsoid (WGS84 is used for Aeolus).

## 6.2 Orbit

The ADM-Aeolus satellite will fly in a polar, sun-synchronous, dawn-dusk orbit. For a sun-synchronous orbit the inclination is chosen such that the orbit normal makes a constant angle with the Sun-Earth direction. As a consequence the equator crossing time is constant. A reference orbit including the effects of the Earth geopotential (EGM96) was generated and the orbit parameters are summarized in Tab. 6-1.

Orbit parameter	Mean Value	Osculating Value
Reference epoch	01/12/2017 00:00:00.000	
Orbit repeat cycle	7 days and 111 orbits	
Orbit altitude at equator	≈ 314 km	
Orbit altitude variation	≈ 314 km – 341 km	
Orbital period	90.81 minutes	
Local Time of Ascending Node (LTAN) crossing	18.00 h ± 10 minutes	
Tolerance of ascending node crossing	± 25 km (cross-track)	
Semi-major axis	6686.2539 km	6695.996 km
Eccentricity	0.0013411	0.0014321
Inclination	96.6908 °	96.6859 °
Right Ascension of ascending node (RAAN)	339.8023	339.8023
Argument of perigee	89.9026 °	69.2473 °
True anomaly	270.0035	290.6590

**Table 6-1:** Parameters of the Aeolus reference orbit (from ADS 2016) in the Mean-of-J2000 frame; orbit altitudes are referenced to WGS84 ellipsoid.

The variation of the Aeolus orbit altitude and the line of sight range is shown in Fig. 6-5. The two minima correspond to the altitude above the equator, whereas the maximum altitude is reached above the Antarctica and the second local maximum is reached above the Arctic. This results in a total altitude variation of 27 km above the WGS 84 ellipsoid. The line of sight range is obtained by taking into account the viewing geometry with the off-nadir angle (Fig. 6-1).

## 6.3 Surface Reference Systems

Because of the inhomogeneous mass density of the Earth, its shape does not form a regular body. The form of the Earth is denoted by the term geoid. For geolocation this geoid is approximated by a geometrical reference surface. Usually, a rotation ellipsoid is used as a reference surface. A worldwide accepted model is the World Geodetic System of 1984 (WGS84) ellipsoid.

A DEM is required to define the exact height of the Earth's surface with respect to the reference ellipsoid. The ACE (Altimeter Corrected Elevation) model will be used as DEM for ADM-Aeolus.

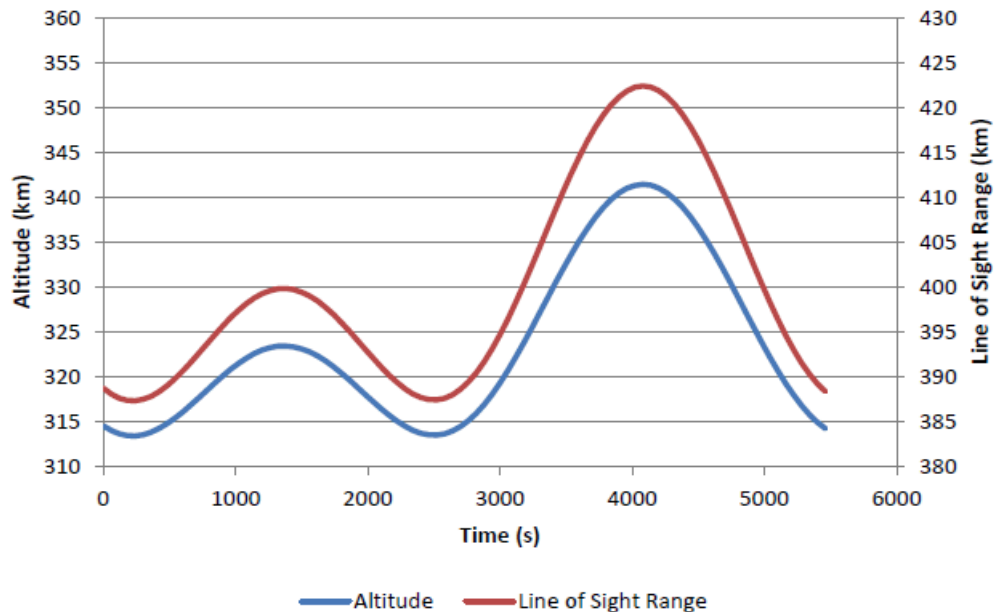


**Figure 6-5:** Altitude (blue) and line of sight range (red) over 1 Aeolus orbit above WGS84 ellipsoid (ADS 2016).

### 6.3.1 WGS84 reference ellipsoid

The WGS84 reference ellipsoid approximates the Earth surface by a rotation ellipsoid with main axis of 6378.137 km and 6356.752 km. Geodetic coordinates (latitude, longitude and altitude) are given with respect to this reference ellipsoid.

### 6.3.2 Geoid Correction

The WGS84 reference ellipsoid is not referenced to sea level – thus the altitude of the oceans is not 0 m (ASL) for the ellipsoid. The geoid is referenced to sea level and the difference between the geoid and the ellipsoid can be derived from a model, e.g. the earth gravitational model from 1996 called EGM96. The deviations of the EGM96 geoid from the WGS 84 reference ellipsoid range from about -105 m to +85 m. This model can be obtained from <http://earth-info.nga.mil/GandG/wgs84/gravitymod/egm96/egm96.html>

Note that the Aeolus L1B data product is referenced to the WGS84 ellipsoid and not to the geoid, so no geoid correction is applied to the Aeolus L1B altitudes, but the value for the geoid correction is contained in the L1B files. Instead the 2B data are referenced to the geoid.

### 6.3.3 Digital Elevation Model

The ACE2 (Altitude Corrected Elevation 2) is used as a global DEM for Aeolus (Berry et al. 2010, Smith and Berry 2010, Smith et al. 2010) formerly the ACE model was used (Johnson et al. 2004 and ESA 2004c). It covers the whole Earth surface with a horizontal grid spacing of 9 arcseconds ( $\approx 300$  m at the equator). The horizontal coordinate system is decimal degrees of latitude and longitude referenced to WGS84 for sea surface and EGM96 geoid for land surface. ACE2 provides an elevation accuracy of 16 m on most parts of the Earth. Figure 6-6 shows the ACE2 elevations for land and sea surfaces with 5 consecutive Aeolus orbits overlaid.

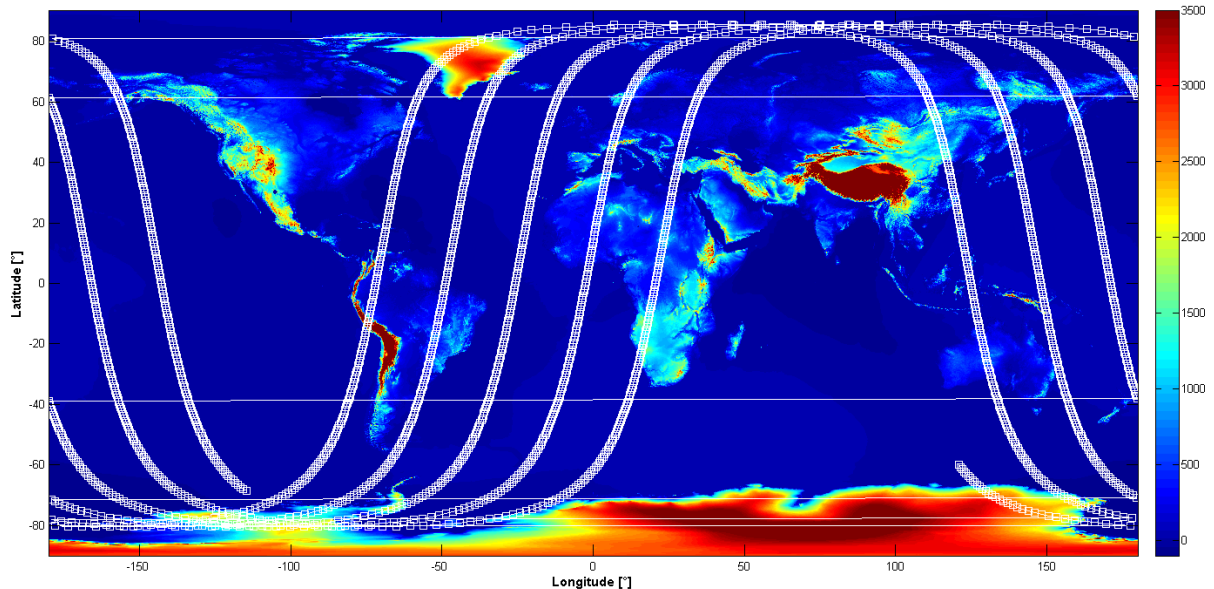


**Figure 6-6:** Altitude from the ACE 2 model with 5 consecutive Aeolus orbits overlaid (white dots, Rompel 2017); colours indicate altitudes wrt ellipsoid (sea) and geoid (land).

## 6.4 Geometrical Processing

### 6.4.1 Attitude and Orbit Control System Data

Attitude and Orbit Control System (AOCS) data represent the position, velocity and attitude of the satellite within the J2000 frame for every 125 ms. Position and velocity are represented by three-dimensional vectors, whereas the attitude is given as a quaternion, which represents the transformation from inertial space to satellite axis. The AOCS data is used to determine the geolocation of the measurement data with respect to the Earth. The processing of the AOCS data with related coordinate transformations, geolocation, satellite LOS velocity and direction computation, and time-basis transformation is performed in a software library (called CFI Customer Furnished Item Version 4.12). used for all Earth Observation Missions (Elecnor Deimos Space and ESA (2016a, b, c)).

### 6.4.2 Satellite Attitude

In nominal mode the instrument axis is rotated by  $-35$  degrees from nadir (i.e. from the z-axis in the LVHV frame) about the roll axis. The AOCS steers the yaw angle to compensate for the earth rotation and systematic orbital height variations such that nominally no relative velocity along the LOS occurs. For the calibration modes MRC and RRC, the instrument axis points to the nadir. Then, steering is applied around the pitch axis. The real relative velocity along the LOS is determined from the actual AOCS attitude data.

### 6.4.3 Earth Locations of Observations

The LOS target is defined as the intersection point between the instrument LOS (without taking into account refraction of the beam) and the WGS84 ellipsoid. These are given in latitudes/longitudes and height above the WGS84 ellipsoid for the atmospheric levels according to the range-bin settings for the centroid times (of a measurement or observation). The horizontal geolocation is slightly altitude dependent, because of the  $35^\circ$  off nadir angle for the LOS in nominal wind measurement mode. From this target the location vectors to the centres of the sensing volumes can be deduced, because the lower altitude of the range bin is provided in the L1b Product (except for the top-most bin, where the upper edge is reported). The incident angle is the angle between the local vertical at the measurement location and the LOS and is slightly altitude dependent due to the curvature of the earth ellipsoid.

The following table lists the requirement for geolocation knowledge for the ADM-Aeolus mission according to the System Requirements Document SRD (ESA 2010).

	Document Nr. <b>AE-RP-DLR-L1B-001</b>	Issue: <b>4.4</b>	Date: <b>20.04.2018</b>	Page: <b>43/117</b>	
	Doc. Title: <b>ADM-Aeolus ATBD Level1B Products</b>				

Parameter	System Requirement
measurement range	50 m (+3-sigma)
horizontal geolocation error	2000 m ( $\pm$ 2-sigma)
vertical geolocation error	200 m ( $\pm$ 2-sigma)

**Table 6-2:** Requirements for geolocation of ADM-Aeolus (ESA 2010)

## 6.5 Time

All instrument data packets in the raw data are provided in GPS time difference to a reference epoch from 6<sup>th</sup> January 1980. GPS times do not contain leap seconds needed for the correction of the Earth rotation, which are contained in the UTC (Universal Time Coordinated) time basis, e.g. GPS time is 18 seconds ahead of UTC for January 2017 (the last leap second was inserted on Dec 31, 2016). The timestamps in the Aeolus data product are provided in UTC time and thus the GPS times are converted to UTC by subtracting of leap seconds ( $UTC = GPS - \text{leap seconds} = GPS - 18 \text{ s}$  (for 2017)).

	Document Nr. <b>AE-RP-DLR-L1B-001</b>	Issue: <b>4.4</b>	Date: <b>20.04.2018</b>	Page: <b>44/117</b>	
	Doc. Title: <b>ADM-Aeolus ATBD Level1B Products</b>				

## 7 Algorithm Theoretical Baseline L0 and L1A Products

The chain of Aeolus processors is illustrated in Fig. 7.1 starting with AISP (Annotated Instrument Source Packets) data downlinked from the Aeolus spacecraft, which are processed to L0, L1A, L1B, L2A, and L2B by the respective processors and the calibration processor. Also the Aeolus End-to-End Simulator (E2S) is capable of producing AISP data in the correct format, which can be directly used in the L0 to L2 processing chain. Measurements from the ALADIN airborne demonstrator A2D can be introduced into the L1B processor for testing the retrieval algorithms for the satellite instrument.

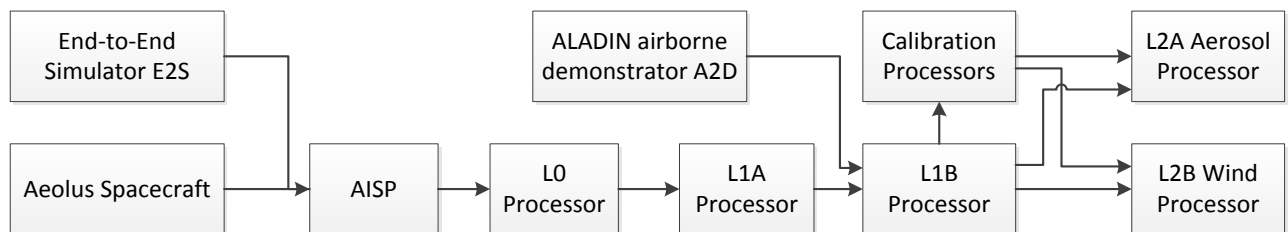


**Figure 7-1:** Chain of Aeolus L0, L1A, L1B, L2A, L2B and calibration processors with input from the Aeolus satellite, End-to-End Simulator and ALADIN airborne demonstrator.

### 7.1 Processing from raw data to L0

Input to the level 0 processing is a raw data file which contains the telemetry source packets AISP downlinked from the satellite during one pass over the receiving ground station. This file may contain source packets from different system and instrument modes. At the beginning or end of a data file a BRC may not be complete. Sometimes raw data files will be concatenated at the ground station. Then, the resulting raw data file may contain duplicates of packets.

So the first major task for a level 0 processor is to extract those BRCs within a given time frame, where at least the mandatory source packets AOCS, housekeeping, and Auxiliary data for Mie and Rayleigh are present, see also chap. 5.1. The second major task is the subsequent validation of each individual source packet. Validation results are added to the source packet header.

#### 7.1.1 Pseudo-Algorithm for Extracting and Sorting

The downlinked telemetry data comprising an individual observation are organized in a set of data structures ("packets") each associated to a particular structure identifier (SID). The extracting and sorting is performed as follows: **Loop** over AISP

- Read SOOBS (Start-of-Observation) time and SID number of packet.
- Move on to reading next SP until new SOOBS time is encountered.
- Check if packets with SID number 1 to 4 (AOCS, Housekeeping data, and Auxiliary data Mie & Rayleigh) have been read for the first SOOBS time.
- If source packets with SID 1 to 4 are present,
  - Find SID No.1 , validate, and extract orbital information needed for the Level 0 MPH and the instrument function mode
  - Validate all packets with that SOOBS time, remove duplicates, and pad missing Measurement data packets with zeros.
  - Write all source packets of the BRC with that SOBS time to the corresponding measurement data set of the Level 0 product.
- Move on reading source packets with the new SOOBS time.

	Document Nr. <b>AE-RP-DLR-L1B-001</b>	Issue: <b>4.4</b>	Date: <b>20.04.2018</b>	Page: <b>45/117</b>	
	Doc. Title: <b>ADM-Aeolus ATBD Level1B Products</b>				

### 7.1.2 Pseudo-Algorithm for Validation

The validation checks the source packet header information which consists of two parts, the Telemetry (TM) source packet header and the Front-End Processor (FEP) annotations. This validation is a sequence of error and consistency checks. If one step in the check is not completed successfully, the packet is not valid.

- Check that packet has no Virtual Channel Data Unit (VCDU) error
- Check Cyclic Redundancy Check (CRC) count
- Verify packet Identification (ID) fields
- Check consistency of sequence control fields
- Verify packet length
- Validate source packet data field header
- Check source data

In a final step the FH, MPH, and SPH of the product are generated using information gathered during the extraction and validation of packets and the MDSs are appended.

## 7.2 Processing from L0 to L1A

Input to the level 1A processing is the previously generated Level 0 data product. The main purpose of the Level 1A data processor is the processing of the AOCS and housekeeping data and the separation of measurement data into different products according to the system and instrument mode.

Thus the Level 1A processor loops over the measurement data sets of the Level 0 product, processes the packets into annotation data sets and measurement data sets and writes the sets into system and instrument mode dependent L1A product files.

For further information on the processing of AOCS packet SID no.1 to generate the geolocation ADS see chapter 6. SID no. 2 is processed for the Housekeeping data ADS, whereas SIDs no. 3 and 4 are processed for the Reference Pulse ADS, and SIDs no. 5 to 34 are processed for the Mie Channel and Rayleigh Channel MDSs. For the Data Quality ADS information from the processing of all the 34 packets is gathered.

### 7.2.1 Housekeeping Processing

Processing of housekeeping involves three different processing steps. In a first one, the quality indicators are derived. For every measurement the various quality flags of the corresponding reference pulses are copied to the data quality ADS. In case the number of locked pulses is above a certain threshold read from the processing parameters file, the *Measurement\_Laser\_Freq\_Locked* quality flag is set to true.

In a second step the housekeeping ADS is filled. Except for average and standard deviation values, housekeeping data are just copied from the Level 0 product. Average and standard deviation values are then calculated.

In a final third step, the total number of reference pulses per observation is calculated from the number of measurements per observation N and the number of laser pulses per measurement P as provided in the L0 product.

### 7.2.2 Reference Pulse Processing

The reference pulse processing checks the presence and validity of the reference pulse data. The overall quality flags *Mie\_Reference\_Pulses\_Present* and *Mie\_Reference\_Pulses\_Sp\_Valid* are filled with the values *Sp\_Missing* and *Sp\_Invalid* as already retrieved during the L0 processing step. The *Mie\_Measurement\_Sp\_Valid* flag is set to true for a specific measurement, in case the values *Sp\_Missing* and *Sp\_Invalid* as already retrieved during the L0 processing step for this packet are set to true.

The number of reference pulses is set while processing the housekeeping information. The reference pulse data itself is just copied from the Level 0 input product to the Level 1A output product.

	Document Nr.	Issue:	Date:	Page:	
	<b>AE-RP-DLR-L1B-001</b>	<b>4.4</b>	<b>20.04.2018</b>	<b>46/117</b>	
Doc. Title:					
<b>ADM-Aeolus ATBD Level1B Products</b>					

### 7.2.3 MSP and RSP Data Processing

The measurement data processing is done in two steps. First the number of measurements, height bins, and ACCD columns are set. Then Level 0 measurement data input packets are subdivided into Mie and Rayleigh packets on the basis of their SID number, and written to the Level 1A output product.

### 7.2.4 Data Quality Processing

Data quality indicators are set while processing the housekeeping information, and the reference data.

## 8 Algorithm Theoretical Baseline L1B Products

The following subchapters describe the algorithm theoretical baseline for deriving the L1B product. The implementation of the algorithms in the processors is described in ADS (2017) and DoRIT and MDA (2017c). A general outline of the wind retrieval processing is shown in Fig. 8-1, which is detailed in the following subchapters. The general process of determination of the wind velocity, which applies to both Rayleigh and Mie data, is described in chapter 8.1. Chapter 8.2 and 8.3 describe the processing from the data from the Mie and Rayleigh spectrometer to a wind observation in wind mode. The processing of the data obtained during the calibration modes MRC and RRC is contained in chapter 9.1 and 9.2. The ground return processing is discussed in chapter 10.1 and the derivation of the signal amplitudes from Mie and Rayleigh spectrometers is included in chapter 10.2 and 10.3. The quality control, identification of corrupted data and derivation of error quantifiers is included in chapter 10.4.

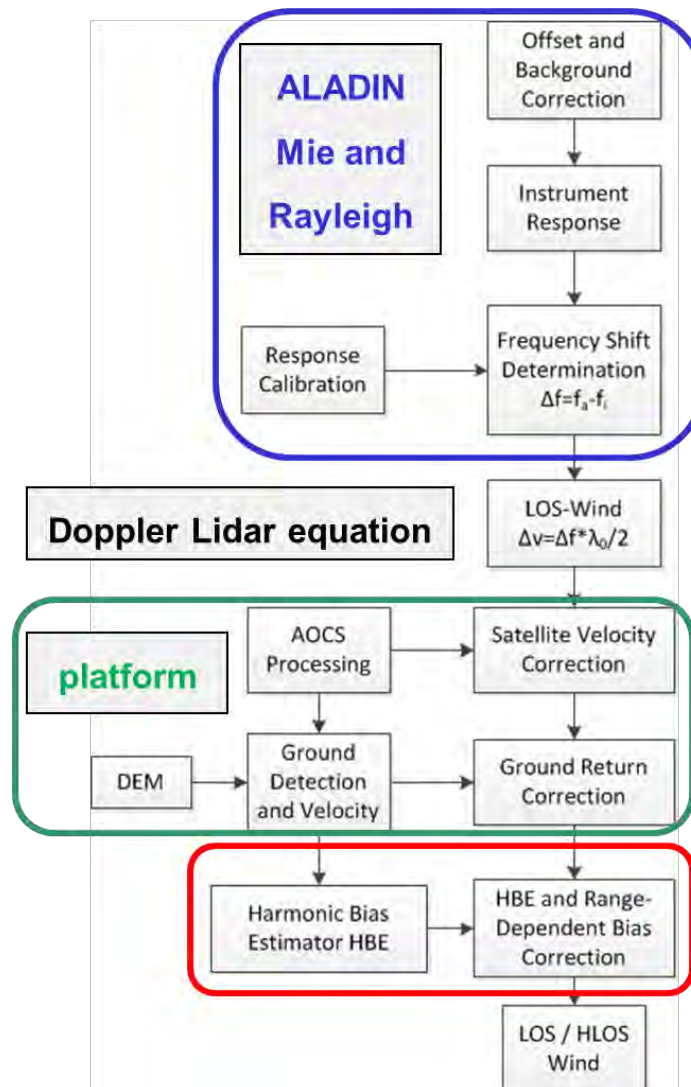


**Figure 8-1:** Principle of L1B wind retrieval algorithms using ALADIN instrument data (blue box) from Mie and Rayleigh spectrometers including response calibration to derive the Doppler frequency shift. This is afterwards corrected with spacecraft platform data from the AOCS and use of a DEM for ground detection to derive satellite LOS velocity and ground return correction velocities (green box). As a last step several bias contributors (harmonic bias (HB) and range-dependent bias (RDB)) are corrected to derive LOS winds (red box), which are projected to the horizontal to HLOS (from Reitebuch et al. 2017).

	Document Nr. <b>AE-RP-DLR-L1B-001</b>	Issue: <b>4.4</b>	Date: <b>20.04.2018</b>	Page: <b>48/117</b>	
	Doc. Title: <b>ADM-Aeolus ATBD Level1B Products</b>				

## 8.1 Wind Velocity Determination

The wind velocity is derived from the data obtained during nominal Wind Velocity Measurement WVM mode. It is possible to derive a wind velocity for each of the 24 altitude range gates from the MSP and RSP, and for each measurement and for an observation.

**Measurement:** The atmospheric signals from each spectrometer for a number of P-1 emitted laser pulses are accumulated on-chip the ACCD to one measurement. A measurement is typically averaged over 20 to 50 laser pulses, which is equivalent to a horizontal length of 3 km to 7 km.

**Observation:** A number of N measurements are averaged on-ground to obtain one observation, which is the nominal L1B data product. An observation is typically averaged horizontally over 90 km.

The L1B wind product is derived for each measurement within one observation and for each observation applying the same algorithms.

In addition to the 24 altitude range gates containing signal from atmospheric targets, a measurement of the atmospheric **background** radiation is performed after the acquisition of the atmospheric range gates for every emitted pulse on the MSP and RSP. The background radiation measurement is accumulated on-chip the ACCD with the same number of P-1 pulses as for atmospheric measurements, but with a longer duration  $t_b$ . This background radiation can be assumed as a constant offset over frequency for the MSP and RSP measurements (see chapter 3.5).

In principle the following contributors to the frequency of the atmospheric range gate have to be considered when deriving the mean LOS velocity within the atmospheric range gate

- frequency of the emitted laser pulse (blue box in Fig. 8-1)
- frequency shift due to the projection of the satellite velocity on the LOS (green box in Fig. 8-1)
- frequency shift due to “known” bias contributors as harmonic bias (HB) and range-dependent bias (RDB) (red box in Fig. 8-1).

A small portion of the emitted laser pulse is directed to both spectrometers MSP and RSP and the signal on the ACCD is not accumulated for these **laser internal reference measurements**, but read out for every single pulse. Thus, for every single shot a laser internal reference signal can be analysed in frequency and used to correct for non-constant internal reference frequencies from measurement to measurement. Instead the laser internal reference ACCD signals are accumulated on-ground to form one measurement and one observation.

The derivation of the **satellite velocity** on the LOS is done with data from the AOCS system including several sensors (star tracker, Global Positioning System GPS, Inertial Measurement Unit IMU) and is described in chapter 6. The satellite contribution to the LOS velocity is computed for every measurement, from the AOCS data, which is available with a rate of 8 Hz (125 ms). The AOCS data will be interpolated to the centroid time of a measurement and observation.

The determination of the frequency of an atmospheric range gate with a zero mean LOS velocity, e.g. from the non-moving earth surface (**ground return**), can be used to correct residual errors. As the frequency of the emitted laser pulse is monitored for every single pulse, the errors can be attributed to the frequency shift of the receiver spectrometers or the satellite velocity on the LOS.

The ground return speeds are also used to estimate the contribution from harmonic biases, which vary from observation to observation along the orbit (but not for the profile of range gates within 1 observation). The reason for harmonic biases could be uncertainties in the knowledge of the attitude angles from the AOCS sensors, or thermo-elastic deformations of the lidar LOS pointing (wrt. AOCS sensor) or thermos-elastic deformations within the instrument due to varying solar illumination along the orbit (ESA 2018b, ch. 6.1).

Another contributor to the bias is varying for different range-gates within 1 observation as a function of range from the satellite to the atmospheric or ground range gate. The dependency of this bias from the range is characterized using ground-return speeds. This is caused by the rotation of the satellite during the round-trip time from the laser pulse to the backscattered light, which results in a varying incidence angle on the receiver spectrometers (RSP and MSP). As this is a known and deterministic process and can be characterized and corrected. As also the range from the satellite to the atmosphere is harmonically varying along the orbit (Fig. 6-5), the RDB shows also some harmonic variation along the orbit. As the causes and the

	Document Nr. <b>AE-RP-DLR-L1B-001</b>	Issue: <b>4.4</b>	Date: <b>20.04.2018</b>	Page: <b>49/117</b>	
	Doc. Title: <b>ADM-Aeolus ATBD Level1B Products</b>				

characteristics of the RDB and HB are different, both contributors need to be separated for the characterisation and correction procedure (DLR 2017c).

From the determined frequency of the atmospheric range gate the mean LOS velocity of this range gate is determined by the Doppler equation (see chapter 3.4). The altitude dependent incidence angle is used to convert from LOS velocity to the horizontal projection, which results in the HLOS velocity. Vertical profiles of the HLOS velocity for every observation are included in the L1B wind measurement product. The algorithm to determine the wind velocity is justified and described in the next subchapters for both the output from the MSP and RSP. Algorithm baselines, which are specific to the MSP and RSP are justified and described in detail in chapter 8.2 and 8.3.

### 8.1.1 Quality Control and Averaging of Measurements to Observations

The raw output of the ACCD from the MSP and the RSP is signal intensity per ACCD pixel (20 pixels total with 4 offset pixels and 16 useful pixels) per atmospheric range gate (25 total including 1 background gate) per measurement, which is a result of an on-board accumulation of returns of P-1 laser pulses. To achieve the mission requirements for random, slope and unknown zero-wind bias errors, the measurements have to be averaged to one observation. There are in principle two possible approaches to determine a wind velocity per observation:

- Determination of a wind velocity per measurement and averaging of the wind velocities to one observation.
- Averaging of the signal levels from single pixels of the ACCD per measurement and determination of the wind velocity from the averaged pixels of the ACCD for one observation.

The second approach is preferred, because of the non-linear process of the determination of the wind velocity from the ACCD pixels, which is justified in chapter 8.2 for the MSP and 8.3 for the RSP. When averaging ACCD pixel signals it has to be assured that no measurements contribute to the observation, which result in gross errors (outliers), or increase the random and systematic errors significantly. Discarding measurements is a trade-off between improving the random error budget by the averaging process and the introduction of additional errors.

Thus a quality control is applied to each single measurement or single laser pulses to discard measurements or laser pulses corrupted by gross errors

- Laser pulse validity status for every single laser pulse: This status word is a combination of several flags, containing the cavity lock status, RLH on/off, RLH cavity temperature in range, RLH tuned, RLH locked and seeder locked. The cavity lock status flag describes, if the master oscillator cavity of the pulsed laser head is locked to the reference laser frequency. If the laser is not locked, than the laser is not operating in seeded mode and the emitted laser frequency is out of range of the expected frequency range and the linewidth of the pulse is much higher than specified (some GHz instead of 50 MHz). This would result in a gross error. The other flags refer to the correct operation of the RLH. If the number of discarded laser pulses exceeds a certain threshold, then the whole measurement is considered as invalid. The laser pulse validity flag is especially important for the processing of the response calibration data in IRC mode or other instrument modes, where the laser frequency is changed as for ISR and IAT mode. During the frequency change from one value to another, e.g. by 25 MHz or 250 MHz the laser pulse validity flag should be false indicating that these laser pulses or atmospheric measurements should not be used for further processing.
- AOCS status flag: This flag provides the information, if the spacecraft points in the nominal direction. If the spacecraft is pointing not in the nominal direction, e.g. due to orbital control manoeuvres the measurement has to be discarded. The AOCS status flag is available for each measurement, derived from the AOCS raw data with a repetition rate of 8 Hz (125 ms).
- Corrupted data flag: This flag describes, if the measurement data itself is showing strong deviations from the “expected” spectral behaviour (see chapter 8.10). A corruption could occur due to signal spikes on the ACCD caused by particles or radiation striking the ACCD.

In principle the quality control of single measurements can be extended to other instrument parameters (not currently implemented in L1B), which influence the zero-wind bias, slope or random errors, e.g.

- other laser housekeeping parameters, e.g. temperatures, energy

	Document Nr. <b>AE-RP-DLR-L1B-001</b>	Issue: <b>4.4</b>	Date: <b>20.04.2018</b>	Page: <b>50/117</b>	
	Doc. Title: <b>ADM-Aeolus ATBD Level1B Products</b>				

- receiver housekeeping parameters, e.g. MSP temperature
- AOCs housekeeping parameters
- derived emitted laser frequency from the laser internal reference
- quality-checks when averaging MSP output
- quality-checks when averaging RSP output, e.g. on the signal strength of the MSP to avoid contamination of the RSP signal (see chapter 8.3)

Only ACCD measurements are averaged, which have not been discarded by the quality control. For the internal laser reference, which is obtained for every single pulse, all ACCD output of the corresponding atmospheric measurement has to be discarded, when the number of flagged reference pulses exceeds a predefined threshold.

### 8.1.2 Correction of Detection Chain Offset

The wind velocity determination from the MSP and RSP are both sensitive to constant offsets. A constant offset on the signals of the ACCD would introduce a bias error for the Rayleigh signals. Therefore, this constant offset has to be determined and subtracted.

One source of constant offset for both MSP and RSP is the detection chain offset (DCO). This can be determined by the signal from pixels of the ACCD, which are not illuminated. A total of 20 pixels is read-out per ACCD line (range gate) with 16 useful, illuminated pixels and 4 non-illuminated offset pixels ("virtual pixels, see ch. 4.2.5.). The mean of two pixel intensities is determined for Mie (pixel no. 19 and 20), while only the signal level of pixel 20 is used for Rayleigh and subtracted from each of the 16 illuminated ACCD pixels. On the Rayleigh ACCD pixel no. 19 is not representative of the offset, due to spurious charges, and thus, averaging over 2 pixels cannot be performed. The averaging process for the determination of the detection chain offset (mean of the offset pixels over 1 ACCD line or over all ACCD lines, mean over one measurement or one observation) needs to be investigated, once real measurements are available. As a current baseline the mean is determined for every measurement and for every single line (range gate) and used for correction of the output of the ACCD from the RSP and MSP.

The other sources of constant offset differ for the RSP and MSP and their origin and determination will be discussed in chapter 8.2 and 8.3.

### 8.1.3 Determination of Mean Frequency of Atmospheric signal and Internal Reference

The determination of the mean frequency of the atmospheric signal from the averaged and corrected ACCD output differs for the MSP and RSP due to the different spectrometer principle (see chapter 4.2). In contrast to the frequency determination from a coherent Doppler lidar, which does not require a frequency calibration, this is required for the direct detection Doppler lidar. The frequency calibration gives the relationship between a derived response from the MSP and RSP and a reference frequency. The response from the MSP is the centroid from the ACCD pixel output in units of pixel index, which has to be converted to a frequency in units of MHz. The response from the RSP is a normalised differential measure of the intensity from the filter A and B, which has to be converted to a frequency in units of MHz.

The calibration constants will be determined during the Instrument Response Calibration IRC consisting of the Mie Response Calibration MRC and Rayleigh Response Calibration RRC, which is an end-to-end calibration using atmospheric returns (chapter 4.3.3). It is foreseen to perform these calibrations once per week. The algorithms deriving the calibration constants from MRC and RRC are described in chapter 8.4 and 8.5. These constants are used for determination of the mean frequency of the atmospheric signal and updated after each valid MRC and RRC.

The cause for the calibration and the principle approach for obtaining the functional relationship between the instrument response  $R$  and the Doppler shift frequency  $\Delta f$  are discussed in Fig. 8-2 for both the L1B and the L2B wind retrievals. It should be noted here, that the term "calibration" in the context of ALADIN is used for the determination of the functional relationship between Mie or Rayleigh response  $R$  and Doppler frequency shift  $\Delta f$ . A radiometric calibration as used for passive remote sensing instruments to convert the measured, raw signal levels at the detector to actual physical quantities, e.g. spectral radiance  $L_\lambda$  [ $\text{Wm}^{-2}\mu\text{m}^{-1}\text{sr}^{-1}$ ] is not

needed for wind retrieval and not pursued with the response calibration IRC. A response calibration  $R(\Delta f)$  is needed for any type of direct-detection DWL, whereas this is not the case for coherent detection DWL (Reitebuch 2012a). Here the measured signals at the detector are converted to frequencies by use of a Fourier transformation due to the optical, heterodyne detection principle.

In principle there are 2 different approaches to determine the relationship between measured responses  $R(\Delta f)$  and Doppler frequency shift as shown in Fig. 8-2. The relationship  $R(\Delta f)$  could be measured as performed during IRC mode or could be computed from the filter transmission  $T(f)$  as obtained during ISR mode. Both approaches are used and combined for Aeolus. The L1B processor uses the function  $R(\Delta f)$  as measured during IRC mode for both Mie and Rayleigh wind retrieval. Whereas the L2B processor uses the computational approach with ISR mode data for Rayleigh winds in combination with an adaptation of the filter transmission functions  $T(f)$  for the atmospheric optical path using the IRC mode (ECMWF 2017b). In addition a Rayleigh-Brillouin lineshape model for the molecular spectrum (Witschas 2001a, b) is used with atmospheric temperature and pressure profiles from a NWP model (e.g. from ECMWF). The L2B Mie winds are also retrieved using the corresponding Mie parameters from the IRC mode (ECMWF 2017b). The algorithms to derive the response calibration parameters are discussed in detail in Ch. 9.

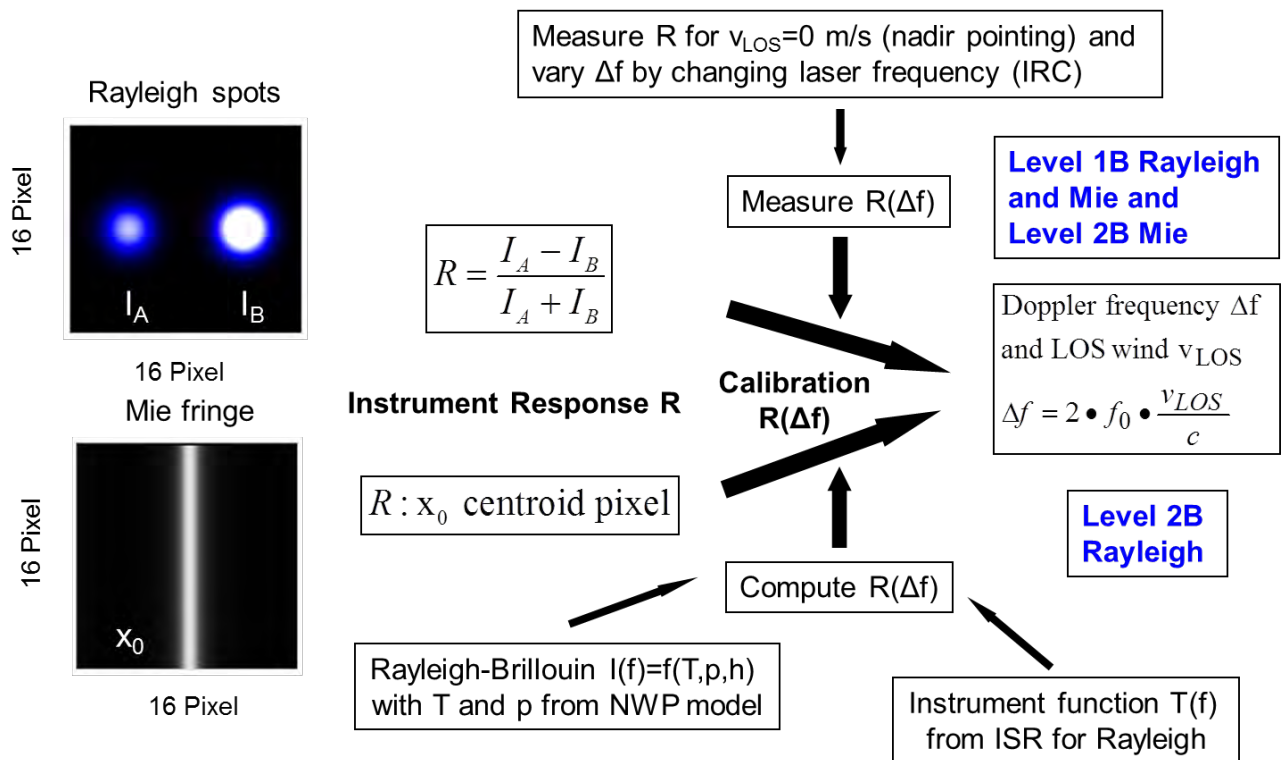


**Figure 8-2:** Illustration of the response calibration from raw signals (left) on the Rayleigh (top) and Mie (bottom) in the image zone of the ACCD; after summing up of the signals of the 16 vertical lines in the memory zone these are used to derive the Rayleigh and Mie instrument responses  $R$ . The response  $R(\Delta f)$ , which is depending on the Doppler shift frequency  $\Delta f$  and is a non-calibrated parameter without physical units needs to be converted to frequency shifts  $\Delta f$  in units of MHz. This is then converted to LOS speeds  $v_{LOS}$  by use of the Doppler shift equation (right, middle). The functional relationship between  $R$  and  $\Delta f$  can be either measured (top) or computed (bottom). The relationship  $R(\Delta f)$  is measured during IRC mode in nadir-pointing by varying the laser frequency  $\Delta f$  and determination of measured responses  $R$  for the Mie (MRC) and Rayleigh (RRC) channel under the assumption that the LOS speed is 0 m/s. This approach is pursued for the L1B processing of Rayleigh and Mie winds and for L2B Mie winds. For L2B Rayleigh winds the response function  $R(\Delta f)$  is computed using the instrument transmission function  $T(f)$  of both RSP filters from the ISR mode and the spectral Rayleigh-Brillouin lineshape from molecular backscattering  $I(f)$ ; for  $I(f)$  the actual atmospheric pressure  $p$  and temperature profile as a function of altitude is needed, which is obtained from a NWP model.

	Document Nr. <b>AE-RP-DLR-L1B-001</b>	Issue: <b>4.4</b>	Date: <b>20.04.2018</b>	Page: <b>52/117</b>	
	Doc. Title: <b>ADM-Aeolus ATBD Level1B Products</b>				

Also the averaged and corrected ACCD outputs from the measurement of the internal laser reference will be used to determine a response and to convert this to a mean frequency by means of calibration constants. It has to be noted that the calibration constants for an atmospheric signal differs from the calibration constant for the internal laser reference due to the different spectral shape and width of both signals. In addition, the calibration constants differ due to the different divergence and incidence angles on the spectrometers and the difference in illumination of the ACCD for the atmospheric path and the internal reference path (see Fig. 4-1). The difference in illumination is more pronounced for the Mie ACCD, because the Mie channel is using an imaging spectrometer. The Mie atmospheric path is fully illuminating the Mie ACCD, while the internal path is only partly illuminating the Mie ACCD, which is characterized in the LBM mode (ch. 4.7.3)

### 8.1.4 Determination of the Frequency Shift from the Atmospheric Wind Velocity

The determined mean frequency of the atmospheric signal and internal reference is a measurement of a frequency difference (in MHz) and not an absolute frequency measurement (in THz). The frequency difference is measured relative to a zero frequency  $f_0$ , where the laser transmitter is set during the spectrometer co-registration, which is derived from the Instrument Spectral Registration (ISR) mode (e.g.  $f_0=844.962$  THz for a laser wavelength of 354.8 nm). The mean frequency of the internal reference is thus the difference between the frequency of the emitted laser pulse and  $f_0$ .

The mean frequency of the atmospheric signal determined from the spectrometers output of RSP and MSP contains several components:

- the frequency of the emitted laser pulse, which is determined by the internal reference measurement
- the Doppler frequency shift due to the atmospheric wind velocity in direction of LOS, which is the projection of the three-dimensional wind vector on the LOS
- the Doppler frequency shift due to the moving satellite, which is determined from AOCs data
- the frequency drift of the spectrometers RSP and MSP with respect to the latest determination of the zero frequency response, which is performed during the calibration modes MRC and RRC

Thus the Doppler shift due to the atmospheric wind velocity in LOS can be determined by subtracting the frequency of the emitted laser pulse and the Doppler shift due to the moving platform from the determined mean frequency of the atmospheric signal. As the frequency of the emitted laser pulse can vary from pulse to pulse, and the Doppler shift of the satellite platform can vary from pulse to pulse, the determination of the atmospheric Doppler shift should be performed for every single pulse. Due to the on-board accumulation of atmospheric signals this cannot be performed and some assumptions have to be made, which are discussed for every component.

#### Influence of variation of laser frequency, satellite ground speed and receiver drift

The frequency of the emitted laser pulse can be determined for every single pulse, but the frequency of the atmospheric signal is determined from an accumulated signal over one measurement (accumulation of P-1 pulses). A variation of the emitted laser pulse frequency can be described in principle by a drift, a random component, and gross outliers, e.g. if the laser is not locked. An accumulation of atmospheric signals over one measurement from emitted laser pulses with varying frequency results in broadening of the frequency spectrum. If the variation of the laser frequency is small (specification is 7 MHz rms over 7 s) compared to the spectral width of the signal on the MSP and RSP, than the averaging process results in a negligible additional broadening. The spectral width of the signal on the MSP is the convolution of the spectral width of the aerosol backscatter signal (50 MHz FWHM laser linewidth) and the spectral transfer function of the Fizeau (159 MHz FWHM). In contrast, the spectral width of the signal on the RSP is much broader because it is determined by the spectral width of the molecular return (FWHM = 1.6 pm = 3.8 GHz, see chapter 3.4). Thus, the influence of laser emitter frequency variations is different for the RSP and the MSP. The quality-control routine on measurements (see chapter 8.1.1) should therefore discard measurements, where single laser pulses have gross outliers in frequency.

This argument is only valid, if the weighting of the frequency of a single pulse is equal for the laser internal reference and the atmosphere. The weighting for the internal reference is determined by the laser pulse energy, where the variations from pulse-to-pulse should be in the percentage range. In contrast, the weighting for the atmospheric signal is determined by the atmospheric backscatter. The atmospheric backscatter could vary from pulse to pulse with a horizontal separation of 140 m significantly in case of clouds (e.g. 1 pulse hitting a cloud and the next pulse without a cloud) or varying ground-returns. The

	Document Nr. <b>AE-RP-DLR-L1B-001</b>	Issue: <b>4.4</b>	Date: <b>20.04.2018</b>	Page: <b>53/117</b>	
	Doc. Title: <b>ADM-Aeolus ATBD Level1B Products</b>				

influence of laser frequency jitter from pulse-to-pulse in combination with heterogeneity in the atmospheric backscatter was studied in DLR (2015). Here it was concluded that the laser frequency jitter becomes detrimental for laser frequency variations above 16 MHz rms in case of opaque, broken cloud coverage within one measurement.

The same arguments on spectral broadening are applicable for the Doppler shift component of the satellite. The pointing accuracy of the AOCS can show variations due to a drift, random errors or gross outliers. Also infrequent orbital control manoeuvres occur, where the instrument is not pointing in the correct LOS direction. Thus, measurements must be discarded, where the AOCS system reports a non-nominal pointing.

The frequency drifts of the spectrometers RSP and MSP with respect to the latest determination of the zero frequency response during RRC and MRC cannot be detected directly with the ALADIN instrument. This requires locking the spectrometers or the emitted laser frequency to an absolute frequency standard, e.g. an atomic or molecular absorption line. Thus, a frequency drift can only be detected indirectly through monitoring of instrumental parameters, which influence the spectral response, e.g. temperatures. A correction could be applied, if an accurate knowledge of the relation of the spectral response on instrumental parameters is known (not implemented in L1bP). Nevertheless it is foreseen to perform an instrument response calibration on a weekly basis. Thus only drifts between the periods of 2 calibrations would be relevant.

Another approach is taken to handle the frequency drift of the two spectrometers:

- parallel processing of the internal reference on both spectrometers, in contrast of using the frequency of the internal reference of the MSP also for wind velocity determination with the RSP. Thus a frequency drift of the RSP with respect to the MSP does not influence the determined mean frequency of both RSP and MSP. The parallel processing of MSP and RSP internal reference measurements is used as the current baseline for L1B processing.
- usage of mean velocity of the return from a non-moving target (e.g. earth surface) for correction of a residual error. This will cancel out drifts of the spectrometers as well as unknown drifts of the AOCS system (see chapter 8.6). The velocity of the ground return is used in case a ground return is detected for an observation, which leads to discontinuous corrections. If a known drift of the residual error can be assumed then the correction terms in case of a detected ground return can also be interpolated between observations with no ground return. It is assumed that the AOCS errors are composed of harmonic components over one orbit with sinusoidal variations. Thus, the ground return frequencies over several orbits are used for determination the residual satellite ground velocity (chapter 8.6).

### **Influence of averaging measurements to observations**

The subtraction of the frequency of the emitted laser pulse and the frequency due to the moving platform is performed for single measurements to obtain an atmospheric velocity for every single measurement, but also on observation level. First an averaged signal of the ACCD is determined for the atmospheric signal and the laser internal reference, then the mean frequency of both is determined (see chapter 8.1.3). The mean Doppler shift frequency for the atmospheric wind velocity is determined from the subtraction of the mean frequency of the laser internal reference and the residual contribution of the satellite moving platform from the atmospheric signal.

This approach introduces an additional spectral broadening of the spectrometer signal and thus an additional random error compared to the case of averaging several laser pulses to one measurement (0.4-1 s). For an observation variations within 12 s or a horizontal averaging length in the atmosphere of 90 km are relevant. It is assumed that the additional random error is negligible, because the laser frequency variation and the frequency variation from the AOCS is small compared to the spectral width of the signal on the MSP (FWHM = 159 MHz = 28 ms<sup>-1</sup> LOS) and thus for the RSP (FWHM = 3.8 GHz = 674 ms<sup>-1</sup> LOS).

### **8.1.5 Determination of LOS and HLOS Velocity**

The LOS velocity is determined from the frequency shift by use of the Doppler equation (see chapter 3) using a constant laser emitter wavelength  $\lambda_0$  of 354.8 nm, whose exact value is determined on ground and contained in the satellite characterisation file.

The actual emitted laser wavelength might differ from the on-ground determined laser wavelength, because the laser emitter frequency is tuned in orbit in over a range of  $\pm 5.5$  GHz equivalent to  $\pm 2.3$  pm. As the LOS

	Document Nr. <b>AE-RP-DLR-L1B-001</b>	Issue: <b>4.4</b>	Date: <b>20.04.2018</b>	Page: <b>54/117</b>	
	Doc. Title: <b>ADM-Aeolus ATBD Level1B Products</b>				

velocity is proportional to the emitted laser wavelength, this would only introduce an error of  $2.3 \text{ pm}/355 \text{ nm} = 6.5 \cdot 10^{-6}$ , which is negligible.

The HLOS velocity is the projection of the LOS velocity to the horizontal plane, by dividing the LOS velocity with the sinus of the incidence angle  $\varphi_i$ . Due to the slant geometry of the beam propagation and the earth geoid curvature the incidence angle is depending on the altitude. Thus, an incidence angle depending on the atmospheric range gate has to be used. A fraction of 0.61 from the horizontal wind speed in LOS direction is projected onto the LOS for a mean incidence angle of  $37.6^\circ$  (resulting from a slant angle at the satellite of  $35^\circ$ , the mean satellite altitude of 320 km, and the Earth curvature). Thus a random error requirement of 1 m/s on the HLOS component is transferring to an even stricter requirement of 0.61 m/s on the measured LOS component.

As already stated in chapter 8.1.3 the measured LOS velocity is the projection of the three-dimensional wind vector onto the LOS. The three-dimensional wind vector can be described by its 2 horizontal components  $u$ ,  $v$ , and the vertical component  $w$ . When converting from LOS to HLOS it has to be assumed that the vertical component  $w$  is negligible; a fraction of  $\cos(37.6^\circ)=0.79$  from the vertical wind is projected onto the LOS direction. This can be assumed for the horizontal averaging length of 90 km for an observation for most conditions.

The vertical component is not negligible under the following conditions:

- horizontal averaging lengths of a measurement, which is between 3 km to 7 km
- strong up- und downdrafts, e.g. in convective situations in the planetary boundary layer (PBL) or above high convective clouds, e.g. cumulonimbus
- during occurrence of atmospheric waves, e.g. gravity waves (Witschas et al. 2017)
- during occurrence of atmospheric turbulence in the PBL or in the higher troposphere, referred as clear-air turbulence (CAT)

	Document Nr. <b>AE-RP-DLR-L1B-001</b>	Issue: <b>4.4</b>	Date: <b>20.04.2018</b>	Page: <b>55/117</b>	
	Doc. Title: <b>ADM-Aeolus ATBD Level1B Products</b>				

## 8.2 Wind Measurement Processing Rayleigh

### 8.2.1 General description of double-edge wind retrieval method

The principles of the wind retrieval from the Rayleigh Spectrometer RSP is discussed shortly in chapter 4.2.4. It is based on the widely used double-edge technique, which was pioneered by Chanin et al. (1989) and Garnier and Chanin (1992) for stratospheric winds using the broadband molecular return with a laser wavelength of 532 nm, and by Korb and Gentry (Korb et al. 1992, 1998; Gentry et al. 2000) for tropospheric winds using laser wavelengths of 1064 nm and 532 nm for the narrowband aerosol return and 355 nm for the molecular return. The double-edge technique relies on the measurement of signal intensities, which are obtained after transmission through two narrowband filters. If the narrowband filters are placed at about the steepest slope of the atmospheric spectral lineshape (“turning point” or “edge”) then a Doppler frequency shift results in a maximum change in filter transmission. Each narrowband filter is usually realized by a Fabry-Perot interferometer, but also molecular absorption lines are used as filters for a single-edge technique (Liu et al. 2007, Baumgarten 2010, Hildebrand et al. 2012).

#### Doppler shift equation

First the basic equations for the wind retrieval of a Doppler frequency measurement, then the specific approach using the double-edge technique are described, before the step-by-step algorithms from the digitized raw signals of the ACCD to the LOS wind speed are discussed. The Doppler frequency shift  $\Delta f$  is defined as the difference between the frequency of the received atmospheric return  $f_a$  and the emitted laser frequency  $f_l$ . It is derived from the Doppler frequency shift equation (Eq. (3.11)) using the frequency  $f_0$  or wavelength  $\lambda_0$  of the laser.

$$\Delta f = f_a - f_l = 2 \cdot f_0 \cdot \frac{v_{LOS}}{c} = 2 \cdot \frac{v_{LOS}}{\lambda_0} \quad (8.1)$$

$$\Delta f = \Delta f_{LOS,wind} + \Delta f_{LOS,S}$$

The measured Doppler frequency shift of the atmospheric range gate  $\Delta f$  is composed of a contribution of the atmospheric LOS wind  $\Delta f_{LOS,wind}$  and the component of the satellite movement  $\Delta f_{LOS,S}$ , which is projected onto the LOS (chapter 8.1.4). The sign convention for the Doppler shift frequency  $\Delta f$  is such, that a positive sign ( $\Delta f > 0$ ,  $f_a > f_l$ ) is related to a LOS wind speed in the direction towards the instrument (“blue wavelength shift”), while a negative sign ( $\Delta f < 0$ ,  $f_a < f_l$ ) indicates a movement in LOS direction away from the instrument (“red wavelength shift”). Thus,  $v_{LOS}$  is positive for movements towards the lidar, while  $v_{LOS}$  is negative for movements away from the lidar in this context (N. B. Here the usual definition of the Doppler shift  $\Delta f = f_{received} - f_{emitted} = 2f_0 \cdot v_{LOS}/c$  is used, but this equation is used differently (but consistent) in the Master Algorithm Document MAD (ADS 2017) and the L1b processor (DoRIT and MDA 2017c) with  $\Delta f_{MAD} = f_{emitted} - f_{received} = 2f_0 \cdot v_{LOS,MAD}/c$ . This means that  $\Delta f_{MAD} = -\Delta f$  and consistently the sign of the LOS velocity is inverted between the text here and the MAD definition:  $v_{LOS} = -v_{LOS,MAD}$ . This implies also that the definition of the satellite-induced speed on the LOS direction is inverted from the definition here and the definition provided in the MAD:  $v_{LOS,S} = -v_{LOS,S,MAD}$ . Both definitions will lead to correct results in case that the sign definition for the satellite induced speed  $v_{LOS,S,MAD}$  is used correctly).

Thus, the atmospheric LOS frequency shift  $\Delta f_{LOS,wind} = \Delta f_{LOS,i}$  (in MHz) and the related LOS wind speed (in  $\text{ms}^{-1}$ ) can be obtained for each atmospheric range gate (subscript i):

	Document Nr. <b>AE-RP-DLR-L1B-001</b>	Issue: <b>4.4</b>	Date: <b>20.04.2018</b>	Page: <b>56/117</b>	
	Doc. Title: <b>ADM-Aeolus ATBD Level1B Products</b>				

$$\begin{aligned}
\Delta f_{LOS,i} &= f_{a,i} - f_I - \Delta f_{LOS,S,i} \\
v_{LOS,i} &= \frac{c}{2f_0} \cdot \Delta f_{LOS,i} = \frac{\lambda_0}{2} \cdot \Delta f_{LOS,i} \\
&= \frac{\lambda_0}{2} \cdot (f_{a,i} - f_I - \Delta f_{LOS,S,i}) \\
&= \frac{\lambda_0}{2} \cdot (f_{a,i} - f_I) - v_{LOS,S,i}
\end{aligned} \tag{8.2}$$

The LOS wind speed is projected onto the horizontal plane by using the local incidence angle  $\varphi_i$  to obtain the HLOS component. This incidence angle is slightly different for each range gate, because it is referenced to the local nadir axis and thus depending on the Earth curvature. Then the HLOS wind speed component can be written as:

$$v_{HLOS,i} = \frac{1}{\sin(\varphi_i)} v_{LOS,i} = \frac{1}{\sin(\varphi_i)} \left[ \frac{\lambda_0}{2} \cdot (f_{a,i} - f_I) - v_{LOS,S,i} \right] \tag{8.3}$$

The incidence angle  $\varphi_i$ , the frequency of the atmospheric range gate  $f_{a,i}$ , and the contribution of the satellite movement to the LOS-direction  $v_{LOS,S,i}$  are all derived for each range gate  $i$ . The incidence angle  $\varphi_i$  and the satellite LOS speed are obtained from the AOCS sensors (see chapter 6). The average values for the incidence angle is  $37.6^\circ$ , and thus different from the  $35^\circ$  slant angle at the satellite due to the Earth curvature. The wavelength of the laser  $\lambda_0$  was determined on ground with a value of 354.8 nm.

### Double-edge Doppler wind lidar

The Doppler frequency for the atmospheric range gates  $f_{a,i}$  and internal laser reference  $f_i$  is derived from the signal  $I_A(f)$  and  $I_B(f)$  transmitted through both filters via a so-called response function  $R(f)$ . The transmitted signal  $I_A$  and  $I_B$  through both filters ("transmissivity") is resulting from the convolution of the filter transmission functions  $T_A$  and  $T_B$  and the lineshape of the atmospheric return  $S_a$  (Fig. 3-4 and Fig. 4-3) or internal laser reference  $S_i$ .

$$\begin{aligned}
I_{A,B,I}(f) &= \int_{-\infty}^{+\infty} T_{A,B,I}(f') \cdot S_i(f') \cdot df' \\
I_{A,B,a}(f) &= \int_{-\infty}^{+\infty} T_{A,B,a}(f') \cdot S_a(f') \cdot df'
\end{aligned} \tag{8.4}$$

The transmission function of both filters  $T_A(f)$  and  $T_B(f)$  can be described by Airy-functions with a period of the Free Spectral Range FSR, the frequency and amplitude of the maximum transmission, and the FWHM or finesse of the filter. Additionally, it was shown by Witschas (2011b) that the Airy-function needs to be convoluted with a Gaussian function, which accounts for filter defects using a defect parameter. Due to the slightly different implementation of both filters, the filter parameters for  $T_A$  and  $T_B$  differ and due to the sequential implementation the function  $T_B$  must take into account the reflection on filter A. This mainly results in a lower maximum transmission for filter B compared to filter A. It should be noted that the atmospheric signal and the internal reference use different optical paths through the instrument (Fig 4-1), which results in a slightly different illumination of both Fabry-Perot interferometers. Thus, the transmission functions  $T_A$  and  $T_B$  could be different for the atmospheric and internal path, which is denoted by the subscript I and a.

The signal of the internal reference  $S_i(f)$  can be approximated by a Gaussian function for the laser pulse lineshape with its laser linewidth parameter ( $\text{FWHM}_{\text{laser}}$  or  $\sigma_{\text{laser}}$ ) and frequency of the emitted laser  $f_0$ . The signal from the atmosphere  $S_a(f)$  with its Doppler shifted frequency  $f_a$  is composed of the broadband Rayleigh-Brillouin lineshape (Witschas et al. 2010), a narrowband Mie backscatter return and a constant offset from the background light. The Rayleigh-Brillouin lineshape depends on atmospheric temperature and pressure, while the narrowband Mie backscatter return can be approximated by the same lineshape as for the internal reference  $S_i(f)$ , neglecting atmospheric broadening by turbulent wind velocity variations. Thus the

	Document Nr. <b>AE-RP-DLR-L1B-001</b>	Issue: <b>4.4</b>	Date: <b>20.04.2018</b>	Page: <b>57/117</b>	
	Doc. Title: <b>ADM-Aeolus ATBD Level1B Products</b>				

measured signal on the atmospheric path is depending not only on the filter transmission  $T_A$  and  $T_B$ , but also on the atmospheric temperature, pressure and scattering ratio (see Eq. (3.5)), which are all strongly altitude dependent. It can be shown (e.g. Flesia and Korb 1999), that the parameters for filter A and B can be optimized such, that the influence of a narrowband Mie return is almost equal to the influence of the broadband Rayleigh return.

Furthermore the signal of the atmospheric range gates contains a contribution not arising from the backscatter of the emitted laser light on molecules, aerosol and cloud particles but also from the background light in the UV spectral region. This extremely broadband signal is arising from reflections of the sunlight on the ground or clouds. Although this background signal is reduced by an interference filter in the front optics (Fig. 4-1) of 1 nm bandwidth, it needs to be measured and corrected during processing, because it acts as a constant signal contribution to  $I_A$  and  $I_B$ . Additional offsets to the signal, which need to be corrected for the double-edge technique could arise within the detection chain from electronic offset voltages, which are applied before digitization (e.g. detection chain offset DCO for ALADIN).

### Definition of Rayleigh response

The signal measured after transmission through filter A and B is depending on the actual frequency  $f$  ( $f$  is used here for both atmospheric  $f_A$  and internal reference  $f_i$ ). The response function can be either defined as the ratio of both filter signals  $R=I_A/I_B$  or by the contrast-function, which is used here:

$$R(f) = \frac{I_A(f) - I_B(f)}{I_A(f) + I_B(f)} \quad (8.5)$$

The ratio-function was used by Korb et al. (1998) Flesia and Korb (1999), Gentry et al. (2000), while the above contrast-function was introduced by Chanin et al. (1989), Garnier et al. (1992) or Souprayen et al. (1999), because it is less sensitive to constant offsets and background light and the contrast function is more linear than the ratio around the frequency of the filter cross point  $I_A=I_B$  (N. B. a thorough investigation of the influence of different error sources on the derived winds using a ratio or contrast is still outstanding, because it is anticipated that the differences in the errors is not significant). The response  $R$  is a function of the Doppler frequency shift  $f$ . While the signals  $I_A$  and  $I_B$  are in units of digitizer counts LSB (Least Significant Bit), the response function  $R$  is dimensionless (a.u. arbitrary units) with typical values between  $\pm 0.3$  for a LOS wind speed range of  $\pm 90 \text{ ms}^{-1}$  (or HLOS range of  $\pm 145 \text{ ms}^{-1}$ ). The response functions  $R(f)$  are different for the internal reference path and the atmospheric path, because the transmission through both filters  $I_A, I_B$  is different mainly due to the difference of  $S_i(f)$  and  $S_a(f)$  (eq. 8.4).

The frequency of the filter crossing point  $f_c$  is defined for equal transmission through filter A and B with  $T_A(f_c)=T_B(f_c)$ . Here the Rayleigh response  $R(f_c)=0$  gets zero. The response function  $R(f)$  is almost linearly depending on frequency  $f$  around the crossing point  $f_c$  for the used filter parameters of ALADIN. The response  $R(f)$  can be linearized around the laser frequency  $f_0$  in a Taylor series, which is close to the filter crosspoint  $f_0 \approx f_c$  (N.B. there is no need to be exactly with the laser frequency  $f_0$  at the filter crosspoint  $f_c$ ) and the filter crosspoint  $f_c$  with  $\Delta f_c = f - f_c$

$$\begin{aligned} R(f) &= \alpha + \beta \cdot (f - f_0) + \gamma (f - f_0) \\ R(\Delta f_o) &= \alpha + \beta \cdot \Delta f_o + \gamma (\Delta f_o) \\ \Delta f_o &= f - f_0 \end{aligned} \quad (8.6)$$

with the intercept (or offset)  $\alpha$  and slope (or sensitivity)  $\beta$  and a term describing the deviation from a straight line, called non-linearity (or residual)  $\gamma$  as a function of the differential frequency  $\Delta f_o = f - f_0$  (N. B. The non-linearity  $\gamma$  is depending on  $f$  and  $f_0$ ). While the frequencies  $f$  or  $f_0$  are absolute frequencies (e.g.  $f_0 = 844.962 \text{ THz}$  for a laser wavelength of 354.8 nm), the delta symbol  $\Delta f_o$  indicates here, that a frequency difference is used. The slope parameter  $\beta$  is called sensitivity, because it describes the change of the response for a change in frequency:

	Document Nr. <b>AE-RP-DLR-L1B-001</b>	Issue: <b>4.4</b>	Date: <b>20.04.2018</b>	Page: <b>58/117</b>	
	Doc. Title: <b>ADM-Aeolus ATBD Level1B Products</b>				

$$\beta = \frac{\partial R_{f=f_0}}{\partial f} \quad (8.7)$$

Typical values for the sensitivity are  $4.5 \cdot 10^{-4} \text{ MHz}^{-1}$  to  $6 \cdot 10^{-4} \text{ MHz}^{-1}$ , depending on the spectral width of the internal reference signal and the atmospheric lineshape. Thus, for a LOS wind speed of 1 m/s, corresponding to 5.639 MHz, the response changes by only 0.3%, which illustrates the high sensitivity on the measurement of the response  $R(f)$  and the related signal intensities  $I_A(f)$  and  $I_B(f)$ . In order to achieve a random error (precision) for the wind of 1 m/s (LOS), the response needs to be determined with a precision of 0.3%. The intercept  $\alpha$  is related to the response value at the offset frequency  $f_0$  (neglecting the non-linearity):

$$\alpha = R(\Delta f_0 = 0) = R(f = f_0) \quad (8.8)$$

The intercept  $\alpha$  is given in units of the response (a.u.). The frequency of the crosspoint  $f_c$  of both filter A and B transmission curves can be derived from the sensitivity  $\beta$  and intercept  $\alpha$  (neglecting the non-linearity) using  $R(\Delta f_0)=0$ :

$$\Delta f_c = f_c - f_0 = \frac{\alpha}{\beta} \quad (8.9)$$

In case the offset frequency  $f_0$  is chosen such, that it is exactly at the filter crossing point  $f_0=f_c$ , then the intercept  $\alpha$  gets zero. Due to the difference in response function for the internal reference and atmospheric signal, also the filter crossing point  $f_c$  is different for the atmospheric  $f_{c,a}$  and internal path  $f_{c,i}$ . Thus, the laser frequency offset  $f_0$  is set to the crossing point of the internal reference, which results in a non-zero offset  $\alpha$  for the atmospheric path.

The Rayleigh response  $R(\Delta f_0)$  is measured during a response calibration mode (RRC) as a function of laser frequency offset  $\Delta f_0$  and the parameters intercept  $\alpha$  and slope  $\beta$  are determined from a straight line fit (see chapter 8.5) for both the atmospheric path and the laser internal reference. The nonlinearity of the response  $\gamma(\Delta f_0)$  is determined as the residual between the measured response  $R(\Delta f_0)$  and the linear fit by:

$$\gamma(\Delta f_0) = R(\Delta f_0) - [\alpha + \beta \cdot \Delta f_0] \quad (8.10)$$

As noted above the signals  $I_A$  and  $I_B$  are depending on the filter transmission function and the lineshape of the atmospheric return or the laser internal reference. Thus the response function  $R(f)$  is different for the atmospheric returns and the laser internal reference. The derived parameters intercept  $\alpha$ , sensitivity  $\beta$  and non-linearity  $\gamma$  are therefore different for the atmospheric range gates and laser internal reference and determined independently during the response calibration with the signal from the atmospheric range gates and the laser internal reference. As the lineshape of the atmospheric return is depending on the atmospheric temperature  $T$  (see ch. 3.4) and to a smaller extent on atmospheric pressure  $p$  due to the Rayleigh-Brillouin lineshape (Witschas et al. 2010, Witschas 2011a), the derived quantities  $\alpha_a$ ,  $\beta_a$  and non-linearity  $\gamma_a$  are valid only for the atmospheric conditions during the response calibration and thus only valid for a specific combination of the temperature and pressure profile. The dependency of the retrieved LOS wind speed on atmospheric temperature  $T$  and pressure  $p$  is not taken into account for processing of the L1B data product, because auxiliary information about the altitude profile for  $T$  and  $p$  is needed. These corrections are performed for L2B data products, which use  $T$ - and  $p$ -profiles from numerical weather prediction NWP models at the location of the observation (Dabas et al. 2008).

For retrieving the frequency offset  $\Delta f_0$  from a response measurement  $R$  and the absolute frequency  $f$ , the parameters  $\alpha$ ,  $\beta$  and non-linearity  $\gamma$  need to be known from a previous response calibration:

	Document Nr. <b>AE-RP-DLR-L1B-001</b>	Issue: <b>4.4</b>	Date: <b>20.04.2018</b>	Page: <b>59/117</b>	
	Doc. Title: <b>ADM-Aeolus ATBD Level1B Products</b>				

$$\Delta f_o = \frac{R - \gamma(\Delta f_o) - \alpha}{\beta} = f - f_0 \quad (8.11)$$

$$f = \frac{R - \gamma(\Delta f_o) - \alpha}{\beta} + f_0$$

During wind measurement the frequency Doppler shift is derived from the difference of the measured frequency of the atmospheric range gate  $f_a$  minus the frequency of the internal reference  $f_i$ :

$$\begin{aligned} \Delta f = f_a - f_i &= \left[ \frac{R_a - \alpha_a - \gamma_a(\Delta f_a)}{\beta_a} + f_0 \right] - \left[ \frac{R_i - \alpha_i - \gamma_i(\Delta f_i)}{\beta_i} + f_0 \right] = \\ &= \frac{R_a - \gamma_a(\Delta f_a)}{\beta_a} - \frac{R_i - \gamma_i(\Delta f_i)}{\beta_i} - \left[ \frac{\alpha_a}{\beta_a} - \frac{\alpha_i}{\beta_i} \right] = \\ &= \frac{R_a}{\beta_a} - \frac{R_i}{\beta_i} - \underbrace{\left[ \frac{\alpha_a}{\beta_a} - \frac{\alpha_i}{\beta_i} \right]}_{f_{c,a} - f_{c,i}} - \underbrace{\left[ \frac{\gamma_a(\Delta f_a)}{\beta_a} - \frac{\gamma_i(\Delta f_i)}{\beta_i} \right]}_{\Delta f_{non-linearity}} \end{aligned} \quad (8.12)$$

It is worth noting here that the offset frequency  $f_0$  is not needed for the wind retrieval, because only the difference between the filter crosspoint frequencies  $f_{c,a} - f_{c,i}$  from the atmospheric range gate and the internal reference is relevant. For simplicity, the contribution from the satellite movement, which is corrected in a later stage is neglected here. Also it should be noted that the above equation is applied for each atmospheric range gate.

The equation 8.12 (third line) shows that the non-linearity correction

$$\begin{aligned} \Delta f_{non-linearity} &= \frac{\gamma_a(\Delta f_a)}{\beta_a} - \frac{\gamma_i(\Delta f_i)}{\beta_i} = \frac{\gamma_a(f_a - f_0)}{\beta_a} - \frac{\gamma_i(f_i - f_0)}{\beta_i} \\ \Delta f_a &= f_a - f_0 \\ \Delta f_i &= f_i - f_0 \end{aligned} \quad (8.13)$$

is depending on the difference between the non-linearity of the atmospheric path at the Doppler shifted frequency  $f_A$  (relative to the offset frequency  $f_0$ ) minus the non-linearity of the internal path at the transmitted frequency  $f_i$  (relative to the offset frequency  $f_0$ ). Thus, the non-linearity correction is depending on the knowledge of the offset-frequency  $f_0$ . Also the non-linearity function  $\gamma(\Delta f)$  is characterized during the response calibration mode RRC and used in the sub-sequent wind retrieval. As the non-linearity function  $\gamma(\Delta f)$  is actually depending on the absolute laser frequency  $f_0$ , a difference in  $f_0$  between response calibration RRC and wind measurement will introduce an error, as different parts of the non-linearity function are used. As the non-linearity function is only a small correction to the response and only slowly varying with frequency, a small frequency difference in absolute laser frequencies will only result in small errors. It was shown, that the non-linearity function for the Rayleigh response can be approximated by a 5<sup>th</sup> order polynomial (DLR 2012a, DLR 2012f, Marksteiner 2012). Thus the coefficients from a 5<sup>th</sup> order polynomial are used to describe the non-linearity function  $\gamma(\Delta f)$  and used in the wind retrieval. These polynomial coefficients are derived from a least-square fit procedure, obtained from the calibration mode data.

If the non-linearity correction is not performed, it is assumed that the non-linearity for atmospheric and internal path is almost equal and constant with frequency. It should be noted here, that the non-linearity part is strongly depending on the applied frequency range for the response calibration around the filter crosspoint, and thus the required wind speed measurement range. The non-linearity is furthermore different for narrowband Mie type signals (internal reference) and broadband Rayleigh type signal, especially when derived from a large frequency range around the crosspoint. Thus also the non-linearity function is different for the laser internal reference (narrowband Mie signal), a ground return (narrowband Mie signal) and

	Document Nr. <b>AE-RP-DLR-L1B-001</b>	Issue: <b>4.4</b>	Date: <b>20.04.2018</b>	Page: <b>60/117</b>	
	Doc. Title: <b>ADM-Aeolus ATBD Level1B Products</b>				

atmospheric returns (broad bandwidth Rayleigh signal). Thus 3 different calibration parameters (internal, ground-return, atmospheric range gate) are used for the wind retrieval.

### Discussion of error sources for Rayleigh response

The influence of constant offsets and signal variations on the signals  $I_A$  and  $I_B$  will result in errors in the determination of the Rayleigh Response  $R=(I_A-I_B)/(I_A+I_B)$ . These errors can be categorized in 3 cases:

#### Case 1: Constant offset C

Both signals  $I_A$  and  $I_B$  are affected by a constant offset C, e.g. background light or detection chain offset. Then the derived Response  $R_c$  becomes

$$R_c = \frac{(I_A + C) - (I_B + C)}{(I_A + C) + (I_B + C)} = \frac{I_A - I_B}{I_A + I_B + 2 \cdot C} \neq R \quad (8.14)$$

Thus, a constant offset C is resulting in an erroneous determination of the Rayleigh response  $R_c$ . The influence of the offset C is depending on the signal level of  $I_A+I_B$  and the response, which determines the signal difference  $I_A-I_B$ . A numerical example with typical values of  $I_A=1000$  LSB,  $I_B=900$  LSB results in a correct response of  $R=0.05263$ . A constant offset of only  $C=10$  LSB ( $=1\% I_A$ ) will give  $R_c=0.05208$ , which differs by  $5.5 \cdot 10^{-4}$  from R, corresponding to an error of  $1 \text{ MHz} = 0.18 \text{ ms}^{-1}$  for a typical response slope. This shows that the offset C has to be determined with high accuracy and subtracted before calculation of the Rayleigh response.

#### Case 2: Constant factor k for both filters

Both signals  $I_A$  and  $I_B$  are affected by a constant factor k, which is related to a variation of signal level. This could be due to variation in atmospheric backscatter or emitted laser energy and the resulting response  $R_k$  is:

$$R_k = \frac{k \cdot I_A - k \cdot I_B}{k \cdot I_A + k \cdot I_B} = \frac{I_A - I_B}{I_A + I_B} = R \quad (8.15)$$

Thus a factor k, affecting both filter signals equally is not resulting in an error of the determined Rayleigh response R, which enables wind measurements under varying atmospheric conditions without further corrections.

#### Case 3: Different factor $k_A$ and $k_B$ for both filters

Signals  $I_A$  is affected by a factor  $k_A$ , while signal  $I_B$  is affected by a different factor  $k_B$ . The resulting response  $R_{k_A, k_B}$  is:

$$R_{k_A, k_B} = \frac{k_A \cdot I_A - k_B \cdot I_B}{k_A \cdot I_A + k_B \cdot I_B} = \frac{\frac{k_A}{k_B} I_A - I_B}{\frac{k_A}{k_B} I_A + I_B} \neq R \quad (8.16)$$

Thus a different factor  $k_A$  and  $k_B$  for both filter signals is resulting in an error of the determined Rayleigh response R. Actually the optical path and detection chain is different for filter A and B by design, due to the sequential implementation of the Fabry-Perot Interferometer, resulting in different filter transmission functions  $T_A$  and  $T_B$ . But these differences are inherently calibrated, when using the derived parameters from the Rayleigh response calibrations. On the other hand any difference in the optical path or detection chain between calibration and wind measurement, which affects both filters differently will result in an error of the retrieved wind. This is the case for a non-uniformity and tilt of the Rayleigh spots on the ACCD in combination with the detection of a ground-return signal during the period of charge transfer from imaging to memory zone of the ACCD (DLR 2010). The influence is mainly depending on the ratio between  $k_A$  and  $k_B$ . A numerical example with typical values of  $I_A=1000$  LSB,  $I_B=900$  LSB results in a correct response  $R=0.05263$ . A ratio of only 0.9 will result in  $R_{k_A, k_B} \neq 0$ , which results in an error of 0.05263, corresponding to  $100 \text{ MHz} = 18 \text{ ms}^{-1}$ . For other double-edge systems a corrective factor is used to account for differences in the optical

	Document Nr. <b>AE-RP-DLR-L1B-001</b>	Issue: <b>4.4</b>	Date: <b>20.04.2018</b>	Page: <b>61/117</b>	
	Doc. Title: <b>ADM-Aeolus ATBD Level1B Products</b>				

path or detection chain sensitivity of both edge filters (Chanin et al. 1989, Garnier and Chanin 1992), which needs to be determined separately by a calibration. For ALADIN the differences are inherently calibrated in the response calibration mode RRC, so only differences in the ratio  $k_A/k_B$  between RRC and wind measurement mode would result in an error.

## 8.2.2 Specific implementation for ALADIN Rayleigh wind retrieval

Now the implemented processing steps for the retrieval of the wind speed from the Rayleigh spectrometer RSP are described. Table 8-1 summarizes the input data, the source, and description for the processing of the measurements for the Rayleigh wind retrieval. The following processing steps are applied both on measurement level, consisting of P-1 accumulated laser pulses on the ACCD, and on observation level, which is obtained after averaging a number of N measurements in the on-ground processing (ch. 8.1.1). The signal output consists of digitized signal levels (in units of LSB: least significant bit) from 20 ACCD pixels per measurement k and per atmospheric range gate i. The 20 pixels are composed of 8 pixels from the Rayleigh filter A (direct path), 8 pixels for filter B (reflected path) and 4 pixels, which are not illuminated. The optical output of each filter A and B is imaged onto a circular spot in the ACCD imaging zone (Fig. 4-3) and combined in the ACCD memory zone in 8 pixels per filter (Fig. 4-4). For the internal reference each laser pulse n is acquired by the ACCD and digitized, and not accumulated as for the atmospheric range gates. Thus, the signals from each laser pulse have to be summed up to be equivalent to the accumulation period for 1 atmospheric measurement and one observation. A quality control is applied before averaging to measurements and observations to discard measurements with corrupted data or laser problems (chapter 8.1.1.) for both the internal reference and the atmospheric range gates.

On the ACCD each detected photon is converted to a signal electron (charges) with certain quantum efficiency. The electronic charges are sequentially transferred and read out from the ACCD after the accumulation period. These ACCD electronic signals are amplified by the Detection Front-End Unit (DFU) and digitized by a 16-bit Analog-Digital-Converter (ADC). The digitized signals for the atmospheric range gates are described as  $S_a(i,j,k)$ , where i denotes the number of the atmospheric range gate (i=1 to 25), j the number of the ACCD pixel (j=1 to 20) and k the number of the measurement (k=1 to N, N: number of measurements per observation).

The situation for the internal reference is different, because it is acquired for each laser pulse n and not accumulated on the ACCD. A maximum number of  $n_{max}$  laser pulses are acquired with  $n_{max}=N*(P-1)$  (P: number of laser pulses per measurement) per observation. The digitized signal from the internal reference is called  $S_l(i=1,j,n)=S_l(j,n)$ .

In addition, the background light through both Rayleigh filters A and B is measured via the atmospheric optical path, after a time period, which is significantly larger than the round-trip time to the ground. This is to ensure, that pure atmospheric background light is acquired, which should not contain any atmospheric backscatter signals from the emitted laser pulse. The background signal is contained in the last atmospheric range gate with i=25 and thus stored in  $S_a(i=25,j,k)$ .

### 1) Correction of Rayleigh detection chain non-linearity

The efficiency of the conversion from photons to signal electrons and the pre-amplification could be varying depending on the signal strength, e.g. a number of 10 photons could lead to a digitized signal of 5 LSB, while a number of 100 photons could only lead to a number of 49 LSB. As the principle of the Rayleigh receiver is based on a very accurate intensity measurement, the non-linearity in the detection chain for different signal levels needs to be characterized on-ground. Here the difference  $E_{RLC}(S)$  between an ideal linear relationship between the input signal to the detection chain and the measured output signal S for a range of signal levels is obtained (RLC: Rayleigh linearity correction). For a perfectly linear signal response  $E_{RLC}(S) = 0$  over the whole signal dynamic range of S.

The first step is to apply non-linearity correction using a priori-knowledge  $E_{RLC}(S)$  for both the atmospheric range gates and internal reference for each pixel. The non-linearity is corrected for each measurement of the atmospheric range gates  $S_a(i, j,k)$  and for each laser pulse of the internal reference  $S_l(j,n)$  before summation to measurements and observations.

	Document Nr. <b>AE-RP-DLR-L1B-001</b>	Issue: <b>4.4</b>	Date: <b>20.04.2018</b>	Page: <b>62/117</b>	
	Doc. Title: <b>ADM-Aeolus ATBD Level1B Products</b>				

$$S_{a,RLC}(i, j, k) = S_a(i, j, k) - E_{RLC}(S_a(i, j, k)) \quad (8.17)$$

$$S_{I,RLC}(j, n) = S_I(j, n) - E_{RLC}(S_I(j, n))$$

This detection chain non-linearity correction is similar than applied for other detectors, e.g. Photo-Multiplier Tubes PMT, or corrections needed for high signal levels, when using a photon-counting method (e.g. McGill 1997. Souprayen et al. 1999).

It was shown by on-ground measurements that the non-linearity of the Rayleigh detection chain is better than 0.1% (EADS-Astrium 2012). It seems that the value of 0.1% is also the accuracy of the characterisation of the non-linearity in the Rayleigh detection chain. A 0.1% non-linearity means that a signal level of 1000 LSB can be determined with an accuracy of 1 LSB. Thus, no non-linearity correction is applied to the Rayleigh signal levels ( $E_{RLC}=0$ ), leading to errors in the order of 1 MHz = 0.18 m/s for a maximum, uncorrected non-linearity of 0.1% (using eq. 8.16 with  $k_A/k_B=0.999$ ).

## 2) Correction for detection chain offset DCO and dark charges

A detection chain offset (DCO) is present on the digitized signals  $S_a$  and  $S_I$  due to an electronic voltage offset within the detection chain from the ACCD to the ADC. This detection chain offset  $E_{DCO}(i, k)$  is constant for all 20 pixel of one row on the ACCD (corresponding to the range gates  $i$ ), but could vary from row-to-row and from measurement to measurement. As a constant offset to the signal is detrimental for the determination of the Rayleigh response, it needs to be measured and corrected. The DCO value  $E_{DCO}(i, k)$  is determined from the signal level for pixels  $j=j_{DCO}$  on the ACCD, which are not illuminated by photons and the following corrections are applied for each range gate  $i$  and measurement  $k$  or laser pulse  $n$ :

$$S_{a,DCO}(i, j, k) = S_{a,RLC}(i, j, k) - E_{a,DCO}(i, j_{DCO}, k) - E_{DC}(DCR, P) \quad (8.18)$$

$$S_{I,DCO}(j, n) = S_{I,RLC}(j, n) - E_{I,DCO}(j_{DCO}, n)$$

Actually 2 pixels are foreseen for measurement of the DCO offset (pixel number 19 and 20) and  $E_{DCO}(i, k)$  would be determined from the average signal of both pixels. But only pixel number 20 could be used for the Rayleigh detection chain, because pixel number 19 is contaminated with spurious charges ( $j_{DCO}=20$ ). The accuracy of the DCO correction is directly influencing the derived Rayleigh response, because it acts as a constant offset. The offset pixels ("virtual pixels", see ch. 4.2.5) on the ACCD are not influenced by photon noise, but contain read-out noise of the ACCD with a Gaussian distribution with zero mean. Thus, in case the DCO value of the offset pixels  $j_{DCO}$  is not varying for different range gates  $i$ , and average value  $E_{DCO}(k)$  for all range gates could be used for correction (DLR 2010, 2011).

An additional correction is applied to the Rayleigh signals arising from the dark current charge offset in the memory zone of the ACCD for the atmospheric signals  $E_{DC}(DCR, P)$ . Dark charges are accumulated on all pixels in the ACCD, leading to a constant offset, which is proportional to the dark current rate DCR (in units of electrons or LSB per pixel per second) and the duration of the charges in the respective zone of the ACCD. Only the dark charges in the memory zone of the ACCD are relevant, because the duration is in the order of 0.4 s for a number of 20 accumulated pulses (and PRF = 50.5 Hz), while the charges stay in the imaging zone of the ACCD only between 2.1-8.4  $\mu$ s. Thus an additional offset  $E_{DC}$  needs to be subtracted from the signal of the atmospheric range gates, depending on the dark current rate DCR and the number of accumulated pulses  $P$ . This offset is obviously constant for each pixel, each range gate and each measurement of one observation. The dark current rate DCR is characterized on-ground and monitored in orbit. No significant amount of dark charges is accumulated for the internal reference, because it is read-out for every single pulse. The detection chain offset pixels do not contain the accumulated dark charges, because they should be considered not as real pixels on the ACCD, but as additional read-out sequences of the ACCD ("virtual pixels"). Thus the dark current offset is not corrected by the DCO offset correction.

## 3) Correction for background light

The background light is measured via the atmospheric path and stored in the last row of the ACCD memory zone with  $i=25$  for both filter A and B. In order to achieve sufficiently high signal levels for the background range gate, the integration times for the background light  $t_b$  is significantly larger than the integration times

	Document Nr. <b>AE-RP-DLR-L1B-001</b>	Issue: <b>4.4</b>	Date: <b>20.04.2018</b>	Page: <b>63/117</b>	
	Doc. Title: <b>ADM-Aeolus ATBD Level1B Products</b>				

for the atmospheric range gates  $t_i$ , e.g. the highest background integration times  $t_b$  is 3750  $\mu\text{s}$ , while the lowest integration time for atmospheric range gates is 2.1  $\mu\text{s}$ . Thus, the contribution of the background light on the atmospheric range gates is a factor of  $t_i/t_b$  smaller than measured during the acquisition of the background light. The following correction is applied for each atmospheric range gate and for each pixel to obtain the background (BCK) corrected signals  $S_{a,bck}$ :

$$S_{a,BCK}(i, j, k) = S_{a,DCO}(i, j, k) - \frac{t_i}{t_b} S_{a,DCO}(i = 25, j, k) \quad (8.19)$$

A background correction is not applied to the internal reference signal  $S_{i,DCO}$ , because the internal optical path is not influenced by background light.

#### 4) Summation of filter A and B signal

As stated above the filter A and B signal are contained in different pixels of the ACCD. In order to obtain the total number of signal of filter A and B, the corresponding pixels have to be summed up. While the filter B signal is contained in pixel with  $j_{\min}=3$  to  $j_{\max}=10$ , the filter A signal is contained in pixel  $j_{\min}=11$  to  $j_{\max}=18$ . The useful signal is contained in 16 pixels (8 for each filter), while the remaining 4 pixels are used as offset pixels. Thus the filter A and B signal for the internal reference is obtained from:

$$I_{A,I}(n) = \sum_{j=11}^{j=18} S_{I,DCO}(j, n) \quad (8.20)$$

$$I_{B,I}(n) = \sum_{j=3}^{j=10} S_{I,DCO}(j, n)$$

and correspondingly for the atmospheric range gates:

$$I_{A,a}(i, k) = \sum_{j=11}^{j=18} S_{a,BCK}(i, j, k) \quad (8.21)$$

$$I_{B,a}(i, k) = \sum_{j=3}^{j=10} S_{a,BCK}(i, j, k)$$

The major part of the filter A and B signal is contained in the 4-5 centre pixels per filter, due to the circular spots on the ACCD. In case that signal is present on the ACCD, which is not arising from the filter A and B transmission, e.g. straylight, parasitic reflections, the summation of the signal pixels could be limited to the 6 or 4 central pixels per filter (DLR 2010).

#### 5) Summation of signals from measurements to observations

As the laser internal reference signal is acquired for each laser pulse, the corresponding signals from the internal reference for the duration of an atmospheric measurement with index  $k$  have to be summed up:

$$I_{A,I}(k) = \sum_{n_{\min,k}}^{n_{\max,k}} I_{A,I}(n) \quad (8.22)$$

$$I_{B,I}(k) = \sum_{n_{\min,k}}^{n_{\max,k}} I_{B,I}(n)$$

Thus, for each atmospheric measurement with index  $k$  a corresponding internal reference measurement with index  $k$  is determined. The wind retrieval is applied to signals on measurement level and after summation of a number of  $N$  measurements to one observation. Thus, both the atmospheric signals and the internal reference signals have to be summed up to obtain the signals A and B per observation.

	Document Nr. <b>AE-RP-DLR-L1B-001</b>	Issue: <b>4.4</b>	Date: <b>20.04.2018</b>	Page: <b>64/117</b>	
	Doc. Title: <b>ADM-Aeolus ATBD Level1B Products</b>				

$$\begin{aligned}
I_{A,I} &= \sum_{k=1}^{k=N} I_{A,i}(k) \\
I_{B,I} &= \sum_{k=1}^{k=N} I_{B,i}(k) \\
I_{A,a}(i) &= \sum_{k=1}^{k=N} I_{A,a}(i,k) \\
I_{B,a}(i) &= \sum_{k=1}^{k=N} I_{B,a}(i,k)
\end{aligned} \tag{8.23}$$

The following processing steps are applied in the same manner for a number of N measurements per observation and for each observation. For simplicity only the processing of the observations is described below (and the index k for each measurement is suppressed).

#### 6) Determination of the Rayleigh response

The Rayleigh response for the internal reference  $R_I$  and for each atmospheric range gate  $R_a(i)$  is determined.

$$\begin{aligned}
R_I &= \frac{I_{A,I} - I_{B,I}}{I_{A,I} + I_{B,I}} \\
R_a(i) &= \frac{I_{A,a}(i) - I_{B,a}(i)}{I_{A,a}(i) + I_{B,a}(i)}
\end{aligned} \tag{8.24}$$

#### 7) Correction of the Rayleigh response non-linearity

As explained above, the Rayleigh response R can be linearized around the filter A and B crosspoint, and the intercept (offset)  $\alpha$  and slope (sensitivity)  $\beta$  is used to derive the frequency of the observation. This approach is acceptable for low wind speeds and thus low Doppler frequency shifts. For the required wind speed range of  $\pm 145 \text{ ms}^{-1}$  (HLOS, equivalent to  $\pm 500 \text{ MHz}$ ) the Rayleigh response shows a non-linear behaviour, which cannot be neglected. In principle, this Rayleigh non-linearity can be described by a polynomial function, and it was shown that a 5<sup>th</sup> order polynomial is sufficient (DLR 2011f, Marksteiner 2012). In principle the frequency f could be determined by an inversion of the non-linear response function R(f) (Marksteiner 2012), but a different approach is used here. The analysis of the Rayleigh response calibration (ch. 8.5) is based on a decomposition of the non-linear response function R(f) in a linear part with parameters  $\alpha$  and  $\beta$  and a residual, describing the non-linearity  $\gamma(\Delta f_0)$ . The measured nonlinearity of the response  $\gamma_m$  (m: measured) is determined for discrete frequency steps  $\Delta f_m$  as the residual between the measured response  $R_m(f_m)$  and the linear fit parameters by:

$$\begin{aligned}
\gamma_m &= R_m(\Delta f_m) - [\alpha + \beta \cdot \Delta f_m] \\
\gamma_m(\Delta f_m) &\Rightarrow \text{function of } \Delta f_m \\
\gamma_m(R_m) &\Rightarrow \text{function of } R_m
\end{aligned} \tag{8.25}$$

The non-linearity  $\gamma_m$  can be described as a function of the frequency step  $\Delta f_m$  or as function of the measured response  $R_m$  at that frequency step  $\Delta f_m$ . In principle the correction of the non-linearity can be performed using both descriptions of the non-linearity  $\gamma_m(\Delta f_m)$  and  $\gamma_m(R_m)$ . The use of the function  $\gamma_m(\Delta f_m)$  would need an inversion procedure, because the frequency  $\Delta f_m$  is not known at the stage of the non-linearity correction. But the measured responses  $R_I$  and  $R_a(i)$  are known, and thus, the correction is applied using the  $\gamma_m(R_m)$  approach with:

	Document Nr. <b>AE-RP-DLR-L1B-001</b>	Issue: <b>4.4</b>	Date: <b>20.04.2018</b>	Page: <b>65/117</b>	
	Doc. Title: <b>ADM-Aeolus ATBD Level1B Products</b>				

$$R_{I,cor} = R_I - \gamma_I (R_I) \quad (8.26)$$

$$R_{a,cor}(i) = R_a(i) - \gamma_a (R_a(i))$$

Alternatively the measured non-linearity  $\gamma_m(R_m)$  could be fitted by a 5<sup>th</sup> order polynomial function and the polynomial function could be used for correction.

Now the corrected responses  $R_{I,cor}$  and  $R_{a,cor}$  are only linearly depending on the frequency difference  $\Delta f$ :

$$R_{I,cor} = \alpha_I + \beta_I \cdot \Delta f_I \quad (8.27)$$

$$R_{a,cor}(i) = \alpha_a + \beta_a \cdot \Delta f_a(i)$$

It should be noted that the parameters  $\alpha$ ,  $\beta$  and  $\gamma$  are derived from the observations during Rayleigh response calibration RRC (ch. 8.5) for the internal reference and the atmospheric range gates and are input parameters to the Rayleigh wind retrieval here. The parameters  $\alpha_a$ ,  $\beta_a$  and  $\gamma_a$  are derived for the sum of several atmospheric range gates, and not as an altitude dependent profile. All parameters are in principle depending on the lineshape of the atmospheric return and depending on atmospheric temperature, pressure and scattering ratio. The intercept  $\alpha_a$ , and non-linearity  $\gamma_a$  are strongly depending on the Rayleigh filter functions  $T_{A,a}(f)$  and  $T_{B,a}(f)$ , while the dependency on the atmospheric parameters is most pronounced for the sensitivity  $\beta_a$  (Paffrath 2006, DLR 2011a, DLR 2011b). This dependency on atmospheric profiles is corrected for the L2B products (Dabas et al. 2008).

A correction for the non-linearity of the Rayleigh response is typically not needed for double-edge Doppler wind lidars operated on ground (DLR 2006), because the wind speed measurement range is significantly smaller ( $\pm 50 \text{ ms}^{-1}$  compared to  $\pm 150 \text{ ms}^{-1}$ ). Here, the considered frequency range around the filter crosspoint can be smaller and a linear dependency of the Rayleigh response on frequency can be used.

## 7) Determination of the Doppler frequency shift

Now the determination of the frequency of the internal reference and the atmospheric range gates is straightforward:

$$f_I = \frac{R_{I,cor} - \alpha_I}{\beta_I} + f_0 = \frac{R_I - \alpha_I - \gamma_I (R_I)}{\beta_I} + f_0 \quad (8.28)$$

$$f_a(i) = \frac{R_{a,cor}(i) - \alpha_a}{\beta_a} + f_0 = \frac{R_a(i) - \alpha_a - \gamma_a (R_a(i))}{\beta_a} + f_0$$

The offset frequency  $f_0$  is equal for both the internal reference and atmospheric range gates and is therefore eliminated, when calculating the Doppler frequency shift  $\Delta f(i)$  per range gate  $i$ :

$$\Delta f(i) = f_a(i) - f_I = \frac{R_a(i) - \alpha_a - \gamma_a (R_a(i))}{\beta_a} - \frac{R_I - \alpha_I - \gamma_I (R_I)}{\beta_I} \quad (8.29)$$

## 8) Determination of LOS and HLOS wind speed

The LOS wind speed and the HLOS wind speed, which is the projection to the horizontal plane with the altitude dependent incidence angle  $\varphi(i)$ , is derived using the Doppler shift equation:

	Document Nr. <b>AE-RP-DLR-L1B-001</b>	Issue: <b>4.4</b>	Date: <b>20.04.2018</b>	Page: <b>66/117</b>	
	Doc. Title: <b>ADM-Aeolus ATBD Level1B Products</b>				

$$\begin{aligned}
v_{LOS}(i) &= \frac{\lambda_0}{2} \cdot (f_a(i) - f_I) - v_{LOS,S}(i) \\
&= \frac{\lambda_0}{2} \cdot \left[ \frac{R_a(i) - \alpha_A - \gamma_a(R_a(i))}{\beta_A} - \frac{R_I - \alpha_I - \gamma_I(R_I)}{\beta_I} \right] - v_{LOS,S} \\
v_{HLOS}(i) &= \frac{1}{\sin(\varphi(i))} v_{LOS}(i) \\
&= \frac{1}{\sin(\varphi(i))} \left[ \frac{\lambda_0}{2} \cdot \left[ \frac{R_a(i) - \alpha_A - \gamma_a(R_a(i))}{\beta_A} - \frac{R_I - \alpha_I - \gamma_I(R_I)}{\beta_I} \right] - v_{LOS,S} \right]
\end{aligned} \tag{8.30}$$

with the correction of the satellite-induced Doppler shift velocity  $v_{LOS,S}$  (in  $\text{ms}^{-1}$ ), which is constant for all altitudes (in contrast to the incidence angle  $\varphi(i)$ ). The incidence angle  $\varphi(i)$  and the satellite induced Doppler shift velocity  $v_{LOS,S}$  is obtained using the AOCS sensors and algorithms.

To our knowledge all other direct-detection Doppler Wind Lidar's (DWL's) using the single or double-edge technique with Fabry-Perot Interferometers or molecular absorption lines as filters do not determine the LOS wind speed  $v_{LOS}$  directly from the measurement in only one LOS pointing direction (Chanin et al. 1989, Garnier and Chanin 1992, Gentry et al. 2000, Flesia et al. 2000, Liu et al. 2007, Wang et al. 2010). The typical approach is to point alternately to several LOS directions (off-zenith, perpendicular and parallel, but opposite azimuth angles, or zenith and off-zenith pointing) in order to retrieve the LOS wind from differences of the LOS winds from different pointing directions. These methods are applied to eliminate possible influences of laser frequency drifts, spectrometer drifts, alignment drifts and other error sources. Thus, the offset parameters  $\alpha_A$  and  $\alpha_I$  in the above equation are eliminated by using different LOS pointing directions. The challenge for ALADIN is that only one LOS pointing direction is used, and the instrument needs to be very stable between response calibrations, where the calibration parameters  $\alpha$ ,  $\beta$ , and  $\gamma$  are determined and the wind measurement. It is foreseen to perform a response calibration once per week in-orbit. Thus the single LOS approach by ALADIN is unique and challenging for a direct-detection DWL. In contrast to DWL's operated on the ground, the airborne A2D and satellite ALADIN operations allow the use of the reflection from the non-moving land surface for correction purpose (DLR 2011b), which is described in the next step.

## 9) Correction for residual ground speed

Although the correction with the satellite induced LOS speed  $v_{LOS,S}$  is applied, there could be a remaining LOS wind, which is not related to an atmospheric wind. This could be due to random or systematic errors in the knowledge of the AOCS parameters (e.g. pitch, roll, heading, LOS pointing direction, satellite ground speed), which result in random or systematic errors of  $v_{LOS,S}$ . Another reason for a residual LOS wind speed, could be erroneous calibration parameters ( $\alpha$ ,  $\beta$  and  $\gamma$ ) or differences between the optical paths during response calibration and wind measurement. This could be induced by thermo-mechanical drifts of the optics, which result in different illumination of the Fabry-Perot interferometers, and thus, differences in Rayleigh response (see further discussion in DLR 2012b).

A residual, noncorrected LOS wind speed should be present on the atmospheric range gates, which contain the return from the non-moving Earth surface (ground return). For land surfaces this LOS wind speed should be zero  $\text{ms}^{-1}$ , while for ocean surfaces this cannot be assumed due to the wind-induced movement of the ocean surface and currents (KNMI 2008). While for nadir-pointing of the ALADIN instrument during response calibration, the LOS wind speed of the ocean surface can be assumed to be almost zero  $\text{ms}^{-1}$ , this cannot be assumed for off-nadir pointing during wind measurements with an average incidence angle of  $37.6^\circ$ . Thus, the usage of the ground return is limited to land surfaces.

The detection of atmospheric range gates, which contain a ground return signal is described in detail in chapter 8.6. The processing of the raw ACCD output  $S_a(i=g,j,k)$  from the range gates containing ground signal ( $i=g$ ) is applied up to step 6 to obtain the Rayleigh response  $R_a(i=g)$ . No averaging of the measurements to observations is applied for ground return signal, because the ground return signal should be sufficiently high already on measurement level. The main reasons is that the ground return signal could be located in several atmospheric range gates, because of the surface terrain variation and the ground speed of the satellite, and due to a vertical movement of the satellite. Thus an averaging of signals in step 5 from

	Document Nr. <b>AE-RP-DLR-L1B-001</b>	Issue: <b>4.4</b>	Date: <b>20.04.2018</b>	Page: <b>67/117</b>	
	Doc. Title: <b>ADM-Aeolus ATBD Level1B Products</b>				

measurements to observations would increase the spread of the range gates, which contain ground return. Actually it will be the case already on measurement level, that the ground return signal will be contained in several range gates  $g_i$ , also due to the range gate overlap induced by the ACCD (DLR 2012a, Marksteiner 2012). The detection and processing of the signals from several range gates  $g_i$  is described in chapter. 8.6, while here the index  $g$  is used for indicating one to several range gates.

The reflection on the non-moving land surface will result in a spectral lineshape, which is similar to the outgoing laser pulse. Thus, the frequency dependency of the Rayleigh response of the ground return is similar to the frequency dependency of the laser internal reference. Nevertheless there are differences in optical illumination through the laser internal path and the atmospheric path. Thus, the calibration parameters for a ground return signal (via the atmospheric optical path) are independently determined during the Rayleigh response calibration RRC. Those parameters  $\alpha_g$ ,  $\beta_g$  and  $\gamma_g$  are used for determination of the frequency of the ground return:

$$f_a(g) = \frac{R_{a,cor}(g) - \alpha_g}{\beta_g} + f_0 = \frac{R_a(g) - \alpha_g - \gamma_g(R_a(g))}{\beta_g} + f_0 \quad (8.31)$$

The frequency shift of the ground return is obtained from

$$\Delta f(g) = f_a(g) - f_l = \frac{R_a(g) - \alpha_g - \gamma_g(R_a(g))}{\beta_g} - \frac{R_l - \alpha_l - \gamma_l(R_l)}{\beta_l} \quad (8.32)$$

In the next step the residual velocity of the ground return measurement is derived. As the ground-return velocity is derived for each measurement (and not for each observation), it must be noted here, that the internal reference response  $R_l$  and the satellite component for the corresponding measurement  $k$  has to be used here.

$$v_{LOS}(g) = \frac{\lambda_0}{2} \cdot \Delta f(g) - v_{LOS,S}(g) = \frac{\lambda_0}{2} \cdot \left[ \frac{R_a(g) - \alpha_g - \gamma_g(R_a(g))}{\beta_g} - \frac{R_l - \alpha_l - \gamma_l(R_l)}{\beta_l} \right] - v_{LOS,S} \quad (8.33)$$

For a perfect instrument, perfect knowledge of the satellite induced LOS wind speed and perfect measurement of the ground-return LOS speed the retrieved value for  $v_{LOS}(g)$  should be zero  $\text{ms}^{-1}$ . Any non-zero value is due to non-perfections of the instrument and or errors in satellite velocity  $v_{LOS,S}$  and random errors in the retrieval of the ground-return LOS speed  $v_{LOS,G}$  due to signal noise. Another source of significant errors in the ground-return speed is due to the sampling of atmospheric backscatter signal within the range gate of typical heights of 250 m or 500 m, which contains the ground return signal (DLR 2006, DLR 2012b, Marksteiner 2012). The atmospheric backscattering particles move with the surface wind and contribute to the total signal, depending on the relative location of the ground within the range gate.

The residual LOS wind speed from the ground return is derived per measurement and the averaging is performed using the retrieved LOS wind speeds (and not the signals as for atmospheric range gates):

$$v_{LOS,G} = \frac{1}{N} \sum_{k=1}^N v_{LOS,G}(k) \quad (8.34)$$

It could be the case that no valid ground return is detected for a measurement (see ch. 8.6 for a discussion of the ground-return detection), which could be due to low SNR (over ocean surfaces or high extinction of atmospheric layers above) or due to a total blocking of the ground return layer by optically thick clouds. A valid ground return value for an observation is derived, if the number of ground returns per observation is above a threshold. If the number of ground-return measurements is too low or even zero, then no valid value for the observation can be derived. In this case the latest valid value for a ground-return velocity **could be** used for the subsequent correction. Actually the approach using the latest valid ground-return is not considered as a robust and accurate method for correction because the temporal separation of the latest ground return to the actual observation could be significant in case of cloudy or low ground albedo scenes (e.g. ocean or some land surfaces, DLR (2018b)). The instrument error sources, which need to be corrected

	Document Nr. <b>AE-RP-DLR-L1B-001</b>	Issue: <b>4.4</b>	Date: <b>20.04.2018</b>	Page: <b>68/117</b>	
	Doc. Title: <b>ADM-Aeolus ATBD Level1B Products</b>				

with the use of ground-return velocities, could have evolved significantly during this time separation. Thus more advanced methods described shortly below and in ch. 8.6 will be used.

This residual LOS wind speed  $v_{LOS,G}$  is used as additional term in the wind retrieval to correct for any offsets:

$$\begin{aligned}
v_{LOS,corr}(i) &= v_{LOS}(i) - v_{LOS,G} \\
&= \frac{\lambda_0}{2} \cdot \left[ \frac{R_a(i) - \alpha_A - \gamma_a(R_a(i))}{\beta_A} - \frac{R_I - \alpha_I - \gamma_I(R_I)}{\beta_I} \right] - v_{LOS,S} - v_{LOS,G} \\
v_{HLOS,corr}(i) &= \frac{1}{\sin(\varphi(i))} \left[ v_{LOS}(i) - v_{LOS,G} \right] \\
&= \frac{1}{\sin(\varphi(i))} \left[ \frac{\lambda_0}{2} \cdot \left[ \frac{R_a(i) - \alpha_A - \gamma_a(R_a(i))}{\beta_A} - \frac{R_I - \alpha_I - \gamma_I(R_I)}{\beta_I} \right] - v_{LOS,S} - v_{LOS,G} \right]
\end{aligned} \tag{8.35}$$

Further corrections using the residual ground return LOS wind speed from a number of observations, which could span several orbits, are applied to the retrieved wind speeds. This will introduce a correction similar to  $v_{LOS,G}$ , which is dependent on the latitude of the observations to account for orbital variations (called Harmonic Bias Estimator HBE, see ch. 8.6). These correction values have to be determined from a number of observations from previous orbits and are treated as additional input values to the wind retrieval, similar as the parameters for the response calibration. So the correction with the ground return  $v_{LOS,G}$  could be either performed using the ground-return velocity from the current (or latest valid) observation (or measurement) or a function depending on the latitude of the orbit and derived from the Harmonic Bias Estimator HBE (EADS-Astrium 2013 b, DLR 2018b). Optional corrections could be applied using the Mie ground return velocity from the current observation and a term accounting for known differences between the Mie and Rayleigh ground return.

	Document Nr. <b>AE-RP-DLR-L1B-001</b>	Issue: <b>4.4</b>	Date: <b>20.04.2018</b>	Page: <b>69/117</b>	
	Doc. Title: <b>ADM-Aeolus ATBD Level1B Products</b>				

Input Variable	Source	Description	Number of Values and Occurrence
$S_a(i,j,k)$	L1A Rayleigh MDS	16-bit digitized raw ACCD output from RSP per atmospheric range bin $i$ , pixel $j$ , and measurement $k$	20 pixel values per atmospheric range gate per measurement; 16 signal pixels and 4 offset pixels; background light in $i=25$
$S_l(j,n)$	L1A Reference Pulse MDS	16-bit digitized raw ACCD output from RSP for laser internal reference per pixel $j$ , and for each laser pulse $n$	20 pixel values per laser pulse
$\alpha_a, \beta_a, \gamma_a(R)$ $\gamma_{a,fit}(R)$	RRC auxiliary file	Rayleigh response intercept, sensitivity, non-linearity and fit-coefficients per response $R$ for atmospheric signal from RSP	1 value for intercept and sensitivity, 5 fit coefficients, 1 value per frequency step obtained during RRC
$\alpha_l, \beta_l, \gamma_l(R)$ $\gamma_{l,fit}(R)$	RRC auxiliary file	Rayleigh response intercept, sensitivity, and non-linearity and fit-coefficients per response $R$ for laser internal signal from RSP	1 value for intercept and sensitivity, 5 fit coefficients, 1 value per frequency step obtained during RRC
$\alpha_g, \beta_g, \gamma_g(R)$ $\gamma_{g,fit}(R)$	RRC auxiliary file	Rayleigh response intercept, sensitivity, and non-linearity and fit-coefficients per response $R$ for ground-return signal from RSP	1 value for intercept and sensitivity, 5 fit coefficients, 1 value per frequency step obtained during RRC
$v_{Los,s}$	L1A geolocation	LOS velocity from satellite	1 value per measurement 1 value per observation
$\varphi(i)$	L1A geolocation	incidence angle per range bin $i$	1 value per measurement and observation per atmospheric range bin $i$
$v_{Los,g}$	ZWC auxiliary file	residual LOS velocity from ground return	1 value per measurement 1 value per observation
$N, P$	L1A housekeeping	instrument settings for number of laser shots per measurement $P$ , number of measurements per observation $N$	1 value per observation for $N$ and $P$
$t_i, t_b$	L1A housekeeping	range bin time $t_i$ for Rayleigh atmospheric range bins and for background measurement $t_b$	24 values for atmospheric range bins per measurement and 1 value for background bin per measurement

**Table 8-1:** Input data, source and description for processing of Rayleigh spectrometer data to wind observations; for a detailed description see DPM (DoRIT and MDA 2017c) and IODD (DoRIT and MDA 2017b).

	Document Nr. <b>AE-RP-DLR-L1B-001</b>	Issue: <b>4.4</b>	Date: <b>20.04.2018</b>	Page: <b>70/117</b>	
	Doc. Title: <b>ADM-Aeolus ATBD Level1B Products</b>				

Input Variable	Source	Description	Number of Values and Occurrence
Validity Flags	L1A data quality	AOCS status flag data corrupted flag laser pulse validity flag	1 value per measurement for AOCS status data corrupted flag, 1 value per laser pulse for validity
$E_{RLC}(S)$	satellite characterisation file	Rayleigh Linearity Correction per signal level S	array of values
DCR	DCMZ auxiliary file	Dark Current Rate in LSB per pixel per second for Rayleigh	1 value
$\lambda_0$	satellite characterisation file	nominal laser wavelength	1 value
processor flag	processor settings	flag indicating, whether LOS or HLOS should be derived	1 value

**Table 8-1 (continued):** Input data, source and description for processing of Rayleigh spectrometer data to wind observations; for a detailed description see DPM (DoRIT and MDA 2017c) and IOOD (DoRIT and MDA 2017b).

Output Variable	Destination	Description	Number of Values and Occurrence
$v_{LOS,corr}(i)$ or $v_{HLOS,corr}(i)$	L1B	LOS or HLOS wind speed in $ms^{-1}$ per atmospheric range gate per observation	24 values per observation
$v_{LOS,corr}(i,k)$ or $v_{HLOS,corr}(i,k)$	L1B	LOS or HLOS wind speed in $ms^{-1}$ per atmospheric range gate per measurement k	24 values per measurement for a total of N measurements
PCD flag	L1B	flag indicating quality of the retrieved wind	24 values per observation 24 values per measurement for a total of N measurements
$v_{LOS,G}$	L1B	residual LOS wind speed in $ms^{-1}$ per observation from ground return bin	1 value per observation
$v_{LOS,G}(k)$	L1B	residual LOS wind speed in $ms^{-1}$ per measurement k from ground return bin	1 value per measurement for a total of N measurements

**Table 8-2:** Output data, source and description for processed Rayleigh spectrometer data; for a detailed description see DPM (DoRIT and MDA 2017c) and IOOD (DoRIT and MDA 2017b).

	Document Nr. <b>AE-RP-DLR-L1B-001</b>	Issue: <b>4.4</b>	Date: <b>20.04.2018</b>	Page: <b>71/117</b>	
	Doc. Title: <b>ADM-Aeolus ATBD Level1B Products</b>				

### 8.3 Wind Measurement Processing Mie

The basic algorithm for processing the data from the MSP is the determination of the centroid of the signal intensities from the 16 pixels of the ACCD, which can be interpreted as 16 frequency bins in case of the MSP. Therefore, the relation between the frequency and the output of 16 bins from the ACCD has to be used to convert from bin number to frequency. This relation is measured during the Mie Response Calibration MRC regularly, to cancel out drifts of the laser transmitter frequency and the Mie spectrometer with respect to each other. The output of the ACCD from the MSP can be considered as a frequency spectra, comparable to a frequency spectra obtained after a Fourier transformation of the signal from a coherent Doppler lidar. Thus, algorithms used for processing of frequency spectra of coherent Doppler lidar, radar or sodar (an overview is given by Reitebuch 1999) can be adapted to the algorithms of the MSP.

The experience from processing of frequency spectra from coherent Doppler lidar, radar and sodar can be adapted to obtain main baselines for processing the data from the MSP:

- Determination of centroid frequency from averaged frequency spectra gives lower random errors than the determination of mean frequency from centroid frequencies which are derived from a single frequency spectrum (coherent integration of spectra vs. incoherent averaging of frequencies)
  - The centroid determined from an averaged MSP frequency spectrum from one observation yields lower random errors than averaging of centroid frequencies from single measurement frequency spectra.
- Centroid determinations results in bias errors in case of non-constant, linear, or higher order offsets
  - Offsets from the Rayleigh signal on the MSP and from the background radiation on the MSP have to be subtracted before determination of the centroid; the detection chain offset is constant for each spectrum, but it needs to be subtracted to obtain a reliable signal and signal-to-noise estimate.
- Discretisation of a continuous frequency spectra into frequency bins results in artefacts (truncation and window effects)
  - Minimisation of discretisation artefacts necessary. This is mainly determined by the implementation and the characteristics of the MSP hardware, e.g. 16 pixels are used to represent the imaged frequency range of 1 USR (1 pixel  $\approx 105$  MHz =  $18.6$  ms<sup>-1</sup>), or effects as pixel response non-uniformity and change in FWHM of the response depending on pixel position. Different centroid estimators show different behaviour for these discretisation effects, and thus were studied and compared (DLR 2006, Paffrath 2006, DLR 2012g).
- Determination of centroid frequency from a frequency spectrum shows a strong non-linear behaviour with respect to the determination of a peak above the noise level
  - Non-linear relationship between signal-to-noise ratio SNR and random error and probability of gross errors. Thus, SNR thresholds and Quality-Control QC methods need to be applied for reliable wind estimates.
- Averaging of frequency spectra can be performed without introducing errors, if the boundaries of each frequency bin stay constant, mainly the boundary of the bin representing a zero-frequency are constant. The zero-frequency can vary from spectrum to spectrum due to a change in outgoing laser frequency, a change in spectral response of the MSP, or a change in the LOS velocity contribution from the satellite.
  - Either frequency spectra are normalised in the frequency axis before averaging, or frequency spectra are discarded, where a change in zero-frequency exhibits a defined threshold (current baseline for L1B processing). Averaging of frequency spectra from several laser pulses will result in spectral broadening of the averaged spectrum. The broadening can be introduced by laser frequency variations of the emitted pulse and of variations in the Doppler frequency shift induced by LOS wind variations due to turbulence effects (turbulent broadening).
- A centroid determination can be performed with several algorithms, all having different performance with respect to random and systematic error, quality-control possibilities, complexity or behaviour in case of outliers (Reitebuch 1999, Flamant et al. 2002, DLR 2006, Paffrath 2006, DLR 2012g). Therefore different algorithms could be considered

	Document Nr. <b>AE-RP-DLR-L1B-001</b>	Issue: <b>4.4</b>	Date: <b>20.04.2018</b>	Page: <b>72/117</b>	
	Doc. Title: <b>ADM-Aeolus ATBD Level1B Products</b>				

- Determination of first moment of spectra
- Determination of weighted first moment of spectra with different weights
- Maximising correlation with different correlation functions like Gaussian or Lorentzian (current baseline for L1B processing using Gaussian function in EADS-Astrium (2013))
- Maximum likelihood estimators
- Levenberg-Marquard non-linear curve fitting algorithms using different fit functions like Gaussian or Lorentzian
- Downhill simplex optimisation algorithm using different fit functions like Gaussian or Lorentzian (current baseline for L1B processing using Lorentzian function in EADS-Astrium (2013))
- Centroid determination and averaging of spectra is dependent on signal normalisation of spectra
  - no normalisation of spectra is performed => frequency spectra with high signal intensities dominate the signal contribution within an averaged spectrum, and frequency spectra with high noise dominate the noise contribution within an averaged spectrum (current baseline for L1B processing)
  - normalisation of spectra to the maximum value => the signal contribution from each spectrum is weighted equally, but frequency spectra with high noise dominate the averaged spectrum

From the above list, it is obvious that the selection and optimisation of a baseline algorithm for the MSP data is a complex task and includes several decisions and trade-offs between possible algorithmic steps. This was done by DLR (2006), Paffrath (2006), and DLR (2012g) with sensitivity analysis of different algorithms implemented in an end-to-end simulator of the instrument and atmosphere. The systematic error of different algorithms as well as the random error for different signal-to-noise-ratios (SNRs) was compared and used for further optimisation of the algorithm implementation.

In principle a centroid computation can be performed from data of one measurement and from the averaged frequency spectrum from one observation. The following subchapters describe the processing steps for each altitude range gate of the MSP. These processing steps have to be applied for each altitude range gate. The input data, source, and description for the processing of the measurements from the MSP is contained in Table 8-3 and the output products in Table 8.4. The symbols for the Mie signal processing are used equivalent as for the Rayleigh signal processing (range gate  $i$ , pixel index  $j$ , measurement index  $k$ , pulse index  $n$ , atmospheric index  $a$ , internal reference index  $l$ ): It has to be noted, that actually the signals are arising from 2 different ACCD detectors.

### 1) Quality Control QC and Averaging of Mie Frequency Spectra (similar to Rayleigh QC)

Due to the non-linear process of determination of a frequency spectral centroid, it is preferred to average frequency spectra from each measurement to one frequency spectrum of one observation. The algorithms and flags described in chapter 8.1.1 are used for that task.

No correction of the detection chain non-linearity is performed for the Mie signals, because the non-linearity in detection chain introduces only small errors for the centroid computation, because the non-linearity as measured for the Rayleigh chain is below 0.1%.

### 2) Summation of signals from measurements to observations (similar to Rayleigh signals)

The summation of laser internal reference signal to measurements and for both the internal and atmospheric signal to observations is performed for Mie signals before correction of offsets and background and before summation of the pixels from each range gate. As a result the frequency spectra for each range gate are summed up to measurements and observations. As the laser internal reference signal is acquired for each laser pulse, the corresponding signals from the internal reference for the duration of an atmospheric measurement with index  $k$  have to be summed up:

	Document Nr. <b>AE-RP-DLR-L1B-001</b>	Issue: <b>4.4</b>	Date: <b>20.04.2018</b>	Page: <b>73/117</b>	
	Doc. Title: <b>ADM-Aeolus ATBD Level1B Products</b>				

$$S_I(j, k) = \sum_{n_{\min,k}}^{n_{\max,k}} S_I(j, n) \quad (8.36)$$

Thus, for each atmospheric measurement with index k a corresponding internal reference spectrum (with pixel index j) with index k is determined. The wind retrieval is applied to signals on measurement level and after summation of a number of N measurements to one observation. Thus, both the atmospheric signals and the internal reference signals have to be summed up to obtain the Mie signal spectra (with pixel index j) per observation.

$$S_I(j) = \sum_{k=1}^{k=N} S_I(j, k) \quad (8.37)$$

$$S_a(i, j) = \sum_{k=1}^{k=N} S_a(i, j, k)$$

The following processing steps are applied in the same manner for a number of N measurements per observation and for each observation. For simplicity only the processing of the observations is described below (and the index k for each measurement is suppressed).

### 3) Correction of Detection Chain Offset

The centroid computation is sensitive to non-constant offsets of the signal. For the MSP the offset consists of the detection chain offset DCO and a signal contribution from the Rayleigh signal and the atmospheric background radiation. Although the DCO can be considered constant for all pixels, and would therefore not influence the centroid computation, it is subtracted, because the determination of the signal amplitude and SNR needs offset corrected signals. The detection chain offset is measured using “virtual” pixels of the ACCD, which are not illuminated. The mean of these pixel intensities can be used as a constant offset, which is subtracted from each spectral frequency bin. Thus a similar DCO offset correction as described for the Rayleigh signals in ch. 8.2 (step 2 without dark-current offset correction) is performed for the Mie signals. As the pixels number 19 and 20 can be used for each range gate ( $j_{DCO1}=19, j_{DCO2}=20$ ) the average of both pixels is used for DCO offset correction for Mie signals.

$$S_{a,DCO}(i, j) = S_a(i, j) - \frac{1}{2} [E_{a,DCO}(i, j_{DCO1}) + E_{a,DCO}(i, j_{DCO2})] \quad (8.38)$$

$$S_{I,DCO}(j) = S_I(j) - \frac{1}{2} [E_{I,DCO}(j_{DCO1}) + E_{I,DCO}(j_{DCO2})]$$

### 4) Correction of Tripod Obscuration for Mie spectra

The Fizeau interferometer is used as an imaging spectrometer. An optical element within the beam path will be imaged onto the ACCD of the MSP. The tripod of the telescope and the secondary mirror obscure part of the telescope optical aperture and are imaged onto the ACCD. This geometrical obscuration leads to a transmission loss, which is depending on the pixel position. As the orientation of the telescope tripod is known wrt to the ACCD image zone, the obscuration of every single pixel can be characterised on ground. The signal intensity of every pixel is divided by a correction factor, which is contained in the Tripod Obscuration  $C_{TOBS}(j)$  array containing 16 values for each pixel ranging from 0.88 to 1.0. A value of 0.88 is applied to the pixel in the centre of the frequency range USR ( $j=8$ ), because this pixel is blocked by the telescope secondary mirror. As the internal reference measurement is not affected by obscurations, this correction is only applied to atmospheric range gate measurements.

$$S_{a,TOBS}(i, j) = \frac{S_{a,DCO}(i, j)}{C_{TOBS}(j)} \quad (8.39)$$

	Document Nr. <b>AE-RP-DLR-L1B-001</b>	Issue: <b>4.4</b>	Date: <b>20.04.2018</b>	Page: <b>74/117</b>	
	Doc. Title: <b>ADM-Aeolus ATBD Level1B Products</b>				

## 5) Determination of Mie Spectra centroid

Several algorithms to determine the spectral centroid for the Mie signal were investigated by Paffrath (2006), DLR (2006) and DLR (2012g), e.g. simple centroid algorithms, Downhill Simplex Algorithm (DSA) with and without weights, Maximum Likelihood methods, or the “Levenberg-Marquardt” nonlinear data modelling algorithm. An algorithm using a downhill simplex optimisation procedure assuming a Lorentzian spectrum from the MSP was chosen to provide the optimum estimate wrt. random and systematic errors. Not only the spectra centroid is obtained with the algorithm, but also the signal amplitude, the spectral width FWHM, the constant offset and the residual fit error. In addition a faster correlation algorithm can be used alternatively. Both algorithms are implemented in the L1B Processor and are described below. It was shown that the DSA (without weights) has better performance in terms of errors than the correlation algorithm (DLR 2012 g). Thus the DSA is used as a baseline. It should be noted here, that both the processing of the Mie spectral data from the calibration mode MRC as well as the data from the wind mode have to be performed with the same algorithm and settings to avoid systematic errors.

The atmospheric signal after the TOBS-correction  $S_{a,TOBS}$  is composed of the narrowband Mie signal – a peak with significant signal over 3-4 pixels (FWHM is about 1.6 pixel) and the broadband Rayleigh signal, which can be assumed constant for all pixels. The signal contribution from the Rayleigh signal is the dominant offset contribution on the Mie frequency spectrum within the USR, assuming the Rayleigh signal is stronger than the background radiation. Therefore the background radiation measurement from the MSP is not used for offset correction. As the useful spectral range of the Mie spectrometer spans only  $\pm 0.36$  pm around the emitted laser wavelength  $\lambda_0$ , the Rayleigh signal within this bandwidth can be assumed as a constant (1.6 pm FWHM, see. Fig.3-4 and 4-3; a Gaussian function with FWHM of 1.6 pm ( $\sigma=0.68$  pm) is decreasing to  $0.87 \cdot \text{peak intensity}$  at the spectral positions of  $\pm 0.36$  pm). As both the broad bandwidth Rayleigh spectrum and the narrow bandwidth Mie spectrum are shifted by the same Doppler frequency, the centroids of both spectra are equal. Thus no systematic error arises from the broad bandwidth Rayleigh spectrum.

### 5a) Determination of Mie spectra centroid with correlation algorithm

This algorithm determines the correlation function between the measured Mie frequency spectra and a model function, which approximates the Mie frequency spectra. A Gaussian model function  $M(x)$  (as an approximation to the Lorentzian function with pixel position  $x=j$ ) is used for simplicity with an unknown centroid pixel position  $x_0$  on the ACCD. The determination of the centroid is performed with a fixed value for the spectral width  $\sigma_x$  of the Gaussian model function (e.g.  $\sigma_x=1.27$  pixel, FWHM=3 Pixel, which is larger than the actual width of the Mie spectrum on the ACCD with FWHM = 1.6 pixel), which is not varied through the correlation algorithm.

$$M(x) = \frac{1}{\sqrt{2\pi}\sigma_x} e^{-\frac{(x-x_0)^2}{2\sigma_x^2}} \quad (8.40)$$

As a constant offset is not included in the model function and determined with the correlation algorithm, it needs to be subtracted, before deriving the correlation function and the centroid computation. Thus a constant offset is estimated by determination the pixel  $j_{\min}$  where the signal intensity  $S_{a,TOBS}$  and  $S_{I,DCO}$  shows a minimum value (N.B. The minimum is also subtracted for the laser internal reference measurement, although the offset is not composed from a Rayleigh or background signal). This minimum signal is subtracted from each frequency pixel.

$$\begin{aligned} S_{a,\min}(i, j) &= S_{a,TOBS}(i, j) - S_{a,TOBS}(i, j_{\min}) \\ S_{I,\min}(j) &= S_{I,DCO}(j) - S_{I,DCO}(j_{\min}) \end{aligned} \quad (8.41)$$

For simplicity the next equations are shown for the signal  $S(x)$  depending on pixel position  $x=j$ , for both the internal reference signal  $S(x)=S_{I,\min}(j)$  and for the atmospheric signal per range gate  $i$  with  $S(x)=S_{a,\min}(i,j)$ . The cross-correlation function of signal  $S(x)$  with the model function  $M(x)$  is:

	Document Nr. <b>AE-RP-DLR-L1B-001</b>	Issue: <b>4.4</b>	Date: <b>20.04.2018</b>	Page: <b>75/117</b>	
	Doc. Title: <b>ADM-Aeolus ATBD Level1B Products</b>				

$$C(x) = \frac{1}{\sqrt{2\pi}\sigma_x} \int S(x) \cdot e^{-\frac{(x-x_0)^2}{2\sigma_x^2}} dx \quad (8.42)$$

The centroid of the Mie spectra is obtained at the pixel position, where the correlation function is maximized, thus its derivative is zero:

$$\frac{dC(x)}{dx} = -\frac{1}{\sqrt{2\pi}\sigma_x^3} \int S(x) \cdot (x-x_0) \cdot e^{-\frac{(x-x_0)^2}{2\sigma_x^2}} dx = 0 \quad (8.43)$$

This leads to an equation to derive  $x_0$ , which could be perceived as an equation for the first moment of the function  $S(x)$  weighted with the model function  $M(x)$ :

$$x_0 = \frac{\int x \cdot S(x) \cdot e^{-\frac{(x-x_0)^2}{2\sigma_x^2}} dx}{\int S(x) \cdot e^{-\frac{(x-x_0)^2}{2\sigma_x^2}} dx} \quad (8.44)$$

The integral representation of the functions is now replaced with the discrete approximation, because the function  $S(x)$  is only measured for a number of 16 pixels ranging from  $x_{\min}=1$  to  $x_{\max}=16$ .

$$x_0 = \frac{\sum_{x=x_{\min}}^{x=x_{\max}} x \cdot S(x) \cdot e^{-\frac{(x-x_0)^2}{2\sigma_x^2}}}{\sum_{x=x_{\min}}^{x=x_{\max}} S(x) \cdot e^{-\frac{(x-x_0)^2}{2\sigma_x^2}}} \quad (8.45)$$

An iterative approach is needed to solve the above equation, because the parameter  $x_0$  is still contained in the exponent of the model function. In order to provide a good estimate for the initial value  $x_{0,start}$  the first moment of the function  $S(x)$  is computed as a “centre of gravity” over the 16 pixels.

$$x_{0,start} = \frac{\sum_{x=x_{\min}}^{x=x_{\max}} x \cdot S(x)}{\sum_{x=x_{\min}}^{x=x_{\max}} S(x)} \quad (8.46)$$

The equation (8.45) is used with  $x_{0,start}=x_n$  to compute a new value for  $x_0=x_{n+1}$ . The iteration is stopped, if the absolute difference between  $|x_{n+1}-x_n|$  is below a threshold (e.g.  $10^{-3}$ ) or after a maximum number of iterations (e.g. 30).

	Document Nr. <b>AE-RP-DLR-L1B-001</b>	Issue: <b>4.4</b>	Date: <b>20.04.2018</b>	Page: <b>76/117</b>	
	Doc. Title: <b>ADM-Aeolus ATBD Level1B Products</b>				

$$x_{n+1} = \frac{\sum_{x=x_{\min}}^{x=x_{\max}} x \cdot S(x) \cdot e^{-\frac{(x-x_n)^2}{2\sigma_x^2}}}{\sum_{x=x_{\min}}^{x=x_{\max}} S(x) \cdot e^{-\frac{(x-x_n)^2}{2\sigma_x^2}}} \quad (8.47)$$

The main limitations of this algorithm are, that it is only providing the centroid position  $x_0$ , but without fitting the width of the spectrum, the amplitude or the constant offset. Another limitation is the use of a Gaussian model function, which is only an approximation to the real Mie signal on the ACCD. The signal from a Fizeau fringe on the ACCD would be better approximated by a Lorentzian (or even an Airy-Function to account for its periodicity) and secondly the effect of the aperture broadening through the discrete pixels is not taken into account. Thus the centroid computation shows some oscillating behaviour with pixel position (see DLR 2006, Paffrath 2006, DLR 2012g). But this is calibrated for the wind retrieval through use of the non-linearity correction from the MRC mode. The main advantage of this correlation algorithm is its robustness wrt to noisy signal (random and artefacts) and the fast computation time.

### 5b) Determination of Mie spectra centroid with Downhill-Simplex Algorithm

A second algorithm was developed, tested and optimized based on a Downhill-Simplex nonlinear optimisation algorithm DSA (also called Nelder-Mead algorithm after Nelder and Mead 1965, Press et al. 1992) to derive the centroid of the Mie spectrum. In addition this algorithm determines the spectral width of the Mie peak, the peak height, and the Rayleigh offset, which is used for the determination of the scattering ratio and SNR, and quality flags. This second algorithm is only used, if the Mie SNR is above a certain threshold (e.g. 10), in order to save extensive computation times with an iterative approach. The Mie spectrum on the ACCD is approximated by a Lorentzian function with peak position  $x_0$ , peak width  $\Delta x$  (as FWHM value), peak height  $A$  and a constant offset  $C$ .

$$M(x) = A \cdot \frac{\Delta x^2}{4 \cdot (x - x_0)^2 + \Delta x^2} + C \quad (8.48)$$

As the parameters peak height  $A$  and the constant offset  $C$  are only linearly included in the model function  $M(x)$ , these are determined by solving a linear equation first. Within the downhill simplex optimisation algorithm only the peak position  $x_0$  and peak width  $\Delta x$  are determined, with fixed peak height and offset  $C$ . This has the advantage that only 2 parameters need to be varied during the non-linear optimisation process rather than 4.

First the minimum value is subtracted from the TOBS and DCO corrected signals as in eq. (8.41).

$$\begin{aligned} S_{a,\min}(i, j) &= S_{a,TOBS}(i, j) - S_{a,TOBS}(i, j_{\min}) \\ S_{I,\min}(j) &= S_{I,DCO}(j) - S_{I,DCO}(j_{\min}) \end{aligned} \quad (8.49)$$

For simplicity here also the signal from both the atmospheric range gates  $S_{a,\min}$  and the internal reference  $S_{I,\min}$  is called  $S(x)$  after minimum subtraction  $S_{\min}(x_{\min})$  with 16 discrete values for the pixel position  $x$ . The spectrum is now normalized to its maximum value  $S(x_{\max})$  with the pixel position  $x_{\max}$ :

$$S_{norm}(x) = \frac{S(x)}{S(x_{\max})} \quad (8.50)$$

As a starting value for the peak position  $x_{0,start}$  is needed, the centroid is computed using the two adjacent pixel values around the maximum  $S(x_{\max-1})$ ,  $S(x_{\max})$ , and  $S(x_{\max+1})$ :

	Document Nr. <b>AE-RP-DLR-L1B-001</b>	Issue: <b>4.4</b>	Date: <b>20.04.2018</b>	Page: <b>77/117</b>	
	Doc. Title: <b>ADM-Aeolus ATBD Level1B Products</b>				

$$x_{0,start} = \frac{\sum_{x=x_{\max}-1}^{x=x_{\max}+1} x \cdot S(x)}{\sum_{x=x_{\min}-1}^{x=x_{\max}+1} S(x)} \quad (8.51)$$

As the spectral width  $\Delta x$  of the signal is only slightly varying for internal and atmospheric signal, a pre-defined value  $\Delta x_{start}$  can be used.

The measured Mie spectrum  $S(x_j)$  is only obtained for 16 discrete pixels  $x_j$ . Nevertheless the imaged fringe from the Fizeau interferometer and the Lorentzian model  $M(x)$  is a continuous function and can be computed for a number of  $N$  discrete pixel positions ( $N=16 \cdot n_s$  with  $n_s$  number of subsamples  $s$  per pixel, typically  $n_s=5$ ), in order to take into account the discretization of a continuous Mie fringe (Lorentzian) on discrete ACCD pixels ("aperture broadening" or "pixel broadening"). Thus the continuous model function  $M(x)$  is now derived for a number of  $n_s$  discrete subsamples per pixel and the resulting values of  $M(x)$  from 1 pixel are averaged to obtain a "pixelated" or discrete Model function  $M_p(x_j)$ :

$$M_p(x_j) = \frac{1}{n_s} \sum_{k=1}^{n_s} \frac{\Delta x^2}{4 \cdot (x_j - 0.5 + \frac{k}{n_s} - \frac{1}{2n_s} - x_0)^2 + \Delta x^2} \quad (8.52)$$

The model function is calculated for each pixel  $x_j$  ( $x_j=1$  to 16) for a number of subpixels  $n_s$  (from  $k=1$  to  $n_s$ ); for the first pixel  $x_j=1$  and  $n_s=5$  the Model function is derived at positions 0.6, 0.8, 1.0, 1.2, and 1.4. Thus  $M_p(x_j=1)$  is the average Lorentzian function  $M(x)$  for pixel positions 0.5 to 1.5 and accordingly for  $x_j$  up to 16. The function  $M_p(x_j)$  is valid for a peak height of  $A=1$  and an offset  $C=0$ . The model function including the parameters  $A$  and  $C$  can be written as

$$M_{p,A,C}(x_j) = A \cdot M_p(x_j) + C \quad (8.53)$$

Now the 4 parameters describing the pixelated Lorentzian model function  $M_{p,A,C}(x)$  are determined within an iterative algorithm (iteration number  $n$ ) and  $x_{n=1} = x_{0,start}$  and  $\Delta x_{n=1} = \Delta x_{start}$  (a value of  $\Delta x_{start}=1.6$  pixel is chosen, which should equal the Mie fringe on the ACCD of 159 MHz; it should be noted here that the performance of the DSA to derive the width  $\Delta x$  depends on the start value for the width  $\Delta x_{start}$  of the spectrum, see e.g. DLR 2012g).

1. Determination of the peak height  $A_n$  and offset  $C_n$  by solving a linear system of equations using the pixelated model function  $M_{p,A,C}(x_j)$  with the start values for  $x_{0,start}$ ,  $\Delta x_{start}$  (for the first iteration) and  $x_n$ ,  $\Delta x_n$  from the previous iteration. The solution for the squared difference  $\chi^2$  (chi-square) between the model function  $M_{p,A,C}(x_j)$  and the normalized spectrum  $S_{norm}(x_j)$  can be determined analytically for fixed values of  $x_0$  and  $\Delta x$ :

$$\chi^2(A_n, C_n) = \sum_{x_j=1}^{16} [A_n \cdot M_p(x_j) + C_n - S_{norm}(x_j)]^2 \quad (8.54)$$

This is equivalent to find the linear fit parameters (slope  $A_n$  and intercept  $C_n$ ) and can be obtained with the following set of equations (linear regression analysis):

$$\begin{pmatrix} \sum_{j=1}^{16} M_p^2(x_j) & \sum_{j=1}^{16} M_p(x_j) \\ \sum_{j=1}^{16} M_p(x_j) & 16 \end{pmatrix} \cdot \begin{pmatrix} A_n \\ C_n \end{pmatrix} = \begin{pmatrix} \sum_{j=1}^{16} S_{norm}(x_j) \cdot M_p(x_j) \\ \sum_{j=1}^{16} S_{norm}(x_j) \end{pmatrix} \quad (8.55)$$

Thus,  $A_n$  and  $C_n$  are obtained after solving these equations.

	Document Nr. <b>AE-RP-DLR-L1B-001</b>	Issue: <b>4.4</b>	Date: <b>20.04.2018</b>	Page: <b>78/117</b>	
	Doc. Title: <b>ADM-Aeolus ATBD Level1B Products</b>				

- Applying the DSA with fixed  $A_n$  and  $C_n$ , and using  $x_{0,start}$ ,  $\Delta x_{start}$  (for the first iteration) and  $x_n$ ,  $\Delta x_n$  from the previous iteration and determine the values for  $x_{n+1}$ ,  $\Delta x_{n+1}$ . The DSA searches for the values of  $x_n$ ,  $\Delta x_n$  which minimize the squared difference  $\chi^2$  between the pixelated Lorentzian  $M_{p,A,C}(x_j)$  and the measured normalized signal  $S_{norm}(x_j)$ . This is similar to a least-square fitting algorithm, but rather an optimization algorithm is used for this purpose. The minimum of the chi-square function  $\chi^2$  is determined by the DSA for the parameters  $x_n$  and  $\Delta x_n$ :

$$\begin{aligned} \chi^2(x_0, \Delta x) &= \sum_{x_j=1}^{16} \left[ A_n \cdot M_p(x_j, x_0, \Delta x) + C_n - S_{norm}(x_j) \right]^2 \\ &= \sum_{x_j=1}^{16} \left[ \frac{A_n}{n_s} \sum_{k=1}^{n_s} \frac{\Delta x^2}{4 \cdot (x_j - 0.5 + \frac{k}{n_s} - \frac{1}{2n_s} - x_0)^2 + \Delta x^2} + C_n - S_{norm}(x_j) \right]^2 \end{aligned} \quad (8.56)$$

The DSA is a type of optimization algorithms, which searches for the optimal values of peak position  $x_0$ , peak width  $\Delta x$ , for the squared difference between a model function (“pixelated Lorentzian”) and the measured signal on the Mie ACCD. The term simplex refers to a geometrical body with  $n+1$  vertices in an  $n$ -dimensional space. Hence in our case of only 2 unknowns (2-dimensional space) a body with 3 vertices (“triangle”) is used. The simplex (“triangle”) encloses the optimum solution (for centroid  $x_0$  and peak width  $\Delta x$ ). For each calculation step the corners of the simplex are analysed and the worst one is replaced by another, by applying a series of operations on the simplex (called “reflection”, “expansion”, “contradiction”, “reduction”) to find the optimal solution. The control parameters as reported by Nelder and Mead (1965) are used in our implementation. In contrast to other non-linear least-square fitting procedures (e.g. Levenberg-Marquard) there is no need to derive the derivative of the fitting function for the DSA. This is an advantage of the method asserting safer convergence.

The optimum search in the Downhill Simplex algorithm is terminated, if the minimum decrease in the residual error  $\chi^2(x_{0,n+1}, \Delta x_{n+1})$  between 2 iterations is below a threshold (e.g.  $10^{-3}$ ) or the number of iterations are higher than a threshold (e.g. 50). As a result new values for  $x_{n+1}$ ,  $\Delta x_{n+1}$  are obtained from the DSA.

- The iterations with step 1 (linear fit) and 2 (nonlinear fit) are continued until function  $\chi^2(x_{0,n+1}, \Delta x_{n+1}, A_n, C_n)$  is below a certain threshold (e.g.  $10^{-3}$ ), or the number of iterations are higher than a predefined threshold for the maximum number of iteration (e.g. 30), or the residual error  $\chi^2$  does not change between subsequent iterations (e.g. difference below  $10^{-8}$ ).

The results from the iterative approach are values for peak position  $x_{n+1}$ , width  $\Delta x_{n+1}$ , peak height  $A_n$  and  $C_n$ : As the iterative algorithm was performed using normalized signals  $S_{norm}(x)$  to the maximum, and the minimum value was subtracted, this has to be re-normalized:

$$\begin{aligned} A &= A_n \cdot S_{max}(x_{max}) \\ C &= C_n + S_{min}(x_{min}) \end{aligned} \quad (8.57)$$

The centroid position  $x_{n+1}$  from both the Mie algorithms (correlation and DSA) are called subsequently Mie response  $R_i$  for the internal reference signal and  $R_a(i)$  for the atmospheric signal of range gate  $i$  to use the same terminology as for the Rayleigh channel processing.

$$\begin{aligned} R_i &= x_{n+1} \text{ for internal reference signal} \\ R_a(i) &= x_{n+1} \text{ for atmospheric range gates } i \end{aligned} \quad (8.58)$$

Nevertheless it should be noted that a Mie response is in units of pixel position, while the Rayleigh response is unitless. The determined centroid is in units of pixel index, which has to be converted to frequency using the response curves obtained during the instrument calibration mode MRC.

	Document Nr. <b>AE-RP-DLR-L1B-001</b>	Issue: <b>4.4</b>	Date: <b>20.04.2018</b>	Page: <b>79/117</b>	
	Doc. Title: <b>ADM-Aeolus ATBD Level1B Products</b>				

## 6) Correction for Response Non-Linearity

The result of the centroid computation from step 5) is a value in units of pixels on the ACCD, called Mie response (equivalent to the Rayleigh response). This centroid in units of pixels needs to be converted in a centroid in units of frequency. This is performed by using the parameters derived from the Mie response calibration MRC, which is establishing a relationship between centroid frequency and centroid pixel position for a narrowband Mie signal observed on the Mie ACCD. The almost linear relationship between pixel position and frequency is approximated by a linear function with slope  $\alpha$  (in units of MHz/pixel) and intercept  $\beta$  (in units of pixel). The deviation of the observed pixel position from the linear fit function is called non-linearity  $\gamma$  (in units of pixel).

This is an equivalent approach as for the Rayleigh channel. The MRC parameters are derived for the internal reference signal and the atmospheric signal separately; the signal return from the ground is used as a representative signal for the atmospheric optical path. Although both the internal and the atmospheric path are illuminated by narrowband Mie signals, both parameter sets are derived independently for internal and atmospheric path, because of small differences in the optical paths in front of the MSP. In contrast to the Rayleigh channel, where the non-linearity function can be approximated by a polynomial function, this approach is not chosen for the Mie channel. The slowly varying variations of the Mie response could be approximated by a polynomial, because this is mainly caused by edge effects for large frequency offsets, where the Mie signal fringe is only partly visible on the ACCD. But in addition a higher-frequency variation is present on the Mie response signal with a variation from pixel-to-pixel due to the coarse frequency resolution of the ACCD (1 pixel about 100 MHz); thus each pixel acts as an aperture, as the Mie signal is not constant over 1 pixel. This would cause a sinusoidal variation of the response with a periodicity of 1 pixel, which could be also modelled. But the response of each pixel to the incoming photon flux is not equal (expressed in a quantity called pixel-response non-uniformity, which is in the order of several %) and the Fizeau interferometer optical aperture is not uniform. Thus the sinusoidal variation is varying with each pixel and no model function was derived up to now, which would be sufficiently determined to model the Mie response non-linearity.

Thus a different approach is used for correcting the Mie response non-linearity, which does not use a model function to decrease the random noise from the measurements during MRC. The derived non-linearity  $\gamma(R)$  from the observation is used directly for correction in the wind retrieval:

$$\begin{aligned}
 R_{I,cor} &= R_I - \gamma_I(R_I) \\
 R_{a,cor}(i) &= R_a(i) - \gamma_a(R_a(i))
 \end{aligned}
 \tag{8.59}$$

The function  $\gamma_I$  and  $\gamma_a$  are available for values  $R_I$  and  $R_a$  obtained during the MRC mode. The MRC mode responses are available for 40 discrete frequency steps (and response values) with a frequency step of 25 MHz (about 4 frequencies per pixel, about 0.25 pixel units) over the frequency range of  $f_0 \pm 500$  MHz. Thus also the functions  $\gamma_I(R_I)$  and  $\gamma_a(R_a)$  are only available at discrete steps. During wind measurement mode the values of  $R_I$  or  $R_a$  are not discrete. Thus a linear interpolation from the two next discrete values (from MRC) is used to obtain the non-linearity correction function  $\gamma_I(R_I)$  and  $\gamma_a(R_a)$  during wind mode.

Now the corrected responses  $R_{I,cor}$  and  $R_{a,cor}$  are only linearly depending on the frequency difference  $\Delta f$ :

$$\begin{aligned}
 R_{I,cor} &= \alpha_I + \beta_I \cdot \Delta f_I \\
 R_{a,cor}(i) &= \alpha_a + \beta_a \cdot \Delta f_a(i)
 \end{aligned}
 \tag{8.60}$$

Thus it is obvious that the same approach and equations are used for correction of the response non-linearity and deriving the frequency from the Mie response signal (in units of pixel) as applied for the Rayleigh response signals (in arbitrary units). The difference here is that the non-linearity is used directly from the MRC observations without applying a polynomial fit function.

	Document Nr. <b>AE-RP-DLR-L1B-001</b>	Issue: <b>4.4</b>	Date: <b>20.04.2018</b>	Page: <b>80/117</b>	
	Doc. Title: <b>ADM-Aeolus ATBD Level1B Products</b>				

## 7) Determination of the Doppler frequency shift

Now the determination of the frequency of the internal reference and the atmospheric range gates is straightforward (and equal as for the Rayleigh derivations):

$$f_I = \frac{R_{I,cor} - \alpha_I}{\beta_I} + f_0 = \frac{R_I - \alpha_I - \gamma_I(R_I)}{\beta_I} + f_0 \quad (8.61)$$

$$f_a(i) = \frac{R_{a,cor}(i) - \alpha_a}{\beta_a} + f_0 = \frac{R_a(i) - \alpha_a - \gamma_a(R_a(i))}{\beta_a} + f_0$$

The offset frequency  $f_0$  is equal for both the internal reference and atmospheric range gates and is therefore eliminated, when calculating the Doppler frequency shift  $\Delta f(i)$  per range gate i:

$$\Delta f(i) = f_a(i) - f_I = \frac{R_a(i) - \alpha_a - \gamma_a(R_a(i))}{\beta_a} - \frac{R_I - \alpha_I - \gamma_I(R_I)}{\beta_I} \quad (8.62)$$

## 8) Determination of LOS and HLOS wind speed

The LOS wind speed and the HLOS wind speed, which is the projection to the horizontal plane with the altitude dependent incidence angle  $\varphi(i)$ , is derived using the Doppler shift equation:

$$v_{LOS}(i) = \frac{\lambda_0}{2} \cdot (f_a(i) - f_I) - v_{LOS,S}(i)$$

$$= \frac{\lambda_0}{2} \cdot \left[ \frac{R_a(i) - \alpha_a - \gamma_a(R_a(i))}{\beta_a} - \frac{R_I - \alpha_I - \gamma_I(R_I)}{\beta_I} \right] - v_{LOS,S}$$

$$v_{HLOS}(i) = \frac{1}{\sin(\varphi(i))} v_{LOS}(i)$$

$$= \frac{1}{\sin(\varphi(i))} \left[ \frac{\lambda_0}{2} \cdot \left[ \frac{R_a(i) - \alpha_a - \gamma_a(R_a(i))}{\beta_a} - \frac{R_I - \alpha_I - \gamma_I(R_I)}{\beta_I} \right] - v_{LOS,S} \right] \quad (8.63)$$

with the correction of the satellite-induced Doppler shift velocity  $v_{LOS,S}$  (in  $\text{ms}^{-1}$ ). The incidence angle  $\varphi(i)$  and the satellite induced Doppler shift velocity  $v_{LOS,S}$  is obtained using the AOCS sensors and algorithms.

## 9) Correction for residual ground speed

The derivation of the residual ground return wind frequency  $\Delta f(g)$  and wind speed  $v_{LOS}(g)$  is very similar as for the Rayleigh channel (for a more detailed discussion see Chapter 8.2, step 9). Thus here only the differences in both derivations are discussed and the equations are presented.

The detection of atmospheric range gates, which contain a ground return signal is described in detail in chapter 8.6. The processing of the raw ACCD output  $S_a(i=g,j,k)$  from the range gates containing ground signal ( $i=g$ ) is applied up to step 6 to obtain the Mie response  $R_a(i=g)$ . The parameters from the MRC mode for an atmospheric signal are obtained from the ground returns. Thus these parameters  $\alpha_a$ ,  $\beta_a$  and  $\gamma_a$  can be used also for the retrieval of the ground return frequency, and no distinction between atmospheric signal and ground needs to be made for these parameters as done for the Rayleigh channel processing. The frequency shift of the ground return is obtained from

	Document Nr. <b>AE-RP-DLR-L1B-001</b>	Issue: <b>4.4</b>	Date: <b>20.04.2018</b>	Page: <b>81/117</b>	
	Doc. Title: <b>ADM-Aeolus ATBD Level1B Products</b>				

$$\Delta f(g) = f_a(g) - f_I = \frac{R_a(g) - \alpha_a - \gamma_a(R_a(g))}{\beta_a} - \frac{R_I - \alpha_I - \gamma_I(R_I)}{\beta_I} \quad (8.64)$$

In the next step the residual velocity of the ground return measurement is derived. As the ground-return velocity is derived for each measurement (and not for each observation), it must be noted here, that the internal reference response  $R_I$  and the satellite component for the corresponding measurement  $k$  has to be used here.

$$v_{LOS}(g) = \frac{\lambda_0}{2} \cdot \Delta f(g) - v_{LOS,S}(g) = \frac{\lambda_0}{2} \cdot \left[ \frac{R_a(g) - \alpha_g - \gamma_g(R_a(g))}{\beta_g} - \frac{R_I - \alpha_I - \gamma_I(R_I)}{\beta_I} \right] - v_{LOS,S}(g) \quad (8.65)$$

The residual LOS wind speed from the ground return is derived per measurement and the averaging is performed using the retrieved LOS wind speeds (and not the signals as for atmospheric range gates):

$$v_{LOS,G} = \frac{1}{N} \sum_{k=1}^N v_{LOS,G}(k) \quad (8.66)$$

If the number of ground-return measurements is too low or even zero, then no valid value for the observation can be derived. In this case the latest valid value for a ground-return velocity is used for the subsequent correction. This residual LOS wind speed  $v_{LOS,G}$  is used as an additional term in the wind retrieval to correct for any offsets:

$$\begin{aligned} v_{LOS,corr}(i) &= v_{LOS}(i) - v_{LOS,G} \\ &= \frac{\lambda_0}{2} \cdot \left[ \frac{R_a(i) - \alpha_A - \gamma_a(R_a(i))}{\beta_A} - \frac{R_I - \alpha_I - \gamma_I(R_I)}{\beta_I} \right] - v_{LOS,S}(i) - v_{LOS,G} \\ v_{HLOS,corr}(i) &= \frac{1}{\sin(\varphi(i))} \left[ v_{LOS}(i) - v_{LOS,G} \right] \\ &= \frac{1}{\sin(\varphi(i))} \left[ \frac{\lambda_0}{2} \cdot \left[ \frac{R_a(i) - \alpha_A - \gamma_a(R_a(i))}{\beta_A} - \frac{R_I - \alpha_I - \gamma_I(R_I)}{\beta_I} \right] - v_{LOS,S}(i) - v_{LOS,G} \right] \end{aligned} \quad (8.67)$$

Similar as for the Rayleigh wind processing the value of  $v_{LOS,G}$  could be used from the current (or latest valid) observation or from a function depending on the latitude of the observation, which is derived from the HBE. It must be noted here that the values for  $v_{LOS,G}$  or the model function from the HBE is different for the Rayleigh and Mie ground returns. If the reason for a non-zero ground-return would be caused by satellite mispointing or AOCS errors (leading to wrong values of  $v_{LOS,S}$ ) then the residual of  $v_{LOS,G}$  would be equal for Rayleigh and Mie. But the reason for non-zero ground returns could be also specific to the optical paths in the MSP and RSP and the derived parameters from the RRC and MRC and the response from the wind mode. Thus the residual ground-return values are different for Mie and Rayleigh winds (see also DLR (2012a) and Marksteiner (2012)).

	Document Nr. <b>AE-RP-DLR-L1B-001</b>	Issue: <b>4.4</b>	Date: <b>20.04.2018</b>	Page: <b>82/117</b>	
	Doc. Title: <b>ADM-Aeolus ATBD Level1B Products</b>				

Input Variable	Source	Description	Number of Values and Occurrence
$S_a(i,j,k)$	L1A Mie MDS	16-bit digitized raw ACCD output from MSP per atmospheric range bin $i$ , pixel $j$ , and measurement $k$	20 pixel values per atmospheric range gate per measurement; 16 signal pixels and 4 offset pixels; background light in $i=25$
$S_l(j,n)$	L1A Reference Pulse MDS	16-bit digitized raw ACCD output from MSP for laser internal reference per pixel $j$ , and for each laser pulse $n$	20 pixel values per laser pulse
$\alpha_a, \beta_a, \gamma_a(R)$	MRC auxiliary file	Mie response slope, zero frequency, non-linearity for atmospheric signal (ground) from MSP	1 value obtained during MRC for slope and zero frequency, 1 value per frequency bin of MSP obtained during MRC
$\alpha_l, \beta_l, \gamma_l(R)$	MRC auxiliary file	Mie response slope, zero frequency, non-linearity for laser internal signal from MSP	1 value obtained during MRC for slope and zero frequency, 1 value per frequency bin of MSP obtained during MRC
$V_{Los, S}$	L1A geolocation	LOS velocity from satellite	1 value per measurement 1 value per observation
$\varphi(i)$	L1A geolocation	incidence angle per range bin $i$	1 value per atmospheric bin per observation and measurement
$V_{Los, Gro}$	ZWC auxiliary file	residual LOS velocity from ground return	1 value per measurement 1 value per observation
$N, P$	L1A housekeeping	instrument settings for number of laser shots per measurement $P$ , number of measurements per observation $N$	1 value per observation for $N$ and $P$
$t_i, t_b$	L1A housekeeping	range bin time $t_i$ for atmospheric range bins Mie and for background measurement $t_b$	24 values for atmospheric range bins per measurement and 1 value for background bin per measurement
validity flags	L1A data quality	spacecraft on target flag data corrupted flag laser lock status flag	1 value per measurement for spacecraft on target and data corrupted flag 1 value per laser pulse for cavity lock status flag
TOBS	Satellite characterisation file	Mie Tripod Obscuration Data	1 value for Mie frequency pixel with a total of 16
DCR	DCMZ auxiliary file	Dark Current Rate in LSB per pixel per second for Mie	1 value
$\lambda_0$	Satellite characterisation file	nominal laser wavelength	1 value
processor flag	processor settings	flag indicating, whether LOS or HLOS should be derived	1 value

**Table 8-3:** Input data, source and description for processing of Mie spectrometer data to wind observations; for a detailed description see DPM (DoRIT and MDA 2017c) and IOOD (DoRIT and MDA 2017b).

	Document Nr. <b>AE-RP-DLR-L1B-001</b>	Issue: <b>4.4</b>	Date: <b>20.04.2018</b>	Page: <b>83/117</b>	
	Doc. Title: <b>ADM-Aeolus ATBD Level1B Products</b>				

Output Variable	Destination	Description	Number of Values and Occurrence
$v_{LOS,corr(i)}$ or $v_{HLOS,corr(i)}$	L1B	LOS or HLOS wind speed in $ms^{-1}$ per atmospheric range gate per observation	24 values per observation
$v_{LOS,corr(i,k)}$ or $v_{HLOS,corr(i,k)}$	L1B	LOS or HLOS wind speed in $ms^{-1}$ per atmospheric range gate per measurement k	24 values per measurement for a total of N measurements
PCD flag	L1B	flag indicating quality of the retrieved wind	24 values per observation 24 values per measurement for a total of N measurements
$v_{LOS,G}$	L1B	residual LOS wind speed in $ms^{-1}$ per observation from ground return bin	1 value per observation
$v_{LOS,G(k)}$	L1B	residual LOS wind speed in $ms^{-1}$ per measurement k from ground return bin	1 value per measurement for a total of N measurements

**Table 8-4:** Output data, source and description for processed Mie spectrometer data; for a detailed description see DPM (DoRIT and MDA 2017c) and IODD (DoRIT and MDA 2017b).

	Document Nr. <b>AE-RP-DLR-L1B-001</b>	Issue: <b>4.4</b>	Date: <b>20.04.2018</b>	Page: <b>84/117</b>	
	Doc. Title: <b>ADM-Aeolus ATBD Level1B Products</b>				

## 9 Instrument Response Calibration

This chapter discusses the processing of the data from the instrument response calibration (IRC) mode (ch. 4.7.3) from the Mie spectrometer (MSP) – called Mie response calibration (MRC) and from the Rayleigh spectrometer (RSP) – called Rayleigh response calibration (RRC). The need for a response calibration and the two approaches for L1B and L2B wind products are outlined in ch. 8.1.3. Here the specific processing of IRC mode data is described in detail.

For the IRC mode the complete satellite is rotated around its roll axis to point in nadir mode (Fig. 4.6). The actual off-nadir angle is not exactly  $0^\circ$ , but slightly offset for an angle of several mrad. The reason is to avoid high specular reflections from the water surfaces (e.g. from lakes with calm wind conditions), which could saturate the detector with detrimental effects. It is planned to perform the IRC mode once per week, with duration of about 45 minutes (1/2 of an orbit). This includes the duration of rolling the satellite to nadir and back (about 30 minutes) and the duration of the IRC mode of 15 minutes.

During the IRC mode the laser frequency is tuned in discrete steps of 25 MHz over a frequency range of 1 GHz around the centre frequency  $f_c$  of the Mie useful spectral range ( $R_{\text{Mie,centre}}=8.5$  pixel) and the Rayleigh filter crossing point ( $R_{\text{Ray,centre}}=0$ ) for the internal path. This centre laser frequency is determined via the Instrument Spectral Registration (ISR) mode (ch. 4.7.3). As the laser frequency can be only changed in steps of 25 MHz, the centring on the Mie and Rayleigh spectrometers can be only achieved within  $\pm 12.5$  MHz. Thus the centring is performed for a frequency  $f_0$ , which is close to the actual  $f_{\text{centre}}$  for Mie and Rayleigh  $f_0 \approx f_{\text{centre}}$ . Subsequently only the relative frequency offset to the absolute frequency  $f_0$  is used  $\Delta f_0 = f - f_0$ , because the absolute laser frequency is not monitored within ALADIN during wind mode and IRC (in contrast to the A2D (DLR 2017b)). It is important to recognize that the relative laser frequency  $\Delta f_0$  is used in the processing of the IRC mode is a commanded frequency and not an actual, measured frequency. Thus this frequency is called commanded frequency  $f_{\text{com}}$ . As only 40 frequency steps are commanded for the IRC mode the relative laser frequency  $\Delta f_0 = f_{\text{com}}$  is tuned from +0.5 GHz to -0.475 GHz in steps of 25 MHz. The laser frequency is changed from one step to the other step every second observation, which results in a number of 81 observations for the IRC mode: 2 times 40 observations plus 1 observation to ensure that each frequency step consists of 2 observations. The change in frequency by 25 MHz is fast compared to the duration of 1 measurement of 0.4 s (with the nominal setting of  $P=20$ ,  $N=30$ ) and is commanded within one measurement.

For each frequency step the internal reference signal and atmospheric signal for both the Mie and Rayleigh spectrometers is recorded. The objective of the IRC is to obtain the linear response parameters intercept  $\alpha$  and slope  $\beta$  (or sensitivity) and the non-linear part  $\gamma$  (or residual) for both Mie and Rayleigh internal and atmospheric signal, which is used for the wind retrieval (ch. 8.1.3) and introduced in eq. 8.6. From the atmospheric signals the range gates, which contain the narrow bandwidth signal return from the earth surface (e.g. ocean, land, ice) – called ground return is used for MRC and RRC processing. In addition the atmospheric range gates from higher altitudes (e.g. between 6 and 16 km) are used for RRC to obtain the response parameters for a broad bandwidth molecular return. The linear and non-linear parameters derived from the internal signal during IRC mode are used during wind mode for the internal reference. The IRC parameters from the ground returns are used for ground velocity derivation in wind mode. The atmospheric wind velocity during wind mode is derived from the parameters of the atmospheric range gates from RRC and from the ground returns from MRC.

Both the internal and atmospheric path signals are needed independently from the IRC mode to derive the linear and non-linear parameters used in wind mode. The illumination of the Mie and Rayleigh spectrometer differs slightly for the internal and atmospheric path, which will result in different responses and thus different linear and non-linear parameters from the IRC mode. Thus the IRC mode is needed to characterize the instrument response function from the atmospheric path, which is also used for L2B wind products (ECMWF 2017b). Due to the difference in illumination, it would be not sufficient to derive the parameters for the atmospheric path only from internal reference measurements, e.g. using only the spectrometer characterisation during ISR mode (ch. 4.7.3).

As the internal and atmospheric signals are needed independently in IRC mode, the internal reference signal cannot be used for a differential approach as during wind mode (using the difference of the atmospheric and internal reference signal for deriving the Doppler frequency shift, eq. 8.2). This differential approach during wind mode is used to avoid dependency on the absolute laser frequency and possible absolute laser frequency drifts. Thus the IRC mode is depending on the absolute laser frequency and possible laser

frequency drifts during the duration of the IRC. Thus, high absolute laser frequency stability has to be ensured during the duration of an IRC mode, in addition to the pulse-to-pulse frequency stability, which is relevant for the wind mode random error. A linear drift in laser frequency during the 15 minutes of an IRC would directly influence the determination of the slope for the internal and atmospheric path, whereas any non-linear drift of laser frequency is imprinted on the non-linearity part of the response function.

Due to the importance of obtaining high quality ground return signals for the IRC mode, these calibrations are performed over surfaces with high albedo in the UV. This is preferably over snow and ice surfaces in the polar regions of the Arctic (Northern Hemisphere winter) and Antarctic (all year). A global map of monthly albedo values derived from the ADAM database (Noveltis 2013), which is based on a climatology for the year 2005, is used to assess the quality of IRC mode observations with end-to-end simulations (DLR 2018b). As the actual duration of the tuning of the laser frequencies during IRC is about 15 minutes (1/6 orbit) the region of Antarctica is preferred for IRC mode due to the longer satellite track over ice in the Antarctic, compared to the tracks over Greenland and the North pole region (Fig. 9-1).

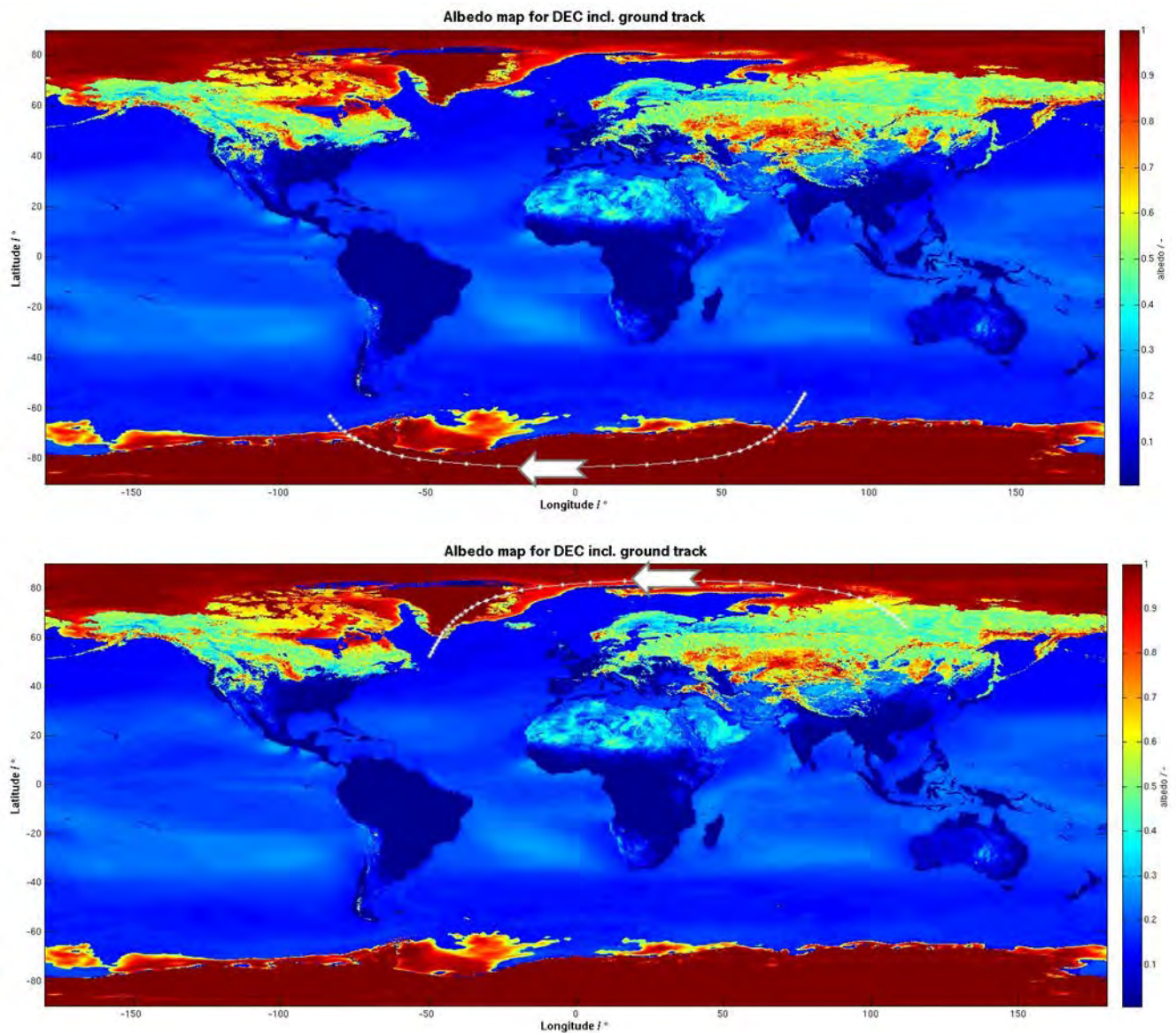


**Figure 9-1:** Map of global albedo values for the month of December for nadir-pointing derived from ADAM including the ground track (white line) for IRC mode over the Antarctic (top) and Arctic (bottom); each white dot corresponds to a frequency step (from DLR 2018b).

	Document Nr. <b>AE-RP-DLR-L1B-001</b>	Issue: <b>4.4</b>	Date: <b>20.04.2018</b>	Page: <b>86/117</b>	
	Doc. Title: <b>ADM-Aeolus ATBD Level1B Products</b>				

The basic assumption for both the ground and atmospheric returns used for IRC is obtaining a signal without Doppler frequency shift from a non-moving ground or atmospheric target. That is the reason, why the satellite needs to point to nadir in order to assume that the Doppler frequency shift from the atmosphere on the line-of-sight (LOS) direction is zero. More specifically it needs to be assured that the average vertical movements of the ground or atmosphere during 1 frequency step consisting of 2 observations ( $\approx 200$  km) are 0 m/s.

This assumption of zero frequency shift during nadir pointing is violated for the following conditions:

- ground returns from sea surface, e.g. oceans with waves moving up- und downward; as the up- und downward moving part can consist of different reflectivity's (e.g. due to foam and breaking waves, see KNMI (2008))
- vertical movement in the atmosphere for the altitude range (e.g. 6-16 km) used for RRC, which is non-zero over vertical scales of 10 km and horizontal scales of 100-200 km; this could be relevant in case of larger-scale gravity waves generated by orography of large mountain ranges typically observed in Southern America (Andes), New Zealand or Northern Scandinavia
- vertical movement in the atmospheric boundary layer close to the ground, which is non-zero over scales of 200 km, e.g. during strong convective activity. This could influence the ground return range bins due to the coarse resolution of the range bins of 250-500 m, which contain both the surface return, but also the atmospheric backscatter above the ground in this range bin.
- slightly off-nadir pointing during IRC mode will result in a projection of the satellite velocity and the horizontal wind speed on the LOS direction. For an off-nadir angle of 3 mrad and a satellite velocity of 7.6 km/s, this would result in a satellite-induced LOS wind speed of 23 m/s. This contribution is corrected during IRC processing, as the LOS wind speed component from the satellite is known. As the off-nadir angle is also slightly varying along the orbit, the correction needs to be applied for every frequency step independently. In contrast the horizontal wind speed is not measured by ALADIN during IRC mode and cannot be corrected during IRC mode processing. Assuming a maximum horizontal wind speed of 100 m/s in the azimuthal direction of the LOS speed, this would result in a contribution of 0.3 m/s. The influence of the horizontal wind speed during an IRC mode needs to be assessed using ECMWF model data from the auxiliary meteorological files (AUX\_MET).

These non-zero frequency shifts will affect the measured ground-return and atmospheric response for 1 frequency step. As the IRC mode consists of 40 frequency steps, this will add random noise on each frequency step, if the atmospheric contributors are not correlated over larger horizontal scales (e.g. several 1000 km). Vertical movements in the atmosphere or ground on scales smaller than 100-200 km, will also increase the random noise for each measurement, but averaged for the response result for each frequency step.

The IRC mode is used to characterize the instrument response for different optical paths (internal, atmosphere) with different optical illumination of the Fizeau interferometer in the MSP and double-edge Fabry-Perot interferometer for the RSP for spectrally narrow bandwidth (laser internal reference, ground returns) and broad bandwidth (atmospheric molecular returns) and their detection on the ACCD detectors. Thus the instrument response is not only depending on the ALADIN instrument parameters – mainly the spectral transmission of the interferometers and the illumination and response of the ACCD detector, but also on the spectral properties of the atmospheric or ground returns. Inherently the instrument response functions are also depending on the actual computation of the response values for Mie and Rayleigh signals and the pre-processing steps (e.g. background and DCO subtraction) before computation of the responses. Thus, the pre-processing and the computation of the responses for Mie and Rayleigh need to be identical for the wind retrieval from the wind mode data and the response computation in IRC mode. As a consequence the IRC mode is also used for “calibration” of the response algorithms (e.g. pixilation effects for MSP data). In case that the response can be calculated with different algorithms as for the Mie response (ch. 8.3, step 5) the same algorithm needs to be applied for the processing of the MRC mode. Otherwise this would lead to systematic errors in the derived wind speed.

## 9.1 Mie response calibration

Now the specific processing for the MRC is discussed. Here only the internal reference signal and the range-gates from the ground return are processed. It is important to note that the response parameters from the MRC using ground returns are used for wind mode processing for atmospheric winds for both the L1B and L2B wind mode. This is justified, because both the ground return and the aerosol/cloud returns from the

	Document Nr. <b>AE-RP-DLR-L1B-001</b>	Issue: <b>4.4</b>	Date: <b>20.04.2018</b>	Page: <b>87/117</b>	
	Doc. Title: <b>ADM-Aeolus ATBD Level1B Products</b>				

atmosphere are spectrally narrowband signals. Thus the spectrally narrowband ground return can be used to characterize the instrument response function from the atmospheric path for the MSP. Although the internal reference signal and the ground-return signal are both spectrally narrow, the internal reference signal from the MRC cannot be used for the atmospheric wind retrieval due to the different illumination of the MSP from the internal and atmospheric path.

The processing of the detector outputs for the laser internal reference  $S_i(j,n)$  ( $j$ : pixel index,  $n$ : laser shot index) and for the atmospheric signals  $S_a(i,j,k)$  ( $i$ : range gate index,  $j$ : pixel index,  $k$ : measurement index) is identical as described in chapter 8.3 (step 1 to 5) with the following main difference:

- a detection scheme for ground-returns is applied to the signal from the atmospheric path  $S_a(i,j,k)$  for each measurement  $k$  (chapter 10.1). The signal  $S_a(i,j,k)$  from all range gates  $i$ , which are detected as ground returns is summed to the resulting ground return signal  $S_g(j,k)$ , which is not any more depending on range gate index  $i$ . Thus all other atmospheric range gates from Mie are not used for further MRC processing.

**Step 1** includes the quality-control (QC) for each measurement, as described in Ch. 8.3 (step 1). As the laser frequency change from one step to the other can affect several laser pulses, the affected measurement from the atmospheric signal  $S_a(i,j,k)$  and the laser pulses from the internal reference  $S_i(j,n)$  need to be eliminated. The laser pulse validity flag is used for that purpose. Also the other flags (spacecraft attitude, data corrupted) are checked and affected measurements are removed (ch. 8.3, step 1, and ch. 8.1.1).

Within **step 2** the signal from the internal reference  $S_i(j,n)$  per laser pulse needs to be summed up to obtain an internal reference signal per measurement  $S_i(j,k)$  (eq. 8.36).

**Step 3** performs the correction for the detection chain offset (DCO) for each measurement of the atmospheric signal  $S_a(i,j,k)$  and internal reference  $S_i(j,k)$  according to eq. 8.38 leading to  $S_{a,DCO}(i,j,k)$  and  $S_{i,DCO}(j,k)$ .

Within **step 4** the obscuration correction with the TOBS array (eq. 8.39) and the solar background correction (as for eq. 8.19 in Rayleigh processing) is performed for the atmospheric signal leading to  $S_{a,BCK}(i,j,k)$ .

Within an additional **step 5** the signal amplitudes for the atmospheric signals  $S_{a,BCK}(i,j,k)$  are computed for each measurement as a sum over all 16 signal pixels (from  $j=3$  to 18):

$$I_a(i,k) = \sum_{j=3}^{j=18} S_{a,BCK}(i,j,k) \quad (9.1)$$

These signal amplitudes contain both the Mie and Rayleigh backscatter signal, because the Rayleigh backscatter signal, which acts as a constant offset, is not subtracted before. The Rayleigh offset cannot be determined at this processing stage, because it is determined within the Mie response determination (ch. 8.3, step 5b). But the signal amplitudes are used at this stage only for the ground detection scheme (ch. 10.1) and the approximation of subtracting the minimum of all pixels would also subtract a significant portion of the Mie signal and could deteriorate the ground-detection.

With the use of a Digital elevation model (DEM) a number of atmospheric range gates (with  $i=g$ ,  $g$  from  $g_{min}$  to  $g_{max}$ ) are selected as ground bin candidates in **step 6**. The selection uses range bins with altitudes close to the altitude of the intersection point of the LOS direction with the DEM. This means, that the pre-selection of the ground return range gates is based on the DEM, and relies on the accuracy of the DEM. In geographical regions, where the DEM is not accurate enough, false or no ground bin candidates will be selected, even for the case, where the signal amplitudes show a clear ground return signal. In addition to the DEM, a gradient check is performed with the signal amplitudes  $I_a(i,k)$  to identify the ground bin candidates.

In **step 7** the Mie response is calculated using one of the algorithms described in ch. 8.3, step 5a or 5b for the measurements of the selected ground range gates of the atmospheric path  $S_{a,BCK}(i,g,k)$  and the signal of the internal path  $S_{i,DCO}(j,k)$  for each measurement. Thus, Mie responses for each measurement are obtained for selected range gates of the atmospheric path  $R_a(g,k)$  and for the internal reference  $R_i(k)$ . Now the difference of the responses  $R_a(g,k) - R_i(k)$  is used for further selection on the ground bin candidates. Finally the range bins  $g_{min}$  to  $g_{max}$ , which contain ground return signal, are identified per measurement.

In **step 8** the selected ground bin signals  $S_{a,BCK}(i,j,k)$  are summed up per measurement to  $S_{g,BCK}(j,k)$  using the ground range gates from  $g_{min}$  to  $g_{max}$ :

	Document Nr. <b>AE-RP-DLR-L1B-001</b>	Issue: <b>4.4</b>	Date: <b>20.04.2018</b>	Page: <b>88/117</b>	
	Doc. Title: <b>ADM-Aeolus ATBD Level1B Products</b>				

$$S_g(j, k) = \sum_{i=g_{\min}}^{i=g_{\max}} S_{a, BCK}(i, j, k) \quad (9.2)$$

Step 5 to 8 are performed to determine the range gates, which contain ground returns and to sum up the signal from the corresponding range gates.

The internal reference signal and the ground return signal for each commanded laser frequency are determined in **step 9**. The laser frequency steps are commanded every second observation but within one measurement. Thus the measurements with index  $k_{\min}$  to  $k_{\max}$  belonging to one commanded frequency step  $f_{com}$  need to be identified. Now the internal reference signal  $S_I(j, f_{com})$  and the ground return signal  $S_g(j, f_{com})$  from each measurement belonging to one frequency step is added:

$$S_g(j, f_{com}) = \sum_{k_i=k_{\min}}^{k_i=k_{\max}} S_g(j, k) \quad (9.3)$$

$$S_I(j, f_{com}) = \sum_{k_i=k_{\min}}^{k_i=k_{\max}} S_I(j, k)$$

This is performed for all 40 frequency steps leading to 40 internal reference signal  $S_I(j, f_{com})$  and a maximum of 40 ground return signal  $S_g(j, f_{com})$ , for the cases that a valid ground-return is detected. Now the Mie response is calculated using one of the algorithms described in Ch. 8.3 (step 5a or 5b) for each frequency step from the summed signals internal  $S_I(j, f_{com})$  and the ground return signal  $S_g(j, f_{com})$  (**step 10**). Thus, Mie responses for each frequency step are obtained for the ground return  $R_g(f_{com})$  and for the internal reference  $R_I(f_{com})$ .

The LOS pointing in IRC mode is slightly off-nadir by a few mrad and is also slightly varying along the orbit. Thus it needs be corrected for each frequency step using the knowledge of the satellite induced velocity  $v_{LOS, S}$  in LOS direction from the AOCS system. The satellite induced velocity  $v_{LOS, S}$  needs to be calculated for each frequency step, and converted from the unit of speed [m/s] into frequencies [GHz] using the Doppler shift equation. As the correction needs to be performed for responses in units of [pixel], an a-priori known, ideal Mie slope  $\beta_{Mie, ideal}$  in units of [pixel/GHz] needs to be assumed:

$$R_{Sat}(f_{com}) = \beta_{Mie, ideal} \cdot \frac{2}{\lambda_0} \cdot v_{LOS, s}(f_{com}) \quad (9.4)$$

Now the ground return responses can be corrected from the satellite induced response with

$$R_{g, corr}(f_{com}) = R_g(f_{com}) - R_{Sat}(f_{com}) = R_g(f_{com}) - \beta_{Mie, ideal} \cdot \frac{2}{\lambda_0} \cdot v_{LOS, s}(f_{com}) \quad (9.5)$$

to obtain the corrected ground return response  $R_{g, corr}(f_{com})$  for each frequency step  $f_{com}$  (**step 11**) (Fig. 9-2). The ideal Mie slope  $\beta_{Mie, ideal}$  is needed, because the actual Mie slope is not available at this processing step, as it is an output of the MRC processing. This value is obtained from end-to-end simulations and needs to be adapted to actual values, once several MRC are processed from in-orbit data. The sign of the correction should be verified in-orbit, because it is depending on the sign definition of satellite speed  $v_{LOS, S}$  and Mie slope  $\beta_{Mie, ideal}$ . Other corrections of the ground-return response  $R_{g, corr}(f_{com})$  are related to harmonic and range-dependent biases.

Now the Mie response for the internal reference  $R_I(f_{com})$  and the ground returns  $R_{g, corr}(f_{com})$  are used to determine the response intercept  $\alpha$  and response slope  $\beta$  parameters for the ground-returns reference ( $\alpha_a, \beta_a$ ) and internal reference ( $\alpha_i, \beta_i$ ). This is performed using a linear least-square fit approach with the commanded frequency as x-parameter and the response R as y-parameter (**step 12**). As the ground returns parameters from MRC are used for Mie wind retrieval of the atmospheric range gates, the subscript a is used for the slope  $\beta_a$  and intercept parameter  $\alpha_a$ .

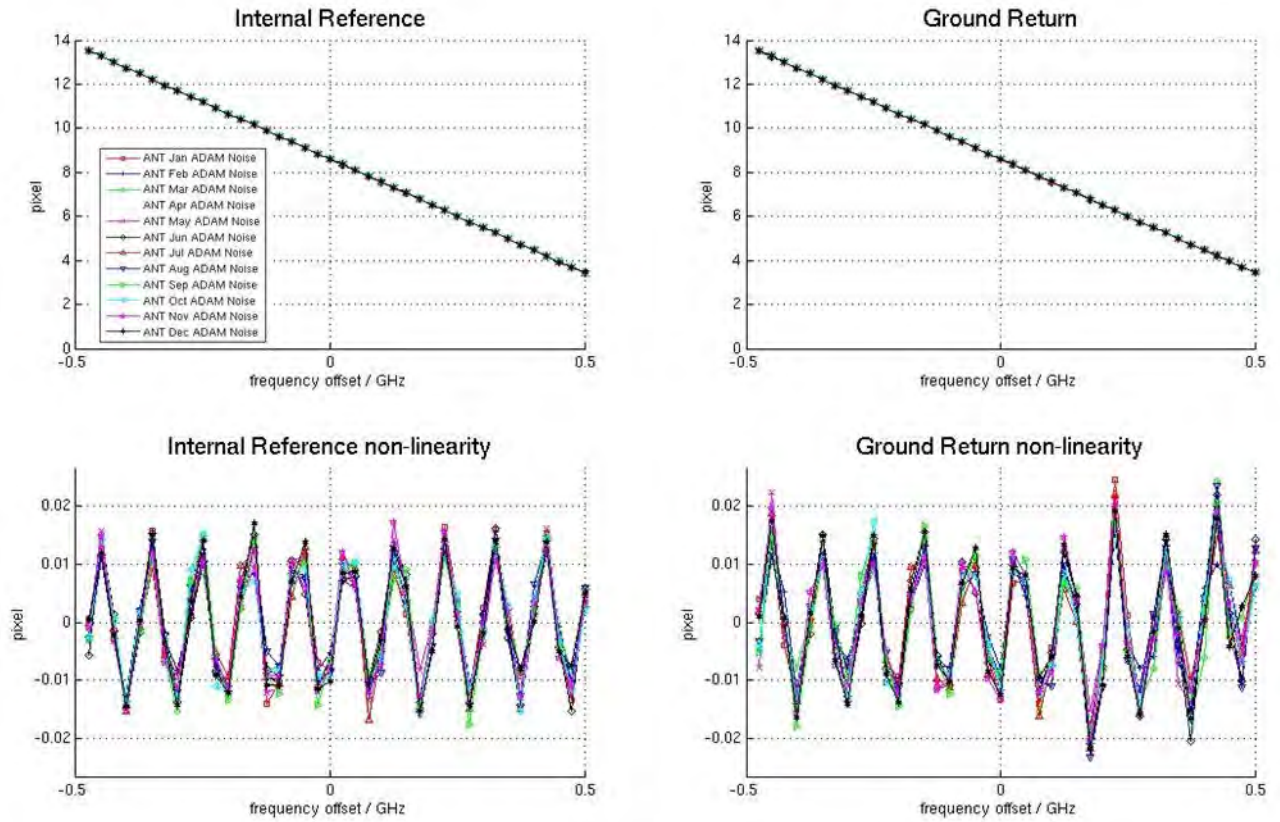


**Figure 9-2:** Mie response for the internal reference  $R_I(f_{com})$  (top left) and ground return  $R_a(f_{com}) = R_{g,corr}(f_{com})$  (top right) over the frequency range of an IRC derived from end-to-end simulations including noise and albedo values for 12 months (different colours); the non-linearity after applying a linear fit is shown for the internal reference  $\gamma_I(f_{com})$  (bottom left) and ground return  $\gamma_a(f_{com})$  (bottom right) for the 12 different simulations (colours) (from DLR 2018b).

The actual intercept  $\alpha$  parameter could vary between different IRC depending on the absolute laser wavelength, as discussed in ch. 8.2.1 for the wind retrieval. The variation of  $\alpha$  is indicating not only a variation in the property of the MSP, but also a variation in laser frequency. This variation is not relevant for wind retrieval as only the difference of the frequency between atmospheric and internal path is used. Similarly the response intercept  $\alpha$  from the internal and atmospheric path can be converted to frequencies using the determined response slope  $\beta$ , which provides the zero-frequencies of the internal  $f_{c,I}$  and atmospheric path  $f_{c,a}$  (see eq. 8.9). Only the difference of these 2 frequencies is a good measure for characterizing the difference in optical illumination of the internal and atmospheric path of the MSP and can be used to monitor its stability and is used within the wind retrieval (eq. 8.12 and eq. 8.62). The zero-frequency for the atmospheric  $f_{c,a}$  and the internal  $f_{c,I}$  path, and their difference  $\Delta f_{c,a-I}$  is calculated (**step 13**) according to:

$$f_{c,I} = \frac{\alpha_I}{\beta_I}$$

$$f_{c,a} = \frac{\alpha_a}{\beta_a} \tag{9.6}$$

$$\Delta f_{c,a-I} = f_{c,a} - f_{c,I} = \frac{\alpha_a}{\beta_a} - \frac{\alpha_I}{\beta_I}$$

As these frequencies correspond to the frequency of the centre of the Mie USR ( $R_{Mie,center} = 8.5$  pixel, Ch. 9) a subscript of  $c$  is used (correspondingly also in eq. 8.12).

	Document Nr. <b>AE-RP-DLR-L1B-001</b>	Issue: <b>4.4</b>	Date: <b>20.04.2018</b>	Page: <b>90/117</b>	
	Doc. Title: <b>ADM-Aeolus ATBD Level1B Products</b>				

The instrument responses for both Mie and Rayleigh are not purely linear, as approximated by the linear least square fit. Therefore a non-linear parameter  $\gamma(f_c)$  needs to be determined and used for wind retrieval (Ch. 8.3, eq. 8.59). The non-linearity of the Mie instrument response is mainly determined by the coarse sampling of the Mie fringe position on the ACCD with only 16 pixels, which leads to a periodic oscillation of the Mie response depending on pixel position – called pixilation effect. The period of this oscillation is 1 pixel and the amplitude is depending on the algorithm to determine the centroid (ch. 8.3, step 5a or 5b). Although the approach in step 5b) uses a Lorentzian fit function with the discretization of this function on a number of sub-pixels (e.g. 5, eq. 8.52), the oscillation can only be minimized but not avoided. Other causes for a non-linear Mie response are related to non-uniformity of the Mie fringe over the illuminated Fizeau optical aperture and non-uniformity in ACCD pixel response (in the order of several %). Thus the oscillation amplitude (and possibly period) is not constant over the frequency range of the MRC. In addition there is a slowly varying variation of the Mie response caused by edge effects for large frequency offsets, where the Mie signal fringe is only partly visible on the ACCD. This slowly varying component could be approximated by a polynomial function. As the illumination is different for the internal and atmospheric path, also the non-linearity of the internal and atmospheric response is different.

The residuals (difference) from the measured responses for the internal reference  $R_I(f_c)$  and the ground returns  $R_a=R_{g,corr}(f_{com})$  to the linear fit is used to determine the Mie response non-linearity  $\gamma_I(f_{com})$  and  $\gamma_a(f_{com})$  for each frequency step  $f_c$  (Fig. 9-2):

$$\begin{aligned}\gamma_I(f_{com}) &= R_I(f_{com}) - (\alpha_I + \beta_I \cdot f_{com}) \\ \gamma_a(f_{com}) &= R_a(f_{com}) - (\alpha_a + \beta_a \cdot f_{com})\end{aligned}\tag{9.7}$$

As this representation of the non-linearity is a function of the frequency  $f_{com}$ , a correction during wind-retrieval could only be applied, if the frequency  $f$  would be known. This is only known after application of the intercept and slope parameters to the measured responses (eq. 8.60). Another way of representing the non-linearity is as a function of measured response  $R$ , because every commanded frequency step  $f_{com}$  corresponds to a measured response  $R_I$  and  $R_a$  (**step 14**):

$$\begin{aligned}\gamma_I(R_I) &= \gamma_I(f_{com} \rightarrow R_I) = R_I(f_c) - (\alpha_I + \beta_I \cdot f_c) \\ \gamma_a(R_a) &= \gamma_a(f_{com} \rightarrow R_a) = R_a(f_c) - (\alpha_a + \beta_a \cdot f_c)\end{aligned}\tag{9.5}$$

The actual values of  $\gamma_I(f_{com})$  and  $\gamma_a(f_{com})$  are identical to the values of  $\gamma_I(R_I)$  and  $\gamma_a(R_a)$ , but they are now used in the wind retrieval as function of the measured response (eq. 8.59). The values of  $\gamma_I(R_I)$  and  $\gamma_a(R_a)$  are only obtained for 40 measured responses, corresponding to the 40 frequency steps with a step size of 25 MHz. During wind measurement mode the measured values of  $R_I$  or  $R_a$  are not at the same resolution as the measured responses during MRC. Thus a linear interpolation from the two next discrete values is used to perform the non-linearity correction function using  $\gamma_I(R_I)$  and  $\gamma_a(R_a)$  during wind mode. It could be envisaged, that the linear interpolation between the next response values could be replaced by a polynomial fit as performed for the Rayleigh non-linearity (ch. 9.2) in combination with a (piecewise, TBD) sinusoidal function.

The standard deviation of the residual of the fit can be used to assess the quality of the MRC by computing the standard deviation over the non-linearity for the internal reference  $\gamma_I(f_{com})$  and the atmospheric path  $\gamma_a(f_{com})$  (**step 15**). In case that another polynomial (and sinusoidal fit) is applied to the non-linearity, then the standard deviation from the residuals to this polynomial fit should be derived.

Now all parameters used for the Mie wind retrieval (ch. 8.3) are derived from the MRC mode data:

- internal path: intercept, slope, non-linearity  $\alpha_I, \beta_I, \gamma_I(R_I)$
- atmospheric path: intercept, slope, non-linearity  $\alpha_a, \beta_a, \gamma_a(R_a)$

Several parameters are contained in the auxiliary file to assess the quality of the MRC within the product confidence data PCD, related to the validity of the overall calibration, or the validity of single frequency steps for internal reference signal and ground-return.

A MRC is considered as valid, if the determined values for the internal and atmospheric path are within an acceptable range and if the standard deviation of the non-linearity is below an acceptable maximum value. These thresholds (not listed in Tab. 9-1) are provided via the L1B processing parameter file. The main input parameters used for MRC mode processing from various source files are contained in Tab. 9-1, while the main output parameters in the MRC auxiliary file are summarized in Tab. 9-2.

	Document Nr. <b>AE-RP-DLR-L1B-001</b>	Issue: <b>4.4</b>	Date: <b>20.04.2018</b>	Page: <b>91/117</b>	
	Doc. Title: <b>ADM-Aeolus ATBD Level1B Products</b>				

Input Variable	Source	Description	Number of Values and Occurrence
$S_a(i,j,k)$	L1A Mie MDS	16-bit digitized raw ACCD output from MSP per atmospheric range bin $i$ , pixel $j$ , and measurement $k$	20 pixel values per atmospheric range gate per measurement; 16 signal pixels and 4 offset pixels; background light in $i=25$
$S_i(j,n)$	L1A Reference Pulse MDS	16-bit digitized raw ACCD output from MSP for laser internal reference per pixel $j$ , and for each laser pulse $n$	20 pixel values per laser pulse
$f_{com}$	L1A housekeeping	commanded laser frequency offset	for each laser pulse; 40 different values in steps of 25 MHz within [-0.475 GHz; +0.5 GHz]
$\lambda_0$	satellite characterisation file	nominal laser wavelength	1 value
$V_{Los, S}$	L1A geolocation	LOS velocity from satellite	1 value per measurement 1 value per observation
	L1A geolocation	Geolocation of DEM intersection (latitude, longitude)	2 values per measurement 2 values per observation
	L1A geolocation	Altitude of Height bin	1 value per measurement and 1 value per observation for each range gate
$N, P$	L1A housekeeping	instrument settings for number of laser shots per measurement $P$ , number of measurements per observation $N$	1 value per observation for $N$ and $P$
$t_i, t_b$	L1A housekeeping	range bin time $t_i$ for atmospheric range bins and for background measurement $t_b$	24 values for atmospheric range bins per measurement and 1 value for background bin per measurement
validity flags	L1A data quality	spacecraft on target flag data corrupted flag laser pulse validity	1 value per measurement for spacecraft on target and data corrupted flag 1 value per laser pulse for pulse validity
TOBS	Satellite characterisation file	Mie Tripod Obscuration Data	1 value for each Mie ACCD pixel; total of 16 values
DCR	DCMZ auxiliary file	Dark Current Rate in LSB per pixel per second for Mie	1 value
$\beta_{Mie,ideal}$	source code	a-priori, ideal Mie response slope	1 value in [pixel/GHz]

**Table 9-1:** Input data, source and description for processing of Mie spectrometer data during Mie Response Calibration; for a detailed description see DPM (DoRIT and MDA 2017c) and IOOD (DoRIT and MDA 2017b).

	Document Nr. <b>AE-RP-DLR-L1B-001</b>	Issue: <b>4.4</b>	Date: <b>20.04.2018</b>	Page: <b>92/117</b>	
	Doc. Title: <b>ADM-Aeolus ATBD Level1B Products</b>				

Output Variable	Destination	Description	Number of Values and Occurrence
$f_{com}$	MRC auxiliary file	commanded laser frequency offset	40 values in steps of 25 MHz from [-0.475 GHz; +0.5 GHz]
$\alpha_a, \beta_a, f_{c,a}$	MRC auxiliary file	Mie response intercept, slope, and zero-frequency for atmospheric (=ground) signal	1 value for intercept, slope and zero frequency
$\gamma_a(R_a)$	MRC auxiliary file	non-linearity for atmospheric signal (=ground)	40 values, for each response step 1 value
$\alpha_i, \beta_i, f_{c,i}$	MRC auxiliary file	Mie response intercept, slope, and zero frequency for laser internal reference	1 value for intercept, slope and zero frequency
$\Delta f_{c,a-i}$	MRC auxiliary file	zero-frequency difference	1 value
$\gamma_i(R_i)$	MRC auxiliary file	non-linearity for laser internal signal	40 values, for each response step 1 value
$R_a(f_c)$	MRC auxiliary file	Mie response per frequency step for atmosphere (=ground)	40 values, for each frequency step 1 value
$R_i(f_c)$	MRC auxiliary file	Mie response per frequency step for internal reference	40 values, for each frequency step 1 value
PCD flag	MRC auxiliary file	flag indicating validity of MRC	1 value
SR(i,k)	MRC auxiliary file	scattering ratio from MRC for each range gate i, and measurement k	1 value per range gate and measurement

**Table 9-2:** Output data, source and description for processed Mie response calibration; for a detailed description see DPM (DoRIT and MDA 2017c) and IOOD (DoRIT and MDA 2017b).

	Document Nr. <b>AE-RP-DLR-L1B-001</b>	Issue: <b>4.4</b>	Date: <b>20.04.2018</b>	Page: <b>93/117</b>	
	Doc. Title: <b>ADM-Aeolus ATBD Level1B Products</b>				

## 9.2 Rayleigh Response Calibration

In addition to the derivation of the response calibration parameters from the internal reference and ground signal as performed for MRC, the Rayleigh response calibration RRC includes the analysis of atmospheric range gates. This is necessary because of the different instrument response of the RSP for a narrow bandwidth signal (laser internal reference, ground return) and a broad bandwidth atmospheric signal from molecular backscatter in the atmosphere. Thus atmospheric range gates need to be analysed with negligible amount of narrowband aerosol or cloud signal. In order to increase the Rayleigh signal for the derivation of the response, a number or range gate signals are added in the upper troposphere (e.g. between 6 km and 16 km) to derive the Rayleigh atmospheric response. This approach using atmospheric signals could cause problems arising from aerosol or cloud signals within this vertical range and approaches were studied, including the use of the scattering ratio from the MSP signal for quality-control of the RSP signal (DLR 2011) during IRC mode processing.

The processing of the detector outputs for the laser internal reference  $S_i(j,n)$  ( $j$ : pixel index,  $n$ : laser shot index) and for the atmospheric signals  $S_a(i,j,k)$  ( $i$ : range gate index,  $j$ : pixel index,  $k$ : measurement index) is identical as described in chapter 8.2.2 with the following main differences:

- a detection scheme for ground-returns is applied to the signal from the atmospheric path  $S_a(i,j,k)$  for each measurement  $k$  (chapter 10.1). The signal  $S_a(i,j,k)$  from all range gates  $i$ , which are detected as ground returns is summed to the resulting ground return signal  $S_g(j,k)$ , which is not any more depending on range gate index  $i$ .
- the atmospheric signals  $S_a(i,j,k)$  are only analysed for the range gates, which are fully within an altitude range from  $h_{min}$  to  $h_{max}$ , e.g. between 6 km and 16 km. This should ensure that the atmospheric signal from this altitude range is dominated by broad bandwidth molecular return without aerosols and clouds.
- in case that a specific processing flag is set to true, only Rayleigh range gates are used, where the corresponding scattering ratio  $SR(i,k)$  derived during MRC processing is below a certain threshold  $SR_{max}$  (e.g. 1.1). This ensures that only range bins with broad bandwidth molecular signal and with significantly low amount of aerosol and without clouds are used to derive Rayleigh response parameters.

In **step 1** the QC for each measurement  $k$  and laser pulse  $n$  is performed (as discussed in Ch. 8.1.1). As the laser frequency change from one step to the other can affect several laser pulses, the affected measurement from the atmospheric signal  $S_a(i,j,k)$  and the laser pulses from the internal reference  $S_i(j,n)$  need to be eliminated. The laser pulse validity flag is used for that purpose. Also the other flags (spacecraft attitude, data corrupted) are checked and affected measurements are removed (ch. 8.1.1).

In **step 2** the atmospheric range gates  $i$  are selected, which are fully within the altitude range from  $h_{min}$  to  $h_{max}$  and where the scattering ratio  $SR(i,k)$  is below a certain threshold  $SR_{max}$ . The check on the scattering ratio is only performed in case that a corresponding processing flag is set. Especially the selection of the optimal parameters  $h_{min}$  to  $h_{max}$  and the threshold  $SR_{max}$  is strongly depending on the atmospheric scene and the occurrence of clouds, e.g. low level clouds close to the ground or Polar Stratospheric Clouds (PSC) in the winter months over the Arctic and Antarctic. Thus a constant value for  $h_{min}$ ,  $h_{max}$ , and threshold  $SR_{max}$  for each RRC is only a starting point for further investigations.

Specifically for Rayleigh channel processing the correction of the Rayleigh detection chain non-linearity using an array of correction values  $E_{RLC}(S)$  as a function of signal intensity  $S$  according to eq. (8.17) for the atmospheric range gates  $S_a(i,j,k)$  and internal reference  $S_i(j,n)$  is performed in **step 3**.

**Step 4** performs the correction for the DCO for each measurement of the atmospheric signal  $S_a(i,j,k)$  and for each pulse of the internal reference  $S_i(j,n)$  according to eq. 8.18 leading to  $S_{a,DCO}(i,j,k)$  and  $S_{i,DCO}(j,n)$ . In addition the dark current contribution DCR (dark current rate) is corrected for atmospheric signals  $S_a(i,j,k)$  per measurement according to eq. 8.18.

Within **step 5** the solar background correction is performed for the atmospheric signal leading to  $S_{a,BCK}(i,j,k)$  using eq. 8.19.

Now the signals for Rayleigh filter A and B are summed for the atmospheric signals  $S_{a,BCK}(i,j,k)$  and internal reference signal  $S_i(j,n)$  for pixel  $j=11$  to 18 (A) and pixel  $j=3$  to 10 (filter B) within **step 6** to obtain the atmospheric intensities  $I_{A,a}(j,k)$  and  $I_{B,a}(j,k)$  (eq. 8.21) per range gate and measurement and the intensities for the internal reference  $I_{A,i}(n)$  and  $I_{B,i}(n)$  (eq 8.20) per laser shot.

	Document Nr. <b>AE-RP-DLR-L1B-001</b>	Issue: <b>4.4</b>	Date: <b>20.04.2018</b>	Page: <b>94/117</b>	
	Doc. Title: <b>ADM-Aeolus ATBD Level1B Products</b>				

The signal from the internal reference  $I_{A,i}(n)$  and  $I_{B,i}(n)$  per laser pulse needs to be added to obtain an internal reference signal per measurement  $I_{A,i}(k)$  and  $I_{B,i}(k)$  (**step 7**).

The ground-return candidate range gates need to be identified for the Rayleigh atmospheric signal similar to the approach described for the MRC (step 6 and 7, ch. 9.1). With the use of a DEM a number of atmospheric range gates (with  $i=g$ ,  $g$  from  $g_{\min}$  to  $g_{\max}$ ) are selected as ground bin candidates in **step 8**. The selection uses range bins with altitudes close to the altitude of the intersection point of the LOS direction with the DEM. In addition to the DEM, a gradient check is performed with the total signal amplitude  $I_a(i,k)$  to identify the ground bin candidates, which is calculated using the sum of the filter A and B signal intensity (**step 9**):

$$I_a(i,k) = I_{A,a}(i,k) + I_{B,a}(i,k) \quad (9.8)$$

In **step 10** the Rayleigh response  $R$  is calculated for each measurement using eq. (8.24) from the atmospheric range bin signals  $I_{A,a}(i,k)$  and  $I_{B,a}(i,k)$  and from the summed signal of the internal path internal reference signal for each measurement  $I_{A,i}(k)$  and  $I_{B,i}(k)$ . Thereby, Rayleigh responses for each measurement are obtained for selected range gates of the atmospheric path  $R_a(g,k)$  and for the internal reference  $R_i(k)$ . Now the difference of the responses  $R_a(g,k) - R_i(k)$  is used for further selection of the ground bin candidates. Finally the range bins  $g_{\min}$  to  $g_{\max}$ , which contain ground return signal, are identified per measurement.

In **step 11** the selected ground bin signals from filter A  $I_{A,a}(i,k)$  and filter B  $I_{B,a}(i,k)$  are added per measurement to  $I_{A,g}(k)$  and  $I_{B,g}(k)$ :

$$I_{A,g}(k) = \sum_{j=g_{\min}}^{j=g_{\max}} I_{A,a}(j,k) \quad (9.9)$$

$$I_{B,g}(k) = \sum_{j=g_{\min}}^{j=g_{\max}} I_{B,a}(j,k)$$

Step 7 to 11 are performed to determine the range gates, which contain ground returns and to obtain the total signal from the corresponding range gates for the ground return.

Similar the signal from the atmospheric range gates is added for all range gates  $a_{\min}$  and  $a_{\max}$  within the altitude range from  $h_{\min}$  to  $h_{\max}$ , e.g. between 6 km and 16 km (**step 12**):

$$I_{A,a}(k) = \sum_{j=a_{\min}}^{j=a_{\max}} I_{A,a}(j,k) \quad (9.10)$$

$$I_{B,a}(k) = \sum_{j=a_{\min}}^{j=a_{\max}} I_{B,a}(j,k)$$

The internal reference signal, the atmospheric and the ground return signal for each commanded laser frequency needs to be determined in **step 13**. The laser frequency steps are commanded every second observation but within one measurement. Thus the measurements (with index  $k_{\min}$  to  $k_{\max}$ ) belonging to one commanded frequency step  $f_{\text{com}}$  need to be identified using the parameter from the L1A housekeeping dataset. Now the internal reference signal  $S_i(j,f_{\text{com}})$ , the atmospheric and the ground return signal  $S_g(j,f_{\text{com}})$  from each measurement belonging to one frequency step is added for filter A and B separately:

	Document Nr. <b>AE-RP-DLR-L1B-001</b>	Issue: <b>4.4</b>	Date: <b>20.04.2018</b>	Page: <b>95/117</b>	
	Doc. Title: <b>ADM-Aeolus ATBD Level1B Products</b>				

$$\begin{aligned}
I_{A,I}(f_{com}) &= \sum_{k_i=k_{min}}^{k_i=k_{max}} I_{A,I}(k) & I_{B,I}(f_{com}) &= \sum_{k_i=k_{min}}^{k_i=k_{max}} I_{A,I}(k) \\
I_{A,g}(f_{com}) &= \sum_{k_i=k_{min}}^{k_i=k_{max}} I_{A,g}(k) & I_{B,g}(f_{com}) &= \sum_{k_i=k_{min}}^{k_i=k_{max}} I_{A,g}(k) \\
I_{A,a}(f_{com}) &= \sum_{k_i=k_{min}}^{k_i=k_{max}} I_{A,a}(k) & I_{B,a}(f_{com}) &= \sum_{k_i=k_{min}}^{k_i=k_{max}} I_{A,a}(k)
\end{aligned} \tag{9.11}$$

This is performed for all 40 frequency steps leading to 40 internal reference signal and a maximum of 40 ground return and atmospheric signals for filter A and B, in case that a ground-return is detected and an atmospheric signal could be obtained in the altitude range  $h_{min}$  to  $h_{max}$  (including a potential check on the scattering ratio).

Now the Rayleigh responses are calculated using eq. 8.24 for the internal reference  $R_I(f_{com})$ , the atmosphere  $R_a(f_{com})$  and the ground return  $R_g(f_{com})$  for each frequency step (**step 14**).

Similar as for the MRC the satellite-induced LOS speed needs to be corrected due to a slightly off-nadir pointing for the atmospheric  $R_a(f_{com})$  and the ground return  $R_g(f_{com})$  responses for each frequency step. As the correction needs to be performed for responses in units of Rayleigh responses [a.u.], an a-priori known, ideal Rayleigh slope for a broad bandwidth atmospheric return  $\beta_{Ray,ideal,a}$  and a narrow bandwidth ground return  $\beta_{Ray,ideal,g}$  in units of [a.u./GHz] needs to be applied:

$$\begin{aligned}
R_{Sat,a}(f_{com}) &= \beta_{Ray,ideal,a} \cdot \frac{2}{\lambda_0} \cdot v_{LOS,s}(f_{com}) \\
R_{Sat,g}(f_{com}) &= \beta_{Ray,ideal,g} \cdot \frac{2}{\lambda_0} \cdot v_{LOS,s}(f_{com})
\end{aligned} \tag{9.12}$$

Now the atmospheric and ground return responses can be corrected from the satellite induced response with

$$\begin{aligned}
R_{a,corr}(f_{com}) &= R_a(f_{com}) - R_{Sat,a}(f_{com}) = R_a(f_{com}) - \beta_{Ray,ideal,a} \cdot \frac{2}{\lambda_0} \cdot v_{LOS,s}(f_{com}) \\
R_{g,corr}(f_{com}) &= R_g(f_{com}) - R_{Sat,g}(f_{com}) = R_g(f_{com}) - \beta_{Ray,ideal,g} \cdot \frac{2}{\lambda_0} \cdot v_{LOS,s}(f_{com})
\end{aligned} \tag{9.13}$$

to obtain the corrected atmospheric  $R_{a,corr}(f_{com})$  and ground return response  $R_{g,corr}(f_{com})$  for each frequency step  $f_c$  (**step 15**). The values for the ideal slopes are obtained from end-to-end simulations and needs to be adapted to actual values, once several RRC are processed in-orbit. Other response correction steps refer to the range-dependent bias. The sign of the correction should be verified in-orbit, because it is depending on the sign definition of satellite speed  $v_{LOS,s}$  and Rayleigh slope  $\beta_{Ray,ideal}$ . Other corrections of the atmospheric and ground-return response are related to harmonic and range-dependent biases.

Now the Rayleigh response for the internal reference  $R_I(f_{com})$ , the ground returns  $R_{g,corr}(f_{com})$  and the atmospheric return  $R_{a,corr}(f_{com})$  are determined for each frequency step  $f_c$  (Fig. 9-3) and can be used to determine the response intercept  $\alpha$  and response slope  $\beta$  parameters for the atmospheric returns ( $\alpha_a, \beta_a$ ), the ground-returns reference ( $\alpha_g, \beta_g$ ) and internal reference ( $\alpha_i, \beta_i$ ). This is performed using a linear least-square fit with the commanded frequency as x-parameter and the response R as y-parameter (**step 16**).

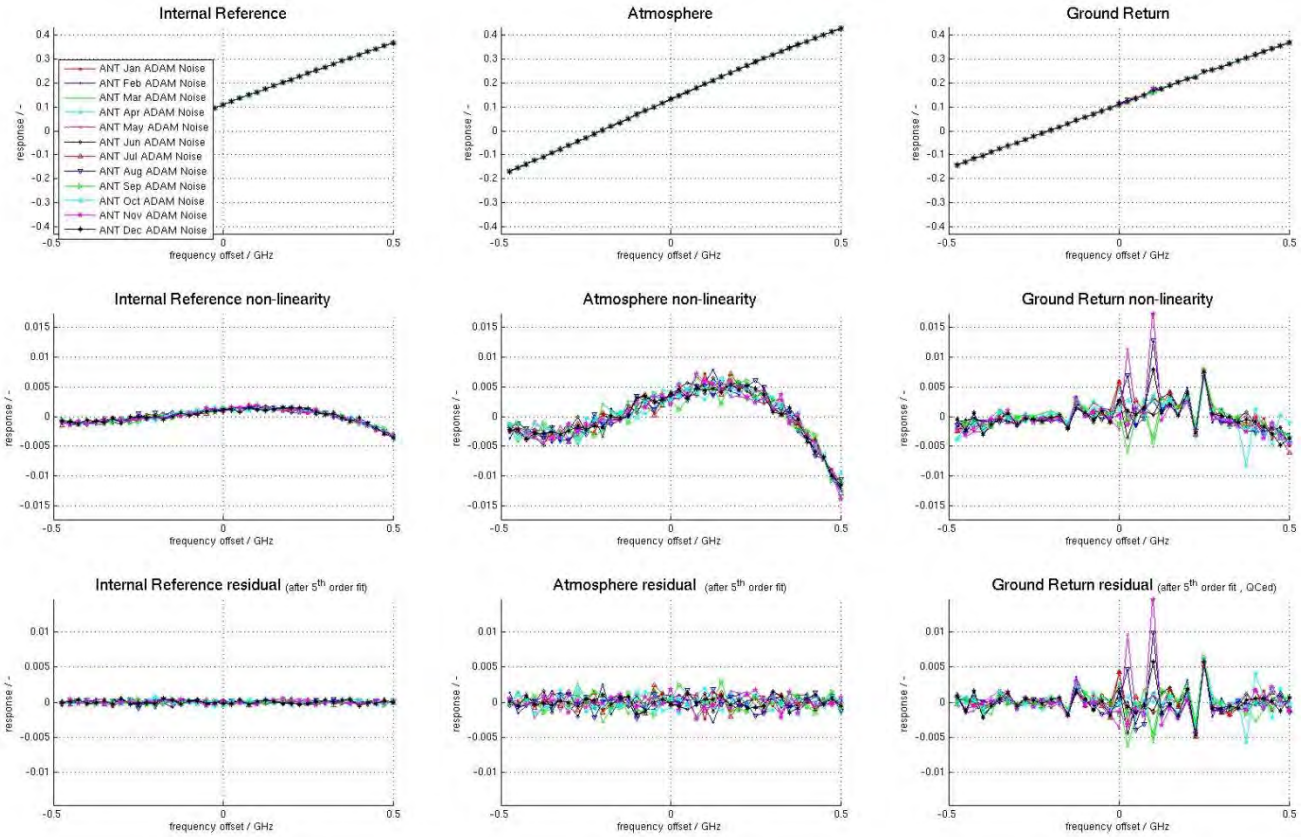


**Figure 9-3:** Rayleigh response for the internal reference  $R_I(f_{com})$  (top left), the atmospheric signal  $R_{a,corr}(f_{com})$  (top middle) and ground return  $R_{g,corr}(f_{com})$  (top right) over the frequency range of an IRC derived from end-to-end simulations including noise and albedo values for 12 months (different colours); the non-linearity after applying a linear fit is shown for the internal reference  $\gamma_I(f_{com})$  (centre left), the atmospheric signal  $\gamma_a(f_{com})$  (centre middle) and ground return  $\gamma_g(f_{com})$  (centre right) for the 12 different simulations (colours); the residuals after applying a 5<sup>th</sup> order polynomial fit are shown in the bottom row (from DLR 2018b).

As discussed for the wind retrieval (ch. 8.2.1) the actual intercept  $\alpha$  parameter could vary from IRC to IRC depending on the absolute laser wavelength. Thus the zero-frequency for the atmospheric  $f_{c,a}$ , the ground return  $f_{c,g}$ , and the internal  $f_{c,I}$  path, and their difference  $\Delta f_{c,a-I}$  and  $\Delta f_{c,g-I}$  are calculated (**step 17**) according to:

$$f_{c,I} = \frac{\alpha_I}{\beta_I} \quad f_{c,a} = \frac{\alpha_a}{\beta_a} \quad f_{c,g} = \frac{\alpha_g}{\beta_g}$$

$$\Delta f_{c,g-I} = f_{c,g} - f_{c,I} = \frac{\alpha_g}{\beta_g} - \frac{\alpha_I}{\beta_I} \quad (9.14)$$

$$\Delta f_{c,a-I} = f_{c,a} - f_{c,I} = \frac{\alpha_a}{\beta_a} - \frac{\alpha_I}{\beta_I}$$

As these frequencies correspond to the frequency of the Rayleigh filter A and B crossing point ( $R_{Ray,center} = 0$ ) a subscript of c is used (correspondingly also in eq. 8.12).

The instrument responses for both Mie and Rayleigh are not purely linear, as approximated by the linear least square fit. Therefore a non-linear parameter  $\gamma(f_c)$  needs to be determined and used for the wind retrieval (Ch. 8.2.2, eq. 8.25). The non-linearity of the Rayleigh instrument response is mainly determined by the spectral transmission function of both filter A and B, which can be approximated by an Airy-Function convoluted with a Gaussian defect function for the internal path and the narrow bandwidth ground return. The non-linearity for the broad bandwidth molecular signal is determined by an additional convolution with a

	Document Nr. <b>AE-RP-DLR-L1B-001</b>	Issue: <b>4.4</b>	Date: <b>20.04.2018</b>	Page: <b>97/117</b>	
	Doc. Title: <b>ADM-Aeolus ATBD Level1B Products</b>				

Rayleigh-Brillouin lineshape (Dabas et al. 2008, Witschas 2012, Witschas et al. 2012), which is depending on atmospheric temperature and pressure. It could be shown by end-to-end simulations (DLR 2012f) and A2D Rayleigh calibrations (Marksteiner 2012, DLR 2012a, DLR 2017b, DLR 2018a) that the internal, atmospheric and ground-return non-linearity can be approximated by a 5<sup>th</sup> order polynomial function.

The residuals (difference) from the measured responses for the internal reference  $R_I(f_c)$ , the atmospheric return  $R_{a,corr}(f_{com})$  and the ground returns  $R_{g,corr}(f_{com})$  to the linear fit is used to determine the Rayleigh response non-linearity  $\gamma_I(f_{com})$ ,  $\gamma_a(f_{com})$  and  $\gamma_g(f_{com})$  for each frequency step  $f_c$  (Fig. 9-3):

$$\begin{aligned}
 \gamma_I(f_{com}) &= R_I(f_{com}) - (\alpha_I + \beta_I \cdot f_{com}) \\
 \gamma_a(f_{com}) &= R_{a,corr}(f_{com}) - (\alpha_a + \beta_a \cdot f_{com}) \\
 \gamma_g(f_{com}) &= R_{g,corr}(f_{com}) - (\alpha_g + \beta_g \cdot f_{com})
 \end{aligned} \tag{9.15}$$

As this representation of the non-linearity is a function of the frequency  $f_{com}$ , a correction during wind-retrieval could only be applied, if the frequency  $f$  is known. This would be only known, after application of the intercept and slope parameters to the measure responses (eq. 8.28). Another way of representing the non-linearity is as a function of measured response  $R$ , because every commanded frequency step  $f_c$  corresponds to a measured response  $R_I$ ,  $R_{a,corr}$  and  $R_{g,corr}$  (**step 18**):

$$\begin{aligned}
 \gamma_I(R_I) &= \gamma_I(f_{com} \rightarrow R_I) = R_I(f_c) - (\alpha_I + \beta_I \cdot f_c) \\
 \gamma_a(R_{a,corr}) &= \gamma_a(f_{com} \rightarrow R_{a,corr}) = R_{a,corr}(f_c) - (\alpha_a + \beta_a \cdot f_c) \\
 \gamma_g(R_{g,corr}) &= \gamma_g(f_{com} \rightarrow R_{g,corr}) = R_{g,corr}(f_c) - (\alpha_g + \beta_g \cdot f_c)
 \end{aligned} \tag{9.16}$$

The actual values of  $\gamma_I(f_{com})$ ,  $\gamma_a(f_{com})$  and  $\gamma_g(f_{com})$  are identical to the values of  $\gamma_I(R_I)$ ,  $\gamma_a(R_{a,corr})$  and  $\gamma_g(R_{g,corr})$  but they are now used in the wind retrieval as function of the measured response (eq. 8.26). The non-linearity values are only obtained for 40 measured responses, corresponding to the 40 frequency steps with a step size of 25 MHz. During wind measurement mode the measured values of  $R_I$ ,  $R_a$  and  $R_g$  are not at the same resolution as the measured responses during RRC. Thus a linear interpolation from the two next discrete values (from RRC) is used to obtain the non-linearity correction function during wind mode.

Alternatively the non-linearity functions  $\gamma_I(f_{com})$ ,  $\gamma_a(f_{com})$  and  $\gamma_g(f_{com})$  are approximated by a 5<sup>th</sup> order polynomial function (**step 19**) and the polynomial coefficients for the internal  $c_{I,i}$ , atmospheric  $c_{a,i}$  and ground return  $c_{g,i}$  ( $i=0$  to 5 for the polynomial order, Fig. 9-3) are used during Rayleigh wind retrieval. This will result in 6 polynomial coefficients for the internal path, for the atmospheric signal and for the ground return.

The standard deviation of the residual of the fit can be used to assess the quality of the RRC by computing the standard deviation over the residual of the 5<sup>th</sup> order polynomial function to the non-linearity for the internal reference  $\gamma_I(f_{com})$ , the atmospheric path  $\gamma_a(f_{com})$  and the ground return  $\gamma_g(f_{com})$  (**step 20**).

Now all parameters used for the Rayleigh wind retrieval (ch. 8.2.2) are derived from the RRC mode data:

- internal path: intercept, slope, non-linearity, polynomial coefficients:  $\alpha_I$ ,  $\beta_I$ ,  $\gamma_I(R_I)$ ,  $c_{I,i}$
- atmospheric return: intercept, slope, non-linearity, polynomial coefficients:  $\alpha_a$ ,  $\beta_a$ ,  $\gamma_a(R_{a,corr})$ ,  $c_{a,i}$
- ground return: intercept, slope, non-linearity, polynomial coefficients:  $\alpha_g$ ,  $\beta_g$ ,  $\gamma_g(R_{g,corr})$ ,  $c_{g,i}$

Several parameters are contained in the auxiliary RRC file to assess the quality of the RRC within the product confidence data PCD related to the validity of the overall calibration, or the validity of single frequency steps for internal, atmospheric and ground-return.

An RRC is considered as valid, if the determined values for the internal, atmospheric and ground return path are within an acceptable range and if the standard deviation of the residual from polynomial fit to the non-linearity is below an acceptable maximum value. In addition the temperatures on the RSP etalon are verified with the maximum minus minimum value is below a certain threshold. Otherwise the RRC calibration will be flagged invalid. These thresholds (not included in Tab. 9-3) are provided via the L1B Processing Parameter file.

The main input parameters used for RRC from various source files are contained in Tab. 9-3, while the main output parameters in the RRC auxiliary file are summarized in Tab. 9-4.

	Document Nr. <b>AE-RP-DLR-L1B-001</b>	Issue: <b>4.4</b>	Date: <b>20.04.2018</b>	Page: <b>98/117</b>	
	Doc. Title: <b>ADM-Aeolus ATBD Level1B Products</b>				

Input Variable	Source	Description	Number of Values and Occurrence
$S_a(i,j,k)$	L1A Ray MDS	16-bit digitized raw ACCD output from RSP per atmospheric range bin $i$ , pixel $j$ , and measurement $k$	20 pixel values per atmospheric range gate per measurement; 16 signal pixels and 4 offset pixels; background light in $i=25$
$S_r(j,n)$	L1A Reference Pulse MDS	16-bit digitized raw ACCD output from RSP for laser internal reference per pixel $j$ , and for each laser pulse $n$	20 pixel values per laser pulse
$f_{com}$	L1A housekeeping	commanded laser frequency offset	for each laser pulse; 40 different values in steps of 25 MHz within [-0.475 GHz; +0.5 GHz]
$\lambda_0$	satellite characterisation file	nominal laser wavelength	1 value
$V_{Los, S}$	L1A geolocation	LOS velocity from satellite	1 value per measurement 1 value per observation
	L1A geolocation	Geolocation of DEM intersection (latitude, longitude)	2 values per measurement 2 values per observation
	L1A geolocation	Altitude of Height bin	1 value per measurement and 1 value per observation for each range gate
$N, P$	L1A housekeeping	instrument settings for number of laser shots per measurement $P$ , number of measurements per observation $N$	1 value per observation for $N$ and $P$
$t_i, t_b$	L1A housekeeping	range bin time $t_i$ for atmospheric range bins and for background measurement $t_b$	24 values for atmospheric range bins per measurement and 1 value for background bin per measurement
validity flags	L1A data quality	spacecraft on target flag data corrupted flag laser pulse validity	1 value per measurement for spacecraft on target and data corrupted flag 1 value per laser pulse for pulse validity
$h_{min}$ to $h_{max}$	L1B processing parameter	minimum and maximum altitude for summation atmospheric Rayleigh response	2 altitude values
$SR(i,k)$	MRC auxiliary file	scattering ratio from MRC for each range gate $i$ , and measurement $k$	1 value per range gate and measurement
$SR_{max}$	L1B processing parameter	maximum scattering ratio used as threshold	1 value

**Table 9-3:** Input data, source and description for processing of Rayleigh spectrometer data during Rayleigh Response Calibration; for a detailed description see DPM (DoRIT and MDA 2017c) and IOOD (DoRIT and MDA 2017b).

	Document Nr. <b>AE-RP-DLR-L1B-001</b>	Issue: <b>4.4</b>	Date: <b>20.04.2018</b>	Page: <b>99/117</b>	
	Doc. Title: <b>ADM-Aeolus ATBD Level1B Products</b>				

Input Variable	Source	Description	Number of Values and Occurrence
$E_{RLC}(S)$	satellite characterisation file	Rayleigh Linearity Correction per signal level S	array of values
DCR	DCMZ auxiliary file	Dark Current Rate in LSB per pixel per second for Rayleigh	1 value
$\beta_{Ray,ideal,g}$	source code	a-priori, ideal Rayleigh response slope for ground-returns	1 value in [a.u./GHz]
$\beta_{Ray,ideal,a}$	source code	a-priori, ideal Rayleigh response slope for atmospheric returns	1 value in [a.u./GHz]

**Table 9-3 (continued):** Input data, source and description for processing of Rayleigh spectrometer data during Rayleigh Response Calibration; for a detailed description see DPM (DoRIT and MDA 2017c) and IODD (DoRIT and MDA 2017b).

	Document Nr. <b>AE-RP-DLR-L1B-001</b>	Issue: <b>4.4</b>	Date: <b>20.04.2018</b>	Page: <b>100/117</b>	
	Doc. Title: <b>ADM-Aeolus ATBD Level1B Products</b>				

Output Variable	Destination	Description	Number of Values and Occurrence
$f_{com}$	RRC auxiliary file	commanded laser frequency offset	40 values in steps of 25 MHz from [-0.475 GHz; +0.5 GHz]
$\alpha_a, \beta_a, f_{c,a}$	RRC auxiliary file	Rayleigh response intercept, slope, and zero-frequency for atmospheric signal	1 value for intercept, slope and zero frequency
$\gamma_a(R_a)$	RRC auxiliary file	non-linearity for atmospheric signal	40 values, for each response step 1 value
$\alpha_g, \beta_g, f_{c,g}$	RRC auxiliary file	Rayleigh response intercept, slope, and zero frequency for ground return	1 value for intercept slope and zero frequency
$\gamma_g(R_g)$	RRC auxiliary file	non-linearity for ground signal	40 values, for each response step 1 value
$\alpha_i, \beta_i, f_{c,i}$	RRC auxiliary file	Rayleigh response intercept, slope, and zero frequency for laser internal reference	1 value for intercept slope and zero frequency
$\gamma_i(R_i)$	RRC auxiliary file	non-linearity for laser internal signal	40 values, for each response step 1 value
$\Delta f_{c,a-l}, \Delta f_{c,g-l}$	RRC auxiliary file	zero-frequency difference for atmosphere and ground	1 value for atmosphere and ground
$c_{a,i}$	RRC auxiliary file	polynomial coefficients for atmospheric non-linearity	6 values for 5 <sup>th</sup> order
$c_{g,i}$	RRC auxiliary file	polynomial coefficients for ground non-linearity	6 values for 5 <sup>th</sup> order
$c_{i,i}$	RRC auxiliary file	polynomial coefficients for internal non-linearity	6 values for 5 <sup>th</sup> order
$R_a(f_c)$	RRC auxiliary file	Rayleigh response per frequency step for atmospheric signal	40 values, for each frequency step 1 value
$R_g(f_c)$	RRC auxiliary file	Rayleigh response per frequency step for ground	40 values, for each frequency step 1 value
$R_i(f_c)$	RRC auxiliary file	Rayleigh response per frequency step for internal reference	40 values, for each frequency step 1 value
PCD flag	RRC auxiliary file	flag indicating validity of MRC	1 value

**Table 9-4:** Output data, source and description for processed Rayleigh response calibration; for a detailed description see DPM (DoRIT and MDA 2017c) and IODD (DoRIT and MDA 2017b).

	Document Nr. <b>AE-RP-DLR-L1B-001</b>	Issue: <b>4.4</b>	Date: <b>20.04.2018</b>	Page: <b>101/117</b>	
	Doc. Title: <b>ADM-Aeolus ATBD Level1B Products</b>				

## **10 Additional algorithms**

TBD for next issue planned for end 2018

### **10.1 Ground Return Detection and Harmonic Bias Estimator**

TBD for next issue planned for end 2018

### **10.2 Signal Amplitude, SNR and Scattering Ratio for Mie**

TBD for next issue planned for end 2018

### **10.3 Signal Amplitude and SNR for Rayleigh**

TBD for next issue planned for end 2018

### **10.4 Quality Control and Quality Flags, Corrupted Data, Error Quantifiers**

TBD for next issue planned for end 2018

	Document Nr. <b>AE-RP-DLR-L1B-001</b>	Issue: <b>4.4</b>	Date: <b>20.04.2018</b>	Page: <b>102/117</b>	
	Doc. Title: <b>ADM-Aeolus ATBD Level1B Products</b>				

## 11 Abbreviations

A2D	ALADIN Airborne Demonstrator
ACCD	Accumulation CCD
ACE	Altimeter Corrected Elevation
ADAM	A surface reflectance Database for ESA's Earth Observation Missions
ADC	Analog-Digital-Converter
ADM	Atmospheric Dynamics Mission
ADS	Annotation Data Set
AISP	Annotated Instrument Source Packets
ALADIN	Atmospheric Laser Doppler Instrument
AOCS	Attitude and Orbit Control System
APF	Aeolus Processing Facility
ATBD	Algorithm Theoretical Basis Document
a.u.	arbitrary unit
BOL	Begin of Life
BRC	Basic Repeat Cycle
CAT	Clear-Air Turbulence
CCD	Charge Coupled Device
CFI	Customer Furnished Item
CRC	Cyclic Redundancy Check
cw	continuous wave
DCC	Dark Current Calibration
DCO	Detection Chain Offset
DCMZ	Dark Current in Memory Zone
DEM	Digital Elevation Model
DFU	Detection Front-End Unit
DLR	Deutsches Zentrum für Luft- und Raumfahrt
DPM	Detailed Processing Model
DSD	Data Set Descriptor
DWL	Doppler Wind Lidar
E2S	End-to-End Simulator
ECEF	Earth Centred Earth Fixed
ECMWF	European Centre for Medium-Range Weather Forecasts
EE	Encircled Energy
EGM96	Earth Gravitational Model from 1996
EOL	End of Life
Eq.	equation
ESA	European Space Agency

	Document Nr. <b>AE-RP-DLR-L1B-001</b>	Issue: <b>4.4</b>	Date: <b>20.04.2018</b>	Page: <b>103/117</b>	
	Doc. Title: <b>ADM-Aeolus ATBD Level1B Products</b>				

FEP	Front-End Processor
FFM	Flip-Flop Mechanism
FH	Fixed Header
Fig.	Figure
FOV	Field of View
FSR	Free Spectral Range
FWHM	Full Width Half Maximum
GADS	Global Annotation Data Set
GPS	Global Positioning System
HB	Harmonic Bias
HBE	Harmonic Bias Estimator
HLOS	Horizontal Line-of-Sight
HWP	Half-Wave Plate
IAT	Instrument Auto Test
ID	Identification
IDC	Instrument Defocus Characterisation
IFF	Interference Filter
IFP	Instrument Full Performance
IMU	Inertial Measurement Unit
IODD	Input Output Data Definitions Interface Control Document
IRC	Instrument Response Calibration
ISR	Instrument Spectral Registration
ITRF	International Terrestrial Reference Frame
KVT	Key Value Terminator
L1	Level 1
L1B	Level 1B
L1BP	Level 1B Processor
LBM	Laser Beam Monitoring
LBO	Lithium-Borate
LBWU	Laser Burst Warmup
LCA	Laser Chopper Assembly
LCM	Laser Chopper Mechanism
LCP	Laser Chopper Phase
LIDAR	Light Detection and Ranging
LOS	Line-of-Sight
LSB	Least Significant Bit
LTAN	Local Time of Ascending Node
LUT	Look Up Table
LVLH	Local Vertical Local Horizontal

	Document Nr. <b>AE-RP-DLR-L1B-001</b>	Issue: <b>4.4</b>	Date: <b>20.04.2018</b>	Page: <b>104/117</b>	
	Doc. Title: <b>ADM-Aeolus ATBD Level1B Products</b>				

MAD	Master Algorithm Document
MAG	Mission Advisory Group
MDS	Measurement Data Set
MOPA	Maser Oscillator Power Amplifier
MPH	Main Product Header
MRC	Mie Response Calibration
MSP	Mie Spectrometer
N. B.	Nota Bene
Nd:YAG	Neodymium doped Yttrium-Aluminium-Garnet
No.	Number
NWP	Numerical Weather Prediction
OBA	Optical Bench Assembly
oR	On specific user Request
PBL	Planetary Boundary Layer
PCD	Product Confidence Data
PDS	Payload Data Segment
PLH	Power Laser Head
Pol	Polarising Beamsplitter
QC	Quality Control
QWP	Quarter-Wave Plate
RAAN	Right Ascension of ascending node
RDB	range-dependent bias
resp.	respectively
RLC	Rayleigh Detection Chain Linearity Correction
RLH	Reference Laser Head
rms	root mean square
RMA	Reference Model Atmosphere
RRC	Rayleigh Response Calibration
RSP	Rayleigh Spectrometer
SOOBS	Start of Observation
SiC	Siliciumcarbid
SID	Structure Identification
SNR	Signal-to-Noise-Ratio
SoW	Statement of Work
SPH	Specific Product Header
SRD	System Requirements Document SRD
TBC	to be confirmed
TBD	to be defined
TC	Telecommand

	Document Nr. <b>AE-RP-DLR-L1B-001</b>	Issue: <b>4.4</b>	Date: <b>20.04.2018</b>	Page: <b>105/117</b>	
	Doc. Title: <b>ADM-Aeolus ATBD Level1B Products</b>				

TM	Telemetry
TN	Technical Note
TOBS	Tripod Obscuration
TRO	Transmit-Receive Optics
TV	Thermal Vacuum
USR	Useful Spectral Range
UV	Ultraviolet
VCDU	Virtual Channel Data Unit
VH	Variable Header
WGS84	World Geodetic System of 1984
wrt.	with respect to
WVM	Wind Velocity Measurement
XML	Extensible Markup Language
ZWC	Zero-Wind Calibration

	Document Nr. <b>AE-RP-DLR-L1B-001</b>	Issue: <b>4.4</b>	Date: <b>20.04.2018</b>	Page: <b>106/117</b>	
	Doc. Title: <b>ADM-Aeolus ATBD Level1B Products</b>				

## 12 Symbols and Constants

### Symbols

Symbol	Description	Unit
$a$	Albedo	1
$A_0$	Area of the telescope (optical aperture)	$m^2$
$A_0/r^2$	Acceptance solid angle	rad
$B$	Backscatter ratio, Scattering Ratio	1
$C(\lambda)$	Instrument transmission depending on wavelength $\lambda$	1
$D$	Telescope diameter	m
$E_L$	Energy of the laser pulse	mJ
$E_{bck}$	Earth background radiant energy	J
$f_0$	Frequency of the transmitted laser pulse	Hz
$L_a$	Aerosol Lidar ratio (aerosol extinction-to-backscatter ratio)	sr
$L_\lambda$	solar spectral radiance	$W m^{-2} \mu m^{-1} sr^{-1}$
$L_m$	Molecular Lidar ratio (molecules extinction-to-backscatter ratio)	sr
$M_\lambda$	solar spectral irradiance	$W m^{-2} \mu m^{-1}$
$N$	Number of measurements per observation	1
$N_{Mol}$	Number of molecules per volume	$m^{-3}$
$p$	Pressure	Pa
$P$	Number of laser pulses per measurement	1
$P_{  }, P_{\perp}$	co-polar (parallel) and cross-polar (perpendicular) component from total particle backscatter power ( $P_{  } + P_{\perp}$ )	W
$r$	Distance from instrument to target	m
$T$	Temperature	K
$T^2$	Atmospheric two-way transmission	1
$t_D$	detection time for solar background	s
$v_{LOS}$	Line-of-sight wind speed	$m s^{-1}$
$z$	Altitude	m

All symbols are included except from chapter 8, which are included in separate Tables at the end of each subchapter.

	Document Nr. <b>AE-RP-DLR-L1B-001</b>	Issue: <b>4.4</b>	Date: <b>20.04.2018</b>	Page: <b>107/117</b>	
	Doc. Title: <b>ADM-Aeolus ATBD Level1B Products</b>				

## Greek symbols

Symbol	Description	Unit
$\alpha_A, \alpha_{Mol}$	Extinction coefficient (aerosol, molecular)	$m^{-1}$
$\beta_A, \beta_{Mol}$	Backscatter coefficient (aerosol, molecular)	$m^{-1} sr^{-1}$
$\delta_{lin}, \delta_{circ}$	linear and circular depolarization ratio	1
$\Delta f_D$	Doppler-shifted frequency difference	Hz
$\Delta \lambda$	wavelength interval, e.g. of optical receiver	nm
$\Delta \lambda_D$	Doppler-shifted wavelength difference	pm
$\Delta \lambda_{FWHM}$	FWHM of a Gaussian or Lorentzian function	pm
$\rho_{eff}$	effective albedo of the atmosphere	1
$\Delta R$	Range bin resolution	m
$\Delta R_{min}$	Minimal range bin resolution	m
$\sigma$	Standard deviation of a signal spectrum	pm
$\sigma_{Mol}$	Rayleigh backscattering cross section	$m^2 sr^{-1}$
$\tau_L$	Physical length of the laser pulse	ns
$\Omega_0$	Acceptance solid angle	sr

## Constants

Symbol	Description	Unit
Avogadro constant	$N_A = 6.0221 \cdot 10^{23}$	$mol^{-1}$
Boltzmann constant	$k = 1.3807 \cdot 10^{-23}$	$J K^{-1}$
Loschmidt's number ( $T = 273.15 K / p = 1013.25 hPa$ )	$N_L = 2.68678 \cdot 10^{25}$	$m^{-3}$
Mean molecular air mass	$m_{air} = 2.885 \cdot 10^{-2}$	$kg mol^{-1}$
Planck's constant	$h = 6.6261 \cdot 10^{-34}$	J s
speed of light (vacuum)	$c = 2.99792458 \cdot 10^8$	$m s^{-1}$

	Document Nr. <b>AE-RP-DLR-L1B-001</b>	Issue: <b>4.4</b>	Date: <b>20.04.2018</b>	Page: <b>108/117</b>	
	Doc. Title: <b>ADM-Aeolus ATBD Level1B Products</b>				

## Processor Settings for L1B, V 7.01

Parameter	Value	Chapter Ch., Equation Eq.
<b>Wind Mode Processing</b>		<b>Ch. 8.1</b>
Maximum no. of bad pulses per measurement	3	Ch. 8.1.1
<b>Rayleigh wind mode processing</b>		<b>Ch. 8.2</b>
Rayleigh filter A pixel positions $j_{\min}$ to $j_{\max}$	11-18	Eq. 8.20
Rayleigh filter B pixel positions $j_{\min}$ to $j_{\max}$	3-10	Eq. 8.20
Minimum no. of Rayleigh ground measurements per observation	0*	Eq. 8.34
Rayleigh SNR threshold	15	
<b>Mie wind mode processing</b>		<b>Ch. 8.3</b>
Mie core 1 Gaussian width $\sigma_x$	1.27 pixel	Eq. 8.40
Mie core 1 max. no. of iterations	30	Eq. 8.47
Mie core 1 residual error threshold	$10^{-3}$	Eq. 8.47
Mie core 2 SNR threshold	10	Eq. 8.48
Mie core 2 start FWHM $\Delta x_{\text{start}}$	1.61 pixel	Eq. 8.48
Mie core 2 residual error threshold	$10^{-3}$	Eq. 86, step 3
Mie core 2 max. no. of iterations	30	Step 3
Mie core 2 no. of spectral subsamples $n_s$	5	Eq. 8.52
Mie core 2 max no. of downhill simplex algorithm iterations	50	step 2
Mie core 2 minimum decrease in residual error in downhill simplex	$10^{-3}$	Eq. 8.56, step 2
Minimum no. of Mie ground measurements per observation	0*	Eq. 8.66

Selection of settings from the operational L1B Processor V 7.01 from the file AUX\_PAR\_1B; \* parameter is set to 0; if >0 are checked needs to be verified within code.

	Document Nr. <b>AE-RP-DLR-L1B-001</b>	Issue: <b>4.4</b>	Date: <b>20.04.2018</b>	Page: <b>109/117</b>	
	Doc. Title: <b>ADM-Aeolus ATBD Level1B Products</b>				

## Satellite Characterisation File

Parameter	Value	Chapter Ch., Equation Eq.
<b>Wind Mode Processing</b>		<b>Ch. 8.1</b>
Laser frequency* $f_0$	844.961832 THz	Eq. 8.1, 8.3, 8.30, 8.33, 8.35
Laser wavelength $\lambda_0$	354.8 nm	8.63, 8.65, 8.67
<b>Rayleigh wind mode processing</b>		<b>CH. 8.2</b>
Rayleigh detection chain linearity error $E_{RLC}$	0	Eq. 8.17
<b>Mie wind mode processing</b>		<b>Ch. 8.3</b>
Mie Tripod Obscuration Correction $C_{TOBS}$	Array of 16 values between 0.88 and 1.0	Eq. 8.39
<b>Other parameters</b>		
Mie radiometric gain	0.684 LSB/e-	
Rayleigh radiometric gain	0.434 LSB/e-	
Mie ACCD time in memory zone	0.02 s	
Rayleigh ACCD time in memory zone	0.02 s	

Selection of the satellite characterisation file used for L1B Processor V 7.01 from file AUX\_CHAR; only laser wavelength specified in AUX\_CHAR file.

## Other parameters used for L1B processing

Parameter	Value	Chapter Ch., Equation Eq.
<b>Mie response calibration</b>		<b>Ch. 9.1</b>
ideal slope ground return $\beta_{Mie,ideal}$	-10.340435 [pixel/GHz]	Eq.9.4, 9.5
<b>Rayleigh response calibration</b>		<b>CH. 9.2</b>
ideal slope ground return $\beta_{Ray,ideal,g}$	0.524298 [a.u./GHz]	Eq. 9.11, 9.12
ideal slope atmospheric return $\beta_{Ray,ideal,a}$	0.608503 [a.u./GHz]	

Selection of other parameters used within the L1B Processor V 7.01.

	Document Nr. <b>AE-RP-DLR-L1B-001</b>	Issue: <b>4.4</b>	Date: <b>20.04.2018</b>	Page: <b>110/117</b>	
	Doc. Title: <b>ADM-Aeolus ATBD Level1B Products</b>				

## 13 References

- ADS Airbus Defence & Space (2016): Mission Analysis. AE-RP-ASU-048, issue 2, 22 Dec 2016.
- ADS Airbus Defence & Space (2017): Level 1B Master Algorithm Document. AE.SW.ASU.GS.023, Issue 9, March 2017, 102 pages.
- Ansmann, A., and D. Müller (2005): Lidar and Atmospheric Aerosol Particles. in: Lidar, Weitkamp C. (Ed.), Springer, New York, 105-141.
- Ansmann A., U. Wandinger, O. Le Rille, D. Lajas, and A. G. Straume (2007): Particle backscatter and extinction profiling with the spaceborne high-spectral-resolution Doppler lidar ALADIN: methodology and simulations. Appl. Opt., 46, 6606–6622.
- Ansmann, A., and U. Wandinger (2013): Aeolus Level 1B/2A Processor – Implementation of Continuous Mode Operations & Extended Pre-Launch Support. WP 1500 Independent Level 2A Validation. AE-TN-IFT-001, Final, 15 March 2013, 77 pages.
- Baker, W., Atlas, R., Cardinali, C., Clement, A., Emmitt, G.D., Gentry, B.M., Hardesty, R.M., Källen, E., Kavaya, M.J., Langland, R., Ma, Z., Masutani, M., McCarty, W., Pierce, A.B., Pu, Z., Riishojgaard, L.P., Ryan, J., Tucker, S., Weissmann, M., Yoe, J.G. (2014): Lidar-Measured Wind Profiles: The Missing Link in the Global Observing System. Bull. Amer. Meteorol. Soc. 95, 543-564
- Baumgarten, G. (2010). Doppler Rayleigh/Mie/Raman lidar for wind and temperature measurements in the middle atmosphere up to 80 km. Atmospheric Measurement Techniques, 3(6):1509-1518.
- Berry, P. A. M., R. G. Smith, J. Benveniste, 2010: ACE2: The New Global Digital Elevation Model. in: Mertikas S. (eds) Gravity, Geoid and Earth Observation. International Association of Geodesy Symposia, vol 135. Springer, Berlin, Heidelberg, 231-237, [http://dx.doi.org/10.1007/978-3-642-10634-7\\_30](http://dx.doi.org/10.1007/978-3-642-10634-7_30).
- Chanin, M. L., A. Garnier, A. Hauchecorne, J. Porteneuve (1989): A Doppler lidar for measuring winds in the middle atmosphere. Geophys. Res. Lett. 16, 1273-1276.
- Cosentino, A., A. Mondello, A. Sapia, A. D'Ottavi, M. Brotini, E. Nava, E. Stucchi, F. Trespidi, C. Mariottini, P. Wazen, N. Falletto, M. Fruit (2004): All-Solid-State Laser Transmitter for Space Based Lidar Applications. Reviewd and Revised Papers 22<sup>nd</sup> Int. Laser Radar Conference (ILRC 2004), Matera, Italy, ESA SP-561, 61-64.
- Cosentino, A., A. D'Ottavi, A. Sapia, E. Suetta (2012): Spaceborne Lasers Development for ALADIN and ATLID Instruments. IEEE Int. Geoscience and Remote Sensing Symposium IGARSS, Munich, Germany, 5673-5676.
- Champion, K. S. W. (1985), Standard and reference atmospheres, in: Handbook of geophysics and the space environment, Unites States Air Force Geophysics Laboratory, p. 14-1.
- Dabas, A., M. L. Denneulin, P. Flamant, C. Loth, A. Garnier, and A. Dolfi-Bouteyre (2008): Correcting winds measured with a Rayleigh Doppler lidar from pressure and temperature effects. Tellus, 60A, 206-215.
- Delaval, A., C. Loth, P. H. Flamant, D. Bruneau (2000a): Experimental Tests to Validate a Multiwavelength backscatter database. Final Report VALID 1, CNRS/IPSL September 2000, 56 pages + annex.
- Delaval, A., P. H. Flamant, C. Loth, A. Garnier, C. Vialle, D. Bruneau, R. Wilson, D. Rees (2000b): Performance Validation of Direct Detection and Heterodyne Detection Doppler WIND Lidars. Final Report VALID 2, CNRS/IPSL September 2000, 76 pages.
- DLR (2004a): Technical Proposal – Consolidation of ADM-Aeolus Ground Processing Algorithms. DLR 3472868MF, 5 April 2004.
- DLR (2004b): Technical Note Review of ALADIN Ground Processing. AE.TN.DLR.GS.TN2.1, V1.0, 30.07.04, July 2004.
- DLR (2006): Technical Note 2.1 Sensitivity Analysis. AE-TN-DLR-L1B-002, Version 3.4, 29.09.2006, September 2006, 78 pages.

	Document Nr. <b>AE-RP-DLR-L1B-001</b>	Issue: <b>4.4</b>	Date: <b>20.04.2018</b>	Page: <b>111/117</b>	
	Doc. Title: <b>ADM-Aeolus ATBD Level1B Products</b>				

- DLR (2007a): Technical Note Enhanced Performance Simulations, AE-TN-DLR-L1B-003, Version 1.1, 27.02.2007, 20 pages.
- DLR (2007b): Technical Note Calibration Issues, AE-TN-DLR-L1B-004, Version 2.1, 11.09.2007, 29 pages.
- DLR (2010) Technical Note 5.1 ADM-Aeolus Campaigns Results, AE.TN.DLR.A2D.TN51.260210, Version 1.1, 26.02.10, 309 pages.
- DLR (2011): Technical Note Rayleigh Response Calibration Quality Control, AE-TN-DLR-L1B-007, Version 1.1, 12.09.2011, 47 pages.
- DLR (2012a): Technical Note 5.2 ADM-Aeolus Airborne Campaigns Results, AE.TN.DLR.A2D.TN52.281011, Version 3.0, 24.02.2012, 202 pages.
- DLR (2012b): Technical Note 5.3. A2D Rayleigh spectrometer alignment sensitivity. AE.TN.DLR.A2D.TN53.120112, Version 2.0, 12.01.2012, 48 pages.
- DLR (2012c) Reitebuch, O., J. Briegel, U. Marksteiner, V. Freudenthaler, M. Wiegner (2012): Technical Note 5.4: A2D Mie Radiometric Performance. V 1.0, 25.04.2012, 25 pages.
- DLR (2012d) Final Report of ADM-Aeolus Campaigns 2004-2012. CD with final report, technical notes, dissertations, peer-reviewed papers, and final meeting handouts. Contract No. 18366/04/NL/MM, 15.06.2012.
- DLR (2012e): Technical Note Additional Computational Steps ADM-Aeolus L1B. V 1.5, 28.11.2012, 25 pages.
- DLR (2012f): Technical Note Rayleigh Channel nonlinearity error. V1.2, 03.12.2012, 42 pages.
- DLR (2012g): Technical Note Mie Core Processing. V 1.1, 05.04.2012, 27 pages.
- DLR (2014a): Aeolus L1B/2A Processor – Enhancements and Launch Extension. DLR Proposal from 07. March 2014.
- DLR (2014b): TN 5.3 A2D Rayleigh spectrometer alignment sensitivity. AE.TN.DLR.A2D.TN53.2.210814, V 3.0, 21.08.2014, 64 pages.
- DLR (2015): TN 51.1 Mie and Rayleigh Algorithm Performance Assessment (WP5100, Phase 1). AE.TN.DLR.5100.1.150930, V1.3, 28 Oct 2015, 64 pages.
- DLR (2016): Final Report Analysis of enhanced noise in A2D observations. AE.FR.DLR.A2D.CN11.110716, V2.0, 11 July 2016, 110 pages.
- DLR (2017a): Technical Note 51.2 Mie and Rayleigh Algorithm Performance Assessment (WP5100, Phase 2). AE.TN.DLR.5100.2.20170207, V1.3, 7 Feb 2017, 179 pages +appendix
- DLR (2017b): Final Report WindVal. Joint DLR-ESA-NASA Wind Validation for Aeolus. FR.DLR. WindVal.270717, V1.1, 27 July 2017, 146 pages + Annex 39 pages.
- DLR (2017c): TN Range-Dependent Bias Characterisation. AE-TN-DLR-L1B-5300-20170929, V1.1, 09 Sept 2017, 37 pages.
- DLR (2018a): Final Report WindVal II: Wind Validation II for Aeolus. FR.DLR. WindVal\_II.020318, V1.0, 02 March 2018, 200 pages + 70 pages annex.
- DLR (2018b): TN Characterization and Verification of Ground Echoes and its application to the Harmonic Bias Estimator (WP5200). AE.TN.DLR.5200.1.280318, V1.2, 28 March 2018, 98 pages.
- DLR and DoRIT (2012): Technical Note on E2S Modelling. AE-TN-DLR-E2S-001. V 1.3, 31.07.2012, 117 pages.
- DoRIT and MDA (2017a): Aeolus L1b Processor and End-to-End Simulator. End-to-End Simulator Detailed Processing Model. ADM-MA-52-1801, Issue 4/00, 2 May 2017, 165 pages.
- DoRIT and MDA (2017b): Aeolus L1b Processor and End-to-End Simulator. Input/Output Data Definitions Interface Control Document. ADM-IC-52-1666, Issue 4/08, 23 Aug 2017, 288 pages.
- DoRIT and MDA (2017c): Aeolus L1b Processor and End-to-End Simulator. Level 1b Processor Detailed Processing Model.. ADM-IC-52-1800, Issue 3/07, 21 July 2017, 210 pages.

	Document Nr. <b>AE-RP-DLR-L1B-001</b>	Issue: <b>4.4</b>	Date: <b>20.04.2018</b>	Page: <b>112/117</b>	
	Doc. Title: <b>ADM-Aeolus ATBD Level1B Products</b>				

- DoRIT and Météo-France (2016): Aeolus Level 2a Processor Input/Output Data Definition. AE-IF-DLR-L2A-004, Issue V 3.05, 29.08.2017, 41 pages.
- Doherty S. J., T. L. Anderson, R. J. Charison (1999): Measurement of the lidar ratio for atmospheric aerosols with a 180° backscatter nephelometer, Appl. Opt., 38 (9), p. 1823-1832.
- Doppler Ch. (1842): Über das farbige Licht der Doppelsterne und einiger anderer Gestirne des Himmels. Abhandlungen der königlich böhmischen Gesellschaft der Wissenschaften (V Folge, Bd. 2), in: Landespressebüro der Salzburger Landesregierung (Hrsg.): Christian Doppler - Leben und Werk. Schriftenreihe Serie Sonderpublikationen 76, 140 pages.
- Dou, X., Y. Han, D. Sun, H. Xia, Z. Shu, R. Zhao, M. Shangguan, and J. Guo (2014): Mobile Rayleigh Doppler Lidar for wind and temperature measurements in the stratosphere and lower mesosphere. Opt. Exp. 22, A1203-A1221.
- Durand, Y., Meynart, R., Endemann, M., Chinal, E., Morançais, D., Schröder, T., Reitebuch, O. (2005): Manufacturing of an airborne demonstrator of ALADIN, the direct detection Doppler wind lidar for ADM/Aeolus. Proc. SPIE Europe Int. Symposium Remote Sensing, 19-22 Sept. 2005, Bruges, Belgium, 5984-01.
- EADS-Astrium (2004a): ALADIN Instrument Operation definition. AE.TN.ASF.AL.00044, Issue 03, 29. October 2004.
- EADS-Astrium (2004b): ALADIN Instrument Design Report. AE.TN.ASF.AL.00101, Issue 02, Rev. 00, 10. November 2004.
- EADS-Astrium (2012): End to End Simulator Instrument input parameters. AE.TN.ASF.AL.00458, Issue 02, Rev. 02, 4 July 2012.
- EADS-Astrium (2013a): Level 1B Master Algorithm Document. AE.SW.ASU.GS.023, Issue 7, May 2013, 98 pages.
- EADS-Astrium (2013b): Technical Note on Harmonic Bias Estimator. AE.TN.ASF.AL.00603, Issue 2, 02/10/2013.
- ECMWF (2017a): ADM-Aeolus Level-2B/2C Processor Input/Output Data Definitions Interface Control Document, AE-IF-ECMWF-L2BP-001, Issue 3.00, 6 Sept 2017, 100 pages.
- ECMWF (2017b): ADM-Aeolus Level-2B Algorithm Theoretical Baseline Document. AE-TN-ECMWF-L2BP-0024, Version 3.1, 31 Jan 2018, 133 pages.
- Elecnor Deimos Space and ESA (2016a): Earth Observation Mission CFI Conventions Document EO-MA-DMS-GS-0001, Issue 4.12, 03 Nov 2016, 60 pages. Available from <https://eop-cfi.esa.int/>
- Elecnor Deimos Space and ESA (2016b): Earth Observation Mission CFI Mission General Software User Manual. EO-MA-DMS-GS-0002, Issue 4.12, 03 Nov 2016, 53 pages. Available from <https://eop-cfi.esa.int/>
- Elecnor Deimos Space and ESA (2016c): Earth Observation Mission CFI Mission Specific Customizations. EO-MA-DMS-GS-0018, Issue 4.12., 03 Nov 2016, 23 pages. Available from <https://eop-cfi.esa.int/>
- ESA (1999): The four candidate Earth explorer core missions: Atmospheric Dynamics Mission ADM, SP-1233-4, 157 pages.
- ESA (2003): Earth Explorer Ground Segment File Format Standard. PE-TN-ESA-GS-0001, Issue 1.4, 13 June 2003.
- ESA (2004a): Consolidation of Ground Processing Algorithms. AE-SW-ESA-GS-011, Issue 01a, 25 February 2004.
- ESA (2004b): ADM-Aeolus Data Products Contents Guidelines. AE-TN-ESA-SY-007, Issue 1B, 12 May 2004.
- ESA (2004c): Intercomparison of ACE and SRTM30 global digital elevation model at global and regional scale. October 2004.
- ESA (2006): ADM-Aeolus Ground Segment Concepts Document. AE-TN-ESA-GS-004, Issue 1C, 3 October 2006.

	Document Nr. <b>AE-RP-DLR-L1B-001</b>	Issue: <b>4.4</b>	Date: <b>20.04.2018</b>	Page: <b>113/117</b>	
	Doc. Title: <b>ADM-Aeolus ATBD Level1B Products</b>				

- ESA (2008): ADM-Aeolus Science Report. ESA SP-1311, ISBN 978-92-9221-404-3, 121 pages.
- ESA (2010): ADM-Aeolus Project System Requirements Document. AE-RS-ESA-SY-001, Issue 3.1, 16 September 2010, 49 pages.
- ESA (2016): ADM-Aeolus Project Mission Requirements Document. AE-RP-ESA-SY-001, Issue 2, Rev. 0, 16 November 2016, 57 pages.
- ESA (2018a): Input parameters for Aeolus End-to-End simulation. AE-TN-ESA-GS-075, Issue 2.2, 22 Jan 2018.
- ESA (2018b): Aeolus Scientific Calibration and Validation Requirements. AE-RS-ESA-GS-005, Issue 3, under review
- Evans B. T. N. (1988): Sensitivity of the backscatter/extinction ratio to changes in aerosol properties: implications for lidar, *Appl. Opt.*, 27 (15), p. 3299-3305.
- Flamant, P., A. Garnier, D. Bruneau, A. Hertzog, C. Loth, A. Dolfi, A. Dabas, J. L. Zarader, B. Gas, C. Werner, J. Streicher, I. Leike, F. Jochim (2002): Evaluation of Direct Detection Doppler WIND Lidar Signal Processing. Final Report on CD, ESA Contract 14442/00/NL/SF.
- Flamant, P. H., J. Cuesta, M. L. Denneulin, A. Dabas, and D. Huber (2008): ADM-Aeolus retrieval algorithms for aerosol and cloud products. *Tellus*, 60A, 273-286.
- Flamant, P. H., V. Lever, P. Martinet, Th. Flament, J. Cuesta, A. Dabas, M. Olivier, and D. Huber (2017): Level 2A Algorithm Theoretical Baseline Document: Particle spin-off products. AE-TN-IPSL-GS-001, V. 5.5, 13 January 2017, 83 pages.
- Flesia, C., and L. Korb (1999): Theory of the double-edge molecular technique for Doppler lidar wind measurement. *Appl. Opt.*, 38, 432-440.
- Flesia, C., C. L. Korb, and Ch. Hirt (2000): Double-edge molecular measurement of lidar wind profiles at 355 nm. *Optics Letters* 25, 1466-1468.
- Garnier, A., and M. L. Chanin, 1992: Description of a Doppler Rayleigh lidar for measuring winds in the middle atmosphere. *Appl. Phys.*, B55, 35-40
- Gentry, B. M., H. Chen, S. X. Li (2000): Wind measurements with 355-nm molecular Doppler lidar. *Optics Letters* 25, 1231-1233.
- Gimmestad, G. G. (2008): Reexamination of depolarization in lidar measurements. *Appl. Opt.*, 47, 3795-3802.
- Han, Y., X. Dou, D. Sun, H. Xia, and Z. Sun (2014): Analysis on wind retrieval methods for Rayleigh Doppler lidar. *Opt. Eng.* 53, 61607-1 – 61607-8.
- Hildebrand, J., Baumgarten, G., Fiedler, J., Hoppe, U.-P., Kaier, B., Lübken, F.-J., and Williams, B. P. (2012). Combined wind measurements by two different lidar instruments in the Arctic middle atmosphere. *Atmospheric Measurement Techniques*, 5, 2433-2445.
- Irgang, T. D., Hays, P. B., and Skinner, W. R. (2002). Two-Channel Direct-Detection Doppler Lidar Employing a Charge-Coupled Device as a Detector. *Applied Optics*, 41(6):1145-1155.
- Johnson, C.P.D., Berry, P.A.M., Hilton, R.D (2004): Report on ACE Version 1 Generation. De Montfort University, Leicester, U.K.
- Kidder, S. Q. and Vonder Haar, T.H. (1995). *Satellite meteorology*. Academic Press, San Diego, 466 pages.
- Korb, C. L., B. M. Gentry, and C. Weng (1992): The edge technique: theory and application to the lidar measurement of atmospheric winds. *Appl. Opt.*, 31, 4202-4213.
- Korb, C. L., B. M. Gentry, B. M., S. X. Li, and C. Flesia (1998): Theory of the double edge technique for Doppler lidar wind measurement. *Appl. Opt.*, 36, 3097-3104.
- KNMI (2008): Technical note on Ocean Albedo as a function of local wind and wave conditions and its effect on the zero-wind calibration. AE-TN-KNMI-L1B-001, 15 April 2008, 30 pages.
- Leike, I., J. Streicher, Ch. Werner, V. Banakh, I. Smalikhov, W. Wergen, A. Cress (2001): Virtual Doppler Lidar Instrument. *J. Atmos. Ocean. Tech.* 18, 1447-1456.

	Document Nr. <b>AE-RP-DLR-L1B-001</b>	Issue: <b>4.4</b>	Date: <b>20.04.2018</b>	Page: <b>114/117</b>	
	Doc. Title: <b>ADM-Aeolus ATBD Level1B Products</b>				

- Lemmerz, Ch., O. Lux, O. Reitebuch, B. Witschas, Ch. Wührer (2017): Frequency and timing stability of an airborne injection-seeded Nd:YAG laser system for direct-detection wind lidar. *Appl. Opt.* 56, 9057-9068.
- LeRille, O., Endemann, M., Culoma, A., and Wernham, D. (2012). ADM-Aeolus: ESA's high spectral resolution Doppler Wind Lidar Mission - Recent achievements and future prospects. In *Proceedings at the 26th International Laser Radar Conference*, pages 643-646, Porto Heli, Greece.
- Li, Z., Ch. Lemmerz, U. Paffrath, O. Reitebuch, and B. Witschas (2010): Airborne Doppler lidar Investigation of Sea Surface Reflectance at a 355-nm Ultraviolet Wavelength. *J. Atmos. Oceanic Tech.*, 693-704.
- Liu Z., N. Sugimoto, T. Murayama (2002): Extinction-to-backscatter ratio of Asian dust observed with high-spectral-resolution lidar and Raman lidar, *Appl. Opt.*, 41 (15), 2760-2766.
- Liu, Z. S., B. Y. Liu, Z. G. Li, Z. A. Yan, S. H. Wu, and Z. B. Sun (2007): Wind measurements with incoherent Doppler lidar based on iodine filters at night and day. *Appl. Phys.*, B88, 327-335.
- Lolli, S., A. Delaval, C. Loth, A. Garnier, and P. H. Flamant (2013): 0.355-micrometer direct detection wind lidar under testing during a field campaign in consideration of ESA's ADM-Aeolus mission. *Atmos. Meas. Tech.*, 6, 3349–3358.
- Lux, O., Lemmerz, C., Weiler, F., Marksteiner, U., Witschas, B., Rahm, S., Schäfler, A., Reitebuch, O. (2018): Airborne wind lidar observations over the North Atlantic in 2016 for the pre-launch validation of the satellite mission Aeolus. *Atmos. Meas. Tech. Discuss.* <https://doi.org/10.5194/amt-2018-19>.
- Manninen, A. (2012): Characterization of returns from ice and land surface acquired with an airborne ultraviolet LIDAR. Master Thesis at Technical University Munich, 69 pages.
- Marksteiner (2009): Technical Note Incorporation, Description and Analysis of Terrain Model & Mispointing scenarios in the E2S and L1B. AE-TN-ESA-GS-0xx, 25.07.2009
- Marksteiner, U., O. Reitebuch, S. Rahm, I. Nikolaus, Ch. Lemmerz, B. Witschas (2011): Airborne direct-detection and coherent wind lidar measurements along the east coast of Greenland in 2009 supporting ESA's Aeolus mission. *Proc. SPIE Remote Sensing*, Vol. 8182, 19-23 September 2011. 81810J-1 – 81820J-8.
- Marksteiner, U. (2012): Airborne wind lidar observations for the validation of the ADM-Aeolus instrument. Ph. D Thesis at Technical University Munich, DLR Forschungsbericht 2013-25, 176 pages.
- Marseille, G. J., A. Stoffelen (2003): Simulation of wind profiles from a space-borne Doppler wind lidar. *Q. J. R. Meteorol. Soc* 129, 3079-3098.
- McGill, M. J., W. R. Skinner, and T. D. Irgang, (1997): Validation of wind profiles measured with incoherent Doppler lidar. *Appl. Opt.*, 36, 1928-1939.
- McGill M. J., W. D. Hart, J. A. McKay, J. D. Spinhirne (1999): Modeling the performance of direct-detection Doppler lidar systems including cloud and solar background variability. *Appl. Opt.*, 38, 6388-6397.
- Measures, R. M. (1992): *Laser Remote Sensing*, Wiley, Florida, 510 pages.
- Meynart, R., Durand, Y., Endemann, M., Chinal, E., Reitebuch, O. (2006): ALADIN Airborne Demonstrator: a Doppler Wind Lidar to prepare ESA's Aeolus Explorer Mission. *SPIE Optics and Photonics*, 13-17 August 2006, San Diego.
- Mondin, L., P. Bravetti (2014): Aeolus high energy UV Laser wavelength measurement and frequency stability analysis. *Proc. International Conference on Space Optics — ICSO 2014; Volume 10563*; doi: 10.1117/12.2304238.
- Morancais, D., F. Fabre, M. Schillinger, J.-C. Barthes, M. Endemann, A. Culoma (2004). ALADIN: The First European Lidar in Space. *Reviewd and Revised Papers 22<sup>nd</sup> Int. Laser Radar Conference (ILRC 2004)*, Matera, Italy, ESA SP-561, 127-129.
- Nelder, J. A. and R. Mead (1965): A simplex method for function minimization, *The Computer Journal*, 7, 308-313.
- Nikolaus, I. and O. Reitebuch (2016): Technical Note on Range-Dependent Bias Characterisation. AE-TN-DLR-L1B-5300-20170206, V 1.1, 06 Feb 2017, 31 pages.

	Document Nr. <b>AE-RP-DLR-L1B-001</b>	Issue: <b>4.4</b>	Date: <b>20.04.2018</b>	Page: <b>115/117</b>	
	Doc. Title: <b>ADM-Aeolus ATBD Level1B Products</b>				

- Noveltis (2013): A Surface Reflectance Database for ESA's Earth Observation Missions (ADAM). NOV-3895-NT-12403. Ed. 2, Rev. 1. from <http://adam.noveltis.fr/>
- Paffrath U. (2006): Performance assessment of the Aeolus Doppler wind lidar prototype. Ph.D. thesis, Technical University Munich, published as DLR Forschungsbericht FB 2006-12, ISSN 1434-8454, 138 pages.
- Paffrath, U., Lemmerz, Ch., Reitebuch, O., Witschas, B., I. Nikolaus, V. Freudenthaler (2009): The airborne demonstrator for the direct-detection Doppler wind lidar ALADIN on ADM-Aeolus: II. Simulations and Rayleigh receiver radiometric performance. *J. Atmos. Ocean. Tech.*, 26, 2516-2530.
- Press W. H., S. A. Teukolsky, W. T. Vettering, B. P. Flannery (1992): Numerical Recipes in C. The Art of Scientific Computing. 2<sup>nd</sup> edition, Cambridge University Press, 1020 pages.
- Reitebuch, O. (1999): SODAR-Signalverarbeitung von Einzelpulsen zur Bestimmung hochaufgelöster Windprofile. Dissertation an der Universität Regensburg; published at Fraunhofer Institut für Atmosphärische Umweltforschung Band 62-1999. 175 pages, in German.
- Reitebuch, O., Lemmerz, Ch., Nagel, E., Paffrath, U., Durand, Y., Endemann, M., Fabre, F., Chaloupy, M. (2009): The airborne demonstrator for the direct-detection Doppler wind lidar ALADIN on ADM-Aeolus: I. Instrument design and comparison to satellite instrument. *J. Atmos. Ocean. Tech.*, 26, 2501-2515.
- Reitebuch, O. (2012a): Wind lidar for atmospheric research. in Schumann U. (Ed.): Atmospheric Physics – Background, Methods, Trends. Springer Series on Research Topics in Aerospace. ISBN 978-3-642-30182-7, p. 487-507.
- Reitebuch, O. (2012b): The space-borne wind lidar mission ADM-Aeolus. in Schumann U. (Ed.): Atmospheric Physics – Background, Methods, Trends. Springer Series on Research Topics in Aerospace. ISBN 978-3-642-30182-7, p. 815-827.
- Reitebuch, O. (2012c): Wind. in Köpke, P. und M. Sachweh (Eds.): Satellitenmeteorologie, Verlag Ulmer UTB, Stuttgart, ISBN 978-3-825-235253, p. 212-230 (in German).
- Reitebuch, O., and B. Witschas (2014): Über den Wolken. Laser-Fernerkundung in der Atmosphäre. *Physik Journal* 13, Vol. 5, 25-31 (in German).
- Reitebuch, O., U. Marksteiner, M. Rompel, M. Meringer, K. Schmidt, D. Huber, I. Nikolaus, A. Dabas, J. Marshall, F. de Bruin, Th. Kanitz, A.-G. Straume (2017): Aeolus End-to-End Simulator and Wind Retrieval Algorithms up to Level 1B. Proc. 28<sup>th</sup> Int. Laser Radar Conf. ILRC, 25 – 30 June 2017, Bucharest, Romania.
- Rompel, M. (2017) Korrektur und Charakterisierung entfernungsabhängiger Fehler bei dem satellitengetragenen Wind-Lidar auf der ADM-Aeolus Mission. Master-Thesis TU Darmstadt, 52 pages.
- Schillinger, M., D. Morançais, F. Fabre, A. Culoma (2003): ALADIN: the LIDAR instrument for the AEOLUS mission. Proc. SPIE Sensors, Systems, and Next-Generation Satellites VI, Vol 4881, 40-51.
- Schröder T., C. Lemmerz, O. Reitebuch, M. Wirth, C. Wührer, and R. Treichel (2007): Frequency jitter and spectral width of an injection-seeded Q-switched Nd:YAG laser for a Doppler wind lidar. *Appl. Phys.*, B87, 437-444.
- Smith, R. G., P. A. M. Berry, J. Benveniste (2010): ACE2: The New Global Digital Elevation Model. Proc. ESA Living Planet Symposium, Bergen, Norway, ESA SP-686.
- Smith, R. G., and P. A. M. Berry: ACE2: Global Digital Elevation Model. User Guide, 22 pages, from: <http://tethys.eaprs.cse.dmu.ac.uk/ACE2/shared/documentation>
- Spinhire J. D., S. Chudamani, J. F. Cabanaugh, J. L. Bufton (1997): Aerosol and cloud backscatter at 1.06, 1.54, and 0.53  $\mu\text{m}$  by airborne hard-target-calibrated Nd:YAG/methane Raman lidar, *Appl. Opt.*, 36 (15), 3475-3489.
- Souprayen, C., A. Garnier, A. Hertzog, A. Hauchecorne, and J. Porteneuve (1999): Rayleigh-Mie Doppler wind lidar for atmospheric measurements. I. Instrumental setup, validation, and first climatological results. *Appl. Opt.*, 38, 2410-2421.

	Document Nr. <b>AE-RP-DLR-L1B-001</b>	Issue: <b>4.4</b>	Date: <b>20.04.2018</b>	Page: <b>116/117</b>	
	Doc. Title: <b>ADM-Aeolus ATBD Level1B Products</b>				

- Stoffelen, A., Pierre Flamant, Måns Håkansson, Erland Källén, Gert-Jan Marseille, Jean Pailleux, Harald Schyberg, Michael Vaughan (2002): Measurement Error and Correlation Impact on the Atmospheric Dynamics Mission (MERC), ESA project report (CD), 2002, ESA contract 15192/01/NL/MM.
- Stoffelen, A., J. Pailleux, E. Källén, J. M. Vaughan, L. Isaksen, P. Flamant, W. Wergen, E. Andersson, H. Schyberg, A. Culoma, R. Meynart, M. Endemann, P. Ingmann (2005): The Atmospheric Dynamics Mission for Global Wind Field Measurements. *Bull. Am. Meteor. Soc.* 86, 73-87.
- Sun, X. J., R. W. Zhang, G. J. Marseille, A. Stoffelen, D. Donovan, L. Liu, J. Zhao (2014): The performance of Aeolus in heterogeneous atmospheric conditions using high-resolution radiosonde data. *Atmos. Meas. Technol. Discussion*, accepted. doi:10.5194/amtd-7-1393-2014.
- Tan D., E. Andersson., J. Kloe, G.-J. Marseille, A. Stoffelen, P. Poli, M.-L. Denneulin, A. Dabas, D. Huber, O. Reitebuch, P. Flamant, O. Le Rille, and H. Nett (2008): The ADM-Aeolus wind retrieval algorithms. *Tellus*, 60A, 191-205.
- Tenti, G., C. D. Boley, and R. C. Desai (1974): On the kinetic model description of Rayleigh-Brillouin scattering from molecular gases. *Can. J. Phys.*, 52, 285-290.
- Vaughan, J. M., D. W. Brown, C. Nash, S. B. Alejandro, G. G. Koenig (1995): Atlantic atmospheric aerosol studies 2. Compendium of airborne backscatter measurements at 10.6  $\mu\text{m}$ , *J. Geophys. Res.*, 100 (D1), 1043-1065.
- Vaughan, J. M., N. J. Geddes, P. H. Flamant, C. Flesia (1998): Establishment of a backscatter coefficient and atmospheric database, ESA contract 12510/97/NL/RE, 110 pages.
- Wandinger, U., A. Hiebsch, I. Mattis, G. Pappalardo, L. Mona, F. Madonna (2011): Final Report Aerosols and Clouds: Long-term Database from Spaceborne Lidar Measurements. ESTEC Contract 21487/08/NL/HE, 235 pages.
- Wang, Z., Z. Liu, L. Liu, S. Wu, B. Liu, Z. Li, X. Chu (2010): Iodine-filter-based mobile Doppler lidar to make continuous and full-azimuth-scanned wind measurements: data acquisition and analysis system, data retrieval methods, and error analysis. *Appl. Opt.*, 49, 6960-6978.
- Weiler, F. (2017): Bias correction using ground echoes for the airborne demonstrator of the wind lidar on the ADM-Aeolus mission. Master Thesis University Innsbruck, 89 pages.
- Weitkamp, C (2005): Lidar Range-Resolved Optical Remote Sensing of the Atmosphere, Springer, New York, 455 pages.
- Werner C. (2005): Doppler wind lidar, in: Lidar, Weitkamp C. (Ed.), Springer, New York, 325-354.
- Witschas, B., M. O. Vieitez, E.-J. van Duijn, O. Reitebuch, W. van de Water, W. Ubachs (2010): Spontaneous Rayleigh-Brillouin scattering of ultraviolet light in nitrogen, dry air, and moist air. *Appl. Opt.*, 49, 4217-4227.
- Witschas, B. (2011a): Experiments on spontaneous Rayleigh-Brillouin scattering in air. PhD Thesis at Friedrich-Schiller-Universität Jena. DLR Forschungsbericht 2011-17, 112 pages.
- Witschas, B (2011b): Analytical model for Rayleigh-Brillouin lineshapes in air. *Appl. Opt.*, 50, 267-270 and errata in *Appl. Opt.*, 50, 5738.
- Witschas, B. (2012): Light Scattering on Molecules in the Atmosphere. in Schumann U. (Ed.): Atmospheric Physics – Background, Methods, Trends. Springer Series on Research Topics in Aerospace. ISBN 978-3-642-30182-7, p. 69-83.
- Witschas, B., Ch. Lemmerz, O. Reitebuch (2012): Horizontal lidar measurements for the proof of spontaneous Rayleigh-Brillouin scattering in the atmosphere. *Appl. Opt.*, 51, 6207-6219.
- Witschas, B., Ch. Lemmerz, O. Reitebuch (2014): Daytime measurements of atmospheric temperature profiles (2-15 km) by Lidar utilizing Rayleigh-Brillouin scattering. *Opt. Lett.* 39, 1972-1975.
- Witschas, B., S. Rahm, A. Dörnbrack, J. Wagner, M. Rapp (2017): Airborne Wind Lidar Measurements of Vertical and Horizontal Winds for the Investigation of Orographically Induced Gravity Waves: *J. Atmos. Oceanic Techn.*, 34, 1371-1386.

	Document Nr. <b>AE-RP-DLR-L1B-001</b>	Issue: <b>4.4</b>	Date: <b>20.04.2018</b>	Page: <b>117/117</b>	
	Doc. Title: <b>ADM-Aeolus ATBD Level1B Products</b>				

Xia, H., X. Dou, D. Sun, Z. Shu, X. Xue, Y. Han, D. Hu, Y. Han, and T. Cheng (2012): Mid-altitude wind measurements with mobile Rayleigh Doppler lidar incorporating system-level optical frequency control method. *Opt. Exp.* 20, 15286-15300.